2014

Electrochemical Reduction of CO2 on Supported Cu2O Catalysts

Joel Niño Galvez Bugayong

Louisiana State University and Agricultural and Mechanical College

ELECTROCHEMICAL REDUCTION OF CO_2
ON SUPPORTED Cu_2O CATALYSTS

A Dissertation

Submitted to the Graduate Faculty of the
Louisiana State University and
Agriculture and Mechanical College
in partial fulfillment of the
requirements for the degree of
Doctor of Philosophy

in

The Department of Chemical Engineering

by
Joel Niño Galvez Bugayong
B.S., University of the Philippines Los Baños, 2004
M.S., Louisiana State University, 2011
December 2014

This work is dedicated to my Mom who passed away in January of 2014.

You are deeply missed.

ACKNOWLEDGMENTS

<p style="text-align:center">

My Family
Dr. Patrisha J. Pham-Bugayong
Lorenzo Theodore P. Bugayong and future 2nd, 3rd or nth child
Adoracion C. Galvez-Bugayong
Rolando G. Bugayong
Jonathan G. Bugayong and family
Dr. Jennifer G. Bugayong-Luna and family
Ma. Joan G. Bugayong-Ocampo and family
Dr. Chay Binh Pham and Dr. Laura A. Julian-Pham
Alessandra J. Pham-Mondala and husband

Sunday

Fryday, Salmon, Mickey and Mouse

And to the Cornerstone, the Great I Am

</p>

TABLE OF CONTENTS

ABSTRACT

We have examined Cu-based catalyst materials that enable the conversion of CO_2 to useful products such as fuels and chemical feedstocks by electrochemical reduction. In particular, we compared the electrocatalytic activity of supported Cu_2O particles prepared using electrodeposition and wet chemical methods. The particles had cubic structure, ranging in size from 40 nm to 900 nm and consisting of low index planes. We observed significantly different product distribution on these catalysts compared to polycrystalline Cu, specifically for methane and ethylene formation. While Cu particles showed higher faradaic efficiency for methane formation compared to ethylene formation, we observed that Cu_2O particles were more selective to ethylene than methane. For example, the C_2H_4/CH_4 ratio on Cu was 0.2 while the C_2H_4/CH_4 ratio on both electrodeposited Cu_2O film and colloidal Cu_2O particles was around 60.

The Cu_2O particles were reducible and the derived particles consisted of higher number of low-coordinated active sites than Cu which we propose are responsible for the increased ethylene selectivity. At $-1.5V_{NHE}$, electrodeposited Cu_2O film and colloidal Cu_2O particles achieved highest average ethylene faradaic efficiency of 9.4% and 38% respectively while Cu foil only showed 1.2%. The colloidal Cu_2O particles also exhibited better CO selectivity than Cu. While Cu showed 5.5% CO faradaic efficiency, colloidal Cu_2O particles achieved highest average CO faradaic efficiency of 22%. Product distribution on Cu_2O catalysts was primarily influenced by potential and was kinetically dynamic. Nafion mixed with Cu_2O particles was shown to enhance and stabilize ethylene formation.

CHAPTER 1
CURRENT U.S. ENERGY STATUS
AND OVERVIEW OF CO₂ ELECTROCHEMICAL REDUCTION

1.1. Introduction

Electrochemical conversion of CO_2 to liquid fuels and chemical feed stocks is an important research area aimed at developing feasible technologies that promote carbon neutral energy cycles (Lewis et al. 2006, Whipple et al. 2010). CO_2 is considered a greenhouse gas and though it only has a global warming potential (GWP) of 1 (compared to 25 for CH_4 and 298 for N_2O) (US Energy Information Administration | Emissions of Greenhouse Gases in the United States 2009), its impact in the environment is significant because of high emission rates from use of fossil fuel (coal, natural gas, crude oil).

Fossil fuels have dominated energy supply in the United States since 1973. In 2012, they accounted for 79% of total energy production and 82% of total energy consumption. In contrast, renewable sources accounted for only 11% of total energy production and 9% of total energy consumption (see Figure 1.1, 2012 Renewable Energy Data Book). Consequently, CO_2 emission rose from 4,735 million metric tons in 1975 to 6,023 million metric tons in 2007 (US Energy Information Administration 2013). CO_2 concentrations in the atmosphere also reached 390 ppm CO_2 in 2010, which is 39% above pre-industrial levels (IPCC Climate Change 2007: Synthesis Report).

Though production from renewable sources is increasing, our high dependence on fossil fuels will continue in the future because it remains the only reliable source that is able to meet our projected demand. If the use of fossil fuels is to continue, it is imperative that we develop commercially viable technologies that capture, store and recycle CO_2 waste. Studies by the Intergovernmental Panel on Climate Change suggest that in order to

1

maintain CO_2 atmospheric content to below 400 ppm, global CO_2 emissions must decrease by 50-80% from the level reported in 2000.
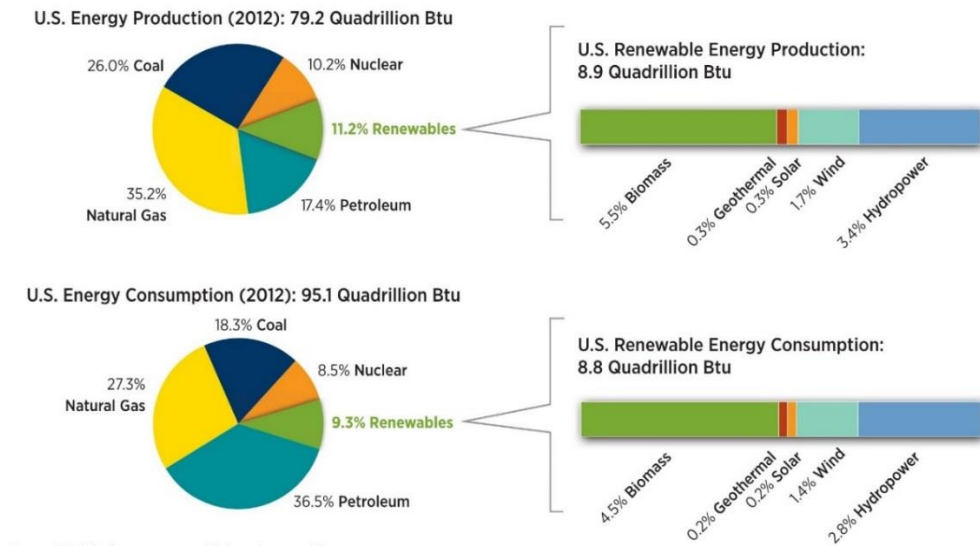
Figure 1.1. 2012 US energy production and consumption.
(Source: 2012 Renewable Energy Data Book, October 2013)

Carbon dioxide (CO_2) capture and storage (CCS) is one of the options considered to stabilize atmospheric greenhouse gas concentrations. It is a process consisting of the separation of CO_2 from industrial and energy-related sources, transport to a storage location in geological formations, in the ocean, and in mineral carbonates, isolated from the atmosphere for an extended period of time or reserved for future use in industrial processes. However, this technology requires an additional 10-40% energy penalty, used mostly for capture and compression of CO_2. There is also concern for potential CO_2 leakage. (IPCC, 2005 Special Report on CCS).

Alternative efforts to mitigate fossil fuel dependence include expanding production from renewable sources. Of these, biomass accounted for 49% of total renewable production (6% of total energy production) in 2011 (US EIA Monthly Energy Review

2

2013). Microalga are used for biofuel production because of their high dry weight oil content. However, sunlight to fuel efficiency is only about 1%. Additionally, large land and water areas are needed to increase supply (Roy et al. 2010).

Other renewable sources include hydroelectric power (4%), wind (2%), geothermal (<1%), and solar (<1%) (US EIA Monthly Energy Review 2013). Hydroelectric power and geothermal power plants have limited growth opportunity because these sources are natural fixtures (Lewis 2007). Nuclear energy source is also an alternative to fossil fuels. However, storage of nuclear waste is a problem. Likewise, when a nuclear power plant is damaged, it creates a serious health problem to surrounding community (Rapier and Thurber 2013).

On the other hand, wind and solar energy have greatest growth potential. For example, to meet the energy demands in the United States, a solar panel with an area of 400 km x 400 km will be required as shown in Figure 1.2 (Lewis 2007).

Figure 1.2. Representation of land requirement for solar panel to meet the energy demands in the United States. (Source: Lewis, N.S. 2007. "Powering the Planet." Engineering and Science No. 2, p. 22)

However these sources are intermittent and unpredictable, requiring electricity storage to minimize supply fluctuation (Whipple et al. 2010). Despite abundant sun power, solar energy is still limited by high manufacturing and grid installation costs (Lewis 2007).

Lastly, wind and solar energy are mainly used to supply electrical energy and have limited application to transportation fuels (Lewis et al. 2006).

1.2. Framework for Integrating CO_2 Electrochemical Reduction

In the future, we envision an energy cycle that utilizes electrochemical reduction as a process to recycle CO_2. The process flow is shown in Figure 1.3. In order for the technology to be sustainable, the required electricity to drive the reaction must come from non-fossil fuel sources such as solar energy, wind energy and nuclear energy. Purified CO_2 will be initially collected from fixed sources such as power plants. Products of CO_2 reduction will be collected, separated and purified through a separate set of unit operations while excess CO_2 will be recycled back to the reactor. Eventually, technology must also be developed to capture atmospheric CO_2 emitted by mobile sources such as automobiles and airplanes.
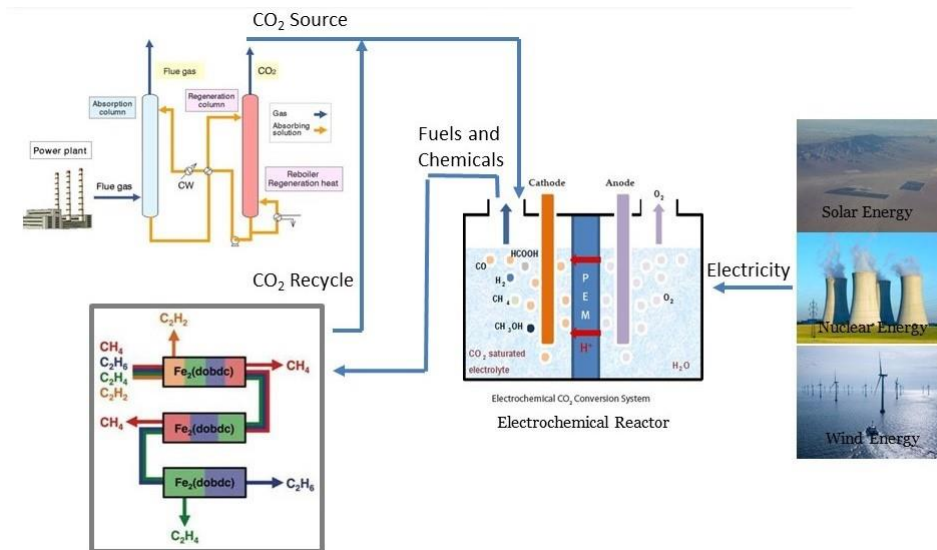
Figure 1.3. Framework for integrating CO_2 electrochemical reduction to existing energy infrastructure. (Image sources: (a) power plant - http://www.chiyoda-corp.com/, (b) electrochemical reactor - http://enpl.cau.ac.kr, (c) separation unit – http://alchemy.cchem.berkeley.edu/, (d) solar energy - http://en.wikipedia.org/wiki/Nevada_Solar_One, (e) nuclear energy – http://herguthlaboratories.wordpress.com, (f) wind energy - http://macaulay.cuny.edu/eportfolios/alternativeenergyinnewyork/wind-energy-in-nyc/.)

1.3. Statement of Problem and Research Objectives

We identify rising CO_2 content in the atmosphere as a critical condition that needs to be resolved. We present electrochemical reduction as a promising technology to control continued increase in CO_2 level by recycling them into fuels and chemical feedstocks. This technology aims to reduce our consumption of fossil fuels which would prevent further growth of CO_2 concentration in the atmosphere. We focus our work on developing electrocatalysts and understanding their catalytic activity towards CO_2 conversion. Particularly, we develop, synthesize and test foreign Cu_2O particles deposited onto a support substrate.

In previous literature, Cu(I) was identified to have the unique ability to produce hydrocarbons and alcohols from CO_2. However, factors affecting selectivity among these CO_2 products remain unclear. Hence, further exploration into the surface of Cu_2O is necessary. In this project, our main objective is to understand the role of oxide in copper during CO_2 conversion to CO, hydrocarbons and alcohols. To facilitate this goal, we will examine several factors that might be expected to affect the stability of the Cu_2O electrode, including (1) influence of Cu_2O particle morphology derived from applying various synthesis conditions, (2) effect of Nafion binder coating, (3) effect of CuO sublayer and (4) type of support substrate used; namely Toray carbon fiber paper, glassy carbon and copper.

1.4. Overview of Dissertation

Chapter 2 is a literature review that covers a brief highlight on CO_2 conversion processes and thermodynamics of CO_2 electrochemical reduction. It also covers details of experimental studies that have been done on copper and copper oxide, particularly,

contributions from the group of Hori, Kuhl, Schouten and Li. Computational studies are also reported, particularly, contributions from the group of Peterson and Nie. The contents are carefully selected and presented in a manner that tailors to the results and discussion on the electrocatalytic activity of Cu_2O.

Chapter 3 provides the general methodology that covers procedure for electrode fabrication and characterization, CO_2 reduction, electrochemical measurements, gas chromatography and data processing.

Afterwards, the main content of this work is then covered in Chapters 4, 5 and 6. Chapter 4 covers our study on polycrystalline copper. We studied the kinetics and potential dependency of CO_2 products on Cu foil to provide the most suitable comparison for our results on Cu_2O.

Chapter 5 covers our work on Cu_2O films fabricated by electrochemical deposition. We studied the effect of oxide thickness on CO formation. We determined the kinetics of CO_2 reduction at a fix potential of $-1.5V_{NHE}$. We then examined the effect of Nafion and growing Cu_2O films on a CuO substrate.

Chapter 6 covers our results on colloidal Cu_2O particles synthesized by wet chemical reduction. In this chapter, we examined the reproducibility of product distribution on Toray supported Cu_2O particles. We studied the effect of different preparation conditions; namely, (1) composition of NaOH, (2) synthesis aging time, (3) amount of Nafion. We also studied the effect of cyclic voltammetry. Finally, we compared the product distribution on two sets of Cu_2O particles at different potentials. In this Chapter, we also studied the electrocatalytic activity of Cu_2O particles supported on glassy carbon and copper.

Finally, we close the dissertation with Chapter 7 for summary, conclusion and recommendations where we highlight key results and provide over-all insights into the conversion of CO_2 on Cu_2O catalysts. We then provided our suggestions for future experiments.

CHAPTER 2
REVIEW OF RELATED LITERATURE

2.1. Overview of CO₂ Conversion Technologies

Centi et al. (2013) published a paper outlining the prospect of integrating renewable energy sources on different CO_2 conversion technologies being developed for the chemical industry. In this dissertation, I referred to this material to highlight the important products that can be derived from CO_2 using different catalytic reactions. The reader is referred to the article published by Centi et al. (2013) for details on the current status and progress on these different CO_2 conversion technologies and how renewable energy sources may be integrated to existing infrastructures.

The list and names of CO_2 reactions are given below. The formation of CO and H_2 opens up pathway for the formation of C_n hydrocarbons and oxygenates through the Fischer-Tropsch (Centi et al. 2013).

$$CO_2 + H_2O \leftrightarrow HCOOH + O_2$$

(electrochemical, photoelectrochemical reduction) [Eq. 2-1]

$$CO_2 + 4H_2 \leftrightarrow CH_4 + 2H_2O \text{ (Sabatier reaction)}$$ [Eq. 2-2]

$$CO_2 + H_2 \leftrightarrow CO + H_2O \text{ (reverse water gas shift reaction)}$$ [Eq. 2-3]

$$CO_2 + CH_4 \leftrightarrow 2CO + 2H_2 \text{ (dry reforming of methane)}$$ [Eq. 2-4]

$$\begin{cases} CO_2 + H_2O \leftrightarrow CO + 3H_2 \\ CH_4 + {}^1\!/_2 O_2 \leftrightarrow CO + 2H_2 \\ CH_4 + 2O_2 \leftrightarrow CO_2 + 2H_2O \end{cases} \text{(tri-reforming of methane)}$$ [Eq. 2-5]

$$\begin{cases} CO_2 + H_2 \leftrightarrow CO + H_2O \\ CO + 2H_2 \leftrightarrow CH_3OH \end{cases} \text{(methanol synthesis from syngas)}$$ [Eq. 2-6]

$$CO_2 + 3H_2 + CH_3OH \leftrightarrow 2CH_3OH + H_2O$$

(tri-catalyst cascading methanol synthesis, Huff and Sanford 2011) [Eq. 2-7]

8

All of these reactions are well established in industrial processes with the exception of electrochemical and photoelectrochemical routes of CO_2 conversion.

2.2. CO_2 Electrochemical Reduction

Electrochemical conversion of CO_2 to liquid fuels and chemical feed stocks is an attractive candidate process in the over-all portfolio of existing CO_2 conversion technologies being developed to provide a sustainable form of energy (Whipple et al. 2010). Hydrogen remains the most mature chemical form of energy storage. Nonetheless, we will continue to deal with its unfavorable characteristics such as low volumetric density and low tolerance towards ignition (Centri et al. 2013). Moreover, use of hydrogen would require addition of new energy infrastructures to existing ones. (Roy et al. 2003, Whipple et al. 2010). On this note, chemical storage of energy from hydrocarbons and oxygenates would be more advantageous. These products of CO_2 reduction have higher energy density than H_2 as well as NiMH, NaS, and Li-ion batteries as shown in Figure 2.1 (Det Norske Veritas 2011). In particular, the liquid phase products of CO_2 are more convenient to handle and store. As such, this technology easily adapts to existing energy infrastructures (Centri et al. 2013).
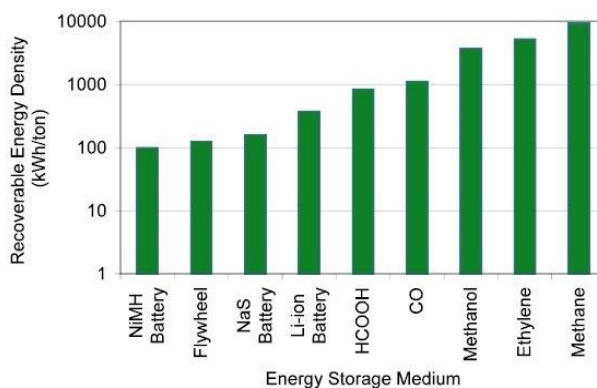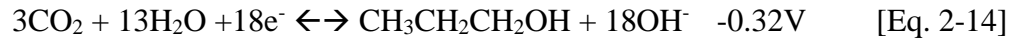

Figure 2.1. Recoverable energy density of products created from electrochemical CO_2 conversion processes compared to selected batteries (Det Norske Veritas 2011).

2.3. Thermodynamics of CO_2 Reduction

CO_2 electrochemical reduction involves electrolysis of a conductive solution saturated with CO_2 between two immersed electrodes at a sufficiently negative potential, larger than the thermodynamic requirement. In aqueous media, products of CO_2 reduction that have been reported in literature include H_2, CO, formate, methanol, CH_4, C_2H_4, ethanol and n-propanol. The stoichiometry of these reactions with their SHE standard reduction potential can be written in the order of electron requirement as follows (Hori 2008, Bard et al. 2001, Varcoe et al. 2004):

$$CO_2 + H_2O + 2e^- \leftrightarrow CO + 2OH^- \qquad\qquad -0.52V \qquad [Eq.\ 2\text{-}8]$$

$$CO_2 + H_2O + 2e^- \leftrightarrow HCOO^- + OH^- \qquad\qquad -0.43V \qquad [Eq.\ 2\text{-}9]$$

$$CO_2 + 5H_2O + 6e^- \leftrightarrow CH_3OH + 6OH^- \qquad\qquad -0.81V \qquad [Eq.\ 2\text{-}10]$$

$$CO_2 + 6H_2O + 8e^- \leftrightarrow CH_4 + 8OH^- \qquad\qquad -0.25V \qquad [Eq.\ 2\text{-}11]$$

$$2CO_2 + 8H_2O + 12e^- \leftrightarrow C_2H_4 + 12OH^- \qquad\qquad -0.34V \qquad [Eq.\ 2\text{-}12]$$

$$2CO_2 + 9H_2O + 12e^- \leftrightarrow CH_3CH_2OH + 12OH^- \qquad -0.33V \qquad [Eq.\ 2\text{-}13]$$

$$3CO_2 + 13H_2O + 18e^- \leftrightarrow CH_3CH_2CH_2OH + 18OH^- \quad -0.32V \qquad [Eq.\ 2\text{-}14]$$
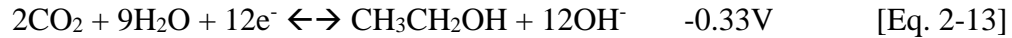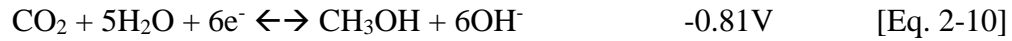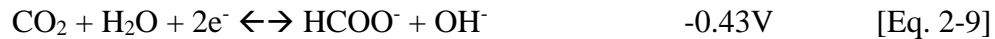
When operating at these negative potentials using Cu_2O electrodes, the SHE standard reduction potential of Cu(I) and Cu(II) to Cu must also be taken into consideration (Bard et al. 1985):

$$2CuO + H_2O + 2e^- \leftrightarrow Cu_2O + 2OH^- \qquad\qquad -0.220V \qquad [Eq.\ 2\text{-}15]$$

$$Cu_2O + H_2O + 2e^- \leftrightarrow 2Cu + 2OH^- \qquad\qquad -0.365V \qquad [Eq.\ 2\text{-}16]$$

$$CuO + H_2O + 2e^- \leftrightarrow Cu + 2OH^- \qquad\qquad -0.290V \qquad [Eq.\ 2\text{-}17]$$

Buffer solutions formed by hydrogen bicarbonates are the most commonly used electrolyte. The thermodynamic equilibria of CO_2 in aqueous bicarbonate solution are given below (Hori 2008):

$$CO_2 + H_2O \longleftrightarrow HCO_3^- + H^+ \qquad pK_{a1} = 6.35 \text{ at } 25^oC \qquad \text{[Eq. 2-18]}$$

$$HCO_3^- \longleftrightarrow CO_3^{2-} + H^+ \qquad pK_{a2} = 10.33 \text{ at } 25^oC \qquad \text{[Eq. 2-19]}$$
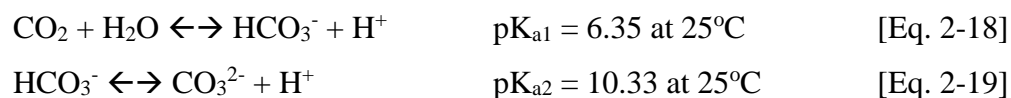
Since hydrogen activity is dominant in acidic conditions and CO_2 molecules do not exist in basic conditions, CO_2 reduction is conducted in neutral pH environment (Hori 2008).

2.4. Electrode Materials

Several electrode materials have been considered for CO_2 electrochemical reduction. The simplest of these are metals. They are conveniently classified as being either HCOO-forming or CO-forming. The HCOO-forming metals include Pb, Hg, In, Sn, Cd, and Tl. The CO-forming metals are further divided into groups based on CO adsorption. They either strongly adsorb CO onto their surface (Ni and Pt) and produce mainly H_2 or weakly adsorb CO (Au, Ag, Zn, Pd, and Ga) and produce mainly CO. (Hori 2008) A unique metal in this group is Cu, which moderately adsorbs CO and as a result produces a wide range of products including hydrocarbons and alcohols (Kuhl et al. 2012, Gattrell et al. 2006, Peterson et al. 2010, Roy et al. 2010). For this reason, Cu is the electrode of interest in this study.

2.5. CO_2 Reduction on Copper Catalysts

2.5.1. Studies on Polycrystalline Cu Electrodes

2.5.1.1. Major Products of Copper

Various forms of Cu electrode have been studied, including single crystal Cu, polycrystalline Cu and alloys of Cu (Hori 2008). Pioneering works by Hori et al. (1989) reported faradaic efficiency of hydrocarbons and alcohols using electrodeposited Cu and are shown in Table 2.1.

Table 2.1. CO_2 products on electrodeposited Cu, -1.65V (SCE) (Hori et al. 1989)[*]

CO$_2$ Products	Faradaic Efficiency, %
CH$_4$	29.4
C$_2$H$_4$	30.1
Ethanol	6.9
n-Propanol	3.0
CO	2.0
HCOO$^-$	9.7
H$_2$	10.9

[[*]Note: Reproduced with permission from The Royal Society of Chemistry.]

Faradaic efficiency is the fraction of total current consumed to reduce CO_2 to a specific product. As such, it gives insight into the selectivity of the catalyst. High faradaic efficiency indicates that a specific product is selectively formed. From Table 2.1, we see that Cu was most selective to CH_4 and C_2H_4 at the applied potential.

Hori's group also demonstrated variations in faradaic efficiencies of CO_2 products with applied potential (see Figure 2.2). The plot shows that CO formation was the first step in CO_2 reduction occurring at an onset potential of about -0.8V$_{NHE}$. The CO selectivity rose to about 20% near -1.25V$_{NHE}$ and then fell to about 2% near -1.45V$_{NHE}$. The onset formation of CO was closely followed by HCOO$^-$ which showed a similar selectivity pattern with that of CO. Ethylene was the next compound produced from CO_2 reduction with an onset potential near -1.1V$_{NHE}$. The ethylene efficiency appeared to peak at -1.45V$_{NHE}$ with a measured selectivity of 23.4%. Finally, methane was the last product detected with an onset potential of -1.2V$_{NHE}$. The CH_4 selectivity rose rapidly and became the more favorable product than C_2H_4 at potentials more negative than -1.32V$_{NHE.}$
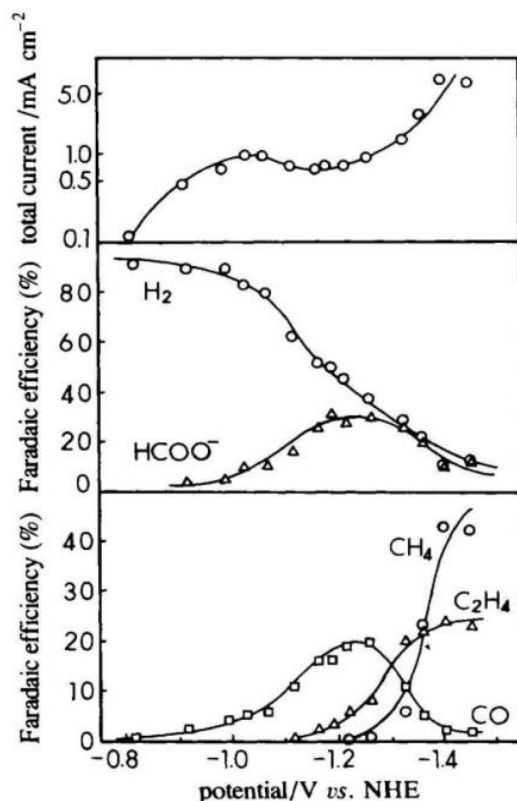
Figure 2.2. Variation of the faradaic efficiencies of the products in electrochemical reduction of CO_2 obtained in controlled potential electrolysis, 0.1 mol/dm^3 KHCO$_3$ at 19 ^{0}C (Hori et al. 1989). [Reproduced with permission from The Royal Society of Chemistry.]

The CH$_4$/C$_2$H$_4$ selectivity reached a high of 1.9 near -1.45V$_{NHE}$. The increase in hydrocarbon formation with potential was coupled with a decline in hydrogen formation which initially dominated the process at a high selectivity of 92% near -0.8V$_{NHE}$. The H$_2$ selectivity fell continuously with potential reaching a low of 12% at near -1.45V$_{NHE}$. Figure 2.2 also showed the total current profile which had a characteristic shoulder near -1.1V$_{NHE}$. Hori attributed this shoulder to adsorption of CO which reduced the activity for H$_2$ formation. The current density was in the range of 0.1 to 5.0 mA/cm^2.

In another early study, Noda et al. (1989) also examined the CO$_2$ product distribution on Cu as a function of applied potential. They used electrochemical reduction conditions that were similar to that of Hori except that they operated the process at 25 ^{o}C

13

instead of 19 ℃. They also used polycrystalline Cu instead of electrodeposited polycrystalline Cu. The potential range they considered was between $-1.35V_{Ag/AgCl}$ to $-1.75V_{Ag/AgCl}$ (equivalent to $-1.15V_{NHE}$ to $-1.55V_{NHE}$) compared to the $-0.80V_{NHE}$ to $-1.45V_{NHE}$ range that Hori's group considered.

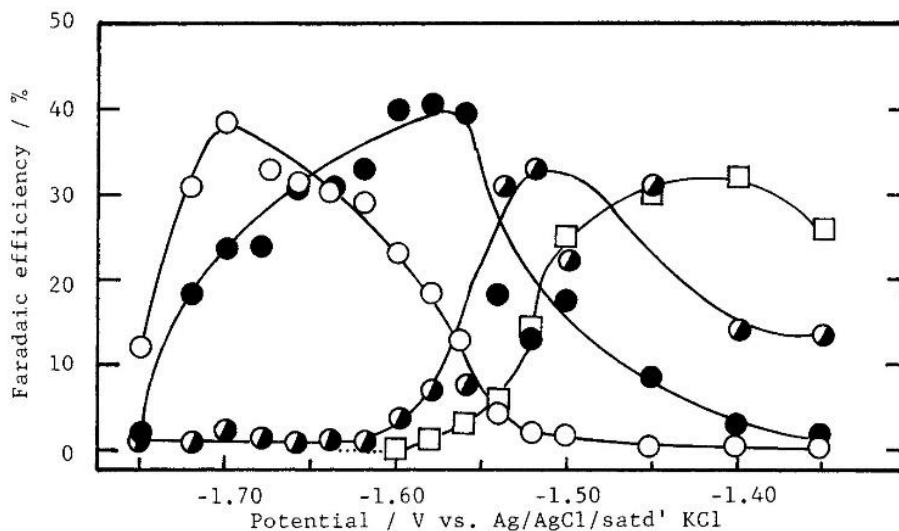Fig. 1. The faradaic efficiency - potential curves for formations of HCOO⁻ (☐), CO (◑), C_2H_4 (●), and CH_4 (○) in 0.1 mol dm⁻³ KHCO₃ aq. solution at 298 K.

Figure 2.3. The faradaic efficiency-potential curves for formations of HCOO⁻, CO, C_2H_4 and CH_4 in 0.1 mol/dm³ KHCO₃ aq. solution at 298K. [Reproduced with permission from the Chemical Society of Japan.]

The CO_2 product distribution plotted in Figure 2.3 are shown in reverse order of potential. They arrived at a similar product distribution. They were able to show that CH_4 faradaic efficiency peaked near $-1.5V_{NHE}$ while ethylene faradaic efficiency peaked near $-1.37V_{NHE}$. They also achieved higher ethylene faradaic efficiency of 41% at the peak potential. Besides gas-phase products, they also observed intermediate amounts of solution-phase products such as acetaldehyde (a.k.a. ethanal) and propionaldehyde (a.k.a. propanal) that were not observed by Hori's group during that time.

14

2.5.1.2. Trace Products of Copper

Kuhl et al. (2012) also conducted CO_2 electrochemical reduction on polycrystalline Cu at different potentials. They measured products using GC and NMR in which they classified them as major, intermediate or minor products (see Figure 2.4).
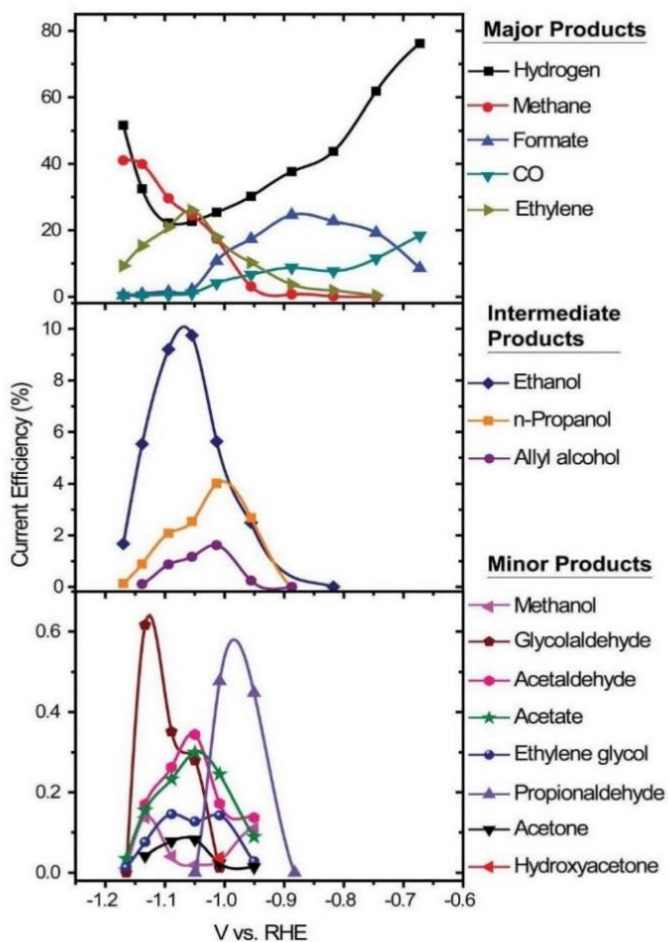
Figure 2.4. Major, intermediate and minor products of CO_2 reduction on polycrystalline Cu (Kuhl et al. 2012). [Reproduced with permission from the Royal Society of Chemistry.]

The important part of their results was the observation of new liquid products that were not previously reported by using NMR. These products include methanol (H_3C-OH), the C_2 oxygenates glycolaldehyde (HO-CH_2-CH=O), ethylene glycol (HO-CH_2-CH_2-OH) and acetone ((H_3C)$_2$-C=O) and the C_3 oxygenate hydroxyacetone (H_3C-CO-CH_2-OH).

15

However, these additional products were only measured in trace amounts (Kuhl et al. 2012).

2.5.2. Effect of Crystal Orientation on Selectivity of Cu

Going back to Hori's group, they also studied and compared a series of different orientations of single crystal Cu and showed that Cu(111) surfaces preferably promote CH_4 over C_2H_4 while Cu(100) surfaces preferably promote C_2H_4 over CH_4. When Cu(111) steps were incorporated to Cu(100) base, C_2H_4 formation was also enhanced. C_2H_4 formation was strongest at Cu(911) and Cu(711) surfaces. Cu(711) surface exhibited the highest C_2H_4/CH_4 faradaic efficiency ratio, at 13.6 (refer to Figure 2.5).
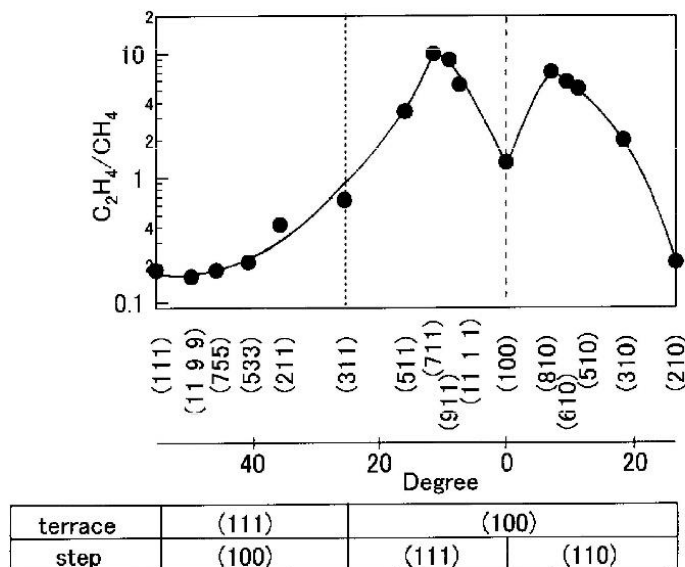

Figure 2.5. Ethylene to methane selectivity at different Cu single crystal planes (Hori et al. 2003). [Reproduced with permission from Elsevier B.V.]

Frese observed a similar trend between CH_4 and C_2H_4 on Cu(100), Cu(110) and Cu(111) (Hori et al. 2002). Hori extended studies on the effect of crystal orientations and have

additionally observed acetic acid as a major product on Cu (110), along with trace amounts of allyl alcohol, acetaldehyde and propionaldehyde.

Tang et al. (2012) examined surface morphological effect of different polycrystalline Cu on CO_2 products by comparing an electropolished Cu (smooth surface) with Cu that was overlaid with Cu nanoparticles (rough surface). With their results, they observed that roughened Cu surfaces improve hydrocarbon selectivity, particularly ethylene, which they attributed to increased number of lowly coordinated edges, defects and steps. Whereas with smooth surface, Cu becomes more H_2 selective due to higher number of low index planes such as Cu (100) and Cu (111).

2.5.3. Other Factors Affecting Selectivity on Cu

Hori's group also studied the effect of temperature and type of salt used in the electrolyte. The electrocatalytic activity of copper towards CH_4, C_2H_4, CO and H_2 was found to be very sensitive to temperature but not towards $HCOO^-$. In particular, CH_4 is favorably produced at 0 °C at a faradaic efficiency of 65%. The CH_4 selectivity then drops steeply to 5% at 40°C. Meanwhile, the effect of temperature on C_2H_4 selectivity is opposite to that of CH_4, with only 3.5% efficiency at 0 °C but rising to 20% at 40°C. Meanwhile, the increase in CO selectivity with temperature is less pronounce, rising only from 1% to 5% between 0-40°C temperature range (Hori et al. 1986). This dramatic temperature effect on selectivity between CH_4 and C_2H_4 was similarly observed by Cook et al. in 1988 using glassy carbon supported Cu_2O electrodeposit.

The selectivity of Cu is also influenced by the type of electrolyte used. For example, the CO_2 product distribution on 0.1M $KC10_4$ at 5 mA/cm^2 is 10.2% CH_4, 48.1% C_2H_4, 15.5% ethanol, 4.2% n-propanol, 2.4% CO, 8.9% $HCOO^-$ and 6.7% H_2. Whereas in 0.1M

K_2HPO_4 at 5 mA/cm^2 the CO_2 product distribution is significantly different; 17.0% CH_4, 1.8% C_2H_4, 0.7% ethanol, 1.3% n-propanol, 5.3% CO and 72.4% H_2. Differences in selectivity were most notable on C_2H_4 and H_2 (Hori et al. 1988).
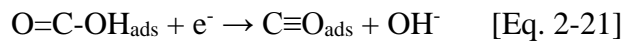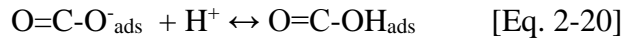
2.5.4. Mechanisms of CO$_2$ Product Formation

2.5.4.1. Experimentally Suggested Pathways

All these results highlight the sensitivity of copper surfaces to different surface and electrochemical conditions which adds to the complexity of its unique attribute. Currently, there is no reaction pathway that completely and accurately describes the reduction of CO_2 on copper to at least 17 different C-containing products (H_2 not included). However, there are several pieces of experimental evidence on Cu and other metals which suggest that the first step in the reduction of CO_2 to hydrocarbons and oxygenates is the formation of adsorbed CO_2^- radical ($O=C-O^-_{ads}$) which is subsequently reduced to adsorbed CO ($C\equiv O_{ads}$) (Hori et al. 1989, Beden et al. 1982, Aylmer-Kelly et al. 1973, McQuillan et al. 1975, Aurian-Blajeni et al. 1983, Chandrasekaran and Bockris 1987, Oda et al. 1996). CO_2 can also be reduced to $HCOO^-$. However, it is thought that this pathway no longer undergo any succeeding reduction steps (Hori et al. 1989).

Two pathways have been suggested for the formation of adsorbed CO from CO_2^-. The first one is protonation followed by reduction;

$$O=C-O^-_{ads} + H^+ \leftrightarrow O=C-OH_{ads} \qquad \text{[Eq. 2-20]}$$
$$O=C-OH_{ads} + e^- \rightarrow C\equiv O_{ads} + OH^- \qquad \text{[Eq. 2-21]}$$

The second one involves reaction with adsorbed H atom.

$$O=C-O^-_{ads} + H_{ads} \rightarrow C\equiv O_{ads} + OH^- \qquad \text{[Eq. 2-22]}$$
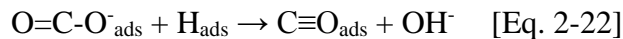
In both of these pathways, H_2 formation reactions play an essential role as well. Since the pH condition of most CO_2 reduction process occurs below pH = 11, the H_2 evolution commence as follows, with the first step being the adsorption of H^+ ion.

$$H^+ + e^- \rightarrow H_{ads} \qquad\qquad \text{[Eq. 2-23]}$$

This is followed by H-H coupling or by an electrochemical desorption (Bockris and Pentland, 1952),

$$2H_{ads} \rightarrow H_2 \qquad\qquad \text{[Eq. 2-24]}$$
$$H_{ads} + H^+ + e^- \rightarrow H_2 \qquad\qquad \text{[Eq. 2-25]}$$

Several optical and spectroscopic studies have observed adsorbed CO at sufficient cathodic potential (Hori et al. 1998, Oda et al. 1996, Smith et al. 1997) Likewise, reduction of CO also resulted in similar product distribution (Hori et al. 1987, Hori et al. 1997, DeWulf et al. 1989) which suggests that all hydrocarbons and oxygenates descend from a CO intermediate. From adsorbed CO, the possible routes become wide open and more difficult to confirm, with each pathway dependent upon kinetic barriers (Nie et al. 2013) and local rate determining step (Taniguchi 1989, Frese et al. 1993, Hori 2003).

Hori's group presented a reaction pathway for the formation of CH_4, C_2H_4, ethanol and n-propanol which closely resembles with the reaction pathways in the Fischer-Tropsch reactions involving CO and H_2. Accordingly, he proposed that all these compounds are formed through a CHOH (hydroxymethylene) then CH_2 (methylene) intermediate. Additionally, he proposed that ethanol and n-propanol would proceed through a $CH_2=C=O$ (ketene) then $CH_2=CH-OH$ (ethenol) intermediate (refer to Figure 2.6). Subsequently, Hori in 1997 further proposed that COH is also an intermediate to CH_4.
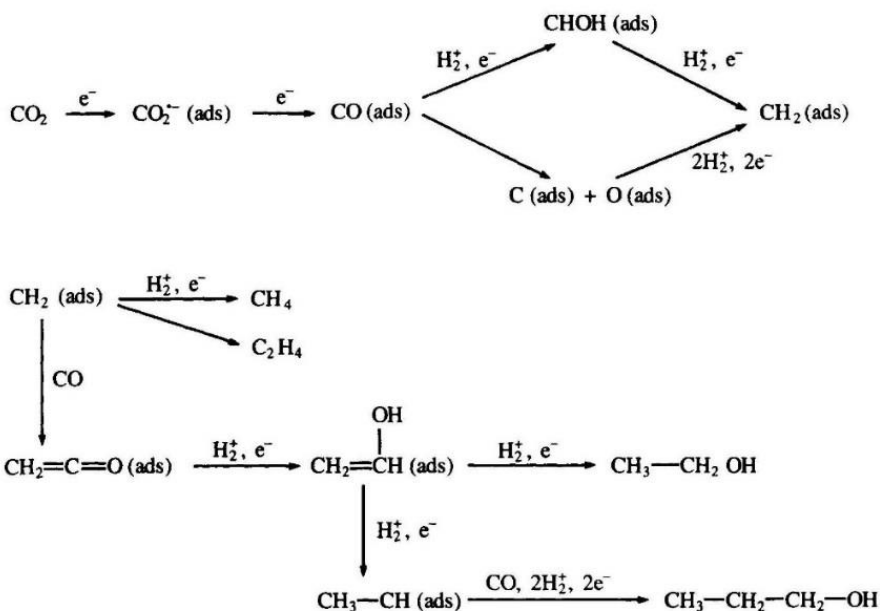
Figure 2.6. Reaction pathways of CO_2 reduction to different hydrocarbons and alcohols proposed by Hori et al. in 1989. [Reproduced with permission from The Royal Society of Chemistry.]

Meanwhile, the group of Kuhl suggested that the precursor to different C_{2+} oxygenates is the formation of an enol-like intermediate (with a representative enol form of glyoxal, $HO-CH_2=C-(OH)_2$). Due to the presence of hydroxyl and/or carbonyl functional group in these C_{2+} oxygenates, Kuhl further proposed that there is a C-C coupling step and that it takes place before the breaking of at least one of the two bonds in CO_2. However, the steps between the adsorbed CO and the enol-like intermediate for both the C_2 and C_3 pathways remain unclear. Additionally, as to which C_1 and C_2 intermediates participate in C-C coupling could not be identified at this point. Nonetheless, the group presented different options for C_1 intermediates derived from computational studies on Cu(211) (Peterson et al. 2010), Cu(111) (Zhao et al. 2011) and experimental studies on Ag surface by Kostecki and Augustynski (1994). These include CO, COOH (carboxyl), CHO (carbonyl), C-(OH)$_2$ (dihydroxycarbene or dihydroxymethylene), COH

20

(hydroxymethylidyne) and formaldehyde (CH_2O). As seen from Figure 2.7, ethylene, ethanol and n-propanol were considered the most reduced form of CO_2 while glyoxal and hydroxyacetone were the least reduced form of CO_2 among the C_{2+} oxygenates and that reactions proceed through a series of $2e^- + 2H^+$ additions.
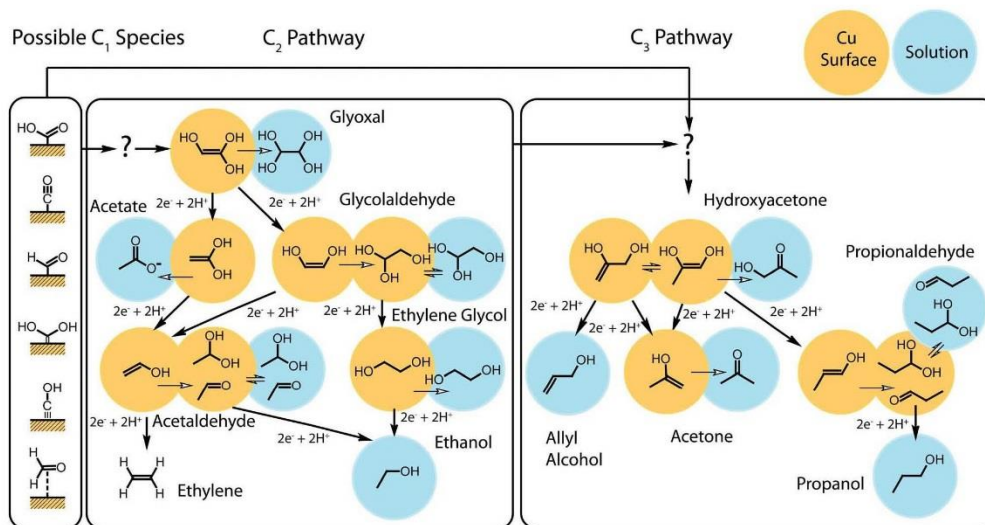

Figure 2.7. Experimentally derived reaction pathways of CO_2 reduction to different hydrocarbons and oxygenates proposed by Kuhl et al. in 2012. [Reproduced with permission from The Royal Society of Chemistry.]

The reaction pathways proposed by Schouten's group in 2011 so far provides the most consistent information for methane and ethylene formation based on a realistic electrochemical environment (see Figure 2.8). In order to verify the reaction intermediates of CO_2 reduction, they considered the reduction of formaldehyde (CH_2O), methanol (methoxy at high pH, CH_3O), glyoxal (OHC-CHO), glycoaldehyde (HO-CH_2-CHO), ethylene glycol (HO-H_2C-CH_2-OH) and ethylene oxide (H_2COCH_2) and monitored products using mass spectrophotometer.

Reduction of formaldehyde (CH_2O) produced methanol (CH_3OH) but not formic acid (HCOOH). However, with long term electrolysis, CH_4 was also formed. Meanwhile,

21

reduction of methanol/methoxy did not produce methane. As such, they suggested that CH_4 is formed through a closely related intermediate to formaldehyde which is formyl (CHO_{ads}) and that CHO_{ads} occurs by hydrogen activated dissociation of CO_{ads} (Ciobica and van Santen 2003, Inderwildi et al. 2008, Shetty et al. 2010, Shetty and van Santen 2010). On the other hand, methanol is formed through the other closely related intermediate to fomaldehyde which is hydroxymethyl (CH_2OH_{ads}). This is in contrast to $Cu/ZnO/Al_2O_3$ catalyzed gas phase methanol synthesis where sequentially formate and formaldehyde are the intermediates to that product (Bowker et al. 1988, Nakatsuji and Hu, 2000).
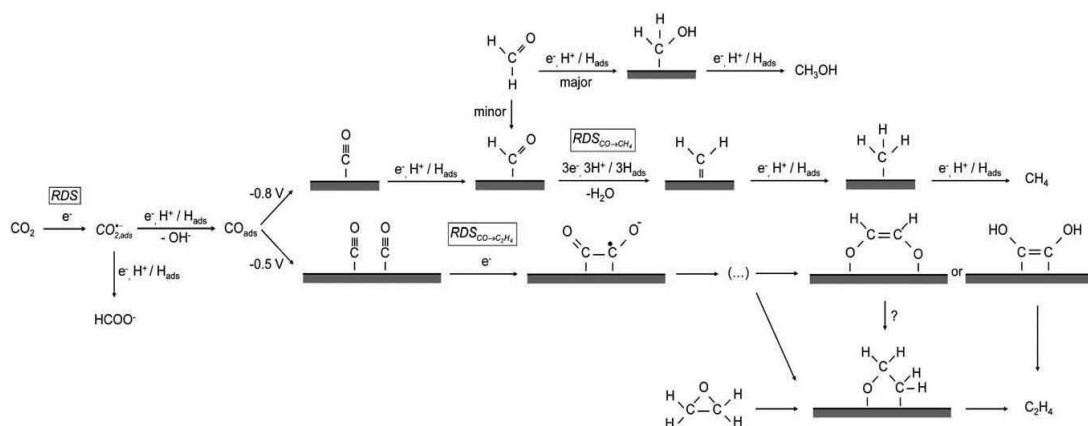

Figure 2.8. Experimentally derived reaction pathways of CO_2 reduction to CH_4, CH_3OH and C_2H_4 proposed by Schouten et al. in 2011. [Reproduced with permission from The Royal Society of Chemistry.]

Reduction of ethylene oxide produced ethylene and no other alcohols and aldehydes. From this result, Schouten's group suggested epoxide in the form of an oxametallacycles as a possible pre-requisite to ethylene. Additionally, they postulated that adsorbed CO dimer ($O=C-C-O^-$) is the first intermediate to the ethylene pathway, similar to that suggested by Gatrell et al. (2006). However, their experimental results are not

sufficient at this point to elucidate the steps proceeding the CO dimer including the epoxide step.

Other experimentally derived reaction pathways include the works of Friebe et al. (1997), DeWulf et al. (1989) and Cook et al. (1988).

2.5.4.2. Computationally Derived Pathways

Computational tools have also been employed to construct the complex reaction pathways of CO_2 conversion to hydrocarbons. To date, calculations using density functional theories have hypothesized CO_2 pathways to CO, HCOO, CH_4, C_2H_4, and CH_3OH using data from reaction free energies and activation barriers (Peterson et al. 2010, Nie et al. 2013). There is a general agreement that CO is an important intermediate to hydrocarbon formation (Kuhl et al. 2012). Peterson et al. (2010) hypothesized that the rate determining step in the formation of CH_4 and C_2H_4 is the hydrogenation of adsorbed CO to form CHO_{ads}. With CH_4, the sequential intermediates involved are adsorbed formaldehyde (CH_2O_{ads}) and adsorbed methoxy (CH_3O_{ads}) through addition of a proton-electron pair. With C_2H_4, Peterson listed possible intermediate pairings, (a) CH_2O_{ads} + CH_2O_{ads} (formaldehyde), (b) CH_2O_{ads} (formaldehyde) + CHO_{ads} (carbonyl), (c) CHO_{ads} + CHO_{ads} (carbonyl), (d) CHO_{ads} (carbonyl) + OCH_{3ads} (methoxy).

On the other hand, Nie et al. (2013) proposed a major branching point for CH_4, C_2H_4 and CH_3OH from the CO intermediate based on DFT calculation that incorporate reaction free energies and reaction kinetics of elementary steps. As shown in Figure 2.9, CO will branch out to either COH_{ads} or CHO_{ads} intermediate. CH_3OH is preferably formed through the CHO_{ads} branch point that involves the formation of detached formaldehyde (CH_2O) followed by an adsorbed methoxy (OCH_3). CH_4 and C_2H_4 are preferably formed

through the COH$_{ads}$ branch point that involves dissociation of OH followed by a series of H addition.
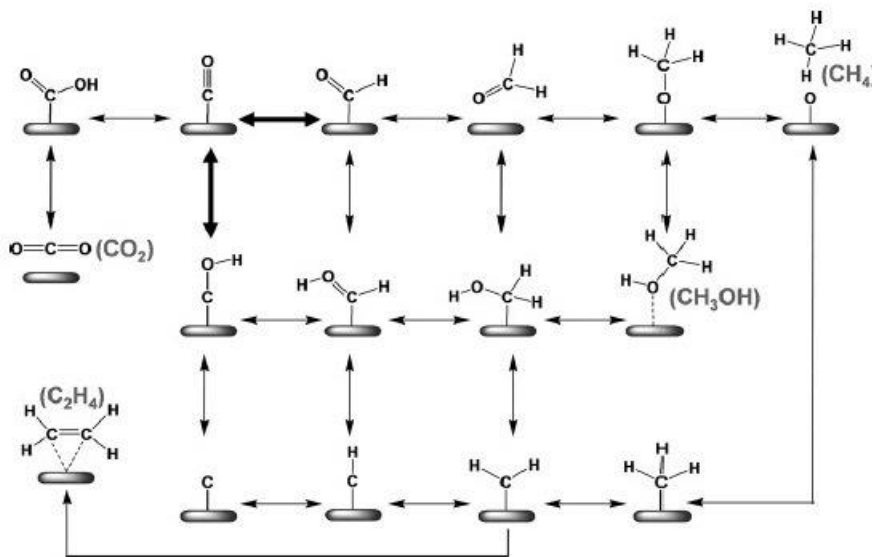

Figure 2.9. Reaction pathways derived from DFT calculations involving reaction free energies and kinetics of elementary steps (Nie et al. 2013). [Reproduced with permission from Wiley-VCH Verlag GmbH & Co.]

This is contrary to the suggestion of Schouten's group wherein CHO$_{ads}$ is the precursor to CH$_4$ and CO dimer formation early in the reduction steps is the precursor to C$_2$H$_4$. CH$_4$ and C$_2$H$_4$ pathways then split at the CH$_2$ intermediate with CH$_4$ formed by two additional proton-electron pair and C$_2$H$_4$ formed by C-C coupling. Cook et al. (1988) also suggest CH$_2$ as the final common intermediate of CH$_4$ and C$_2$H$_4$. Details on C$_2$H$_4$ formation however are not given.

Meanwhile, Durand et al. (2011) focused on computational studies to determine the effect of crystal orientation of Cu(100), Cu(111) and Cu(211). Their group showed that Cu(211) has the strongest adsorbing sites for CO$_2$ intermediates while Cu(111) generally has the weakest adsorbing sites.

2.6. CO₂ Reduction on Copper Oxide Catalysts

2.6.1. Properties of Cu₂O and their Synthesis

Cuprous oxide (Cu_2O) is one of the three stable oxide forms of Cu having an oxidation state of +1. The unit cell which consists of 4 Cu atoms and 2 O atoms has a lattice constant of 4.2696 Å. Cu atoms are arranged in a face-centered manner while O atoms are arranged in a body-centered manner. Cu atoms are linearly coordinated to two O atoms while O atoms are tetrahedrally coordinated to four Cu atoms (see Figure 2.10). Cu_2O usually crystallizes into cubes with size ranging from 10 nm to 10,000 nm. It physically exhibits a reddish orange color (Chen and Xue 2013, Meyer et al. 2013).
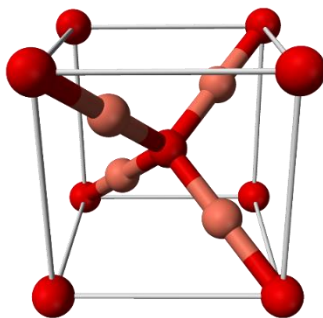

Figure 2.10. Unit cell of Cu_2O. (Image was taken from
http://en.academic.ru/dic.nsf/enwiki/282750)

Cu_2O nanowires and polyhedrons can also be obtained by tailoring the synthesis condition. Several review articles summarized the different techniques applied to fabricate Cu_2O particles and are listed in Figure 2.11. The reader is referred to these materials for more details (Zoolfakar et al. 2014, Filipic and Cvelbar 2012).
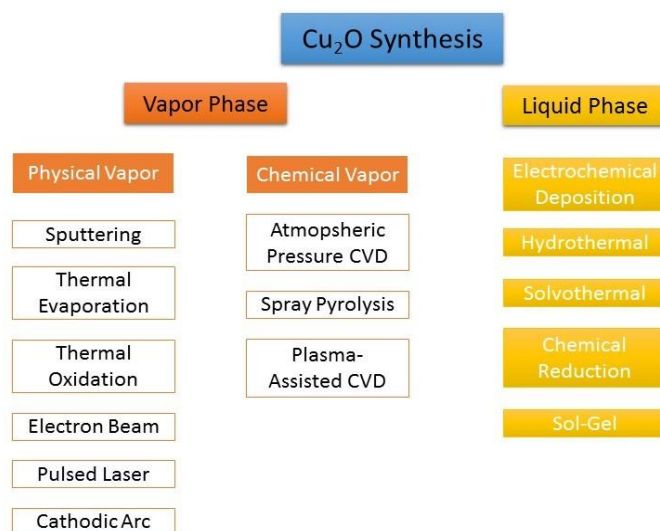
Figure 2.11. Classification of different Cu_2O synthesis methods (Zoolfakar et al. 2014, Filipic and Cvelbar 2012).

In this work, we focus on liquid phase Cu_2O synthesis, particularly wet chemical reduction and electrochemical deposition. In wet chemical reduction, Cu_2O particles are chemically formed by mixing Cu^{2+} precursor salts with reducing agents and other additives e.g. surfactants and precipitators. NaOH is typically used to precipitate Cu^{2+} into $Cu(OH)_2$ before adding the reducing agent to convert $Cu(OH)_2$ to Cu_2O. The size and morphology of Cu_2O is sensitive to the composition of reagents used which influence the relative growth of (100) and (111) planes.

In electrochemical reduction, electric current is supplied to simultaneously convert Cu^{2+} precursor salts and grow Cu_2O on a conducting support substrate. The electroplating bath typically consists of the Cu^{2+} precursor salt and chelating agent such as lactic acid. The pH of the bath is adjusted to alkaline condition by addition of NaOH. Morphology is

controlled by the applied potential, pH and the nature of the growth substrate. (Zoolfakar et al. 2014, Filipic and Cvelbar 2012, Chen and Xue 2013)

2.6.2. Catalyst Work on Cu$_2$O

A small number of groups have studied Cu$_2$O as electrocatalyst for CO$_2$ conversion. These reports are interesting because they observed methanol as a major CO$_2$ product. Frese (1991) was the first to study Cu$_2$O when he demonstrated direct CO$_2$ reduction to methanol. He compared anodized Cu foil, thermally air-oxidized Cu, and air-oxidized Cu on oxidized Ti at different potentials. Highest methanol rates were observed from anodized Cu. The authors suggested that the stronger binding energy of CO$_2$ and CO on Cu$_2$O and other Cu(I) sites may have facilitated hydrogenation of CO to CH$_3$OH.

Le et al. (2011) also studied different oxidized copper (Cu$_2$O) and similarly reported methanol as the major CO$_2$ product with trace amounts of CO. They compared anodized Cu, thermally air-oxidized Cu, and electrodeposited Cu$_2$O and showed highest methanol rates and faradaic efficiencies with electrodeposited Cu$_2$O. Potential-dependent methanol formation from CO$_2$ was evaluated between -1.0V and -2.0V (SCE) and rates reportedly decreased at electrolysis time greater than 30 minutes which was accompanied by a rise in CH$_4$ formation. Cu$_2$O was simultaneously reduced and may have been the reason for the loss in activity. Though they reported high methanol rate on electrodeposited Cu$_2$O, reproducibility of sample preparation and long term stability was a major problem. Nonetheless, Cu(I) sites were believed to be key to high CH$_3$OH generation.

Chang et al. (2009) prepared Cu$_2$O nanoparticles by a chemical reduction synthesis and used carbon cloth as support substrate. They qualitatively observed methanol and demonstrated electrochemically stable Cu$_2$O based on data from cyclic voltammetry.

27

Li et al. (2012) on the other hand worked on thermally oxidized copper with different thickness prepared by annealing Cu in air. They observed that oxide-derived Cu reduces CO_2 to CO at lower onset potential at a significantly higher rate and 20 times better selectivity compared to Hori's copper samples at -0.9V_{NHE}. Additionally, they reportedly observed ethanol, propanol and ethane but not methanol and methane on completely reduced Cu_2O. The increased CO selectivity at less negative potential may be due to high concentration of grain boundaries with unstable atomic coordination resulting from the reduction of thick Cu_2O. Rough copper surfaces consist of high number of low coordinated sites and is believed to enhance the formation of hydrocarbons, particularly ethylene and methane (Tang et al. 2012).

CHAPTER 3
GENERAL METHODOLOGY

3.1. Synthesis of Cu₂O Particles

Cu$_2$O particles were synthesized using two methods; namely, (1) electrochemical reduction and (2) wet chemical reduction. With electrochemical reduction, Cu$_2$O particles were synthesized and simultaneously electroplated to the support substrate without a separate additional mounting step. With wet chemical reduction, Cu$_2$O particles were formed from dissolved copper salts into powder form as the end product. With this method, we developed various techniques to mount these particles onto the support substrate.

3.1.1. Electrochemical Deposition

Cu$_2$O particles were synthesized by electrochemical reduction following the procedure described by Golden et al. (1996). The 15 mL electroplating bath consisted of 0.4M copper sulfate pentahydrate solution (CuSO$_4$·5H$_2$O, Sigma-Aldrich, ≥ 98% metals basis) and 3.0M lactic acid solution (CH$_3$CH(OH)COOH, Sigma-Aldrich, ≥ 85% metals basis). The pH of the solution was adjusted to 9.0 while heated at 65^{0}C by the addition of 1.0M sodium hydroxide (NaOH) solution (Mallinckrodt Chemicals). Cu$_2$O was electrochemically deposited on to the support substrate at 65^{0}C and at -0.51V$_{Ag/AgCl}$ using a Pt counter electrode (2 cm x 1 cm x 0.015 cm, ESPI Metals, 99.99% metals basis).

3.1.2. Wet Chemical Reduction

With this method, we adopted two sets of procedure which produced Cu$_2$O particles with distinct particle size range in the micro scale and nanoscale level. The first one followed the procedure described by Chang et al. (2009). First, 0.005M aqueous solution of copper (II) chloride (CuCl$_2$, Sigma-Aldrich, 99.999% trace metals) was mixed with 0.002M polyethylene glycol (H(OCH$_2$CH$_2$)$_n$OH or PEG, Sigma-Aldrich, BioUltra,
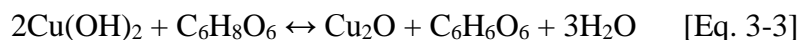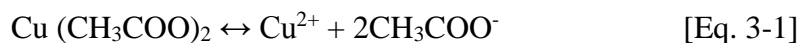
MW = 200) surfactant, followed by addition of 0.2M sodium hydroxide solution (NaOH, Sigma-Aldrich, ≥98%, pellets (anhydrous)) and 0.05M (+)-Sodium L-ascorbate ($C_6H_7NaO_6$, LAAS, Sigma-Aldrich, ≥99%) at 1:1:1:1 volumetric ratio. The solution was aged for 6 hours to allow sufficient time for Cu_2O nucleation, growth and sedimentation. The colloidal Cu_2O mixture is shown is Figure 3.1.

Figure 3.1. Colloidal Cu_2O mixture after wet chemical reduction.

Upon completion, the Cu_2O precipitates were collected and rinsed with deionized water to remove excess amount of PEG, NaOH and LAAS.

The second one followed the procedure described by Li et al. (2013). Twelve mL of 0.001M copper (II) acetate ($Cu(CH_3COO)_2$) (ACS Reagent, Acros) was added to 108 mL deionized H_2O. This was followed by the addition of 6.0g of polyethylene glycol pellets ($H-(O-CH2-CH2)_n-OH$, MW = 10,000, Sigma). The mixture was allowed to homogenize. This was then followed by the addition of 6.0 mL of 0.6M sodium hydroxide (NaOH, ≥ 98%, Aldrich). The mixture was allowed to precipitate for 10 minutes. This was then followed by the addition of 24 mL of 0.1M L-Ascorbic Acid ($C_6H_8O_6$, AA, 99% ACS Reagent, Acros). The mixture was allowed to reduce for 30 minutes.

$$Cu\ (CH_3COO)_2 \leftrightarrow Cu^{2+} + 2CH_3COO^- \qquad \text{[Eq. 3-1]}$$
$$Cu^{2+} + 2OH^- \leftrightarrow Cu(OH)_2 \qquad \text{[Eq. 3-2]}$$
$$2Cu(OH)_2 + C_6H_8O_6 \leftrightarrow Cu_2O + C_6H_6O_6 + 3H_2O \qquad \text{[Eq. 3-3]}$$

The Cu_2O nanoparticles were then collected by centrifugation at 19,000 rpm for 10 minutes using Jouan MR 22i Centrifuge located at the LSU Department of Chemical Engineering under the supervision of Professor Michael Benton. The particles were washed with deionized H_2O three times and air dried in open container.

3.2. Characterization of Cu_2O Particles

The Cu_2O electrocatalysts were characterized using different analytical tools. The FEI Quanta 3D FEG dual beam SEM/FIB system was used to examine the morphology of the supported Cu_2O particles. We used the SEM to measure particle size, determine surface coverage and distribution of particles in the support substrate. The Rigaku MiniFlex X-ray Diffractometer was used to determine the oxidation state of Cu and their crystal orientation. We used the XRD to qualitatively identify the bulk composition of different crystal orientations present. Finally, the Kratos AXIS-165 XPS/Auger surface analysis system was used to determine the surface composition of the electrocatalyst. These tools helped us understand the electrocatalytic activity of Cu_2O towards conversion of CO_2 macroscopically. The SEM/FIB and XPS equipment are located at the LSU Materials Characterization Center Shared Instrumentation Facility of the Department of Chemistry. The XRD tool is located at the MCC Lab of the Department of Mechanical Engineering. These equipment are under the supervision of Dr. Congmei Cao.

3.3. Development of Support Electrode Assembly

The support electrode assembly was constructed and used in some of the electrochemical studies on Cu_2O. To provide a suitable intermediary connection to the

potentiostat, a 4N Cu wire was attached to the sleeve of the support substrate using a silver epoxy paste (EJ-2189, Epoxy Technology). This was followed by a second coating of an insulating epoxy paste (DP-270, 3M) to cover the conducting epoxy as well as the backside of the support substrate and the Cu wire (see Figure 3.2). Other Cu_2O electrodes were not mounted on these support electrode assembly but instead were directly clamped to a stainless steel alligator clip.
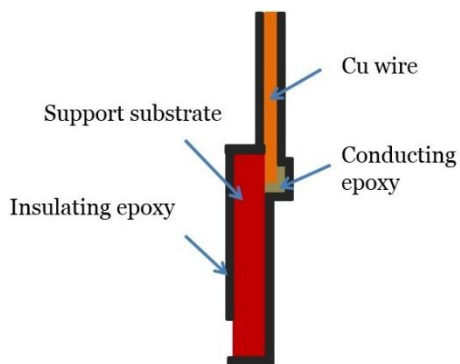

Figure 3.2. Diagram of the support electrode assembly.

3.4. CO₂ Electrochemical Reduction

CO₂ electrochemical reduction was performed in a custom H-type electrochemical cell assembly made of borosilicate glass (see Figure 3.3). The two compartments of the cell were clamped and sealed with a Viton O-ring. The catholyte and anolyte were separated by Nafion PFSA Membrane 117 (DuPont). The reactor had outlets for connection to the potentiostat (Princeton Applied Research (PAR) Model 263A), the gas chromatography equipment (Shimadzu GC-2014) and the CO_2 mass flow controller (Omega Engineering Inc). The Cu_2O electrode was assembled on the catholyte compartment immersed in a 15-20 mL solution of 0.5M potassium bicarbonate ($KHCO_3$, Sigma-Aldrich, 99.7% metals basis) pre-saturated with CO_2 (99.9999%, Airgas) for 30 minutes. The pH of the electrolyte was 7.6-7.7. Meanwhile, the anolyte compartment was

equipped with a Pt counter electrode. Electrolysis was conducted at different potentials from $-1.0V_{NHE}$ to $-2.1V_{NHE}$.
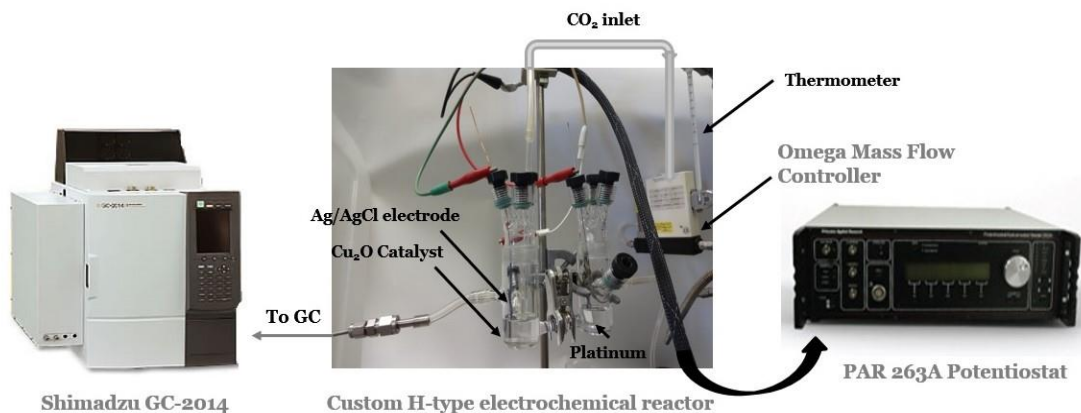
Figure 3.3. Process flow equipment for CO_2 electrochemical reduction.

3.5. Electrochemical Measurements

3.5.1. Uncompensated Resistance Determination

The uncompensated resistance (R_u) determination was performed using the PowerSuite software that controlled the Princeton Applied Research potentiostat. The baseline potential was set at 0.0V and the pulse height at 1.0mV. The software automatically generated the value of the solution resistance after the run. From this value, the potential drop was calculated using the equation derived from Ohm's Law,

$$V_{drop} = I * R_u \qquad \text{[Eq. 3-4]}$$

Finally, the actual potential at the electrode surface was determined,

$$V_{actual} = V_{applied} - V_{drop} \qquad \text{[Eq. 3-5]}$$

3.5.2. Cyclic Voltammetry

Cyclic voltammetry (CV) was performed to evaluate the electrochemical property of Cu_2O particles pertaining to their reduction-oxidation reactions to Cu and CuO states

and identify the potential at which these transitions occur. The potential sweep was between $-1.2V_{Ag/AgCl}$ and $0.6V_{Ag/AgCl}$ done at four cycles with a sweep rate of 50 mV/s. Cyclic voltammetry was performed under the same electrochemical set-up as CO_2 electrochemical reduction. CV was also used as a post synthesis step to prepare a modified Cu_2O surface for testing as a different and separate Cu_2O electrocatalyst.

3.6. Gas Chromatography

We used a Shimadzu GC-2014 gas chromatography (GC) system to separate, identify and quantify gas and liquid phase products of CO_2 electrochemical reduction. It was an integral unit in the over-all process equipment design that also consisted of the H-type electrochemical reactor, the potentiostat and mass flow controller. The components were separated by differences in their boiling point, polarity and/or intermolecular force of attraction. Given the same molecular characteristics, those with lower boiling points will move faster than those with higher boiling points. The sample gas (or vaporized liquid) along with the carrier gas e.g. He constituted the moving phase while the packing materials along the lining of the column constituted the stationary phase. The columns had adequate length to allow for complete separation of the components.

The GC was equipped with the following features: (a) thermal conductivity detector (TCD), (b) dual flame ionization detector (dual-FID), (c) methanizer, (d) HP plot-u column and (e) multiple gas columns (MS5A, Hayesep Q (H-Q) and T (H-T) and Shimalite Q). The TCD was used to detect and quantify concentrated gas products of CO_2, ethylene, H_2, methane and CO. The TCD could also detect any N_2 and O_2 from the air mixture. There were two FID's. The first FID was used to detect and quantify CO and CH_4 while offering better sensitivity towards trace amounts. The second FID was used to detect and quantify

ethanol and n-propanol. The methanizer was installed to quantify CO_2 and CO by first converting them into methane.

The gas flow chart for the GC installed in the lab is given in Figure 3.4. Gas sampling was done by automated injection through inlet valve 2 and inlet valve 3. Liquid samples could be alternatively introduced through inlet valve 1 but was not used in our experiment. Gas samples entered both analysis valve 2 (10-port configuration) and analysis valve 3 (10-port configuration) at 1 mL loop for each valve switching cycle.

Multiple gas columns were installed in order to sufficiently separate a wide range of gas products. Two MS5A columns were used to separate O_2, N_2, CH_4 and CO. One of them routed the products to the TCD from inlet valve 3 and the other routed the products to the FID-R from inlet valve 2. Two Hayesep Q columns were also used to separate CO_2, CH_4 and C_2H_4. One was linked to the TCD while the other was linked to the FID-R. One Hayesep T column was also installed along the lines between the analysis valve 3 and TCD. Finally, Shimalite Q was also added to separate H_2, O_2, N_2, CO_2, CO, and CH_4 and restrict flow of H_2O to TCD. Two columns were present for the TCD line. Gas samples that entered analysis valve 2 also entered through analysis valve 3. Any CO and CO_2 molecules present were first reduced to CH_4 when they passed through the methanizer before they could be identified by the FID-R as CH_4 signals. Other gas species passed through the methanizer unreacted before they were oxidized by flame and air in the FID-R. Separation of gas products therefore involved a simultaneous two path process, one for the TCD and the other for the FID-R.
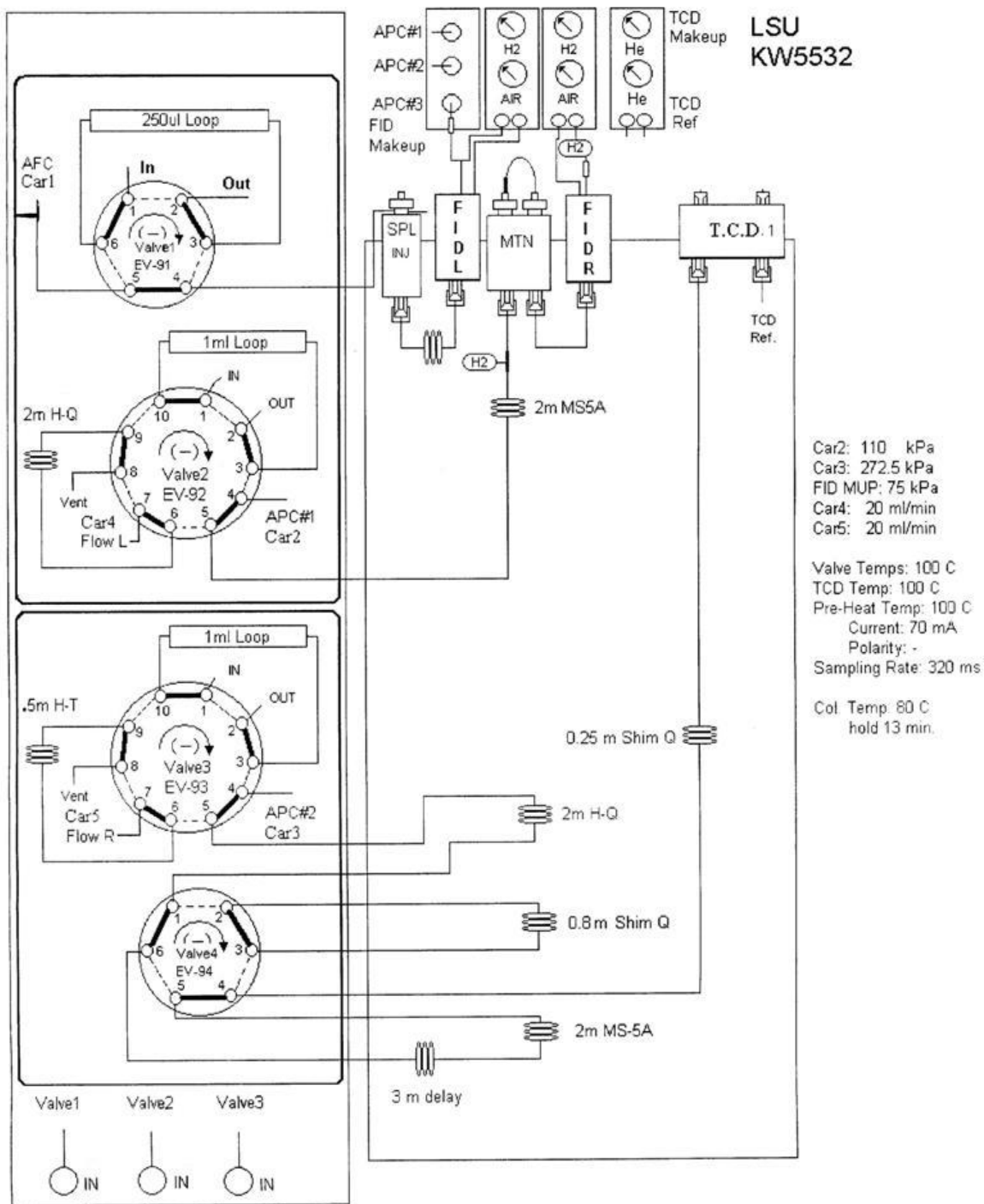
Figure 3.4. Gas-liquid flow diagram of Shimadzu GC-2014 Gas Chromatograph (illustration provided by Shimadzu Corp).

An actual picture inside the oven of the GC is shown in Figure 3.5.
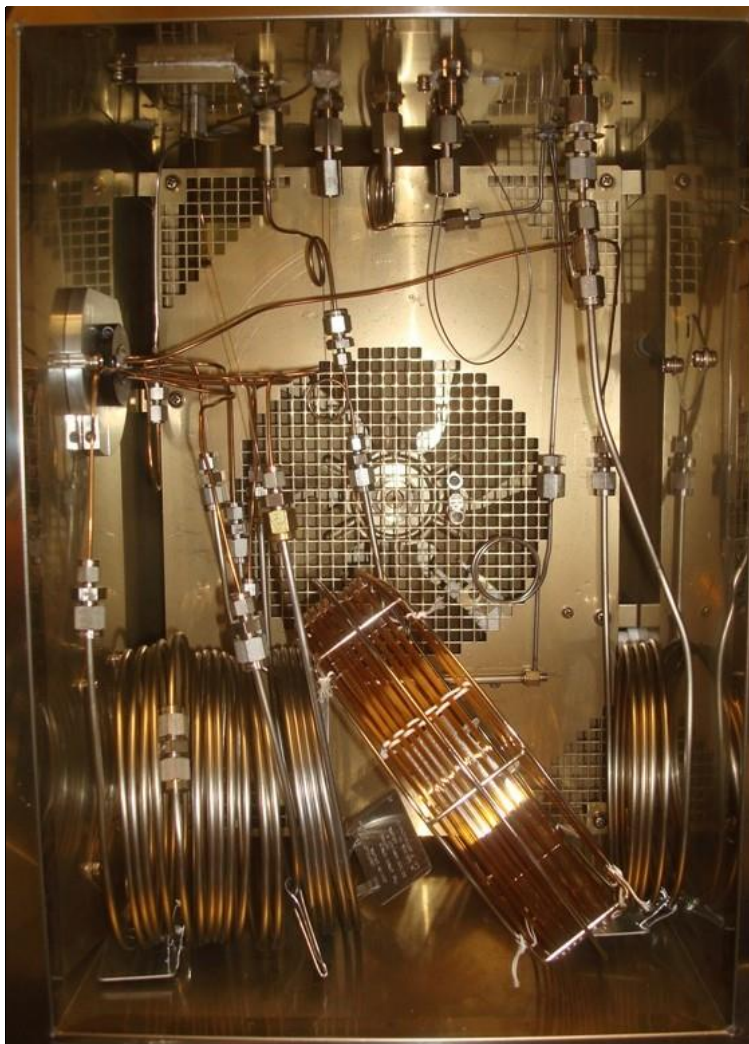
Figure 3.5. Photo of actual column oven of Shimadzu GC-2014 gas chromatograph installed in the lab.

The gas separation was operated under the following temperature setting: Methanizer - 380 $^{\circ}$C, Column Oven - 80 $^{\circ}$C, TCD - 100 $^{\circ}$C and FID-R - 316°C. The carrier gases were He and Ar. The program time was 13 minutes per sampling. The derived calibrated peaks of different gases on TCD is given in Figure 3.6.
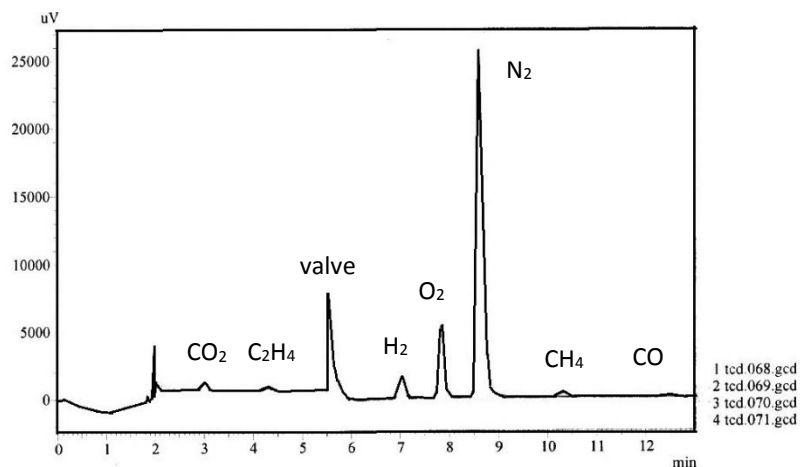
Figure 3.6. TCD peaks of gas products.

Meanwhile, the derived calibrated peaks of different gases on FID is given in Figure 3.7.
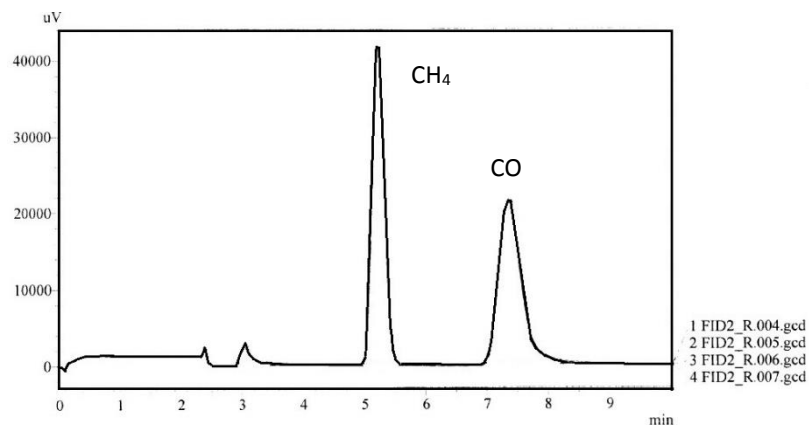
Figure 3.7. FID peaks of gas products.

The GC was initially equipped with Stabilwax column (Agilent) which was later replaced by an HP plot-U column (Agilent). The latter column provided better separation of ethanol and n-propanol. The column consisted of divinylbenzene/ethylene glycol dimethacrylate as stationary phase which has the ability to separate C_1 to C_7 hydrocarbons,

CO₂, methane, air/CO, water, oxygenates, amines, solvents, alcohols, ketones and aldehydes. Liquid products were manually injected to the GC from the injection port where they were quickly vaporized. The injection port featured a split-split less configuration.

I developed the GC method for HP plot-U column, optimized the separation after multiple trials and arrived at the following recipe. The split ratio at the injection port was set at 40 with a fixed temperature of 125 °C. The FID-L temperature was set at 150 °C. The carrier gas was He (99.9999%). The temperature of the column oven was programmed as follows: (step 1) fixed temperature of 130 °C for the first 5 minutes, (step 2) ramped temperature from 130 °C to 150 °C for the next 2 minutes at 100 °C/min and (step 3) fixed temperature of 150 °C for the last 4.5 minutes. The total program time was 11.5 min per sampling and trial. I obtained the following peak separation for methanol, ethanol, 1-propanol and 2-propanol.
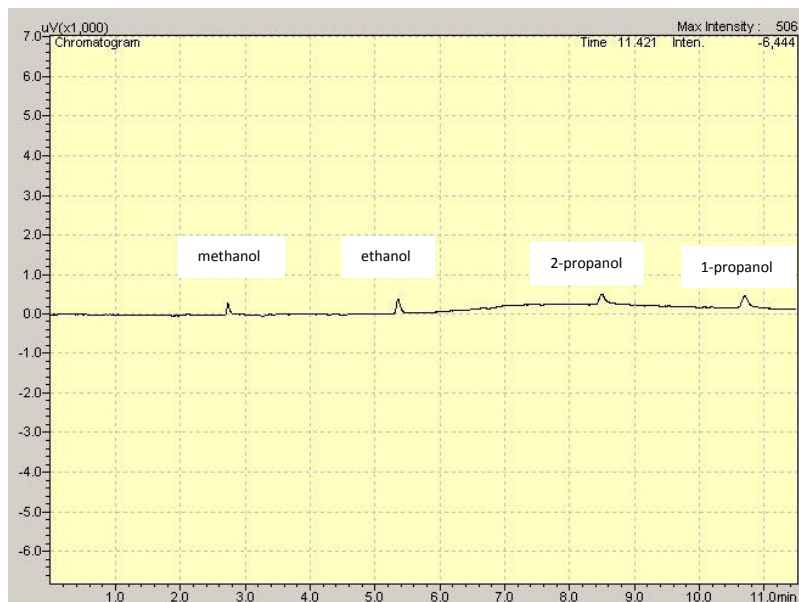
Figure 3.8. FID peaks of different alcohols considered.

3.7. Data Processing

3.7.1. Oxide Thickness and Mass of Cu₂O Reduced

Data from current versus time profile could be used to estimate the oxide thickness and the mass of Cu_2O reduced. The trapezoidal rule was used to estimate the area under the curve. The area under the curve gave a unit of Coloumb. From the charge obtained, the oxide thickness and mass of Cu_2O reduced can be computed as follows.

$$l = \frac{Q*M}{f*e*\rho*A} \qquad \text{[Eq. 3-6]}$$

$$m = \frac{Q*M}{f*e} \qquad \text{[Eq. 3-7]}$$

where,

$l = oxide\ thickness, cm$
$m = mass\ of\ Cu_2O\ reduced$
$Q = charge, C$
$M = molecular\ weight\ of\ Cu_2O, 143\ g/mol$
$f = faraday\ constant, 96{,}485\ \dfrac{C}{mol\ e}$
$e = electron\ required, 2\ mol\ e$
$\rho = density\ of\ Cu_2O, 6\ g/cm^3$
$A = electrode\ area, cm^2$

We used the following redox reaction as the basis for the electron requirement.

$$Cu_2O + 2H^+ + 2e^- \rightarrow 2Cu + H_2O \qquad \text{[Eq. 3-8]}$$
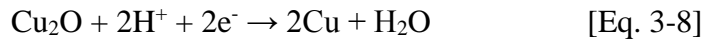
3.7.2. Formation Rate and Faradaic Efficiency

The electrocatalytic activity of Cu_2O was measured on two metrics, formation rate and faradaic efficiency. Formation rate measured the amount of product generated per given time and electrode area. Faradaic efficiency measured the percentage of total charge used to reduce CO_2 to a particular product. Faradaic efficiency determined the CO_2 product distribution and selectivity of the catalyst. The equation used for liquid products were

slightly different from gas products because gas measurements were instantaneous while liquid measurements were compounded. The formation rate and faradaic efficiency were computed using the following formulae,

$$G_R = [G] * \frac{r}{T*A*g} \qquad \text{[Eq. 3-9]} \qquad\qquad L_R = [L] * \frac{V}{t*A*M} \qquad \text{[Eq. 3-10]}$$

$$G_E = G_R * \frac{f*e*A}{I} \qquad \text{[Eq. 3-11]} \qquad\qquad L_E = L_R * \frac{f*e*A*t}{Q} \qquad \text{[Eq. 3-12]}$$

where,

$G_R = gas\ formation\ rate, \frac{\mu mol}{cm^2*hr}$ $g = ideal\ gas\ constant, 0.0821\ \frac{L*atm}{mol*K}$

$G_E = gas\ faradaic\ efficiency, \%$ $V = volume, L$

$[G] = gas\ concentration, mL/L$ $t = time, hr$

$L_R = liquid\ formation\ rate, \frac{\mu mol}{cm^2*hr}$ $M = molecular\ weight, \frac{g}{mol}$

$L_E = liquid\ faradaic\ efficiency, \%$ $f = faraday\ constant, 96485\ \frac{C}{mol\ e}$

$[L] = liquid\ concentration, mg/L$ $e = electron\ required, mol$

$r = carrier\ gas\ flow\ rate, 40\ mL/min$ $Q = charge\ transfer, C$

$T = temperature, K$ $I = instantaneous\ curent, \frac{C}{s}$

$A = electrode\ area, cm^2$

The electron requirement needed in the equations above were based on the reaction stoichiometry given in [Eq. 2-8] to [Eq. 2-14].

CHAPTER 4
CO$_2$ ELECTROCHEMICAL REDUCTION
ON POLYCRYSTALLINE COPPER

4.1. Introduction

In this chapter, we present our results on polycrystalline copper (Cu). We studied the kinetics and potential dependence of CO$_2$ products selectivity on Cu foil in order to obtain results derived from the same reactor design and process condition as those applied on the Cu$_2$O samples. We then compared these results to our Cu$_2$O samples in Chapter 5 and 6.

4.2. Materials and Methods

We used two pieces of 99.999% Cu foil (1cm x 2cm x 0.0254 cm). For the kinetic study, the first Cu foil was dipped in 1.0M HCl and sonicated sequentially in 2-propanol, acetone and deionized H$_2$O. CO$_2$ electrochemical reduction was conducted at a fix potential of -1.5V$_{NHE}$ for 110 minutes. For the potential step experiment, the second Cu foil was prepared differently. The electrode was mechanically polished with fine grit pad and sonicated in deionized H$_2$O. CO$_2$ electrochemical reduction was conducted sequentially from -1.0V$_{NHE}$ to -1.8V$_{NHE}$ with 30 minute electrolysis at each potential.

4.3. Results and Discussion

4.3.1. Kinetics of CO$_2$ Product Formation

In this section, we studied the kinetics of CO$_2$ reduction on Cu at a fix potential of -1.5V$_{NHE}$ for 110 minutes. We examined the product distribution in terms of formation rate and faradaic efficiency.

4.3.1.1. Characterization of Copper Electrode

SEM Analysis. The SEM images of Cu before and after CO_2 reduction are shown in Figure 4.1 and 4.2. The notable change in surface feature was the appearance of nanoparticles. Visually, we also observed blackish discoloration on the surface of Cu after CO_2 reduction. DeWulf et al. (1989) and Wasmus et al. (1990) similarly observed black film on the Cu surface after CO_2 reduction. Different groups have identified these surface contaminants as carbonaceous or organic species (Kyriacou and Anagnostopoulos 1993, Jermann and Augustynski 1994, Friebe et al. 1997, Wasmus et al. 1990).
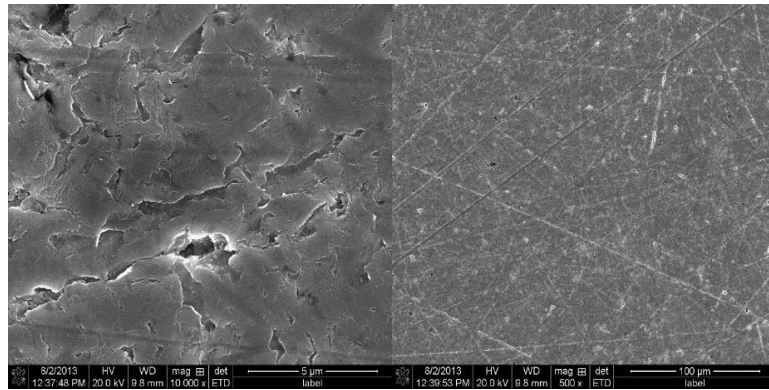
Figure 4.1. SEM of polycrystalline Cu before CO_2 reduction.
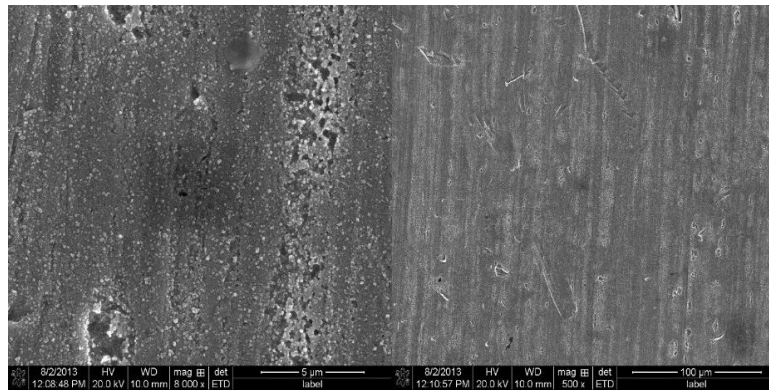
Figure 4.2. SEM of polycrystalline Cu after CO_2 reduction.

XRD Analysis. Figure 4.3 shows the XRD peaks of different Cu crystals. The electrode consisted mainly of Cu(200) particles followed by Cu(220), Cu(311) and Cu(111) crystal planes. The XRD scan of Cu before and after CO_2 reduction were the same which indicates no change in crystal structure. No crystalline carbon peaks were observed. Therefore, the black deposits on the Cu electrode were amorphous.
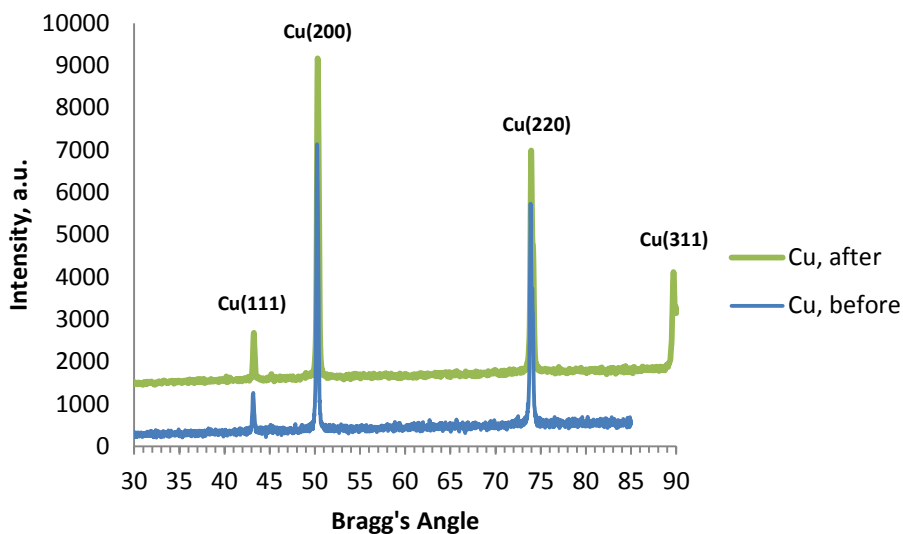
Figure 4.3. XRD profile of polycrystalline Cu before and after CO_2 reduction.

XPS Analysis. We also examined the surface composition of Cu before and after CO_2 reduction using XPS and the data is given in Table 4.1. The surface of copper consisted of Cu, C and O atoms. The surface of Cu had an unusually high atomic percentage of carbon. The Cu electrode may have been contaminated with carbon impurities during XPS analysis. Nevertheless, we observed a 4% increase in atomic C and 6% increase in atomic O coverage after CO_2 electrolysis. The increase in C atomic percentage supports the visual

observation of a black film. On the other hand, the increase in O atomic concentration was a result of surface oxidation during aqueous electrolysis of CO_2 (Frese 1991).

Table 4.1. Surface composition of polycrystalline Cu before and after CO_2 reduction.

Element	Before ECR		After ECR	
	[Atomic] %	[Mass] %	[Atomic] %	[Mass] %
Cu, 2p	23.5	59.9	13.8	43.3
C, 1s	55.6	26.7	59.5	35.5
O, 1s	20.9	13.4	26.7	21.3

4.3.1.2. CO_2 Electrochemical Reduction

Current Profile. We monitored the current during CO_2 reduction on Cu electrode at $-1.5V_{NHE}$. The electrolysis of CO_2 on copper generated a current versus time profile given in Figure 4.4. The process registered an initial current density of 13.3 mA/cm^2 which decreased to 7.7 mA/cm^2 for an average of 9.2 mA/cm^2. The measured current density at the end of electrolysis was comparable to that obtained by Hori et al. (1989). The loss in current activity was a result of the adsorption of carbon deposits on the surface of Cu (Hori 2008).
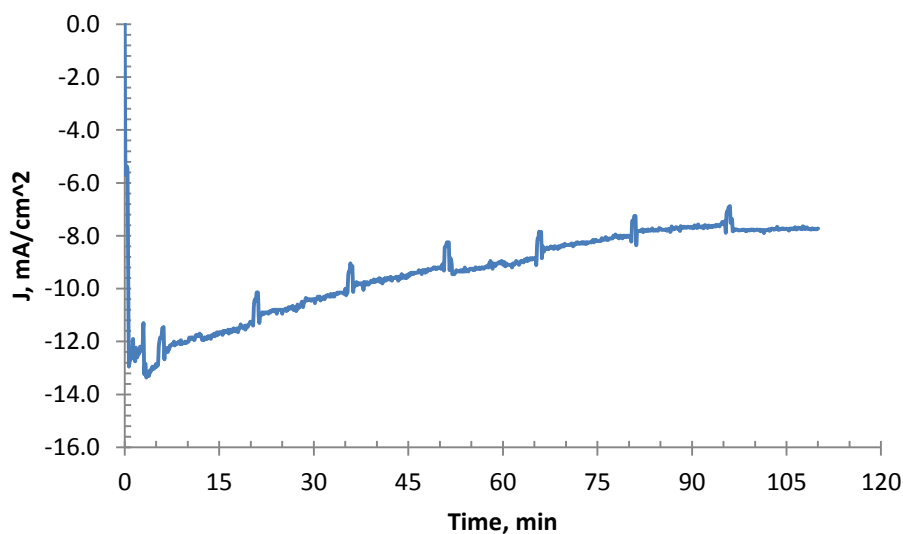
Figure 4.4. Current profile of polycrystalline Cu during CO_2 reduction at $-1.5V_{NHE}$.

Product Formation Rates. Figure 4.5 shows the formation rates of methane, ethylene, CO and H_2 between 60 minutes and 110 minutes. We computed the time average rates and obtained mean measurements of 2.8, 0.3, 8.3 and 176 $\mu mol/cm^2*hr$ respectively. We saw a 27% decrease in the total formation rates. Individually, the values of H_2, CH_4 and C_2H_4 formation rates decreased by 28%, 18% and 27% respectively while CO formation rate was unchanged. We did not observe any detectable methanol, ethanol and n-propanol products. Moderate to trace amount of these products have been observed on Cu from the work of Hori's group and Kuhl's group under similar reaction conditions.
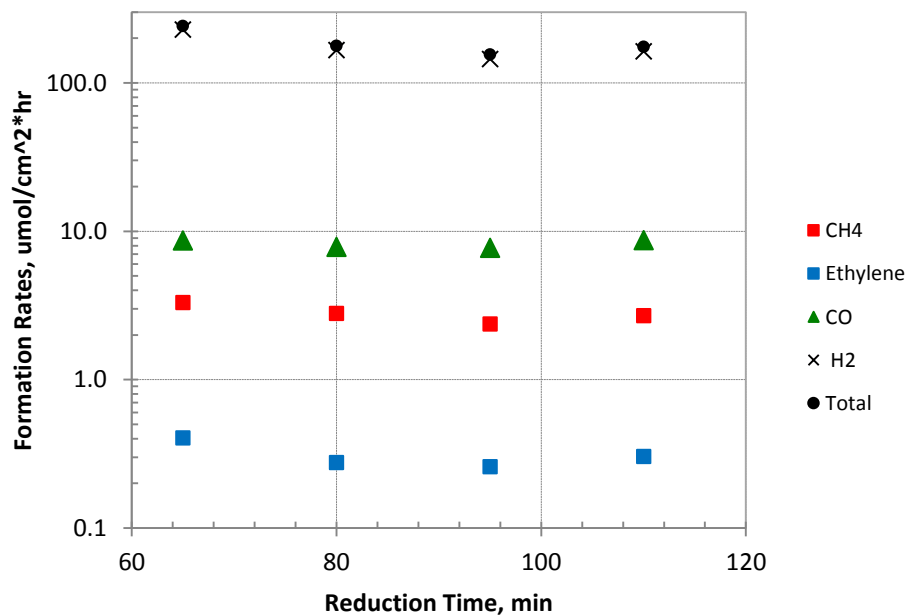
Figure 4.5. Formation rate of products on polycrystalline Cu during CO_2 reduction at -1.5V_{NHE}.

Product Faradaic Efficiencies. Figure 4.6 shows the faradaic efficiencies of methane, ethylene, CO and H_2 between 60 minutes and 110 minutes. We classified the products of CO_2 reduction into three groups based on faradaic efficiency. Major products

would have >10% faradaic efficiency. Intermediate products would have 1%-10% faradaic efficiency. Minor products would have <1% faradaic efficiency. Based on this classification; methane, ethylene and CO were intermediate products with average faradaic efficiencies of 7.5%, 1.2% and 5.5% respectively.
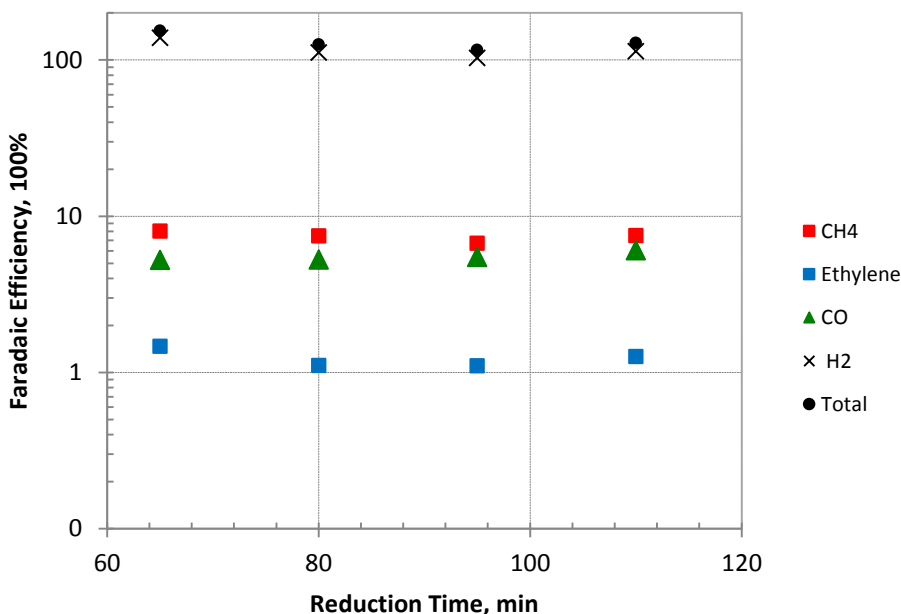
Figure 4.6. Faradaic efficiency of products on polycrystalline Cu during CO_2 reduction at $-1.5V_{NHE}$.

We computed the C_2H_4/CH_4 and $(C_2H_4+CH_4)/CO$ selectivity ratios and obtained values of 0.2 and 1.6 respectively. In comparison, Hori's group obtained a C_2H_4/CH_4 selectivity ratio of 0.5-0.9 which is in the same range as ours. Meanwhile, their $(C_2H_4+CH_4)/CO$ selectivity ratio was 8.9-32.3 at $-1.5V_{NHE}$. The difference in the ratio of the latter is due to the larger difference in faradaic efficiency between CO and the two hydrocarbons.

We observed higher H_2 faradaic efficiency compared to those obtained by Hori's group. One source of difference in selectivity ratios could come from using 0.5M instead

of 0.1M $KHCO_3$ solution. According to Hori (2008), with more concentrated $KHCO_3$ solution, a greater number of HCO_3^- ions are available to react with OH^- ions that are released during CO_2 reduction. Consequently, the pH at the electrode-electrolyte interface will be less basic promoting H_2 evolution. The presence of carbonaceous species could have also contributed to this high H_2 activity. In Chapter 6, we show that carbon electrodes mainly produce H_2.

4.3.2. Effect of Potential on Product Distribution

4.3.2.1. Current Profile

The current profile generated during CO_2 reduction at different potentials is presented in two ways. Figure 4.7a shows the current profile at all potentials. Meanwhile, Figure 4.7b shows the current profile between $-1.0V_{NHE}$ and $-1.5V_{NHE}$ to magnify the features at this potential range. As seen in Figure 4.7a, current density increased exponentially with potential between $-1.3V_{NHE}$ and $-1.8V_{NHE}$.
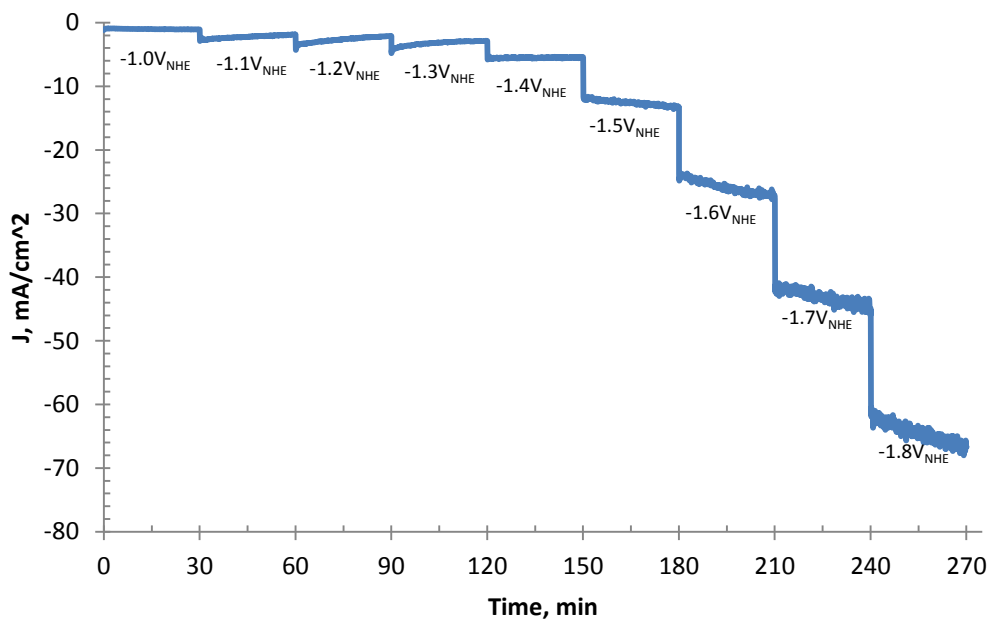
Figure 4.7a. Current profile of polycrystalline Cu during CO_2 reduction at different potentials.

In Figure 4.7b, we observed a decrease in current density with time at $-1.1V_{NHE}$, $-1.2V_{NHE}$ and $-1.3V_{NHE}$. Current density was steady at $-1.4V_{NHE}$. While at potential more negative than $-1.4V_{NHE}$, current density increased with time. These results indicate that Cu electrode is more susceptible to deactivation at less negative potential.
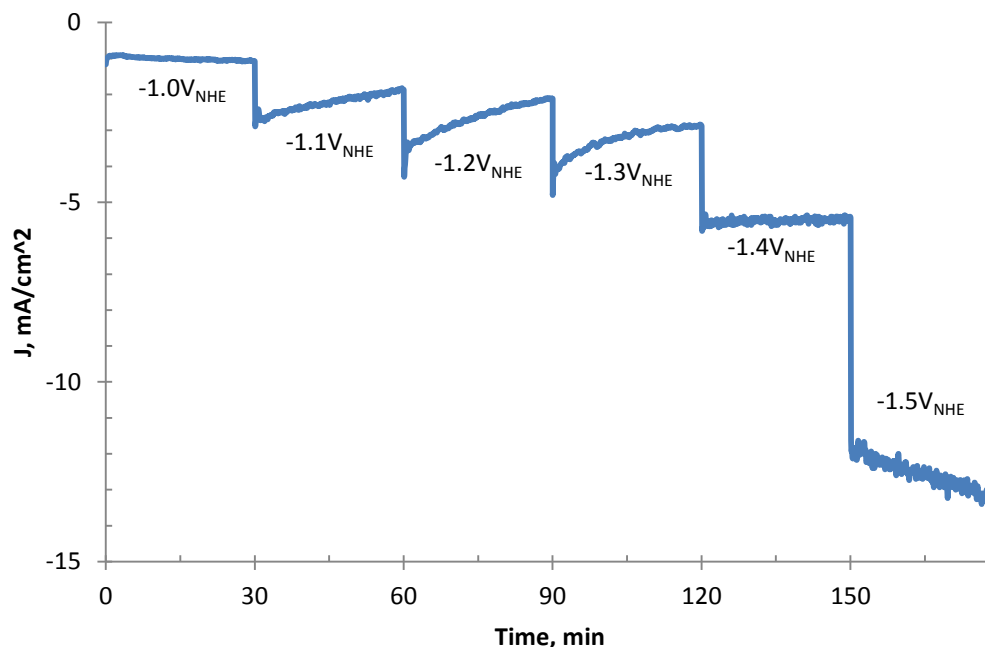
Figure 4.7b. Magnified current density versus time profile of poly-Cu at potentials between $-1.0V_{NHE}$ and $-1.5V_{NHE}$.

We then used the data in Figure 4.7a to obtain the total current versus potential (I-V) curve shown in Figure 4.8. The plot shows presence of shoulder which indicates formation of adsorbed intermediates that temporarily slowed the reduction steps (Hori et al. 1989). The adsorption and reduction of adsorbed species then accelerated at potentials more negative than $-1.3V_{NHE}$ which indicate increased turnover frequency.
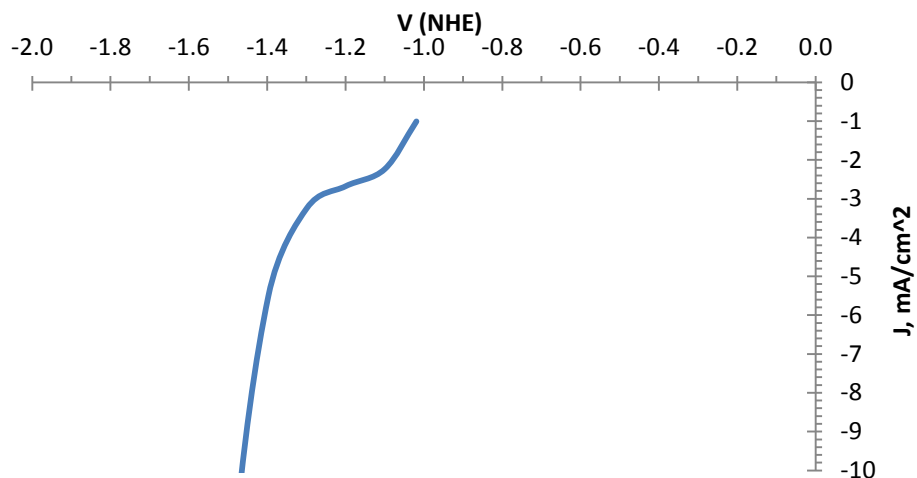
Figure 4.8. Equivalent voltammogram of polycrystalline Cu resulting from the potential step electrolysis of CO_2.

We also calculated the total current density used to make hydrocarbons and plotted them versus potential in Figure 4.9. The total hydrocarbon current density was computed by multiplying total hydrocarbon faradaic efficiency with total current density.
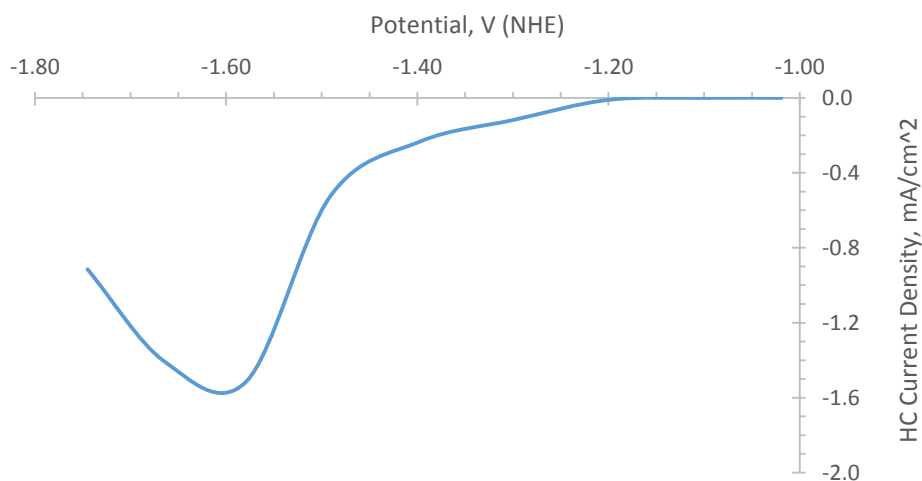
Figure 4.9. Current density versus potential of total hydrocarbon formation on polycrystalline Cu.

The graph showed a reverse in the hydrocarbon current at -1.6V_{NHE}, while the total current in Figure 4.8 continued to increase. This shows that the electrochemical activity towards hydrocarbon formation reached a peak at -1.66V_{NHE} and decreased from there onwards. On the other hand, H_2 activity continued to increase exponentially.

4.3.2.2. CO_2 Product Formation Rates

Figure 4.10 shows the formation rates of methane, ethylene, CO and H_2. Reduction of H_2O to H_2 dominated the process at all potentials and was the only detectable product at -1.0V_{NHE} and -1.1V_{NHE}. H_2 formation rates accelerated beyond -1.4V_{NHE} and was responsible for the majority of the charge transfer activity. H_2 formation is a kinetically favorable process on this copper electrode under the electrochemical conditions applied due to the abundance of H_2O species and lower kinetic barrier for hydrogen adsorption and coupling (Frese, 1991).
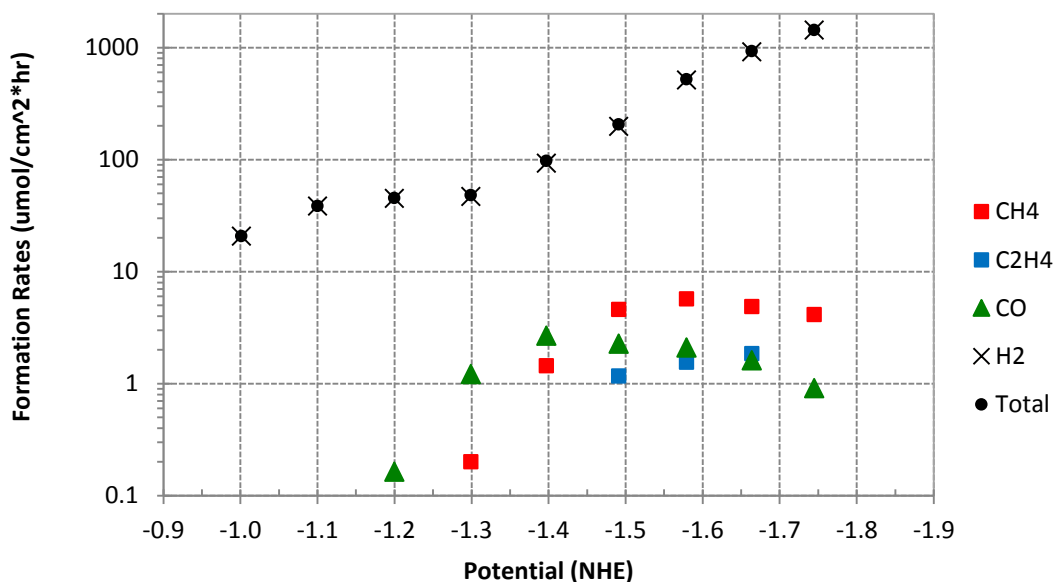
Figure 4.10. Formation rate of products on polycrystalline Cu during CO_2 reduction at different potentials.

Meanwhile, among the reduction products arising from CO_2, CO was the first product detected, at -1.20 V_{NHE}, followed by CH_4 at -1.30 V_{NHE} and C_2H_4 at -1.49 V_{NHE}. The CO formation rate peaked at -1.40 V_{NHE} with a rate of 2.7 µmol/cm^2*hr. The CH_4 formation rate peaked at -1.58 V_{NHE} with a rate of 5.7 µmol/cm^2*hr. The C_2H_4 formation rate peaked at -1.66 V_{NHE} with a rate of 1.6 µmol/cm^2*hr.

4.3.2.3. CO_2 Product Faradaic Efficiencies

Figure 4.11 shows the faradaic efficiency of methane, ethylene, CO and H_2 in logarithmic scale. Over-all, H_2 production showed highest faradaic efficiency. Between -1.0V_{NHE} and -1.5V_{NHE}, we observed a decrease in H_2 faradaic efficiency. During this period, we simultaneously observed an increase in total hydrocarbon faradaic efficiency.
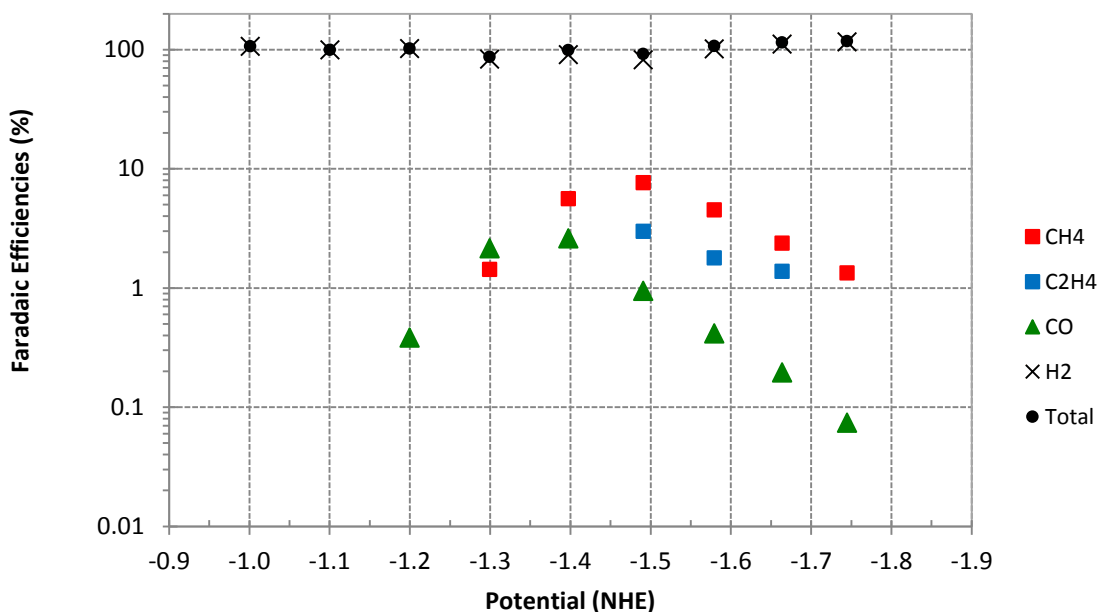
Figure 4.11. Faradaic efficiency of products on polycrystalline Cu during CO_2 reduction at different potentials.

Our product distribution on Cu was similar to those obtained by Hori and Kuhl's groups but with minor differences. CO was the only detectable product derived from CO_2 at -1.20 V_{NHE}. CH_4 was the next CO_2 product detected at -1.30 V_{NHE} followed by C_2H_4 at -1.49 V_{NHE}. In Hori's experiment, ethylene was first detected before methane. In Kuhl's work, ethylene and methane were first observed at the same potential. The CO selectivity peaked at -1.40 V_{NHE} with a faradaic efficiency of 2.6%. The CH_4 selectivity peaked at -1.49 V_{NHE} with a faradaic efficiency of 7.7%. The C_2H_4 selectivity peaked at   -1.49 V_{NHE} with a faradaic efficiency of 3.0%.

Additionally, we did not observe an intersection of the faradaic efficiency curves between methane and ethylene. In the potential step studies done by Hori's group in 1989, Cu showed higher ethylene selectivity than methane selectivity at potentials less negative than -1.36V_{NHE} and lower ethylene selectivity than methane selectivity at potentials more negative than -1.36V_{NHE} (see Figure 2.2). Noda's group in 1989 similarly observed a switch point in ethylene and methane selectivity at -1.45V_{NHE} (see Figure 2.3). In our case, methane selectivity was higher than ethylene selectivity at all potentials between -1.3V_{NHE} and -1.7V_{NHE}.

The faradaic efficiencies of CO and CH_4 formation in this mechanically polished electrode at -1.5V_{NHE} were lower than in the HCl treated Cu electrode, but do not adequately suggest that HCl treatment would offer better pre-cleaning step. Although both pre-cleaning steps remove native oxides on the Cu surface, Cu surfaces are known to re-oxidize immediately when re-exposed to air (Frese 1991). Frese reported that HCl treatment leads to formation of CuCl but did not examine its effect on Cu selectivity. Use of chloride ions to Cu surface were reported to improve hydrocarbon formation in Cu

(Kyriacou and Anagnostopoulos 1992). On the other hand, mechanically polishing with micro-sized grit pad are expected to roughen the Cu surface. Roughened Cu surfaces were observed to enhance ethylene formation (Tang et al. 2012). However, we did not observe comparable ethylene formation with that of Tang's group as a result of mechanical polishing.

This dynamic product distribution indicate a changing surface coverage of intermediate species with applied potential. The catalyst surface was initially covered with H_{ads} species that were subsequently reduced to H_2. With additional overpotential, CO_{ads} intermediates begin to form and replace some of the H_{ads} species. At more negative potential, some of the CO_{ads} intermediate were also further reduced to COH_{ads} and CHO_{ads} intermediate while the momentum of H_2 formation was regained.

These results also suggest that Cu surfaces has a potential window favorable for hydrocarbon formation in the vicinity of $-1.5V_{NHE}$. Outside this potential range, Cu becomes strongly selective towards H_2.

Additionally, these results also show evidence that there are fewer catalytic sites in Cu that reduces CO_2 to CO_{ads} intermediates. More sites on the Cu surface produce H_2 regardless of the electrode potential applied and these sites likely include C-terminated surfaces from carbonaceous impurities. H_2O molecules are also more readily accessible at the surface than CO_2 and do not suffer from transport limitation that CO_2 molecules experience (see Figure 4.9). Li et al. (2014) reported that the decline in hydrocarbon formation at more negative potential is due to onset of mass-transfer limitation of CO molecules.

We did not observe detectable amounts of methanol, ethanol, n-propanol and other oxygenates which have been reported in related literature because the sensitivity of the GC limits its detection to about 0.05% faradaic efficiency. Additionally, we do not have an existing calibration method to detect and measure other C_{2+} gas phase products.

4.3.2.4. Comparison of Key Selectivity Ratios

We compare our results with those obtained by Hori et al. (1989), Noda et al. (1989) and Kuhl et al. (2012). Particularly, we looked at comparing selectivity ratios based on key branching points of the CO_2 reaction pathway; namely, (1) the desorption of CO_{ads} intermediate versus further reduction of the CO_{ads} intermediate and (2) the C-C coupling step. Based on experimental data, C-C coupling step is thought to occur via the dimerization of CO_{ads} early in the reduction pathway (Schouten et al. 2011). Therefore the selectivity ratios considered were the following, $\frac{C_2H_4}{C_2H_4+CH_4}$ and $\frac{C_2H_4+CH_4}{C_2H_4+CH_4+CO}$ which will have values between 0 and 1. {Note that different selectivity ratio equations were used to compare the electrocatalytic activity of our Cu and Cu_2O electrodes [C_2H_4/CH_4 and (C_2H_4 + CH_4)/CO] }.

Figure 4.12 shows the selectivity ratio based on the C-C coupling branching step. The data from our copper electrode is marked in yellow color. Between $-1.2V_{NHE}$ and $-1.5V_{NHE}$, the groups have shown that the selectivity of Cu to C_2H_4 over CH_4 decreased with potential. However, the data points from Hori and our group also indicate the possibility that the selectivity of Cu to C_2H_4 over CH_4 could alternatively increase at more negative potential.
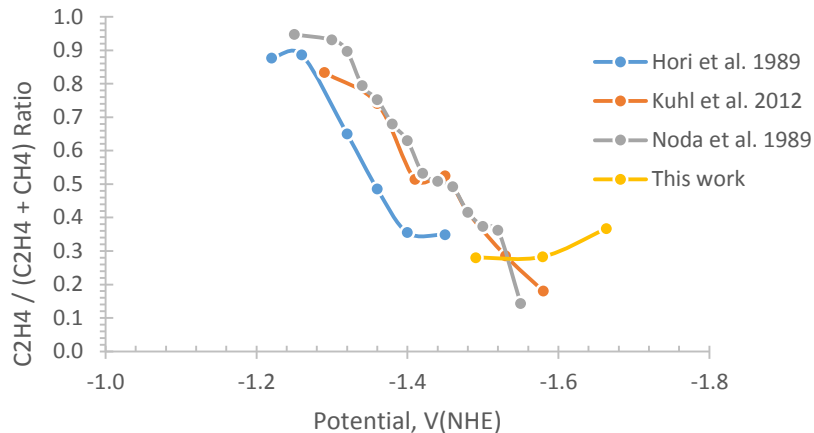
Figure 4.12. Ethylene to (ethylene + methane) ratio of different polycrystalline Cu samples.

Figure 4.13 shows the selectivity ratio based on the branching point of the CO_{ads} intermediate to either CO or hydrocarbon (see reaction mechanism diagrams in Figure 2.8 and 2.9). The data from our copper electrode is marked in yellow color. Between $-1.1V_{NHE}$ and $-1.7V_{NHE}$, there is a general agreement among different groups that the selectivity of Cu to hydrocarbons (particularly CH_4 and C_2H_4) increases with potential to nearly 1. The rise of hydrocarbon selectivity in our Cu electrode is less steep than that of Hori's group. They also observed the steepest increase in hydrocarbon selectivity with potential. This was followed by the Cu electrode studied by Kuhl's group.
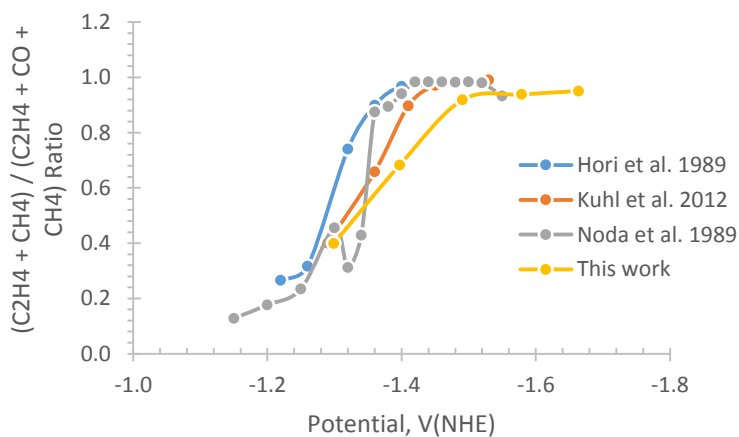
Figure 4.13. (Ethylene + methane) / (ethylene + methane + CO) ratio of different polycrystalline Cu samples.

4.4. Summary and Conclusion

We studied the kinetics and potential dependence of CO_2 reduction on polycrystalline Cu. Our kinetic study at the fixed potential of $-1.5V_{NHE}$ showed that CO, CH_4 and C_2H_4 were produced at intermediate levels. We obtained higher selectivity on CH_4 than C_2H_4 similar to what Hori's group has observed. With our potential step experiments, we detected methane before ethylene, which is different to what Hori and Kuhl's group have observed. Moreover, our H_2 faradaic efficiencies were higher. As such, the faradaic efficiency of our CO and hydrocarbon products were lower compared to Hori's numbers. In the next two chapters, we used our results on Cu to compare the electrocatalytic activity of Cu_2O, with special focus on C_2H_4, CH_4 and CO selectivity.

CHAPTER 5
CO$_2$ ELECTROCHEMICAL REDUCTION
ON ELECTRODEPOSITED Cu$_2$O FILM

5.1. Introduction

In this chapter we studied the electrocatalytic activity of Cu$_2$O synthesized by electrochemical deposition. In Section 5.3.1, we examined the effect of oxide thickness on CO formation. In Section 5.3.2, we studied the kinetics of CO$_2$ reduction at $-1.5V_{NHE}$ and monitored other products. For these Cu$_2$O electrodes, we used Cu as the growth substrate. In Section 5.3.3, we studied the effect of Nafion on the stability and product distribution of Cu$_2$O film. With this experiment, we used Toray as the growth substrate. Finally in Section 5.3.4, we studied the electrocatalytic activity of Cu$_2$O electrodeposited on CuO sublayer.

5.2. Materials and Methods

5.2.1. Effect of Oxide Thickness on CO Formation

To study the effect of oxide thickness, we considered three different deposition times during electroplating of Cu$_2$O; namely, (1) 1 minute, (2) 10 minutes and (3) 60 minutes. We used Cu foils as the growth substrate and they were electropolished in 85% H$_3$PO$_4$ at $0.4V_{Ag/AgCl}$ before the electroplating step. Cu$_2$O films were electrodeposited using procedure described in Chapter 3.1.1.

5.2.2. Kinetics of CO$_2$ Reduction

In this section, we also used Cu electropolished in 85% H$_3$PO$_4$ at $0.4V_{Ag/AgCl}$ as the growth substrate. Cu$_2$O film was electrodeposited for 30 minutes using the standard procedure given in Chapter 3.1.1 for 30 minutes.

5.2.3. Effect of Nafion

To study the effect of Nafion, two different Toray supported Cu_2O electrodes were prepared. The first sample consisted of a Toray support base, a first layer of Nafion and a second layer of Cu_2O film. A thick layer of Nafion (5 wt% in perfluorinated resin solution mixed with aliphatic alcohols and water, Sigma-Aldrich) was brush-coated onto the Toray substrate and the solvents were allowed to evaporate completely. This was followed by electrodeposition of the Cu_2O film for 30 minutes. The second sample consisted of a Toray support base with a first layer of Nafion, a second layer of electrochemically deposited Cu_2O and a third layer of Nafion. The same procedure was applied for the first two layers. The third layer of Nafion was then brush-coated onto the Cu_2O covered Toray substrate and the electrode was allowed to dry.

5.2.4. Kinetic Study on Cu_2O Film Electrodeposited on CuO Layer

To study the effect of depositing Cu_2O layer to an existing CuO film, we used Cu support substrate dipped in 1.0M HCl. Before the electroplating step, we oxidized the Cu foil by thermal oxidation in the presence of air using a Lindberg/Blue 3 Zone Furnace at 400 °C for 4 hours with a 25 °C/min heating ramp and a natural cool down. The Cu_2O layer was then electrodeposited for 10 minutes.

5.3. Results and Discussion

5.3.1 Effect of Oxide Thickness on CO Formation[1]

In this section, we compared the electrocatalytic activity of Cu_2O films with different oxide thicknesses. We only considered the effect of oxide thickness on the first step of CO_2 activation which is CO formation. In the succeeding sections, we have also considered the formation of other hydrocarbons and oxygenates.

[1]This section previously appeared on reference: Tsai, C-C., J. Bugayong, G.L. Griffin. 2012. "Role of Surface Oxide Layer during CO_2 Reduction at Copper Electrodes." MRS Proceedings 1446: 59-64. [Reproduced with permission from the Cambridge University Press.]

5.3.1.1. Current Profile

Figure 5.1 shows the current profile generated by the three Cu_2O electrodes during CO_2 reduction for 20 minutes. Transient currents associated with copper oxide reduction were observed within the first 5 minutes. The 1 minute Cu_2O sample had the smallest shoulder, followed by the 10 minute Cu_2O sample, then the 60 minute Cu_2O sample. When all reducible copper oxide particles were converted to copper (see below), the current then reached a steady-state value of approximately 3.0 mA/cm^2.
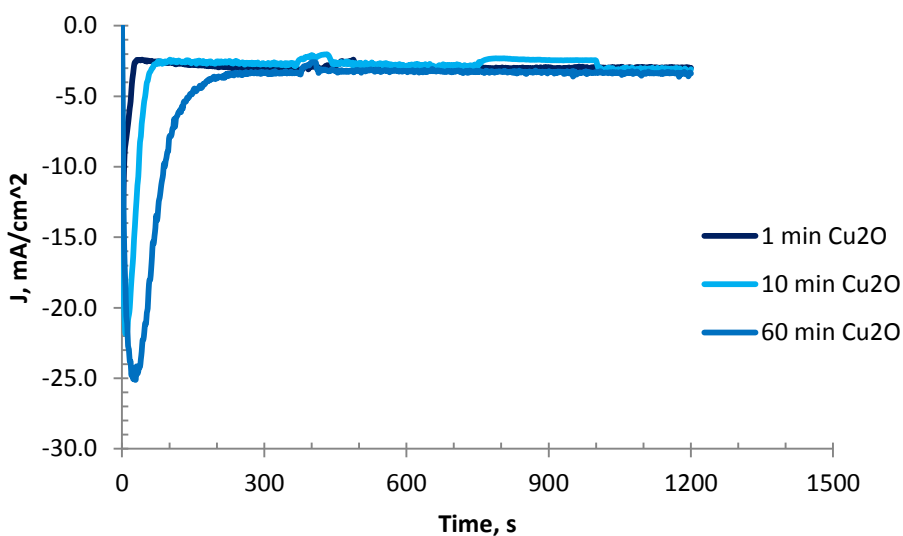
Figure 5.1. Current profile generated during CO_2 reduction on Cu_2O film at $-1.1V_{NHE}$.

5.3.1.2. Characteristics of Cu_2O Films and Their Thicknesses

The electrodeposited Cu_2O films produced different colors (see Table 5.1). The 10 minute and 60 minute copper oxide films were purple in color. Meanwhile, the 1 minute Cu_2O film was mainly gold color with green and purple spots. During CO_2 reduction at $-1.1V_{NHE}$, color changes were observed at the surface which indicates that the Cu_2O layers were altered. The difference in color of the Cu_2O film is due to the difference in how light travels through the film (Lee et al. 2013). The color has been used to estimate oxide

thickness of thin films such as SiO_2 and Si_3N_4 in wafer processing (Henrie et al. 2004).

However, we used our data on current density versus time curves to estimate the oxide

thickness using trapezoidal method. The computed oxide thickness of the Cu_2O films are

given in Table 5.1. The oxide thicknesses were between 0.1 and 2.0 µm. As expected, the

oxide thickness increased with deposition time.

Table 5.1. Characteristics of Cu_2O Electrodeposited on Cu at 1, 10 and 60 minutes.

Cu_2O	Film Color	Oxide Thickness, µm
1 min	Gold, other color spots	0.1396
10 min	Purple, uniform	0.7144
60 min	Purple, uniform	1.9874

However, the growth rate of the oxide layer decreased with time. The data points fit a decay

function of the form, $y = 0.1453x^{0.6515}$ ($R^2 = 0.9964$), as shown in Figure 5.2. This was due

to an increased diffusion distance for oxygen to travel to the Cu layer.
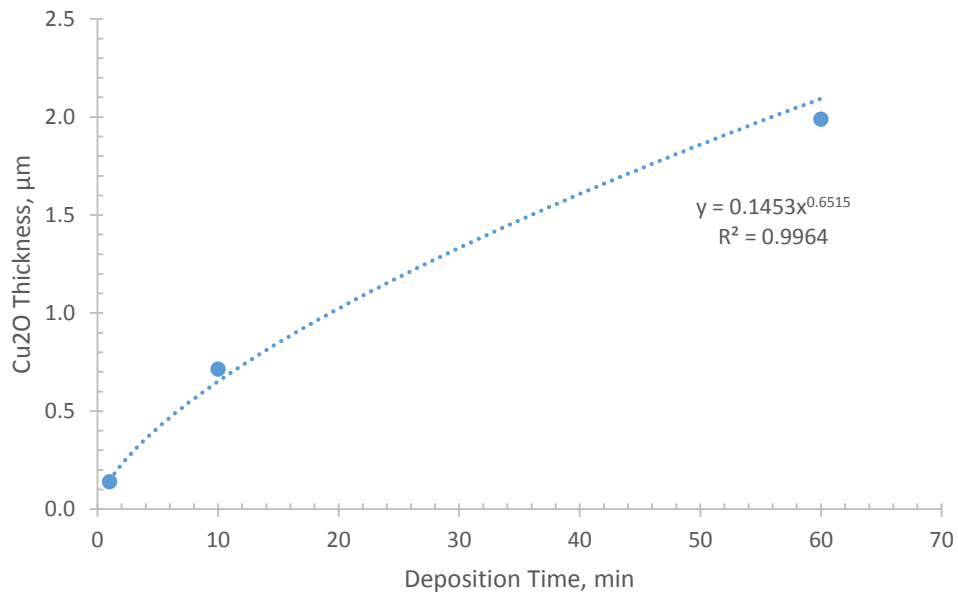
Figure 5.2. Thickness profile of Cu_2O on Cu estimated from the current density versus
time plot in Figure 5.1.

Consequently, the time it took to reach steady state current also increased with deposition time as follows: (a) t = 41 s for the 1 minute Cu_2O sample, (b) t = 79 s for the 10 minute Cu_2O sample and (c) t = 270 s for the 60 minute Cu_2O sample. Interestingly, the relationship between the deposition time and the amount of reduction time under transient current condition is highly linear (R^2=0.9998) as shown in Figure 5.3. This suggest that the time required to reduce Cu_2O particles are linearly proportional to the amount of time used during electrodeposition. The transient and deposition times were not in a one-to-one correspondence because the deposition and reduction processes were operated at different potentials.
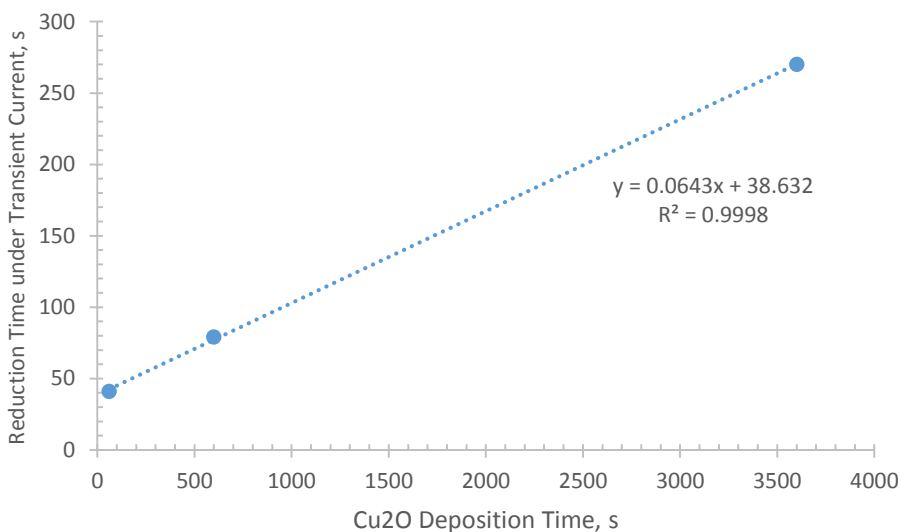
Figure 5.3. Plot of Cu_2O deposition time and transient time needed to convert Cu_2O to Cu.

5.3.1.3. Gas Product Analysis

CO Formation Rate. Figure 5.4 shows the formation rates of CO on these electrocatalysts. CO formation rate increased with oxide thickness. This indicates that copper surfaces derived from the reduction of thicker copper oxide increasingly favor CO

formation, perhaps metastable oxide as suggested by Li et al. in 2012. However, the graph

also showed that the increase in CO formation rate decreased with oxide thickness which

suggest that activity was mostly confined at the outer layer where mass transfer effect is

lower. CO formation rate was higher at 5 minutes than at 20 minutes reduction time. This

suggests that between 5 minutes and 20 minutes, the active sites of the catalyst layer have

switched preference even though current was mostly steady. The reduction of copper oxide

would cause rearrangement of atoms which would lead to about 11% decrease in volume

because Cu atoms are smaller than Cu_2O molecules.
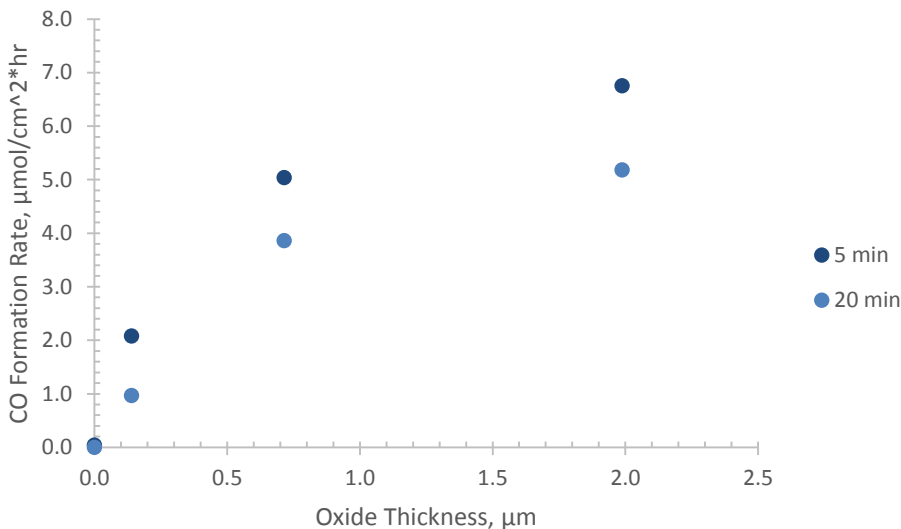
Figure 5.4. CO formation rates on Cu_2O film with different oxide thicknesses.

CO Faradaic Efficiency. Figure 5.5 shows the faradaic efficiency of CO on these

electrocatalysts. The faradaic efficiency rose faster than its formation rate between the 1

minute and 10 minute Cu_2O electrodes and rose slower between the 10 minute and 60

minute Cu_2O electrodes. The difference in slope between faradaic efficiencies and

formation rates is a result of the relative magnitude of the formation rate of CO and H_2 at

the surface.
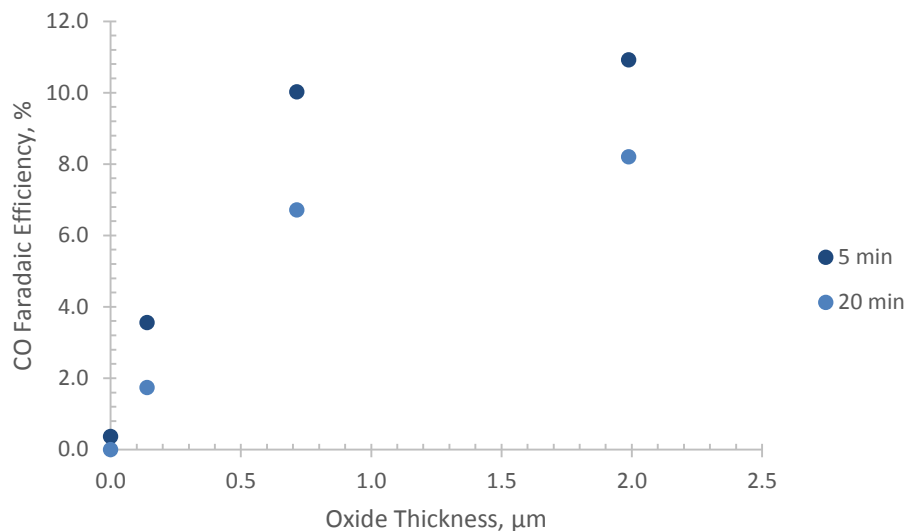
Figure 5.5. CO faradaic efficiencies on Cu_2O film with different oxide thicknesses.

H_2 Formation Rate. Figure 5.6 shows the formation rates of H_2 production. The H_2 rates were one order of magnitude higher than the CO rates, similar to what we have observed on polycrystalline Cu in Chapter 4.
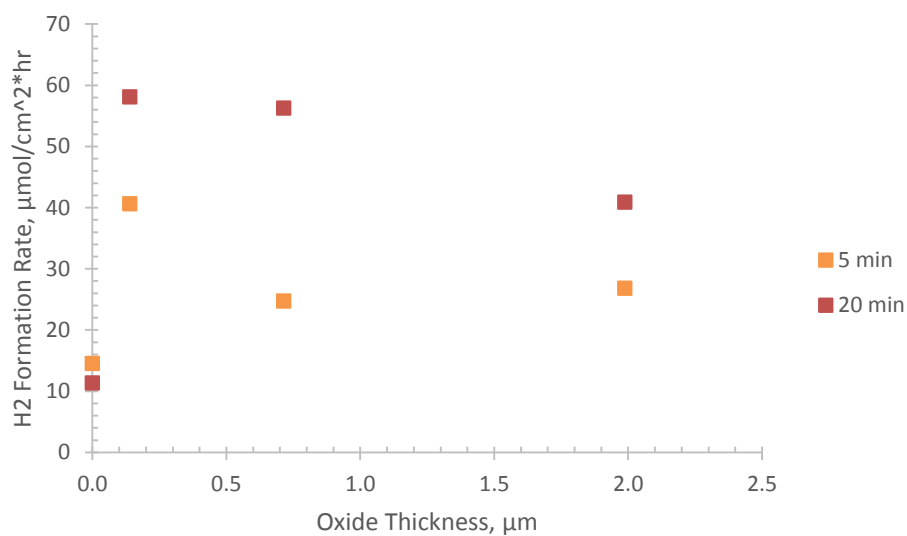
Figure 5.6. H_2 formation rates on Cu_2O film with different oxide thicknesses.

The H_2 formation rates of the Cu substrate with no initial electrodeposited Cu_2O were lower than that of the oxide-derived Cu electrodes because of surface area difference. As such, the CO formation rates were also lower. The formation rate increased with reduction time for the oxide-derived Cu electrodes and decreased with time in the non-oxidized Cu electrode.

H_2 Faradaic Efficiency. Figure 5.7 shows the faradaic efficiency of H_2 formation on these electrocatalysts. H_2 faradaic efficiency decreased with oxide thickness, which is opposite of what we observed on CO. This indicates that Cu surfaces derived from thicker Cu_2O films suppress H_2 formation better. Nevertheless, the present Cu_2O electrodes were still more efficient towards H_2 than CO. In Chapter 4, we listed the possible reasons for this observation which included presence of carbon impurities and higher concentration of H_2O molecules on the electrolyte. H_2O molecules compete with sites where CO_2 intermediates are adsorbed. The rate of CO and H_2 formation is partly controlled by the amount of CO_{ads} intermediate on the surface (Hori et al. 1991).
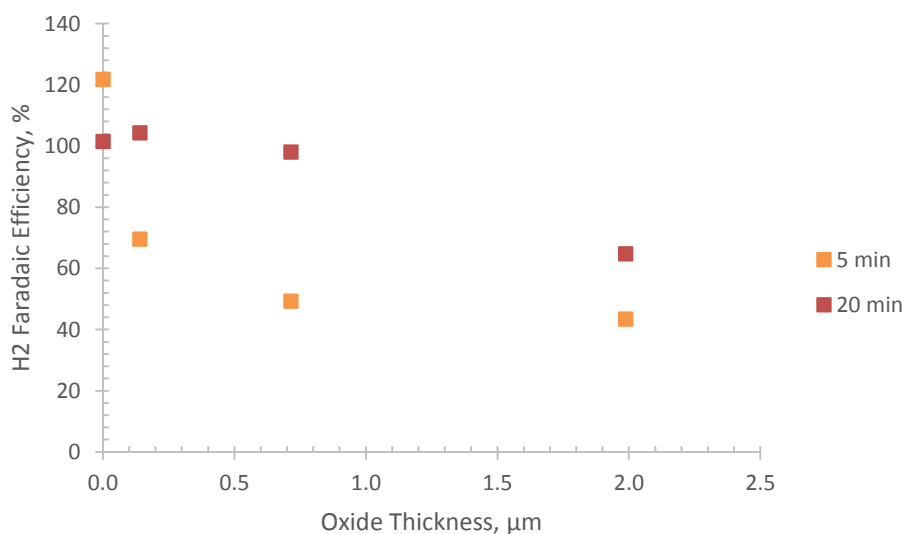
Figure 5.7. H_2 faradaic efficiencies on Cu_2O film with different oxide thicknesses.

5.3.2. Kinetics of CO$_2$ Reduction

In this section, we studied the electrocatalytic activity of Cu$_2$O film (Cu/$_{ECD}$Cu$_2$O) and measured other products of CO$_2$ reduction. We extended the reduction time from 20 minutes to 110 minutes to examine the activity of Cu$_2$O electrodes at longer time period. We increased the applied potential from -1.1V$_{NHE}$ to -1.5V$_{NHE}$ to determine if we can improve the productivity and selectivity of Cu$_2$O to CO and hydrocarbons. We characterized the catalysts using SEM and XRD before and after CO$_2$ reduction.

5.3.2.1. Electrode Characterizations

SEM Analysis. Figure 5.8 shows the SEM image of Cu$_2$O film grown on Cu substrate. The Cu support substrate was completely covered by the Cu$_2$O layer. The Cu$_2$O film consisted mainly of cubes and few rectangular pyramids. The particles grew non-uniformly with average length of 800 nm.
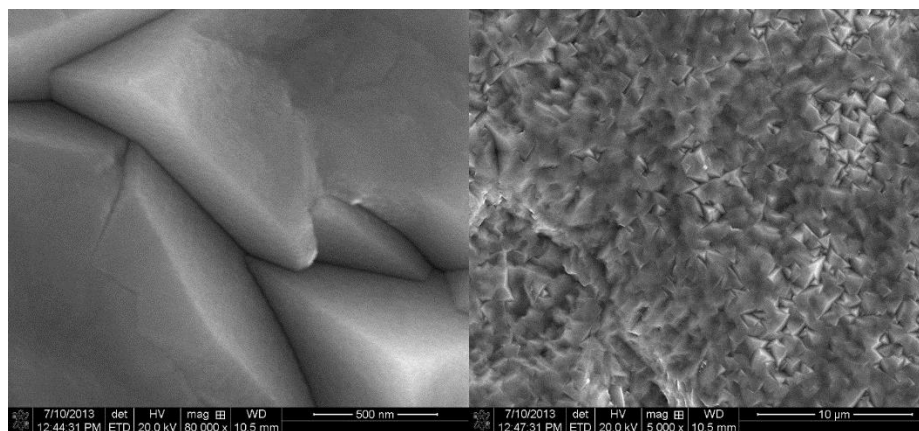
Figure 5.8. SEM of Cu/$_{ECD}$Cu$_2$O electrode before CO$_2$ reduction at -1.5V$_{NHE}$ (left) 80,000x and (right) 5,000x magnification.

After CO$_2$ reduction, Cu$_2$O evolved into smaller particles clustered into their original cubic structure (see Figure 5.9). Canals also formed on the reduced film likely aided by the lattice strain build-up caused by the decrease in particle volume during the

66

reduction of Cu_2O to Cu. Aggressive H_2 evolution likely compounded the breaking of the films too.
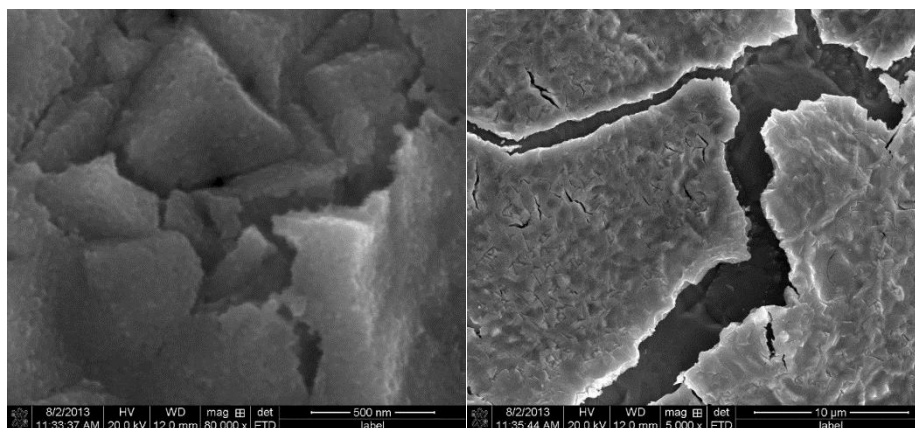
Figure 5.9. SEM of $Cu/_{ECD}Cu_2O$ electrode after CO_2 reduction at $-1.5V_{NHE}$ (left) 80,000x magnification and (right) 5,000x magnification.

XRD Analysis. The XRD scan of $Cu/_{ECD}Cu_2O$ electrode before CO_2 reduction is given in Figure 5.10. The scan revealed $Cu_2O(111)$ oriented crystal planes. There were also $Cu_2O(222)$, $Cu_2O(202)$ and $Cu_2O(200)$ crystal planes that were present in smaller quantities.
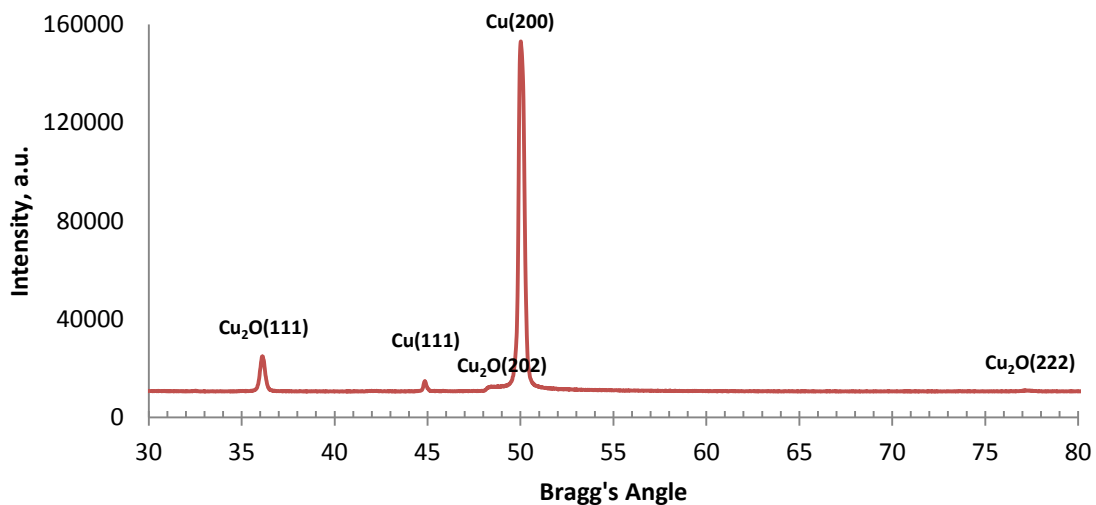
Figure 5.10. XRD scan of $Cu/_{ECD}Cu_2O$ electrode before CO_2 reduction.

Meanwhile, the XRD scan after CO_2 reduction is given in Figure 5.11. The XRD peaks of Cu_2O particles disappeared, except for $Cu_2O(202)$. The intensity of Cu(200) oriented planes increased. Our XRD and SEM results confirm our earlier observation of color change when the Cu_2O film was simultaneously reduced to Cu. However, we observed residual Cu_2O particles.
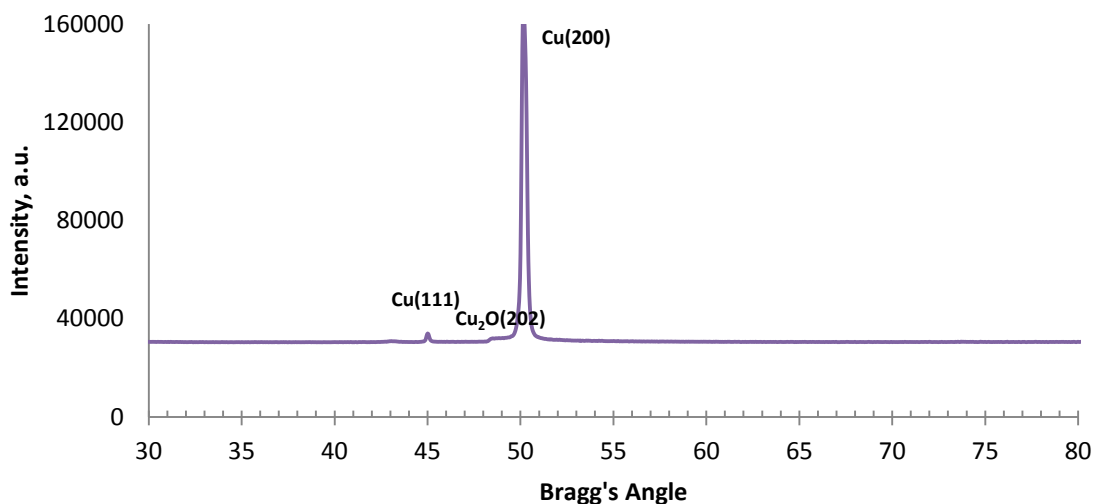
Figure 5.11. XRD scan of $Cu/_{ECD}Cu_2O$ electrode after CO_2 reduction.

5.3.2.2. Current Profile

Figure 5.12 shows the current profile of the $Cu/_{ECD}Cu_2O$ electrode during CO_2 reduction at $-1.5V_{NHE}$. The reduction current was constant at 15 mA/cm^2 but with oscillation possibly caused by uneven H_2 bubble formation. The transient current at the beginning of electrolysis corresponded to approximately 1.29 μm oxide thickness which fits the decay function in Figure 5.2.
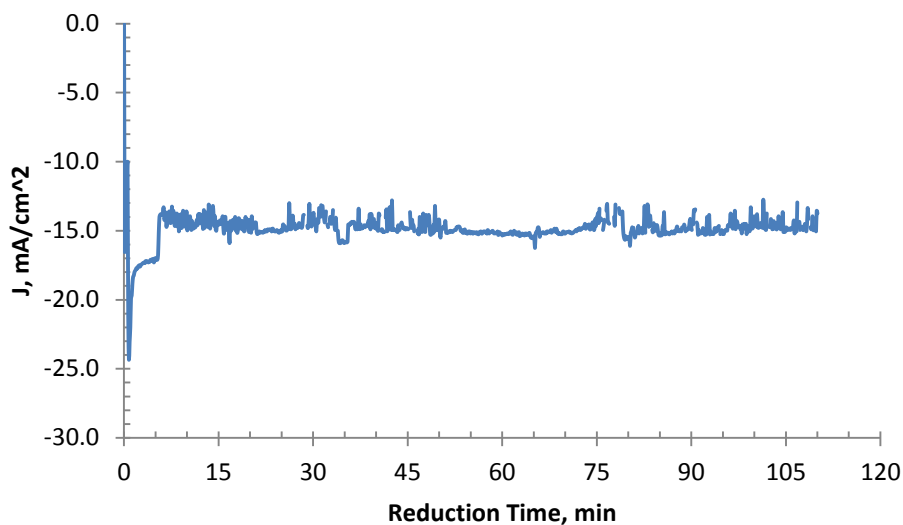
Figure 5.12. Current profile during -1.5V_{NHE} electrolysis on Cu/$_{ECD}$Cu$_2$O electrode.

5.3.2.3. GC Product Analysis

Product Formation Rates. Figure 5.13 shows formation rates of different liquid and gas phase products. Hydrogen was the main product with average rates of 411 μmol/cm^2*hr.
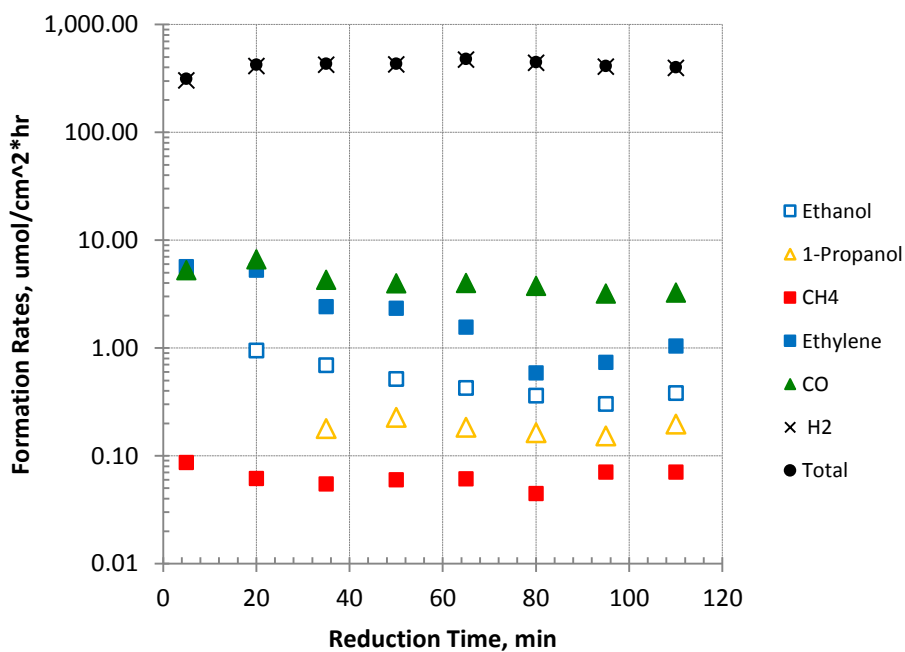
Figure 5.13. Formation rate of products on Cu/$_{ECD}$Cu$_2$O electrode during CO$_2$ reduction at -1.5V_{NHE}.

CO was produced at a lower rate of 4.3 µmol/cm^2*hr followed by ethylene at 2.5 µmol/cm^2*hr. Methane was also detected at trace amounts of less than 0.1 µmol/cm^2*hr. Liquid products such as ethanol and n-propanol were also produced with rates of 0.52 and 0.18 µmol/cm^2*hr respectively.

    Product Faradaic Efficiencies. Figure 5.14 shows the corresponding faradaic efficiencies of the CO_2 (and H_2O) reduction products. The product distribution was dynamic despite a steady current flow. The CH_4 selectivity was very low but stable near 0.1%. Ethylene had an initial faradaic efficiency of 11% which decreased to around 2.0% for an average of 5.2%. The decrease in ethylene faradaic efficiency did not lead to an increase in CH_4 or CO faradaic efficiency. H_2 faradaic efficiency was also relatively flat. The average CO faradaic efficiency was 1.5%.
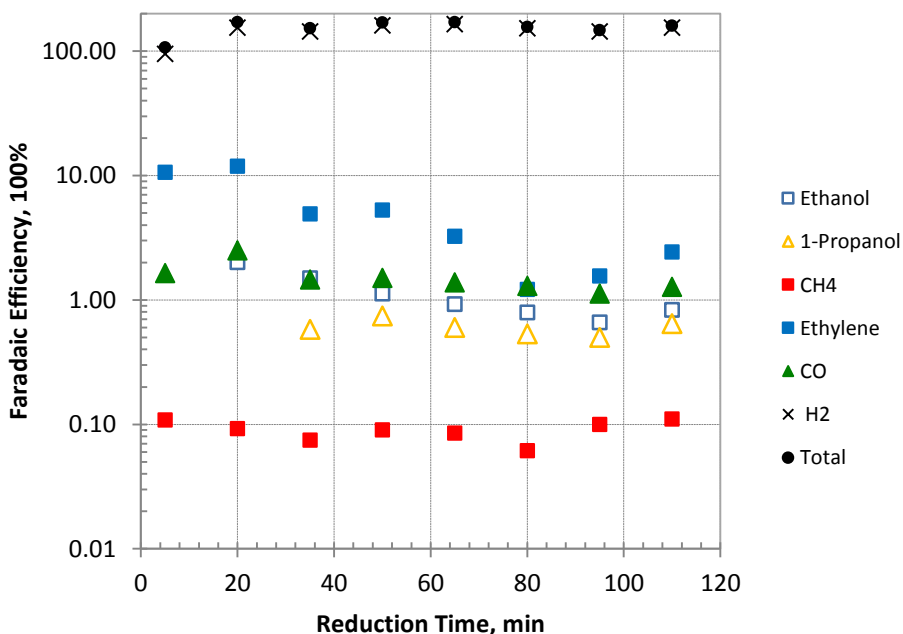
Figure 5.14. Faradaic efficiency of products on Cu/$_{ECD}$Cu$_2$O electrode during CO$_2$ reduction at -1.5V$_{NHE}$.

Most likely, there was an increase in formate selectivity which we did not monitor. The pathway to formation of $HCOO^-$ does not pass through the CO_{ads} intermediate unlike the hydrocarbons and oxygenates. The formate route is also considered terminal. Although more Cu particles were (200) oriented than (111), we do not have information on the relative composition at the surface. But ethylene selectivity was better than methane selectivity which is different to what we have observed with polycrystalline Cu.

In comparison to our results at $-1.1V_{NHE}$ electrolysis (see Section 5.3.1), the CO faradaic efficiency at $-1.5V_{NHE}$ was lower. This is in agreement with Hori's observation on CO. Meanwhile, the H_2 faradaic efficiency at $-1.5V_{NHE}$ was higher than at $-1.1V_{NHE}$ which is opposite to Hori's observation on H_2.

We also compared the C_2H_4 and CH_4 selectivity of electrodeposited Cu_2O with that of polycrystalline Cu in Chapter 4. The C_2H_4/CH_4 efficiency ratio in the Cu catalyst was 0.2. With electrodeposited Cu_2O catalyst, the C_2H_4/CH_4 efficiency ratio increased to 57.2. The enhanced ethylene selectivity in Cu resulting from the reduction of electrodeposited Cu_2O is due to the formation of more low-coordinated active sites (Li et al. 2012; Tang et al. 2012).

5.3.3. Effect of Nafion

Nafion is commonly used as both electrolyte and support substrate in proton exchange membrane fuel cells (PEMFCs) and PEM electrolyzers. They are excellent materials in these applications because of their high proton conductivity and low electron conductivity (Yaroslavtsev 2013, Peighambardoust et al. 2010, Ito et al. 2011, DeWulf and Bard 1988). Nafion was also used to improve wettability of carbon nanotubes (CNTs) in the preparation of amperometric biosensors (Wang et al. 2003).

In this section, we studied the effect of Nafion on the selectivity of electrodeposited Cu_2O film. Nafion is incorporated to the electrode in two configurations; namely, (1) Toray/Nafion/Cu_2O and (2) Toray/Nafion/Cu_2O/Nafion. Toray was coated with Nafion before Cu_2O was electrodeposited for 30 minutes. Electrolysis of CO_2 was performed at $-1.5V_{NHE}$ for 110 minutes. We monitored CO, CH_4, C_2H_4, ethanol, n-propanol and H_2 products with our GC instrument and characterized the electrodes with SEM, XRD and XPS.

5.3.3.1. Electrode Characterizations

SEM of Toray/Nafion/Cu_2O. The fresh Cu_2O film electrodeposited on Toray exhibited a microsphere structure of overlapping cubes (see Figure 5.15). As seen in the right image, there were exposed parts of the Toray growth substrate.
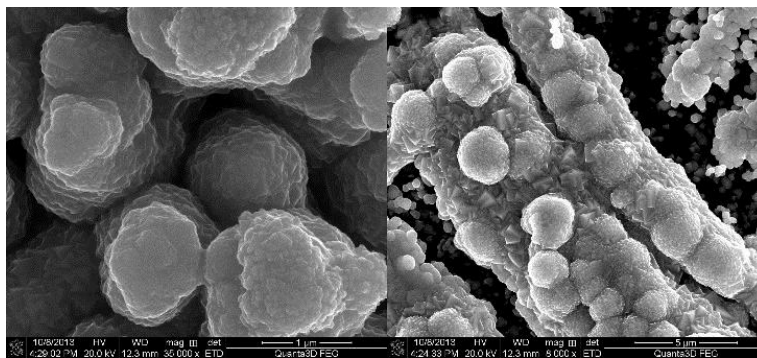
Figure 5.15. SEM of fresh Toray/Nafion/Cu_2O taken at different magnifications, (left) 35,000x and (right) 8,000x.

After CO_2 electrolysis, an evolution of morphology was observed (see Figure 5.16). The microspheres became less defined and there was formation of nanoparticles. The formation of nanoclusters appeared to increase the surface area available for CO_2 reduction.
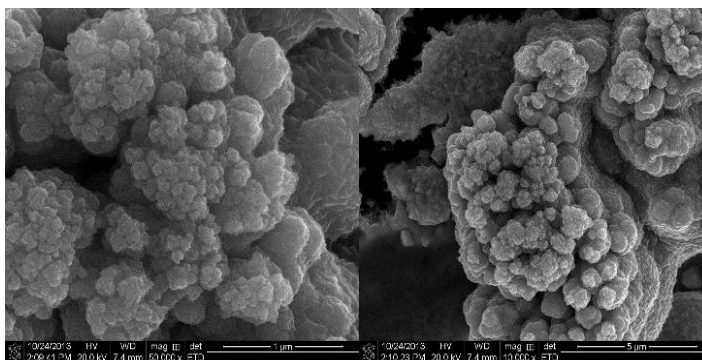
Figure 5.16. SEM of Toray/Nafion/Cu$_2$O taken at 50,000x (left) and 10,000x (right) magnification.

SEM of Toray/Nafion/Cu$_2$O/Nafion. Figure 5.17 shows the SEM of the fresh Cu$_2$O electrode with an outer layer of Nafion. The image on the left only shows Nafion because the Cu$_2$O particles were fully covered in this region of the electrode. Since we did not obtain a good image of the TNEN electrode due to poor surface conductivity, a representative image was taken from the TNE electrode for the image on the right. Note that both Cu$_2$O electrodes were prepared sequentially on the same plating bath and operating condition. Likewise, as will be shown in the SEM after CO$_2$ reduction (in Figure 5.18), there was evidence of an initial formation of microspheres similar to what we observed with our TNE electrode.

Despite saturating the surface of the Cu$_2$O film with the Nafion solution, we still observed regions of the electrode surface that were not covered with Nafion. This was because when excess amount of the Nafion solution dried out, the solidified Nafion clumped together to achieve physical equilibrium. We have also observed this event while coating Nafion to the polished glassy carbon plate. Nevertheless, Cu$_2$O-nafion interfaces were present and may offer unique electrocatalytic activity towards CO$_2$ conversion. The SEM in Figure 5.17 shows microspheres of Cu$_2$O cubes.

73
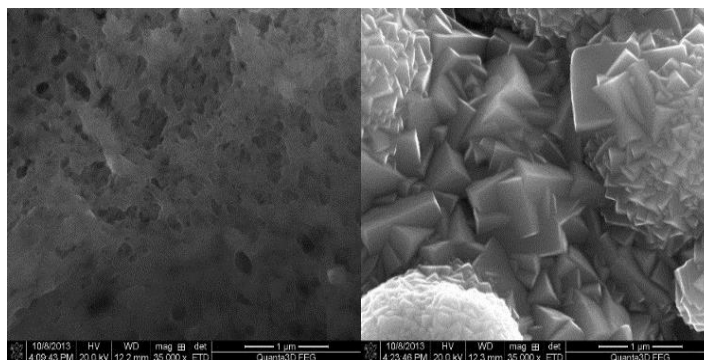
Figure 5.17. SEM of Toray/Nafion/Cu$_2$O/Nafion before CO$_2$ reduction (left) Cu$_2$O not visible and fully covered in Nafion (right) representative image taken from the TNE sample.[*] ([*]Note: Both electrodes were prepared sequentially on the same bath and electrodeposition condition).

After CO$_2$ reduction, the Cu$_2$O microspheres again evolved into dispersed nanoclusters that did not retain their cubic architecture (see Figure 5.18).
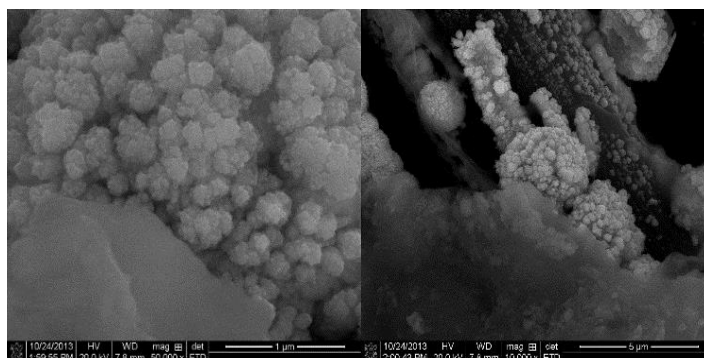
Figure 5.18. SEM of Toray/Nafion/Cu$_2$O/Nafion after CO$_2$ reduction taken at (left) 50,000x and (right) 10,000x magnifications.

XRD Scan of Toray/Nafion/Cu$_2$O. The XRD scan of Toray/Nafion/Cu$_2$O before CO$_2$ reduction is given in Figure 5.19. The oxide is mostly made up of Cu$_2$O(110) crystal planes with lower number of Cu$_2$O(200) and Cu$_2$O(220) crystal planes. This is different from Cu$_2$O film electrodeposited on Cu which were mostly oriented in the (111) direction.
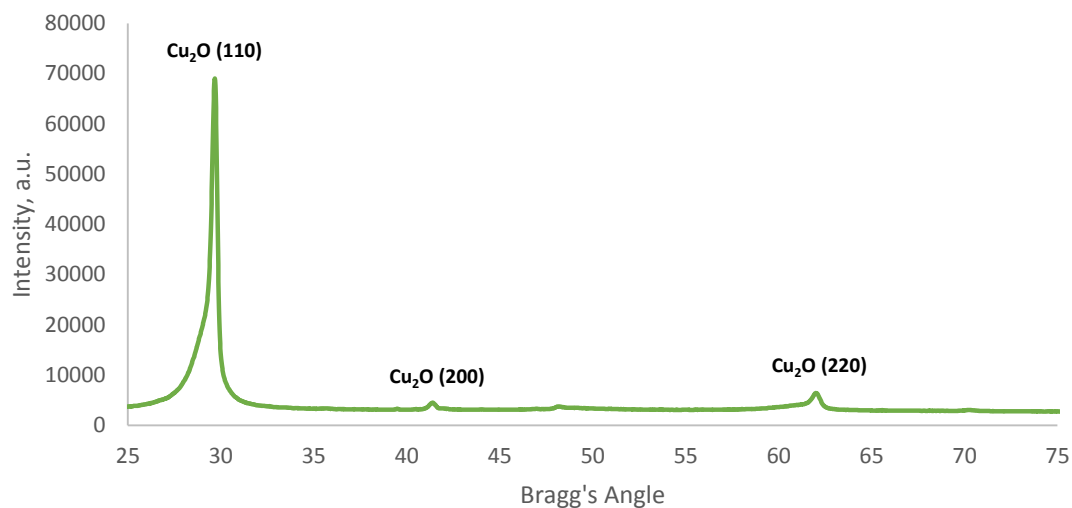
Figure 5.19. XRD scan of Toray/Nafion/Cu_2O electrode.

XRD Scan of Toray/Nafion/Cu_2O/Nafion. The XRD scan before CO_2 reduction is given in Figure 5.20. The oxide has similar distribution of crystal phases as that of the Toray/Nafion/Cu_2O electrode.
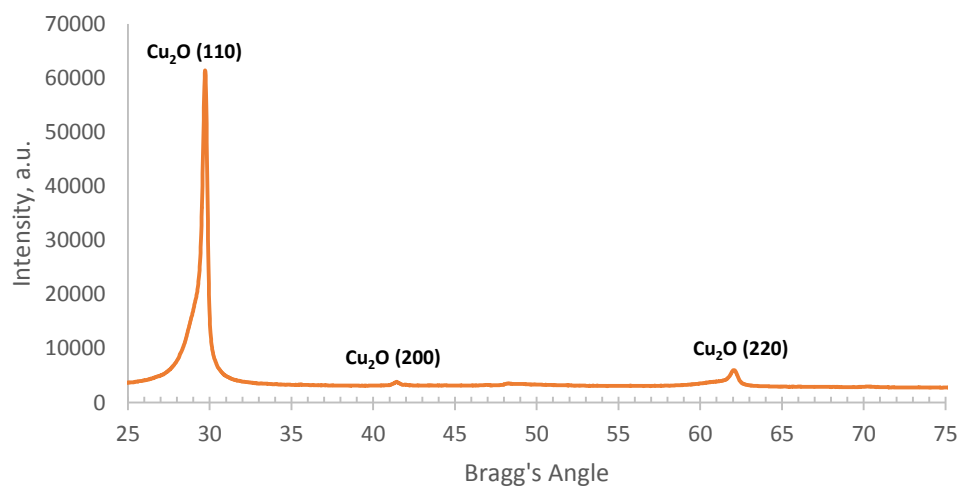
Figure 5.20. XRD scan of Toray/Nafion/Cu_2O/Nafion electrode.

XPS Scan of Toray/Nafion/Cu$_2$O. The XPS spectra and elemental composition of Toray/Nafion/Cu$_2$O electrode were determined. The XPS profile is given in Figure 5.21 and shows the peaks of Cu^{2p}, F^{1s}, O^{1s}, C^{1s} and contaminants typically observed during XPS analysis at their characteristic binding energies.
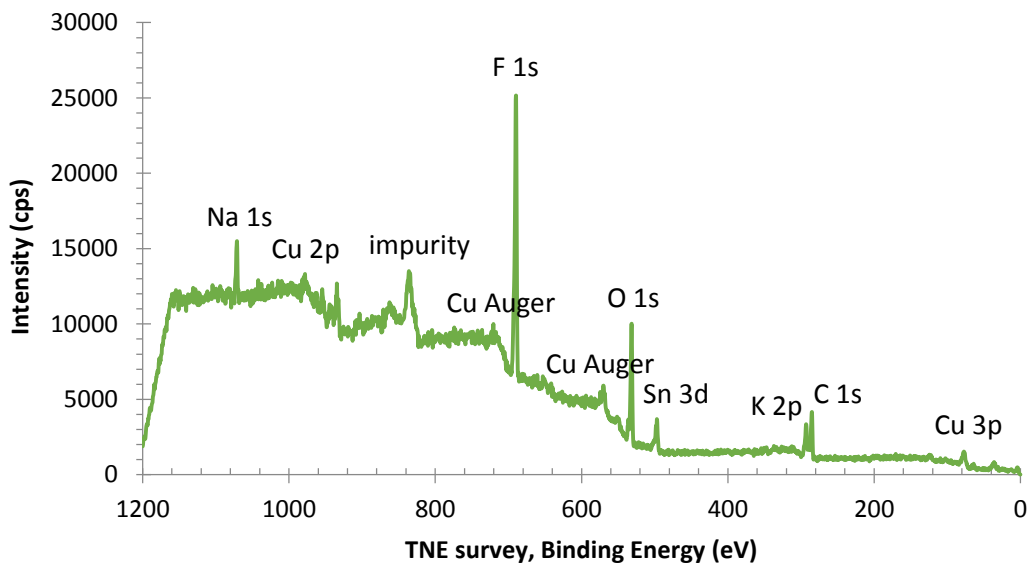
Figure 5.21. XPS spectra of surface elements in Toray/Nafion/Cu$_2$O electrode.

Meanwhile, the surface composition derived from the elemental peak areas is given in Table 5.2. Flourine made up the bulk of the surface with about 57% atomic and 56% mass concentration. Nafion which has a molecular formula of C$_7$HF$_{13}$O$_5$S·C$_2$F$_4$ contributed to the high signal of fluorine. Stoichiometrically, the Cu$_2$O particle would have an atomic Cu/O ratio of 2. However in our sample, the Cu/O ratio was only 0.26. This is because O atoms from Nafion were also accounted.

Table 5.2. Surface composition of Toray/Nafion/Cu$_2$O electrode.

Element	[Atomic] %	[Mass] %
Cu 2p	5.0	16.4
O 1s	19.3	16.0
F 1s	56.9	56.0
C 1s	18.8	11.6

XPS Scan of Toray/Nafion/Cu$_2$O/Nafion. The XPS spectra and elemental composition of Toray/Nafion/Cu$_2$O/Nafion electrode were aso determined. The XPS profile is given in Figure 5.22.
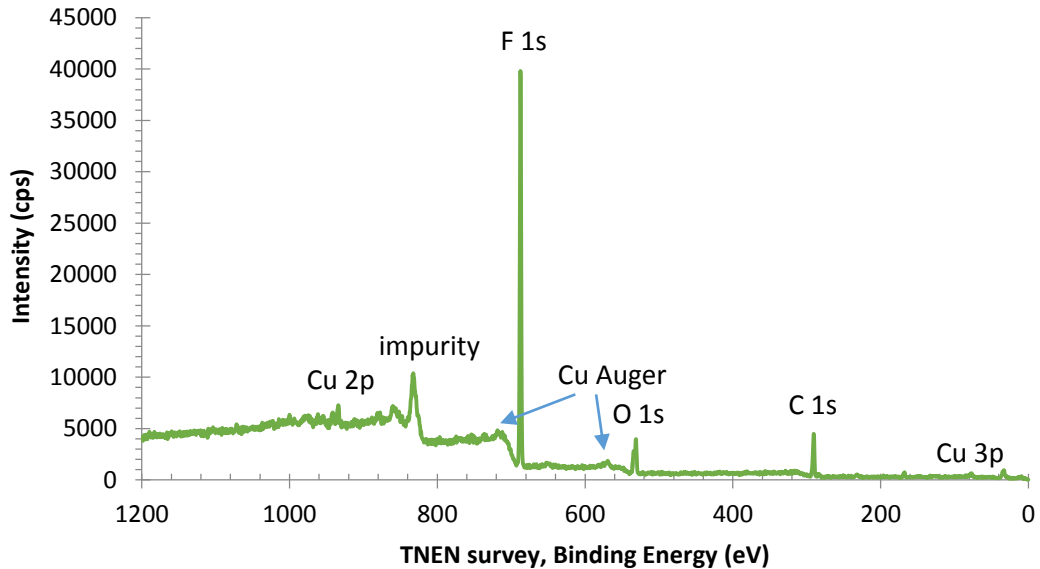
Figure 5.22. XPS spectra of surface elements in Toray/Nafion/Cu$_2$O/Nafion electrode.

Meanwhile, the surface composition derived from the elemental peak areas is given in Table 5.3. Flourine again made up the bulk of the surface with about 81% atomic and 77% mass concentration. The higher F content is due to the additional Nafion layer applied over the Cu$_2$O film. The Cu/O ratio was 0.30.

Table 5.3. Surface composition of Toray/Nafion/Cu_2O/Nafion electrode.

Element	[Atomic] %	[Mass] %
Cu 2p	3.7	11.8
O 1s	12.4	9.9
F 1s	80.8	76.5
C 1s	3.0	1.8

5.3.3.2. Current Profile

Figure 5.23 compares the amount of current that flowed on both electrodes during CO_2 reduction. In the Toray/Nafion/Cu_2O (TNE) electrode, the reduction process achieved steady-state current of -18 mA after 20 minutes.
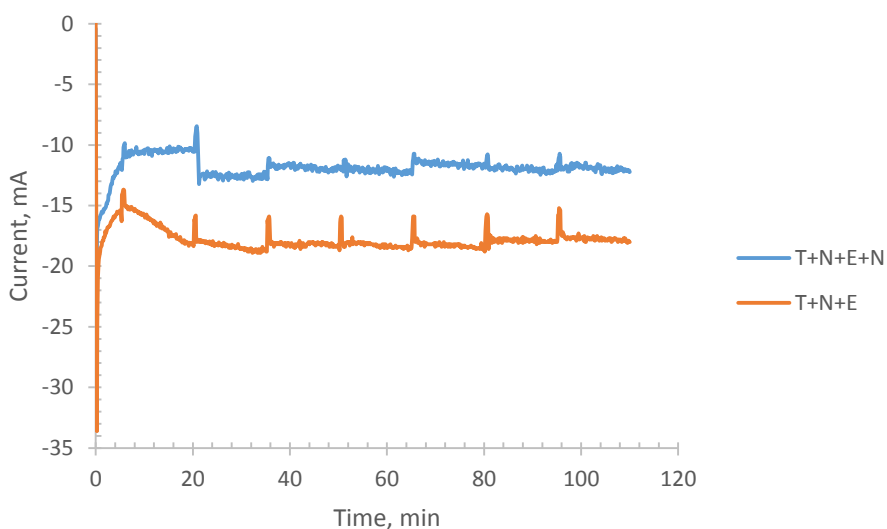
Figure 5.23. Current profile of TNEN and TNE electrodes during CO_2 electrolysis at -1.5V$_{NHE}$.

In the Toray/Nafion/Cu_2O/Nafion (TNEN) electrode, the reduction process achieved steady-state current of -12 mA after 20 minutes. The lower current in TNEN electrode suggests that the Nafion coating may be inhibiting current flow to the Cu_2O surfaces.

5.3.3.3. GC Product Analysis

Comparison of Product Formation Rates. We then compared the electrocatalytic activity of the two electrodes by looking at their product formation rates. Figure 5.24 shows the product formation rates in the TNE electrode. The initial production rate of CO and C_2H_4 were 7.3 and 4.2 µmol/cm^2*hr respectively. However, the rates decreased to 1.6 and 0.8 µmol/cm^2*hr at the end of the process for an average of 3.1 and 1.8 µmol/cm^2*hr.
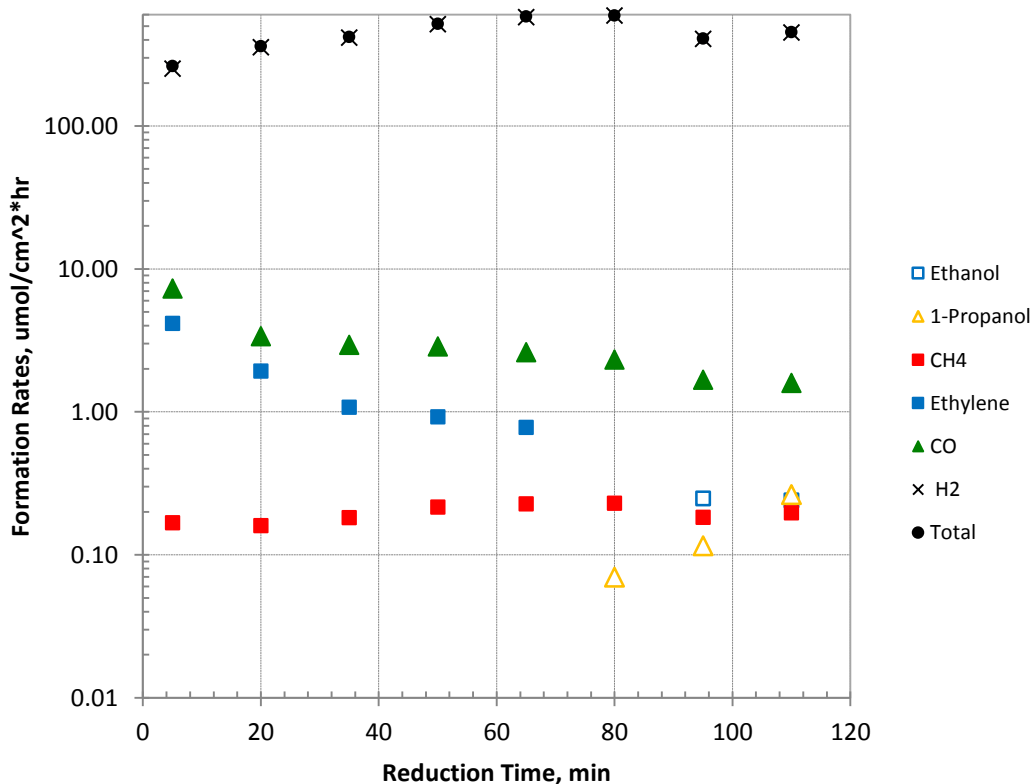
Figure 5.24. Formation rate of products on TNE electrode during CO_2 reduction at -1.5V$_{NHE}$.

Meanwhile, Figure 5.25 shows the product formation rates in the TNEN electrode where the production rate of CO and C_2H_4 were more stable with mean measured values of 5.3 and 3.2 µmol/cm^2*hr respectively. The liquid products ethanol and n-propanol

increased then stabilized with time for an average rate of 0.6 and 0.2 µmol/cm^2*hr respectively. We did not observe trace amount of CH_4 in the TNEN electrode.
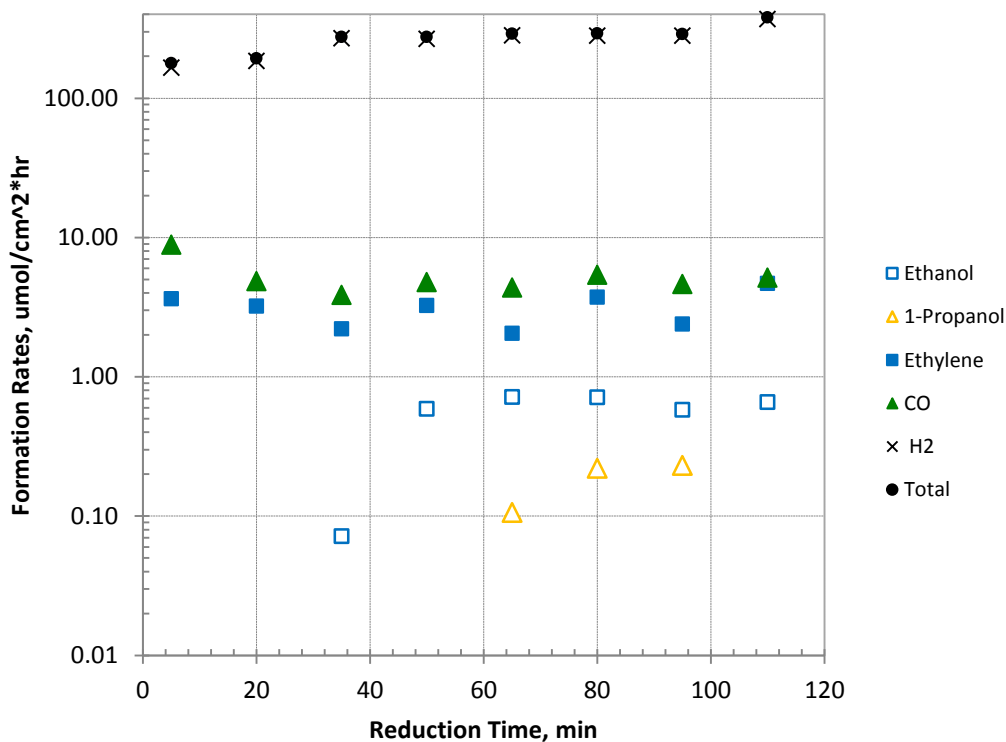
Figure 5.25. Formation rate of products on TNEN electrode during CO_2 reduction at -1.5V$_{NHE}$.

The mean total product formation rate was 450 µmol/cm^2*hr in the TNE electrode and 272 µmol/cm^2*hr in the TNEN electrode. The difference in the total product formation rate was in agreement with the difference in their steady state current. The bulk of production came from the reduction of H_2O to H_2.

Comparison of Product Faradaic Efficiencies. Figure 5.26 shows the product distribution on the TNE electrode. CO selectivity decreased from the faradaic efficiency of 3.0% to 0.6%. Ethylene selectivity also decreased from the faradaic efficiency of 10.0% to

1.6% at 65 minutes before it became undetectable. The average faradaic efficiency of ethylene and CO were 4.0% and 1.1% respectively. Both ethanol and n-propanol were detected later into the process at average faradaic efficiencies of less than 1.0%.
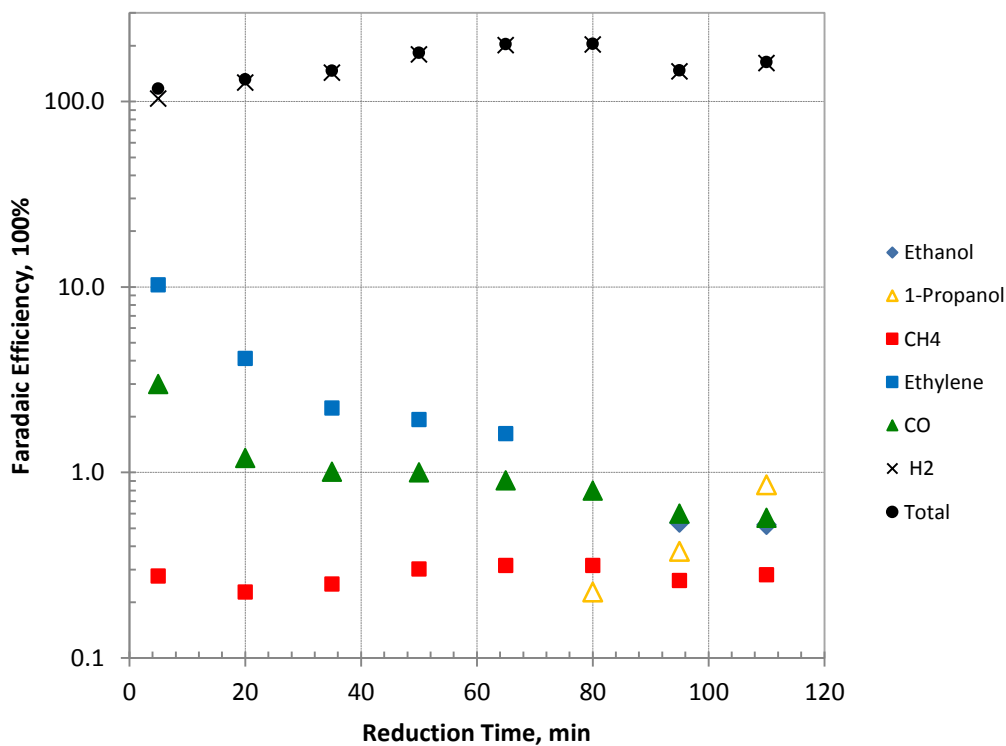
Figure 5.26. Faradaic efficiency of products on TNE electrode during CO_2 reduction at $-1.5V_{NHE}$.

For the TNEN electrode, we observed a better maintained selectivity towards CO and C_2H_4 (see Figure 5.27). Meanwhile, ethanol selectivity increased with reduction time then stabilized between 50 and 110 minute reduction time. However, we did not detect any methane in the TNEN sample. The average faradaic efficiency of ethylene, CO, ethanol and n-propanol products were 8.6%, 2.4%, 1.5% and 0.8% respectively.
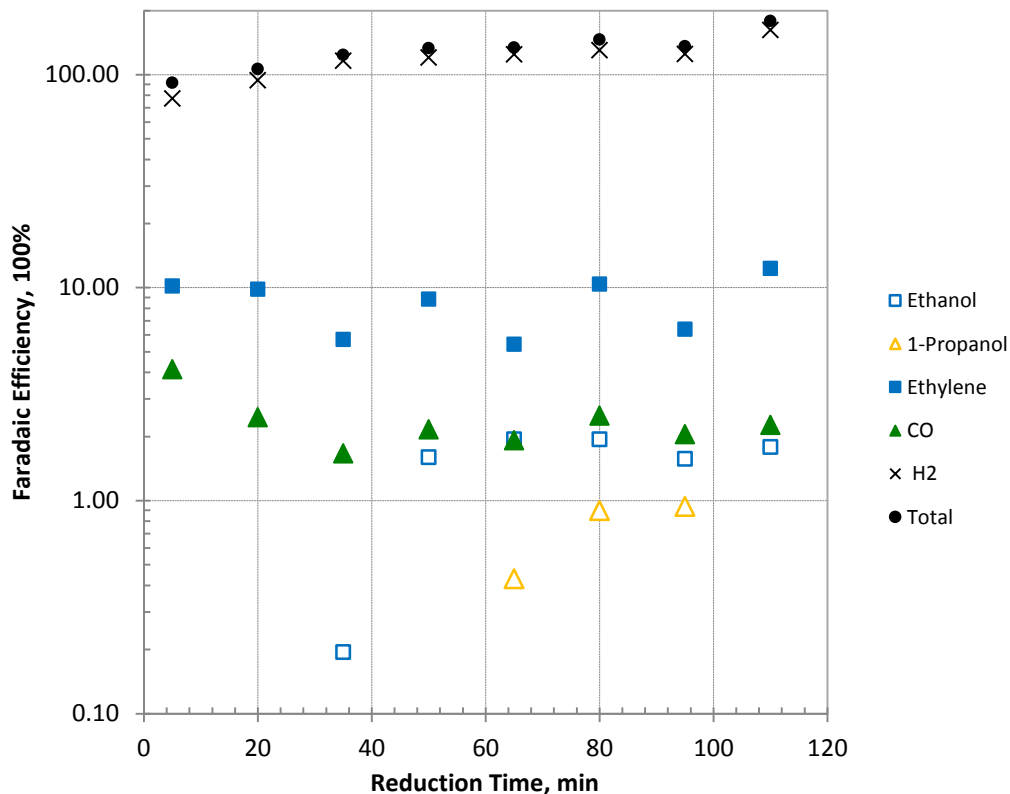
Figure 5.27. Faradaic efficiency of products on TNEN electrode during CO_2 reduction at $-1.5V_{NHE}$.

These results suggest that Nafion may be stabilizing the formation of CO and C_2H_4. The reduced Cu-nafion interface may be active site in the formation of CO and C_2H_4 while being more selective to C_2H_4 than to CH_4. The Nafion overlayer may be inhibiting a key intermediate in the formation of CH_4 while promoting the C-C coupling step. Hori suggested that CH_4 formation is enhanced by H_2 formation, however we did not consistently observe that with our results.

5.3.4. Kinetic Study on Cu_2O Film Electrodeposited on CuO Layer

We also studied the electrocatalytic activity of Cu_2O film deposited on a thermally grown CuO. This catalyst was examined by Ghadimkhani's group using

photoelectrochemical reduction of CO_2. In their experiment, the photoelectrode was irradiated with visible light and simultaneously electrolyzed at $-0.2V_{NHE}$ for 90 minutes. They obtained 85 µM methanol at 95% selectivity. In this section, we substituted photogenerated current with application of a more negative potential ($-1.5V_{NHE}$) and examined the product distribution.

5.3.4.1. Electrode Characterizations

SEM Analysis. SEM images were taken at different stages of the fabrication of $Cu/_{TH}CuO/_{ECD}Cu_2O$ electrocatalyst. We denote $_{TH}CuO$ as the thermal oxide and $_{ECD}Cu_2O$ as the electrodeposited Cu_2O. The Cu electrode was thermally oxidized and the SEM of the resulting surface is shown in Figure 5.28. The $Cu/_{TH}CuO$ surface consisted of irregularly shaped CuO particles and few overgrowth of nanorods.
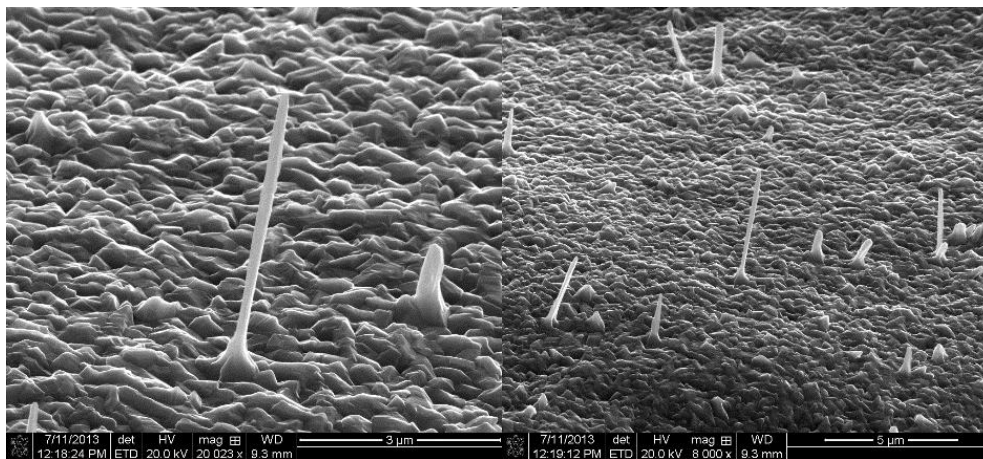
Figure 5.28. SEM of $Cu/_{TH}CuO$ electrode.

Cu_2O was then electrodeposited to the CuO layer and nanorods. The resulting SEM is shown in Figure 5.29. The surface of $Cu/_{TH}CuO/_{ECD}Cu_2O$ consisted of triangular pyramidal Cu_2O particles overlayering the CuO film and nanorod overgrowths.
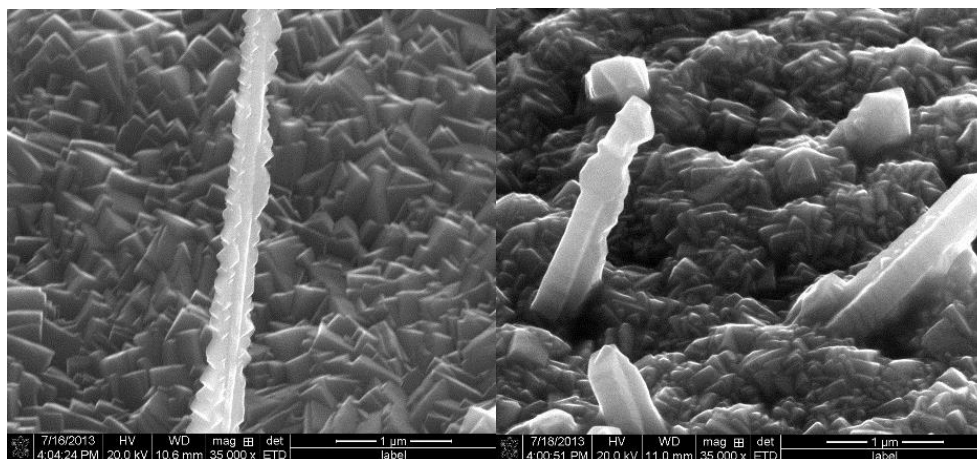
Figure 5.29. SEM of Cu/$_{TH}$CuO/$_{ECD}$Cu$_2$O electrode before CO$_2$ reduction.

Finally, after CO$_2$ reduction, the electrode surface was again monitored by SEM. Figure 5.30 shows that nanowires disappeared and Cu$_2$O micro pyramids were broken down into nanoparticles.
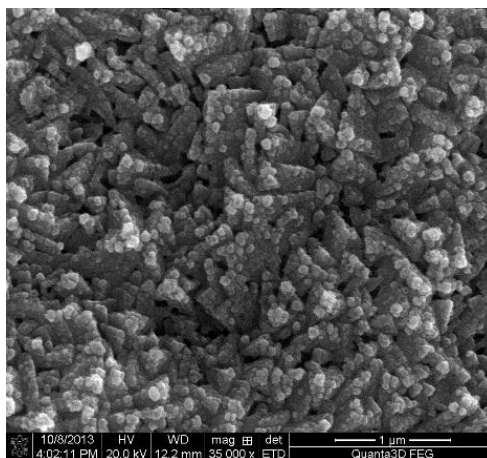
Figure 5.30. SEM of Cu/$_{TH}$CuO/$_{ECD}$Cu$_2$O electrode after CO$_2$ reduction at -1.5V$_{NHE}$ for 110 minutes.

XRD of Cu/$_{TH}$CuO/$_{ECD}$Cu$_2$O. The Cu/$_{TH}$CuO/$_{ECD}$Cu$_2$O electrode was then analyzed by XRD. The XRD profile given in Figure 5.31 shows different crystal phases of Cu, CuO and Cu$_2$O. The Cu crystals consisted of a mixture of Cu(111), Cu(200) and Cu(220)

84

oriented particles. Meanwhile the CuO particles consisted of a mixture of CuO(002) and CuO(111) crystal phases. Lastly, the Cu_2O film consisted of $Cu_2O(111)$, $Cu_2O(200)$ and $Cu_2O(222)$ crystal orientations.
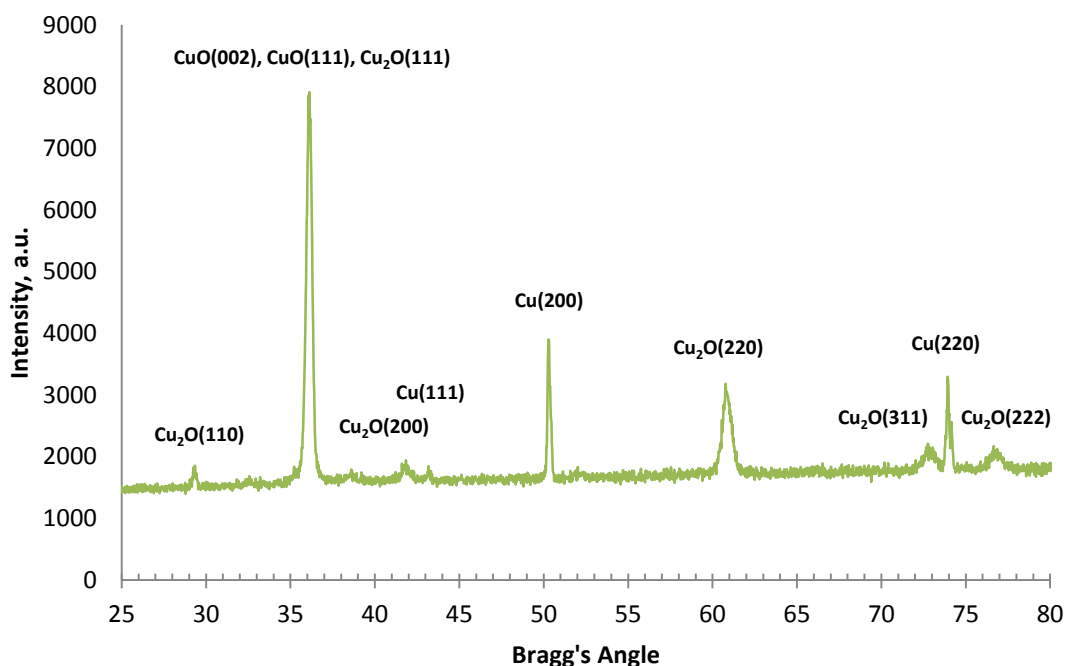
Figure 5.31. XRD scan of Cu/$_{TH}$CuO/$_{ECD}$Cu$_2$O electrode before CO$_2$ reduction.

Additionally, there were new Cu_2O crystal planes that were not present in other Cu_2O electrodes. They included $Cu_2O(110)$, $Cu_2O(220)$ and $Cu_2O(311)$ oriented particles. These additional crystal orientations likely resulted from growth on the CuO sublayer.

The XRD of the Cu/$_{TH}$CuO/$_{ECD}$Cu$_2$O electrode after CO$_2$ reduction at -1.5V$_{NHE}$ was also determined. As seen in Figure 5.32, the original CuO and Cu_2O crystal planes disappeared except for presence of residual $Cu_2O(200)$ planes in very small number. Interestingly, we also observed formation of CuO(202) particles that were not previously

present before CO_2 reduction. This observation suggest that the electrode maintained its oxidized state despite the application of high negative potential. However, the particles still underwent an electrochemical transformation, but they were not completely reduced to Cu. We have not previously observed this phenomenon with our electrodeposited Cu_2O particles.
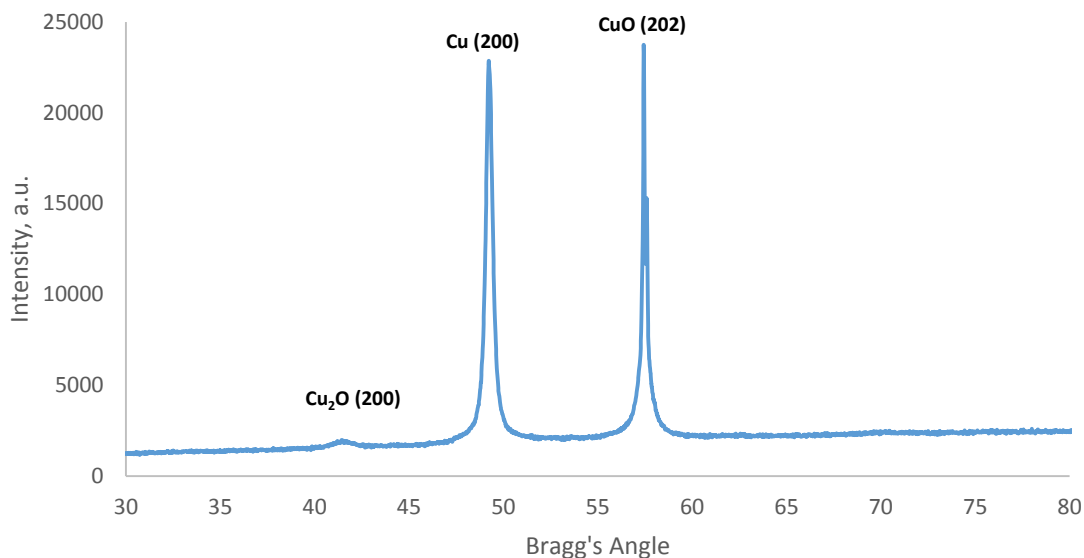
Figure 5.32. XRD scan of $Cu/_{TH}CuO/_{ECD}Cu_2O$ electrode after CO_2 reduction.

XPS of $Cu/_{TH}CuO/_{ECD}Cu_2O$. The XPS profile before CO_2 reduction is given in Figure 5.33. The XPS scan revealed Na 1s, Cu 2p, O 1s and C 1s elemental species at the surface of the electrode. The Na contaminants may have risen either during the fabrication of the electrode or during preparation for XPS analysis. They may only be physically lodged. The XPS shows large O 1s and C 1s peak relative to Cu 2p peak.
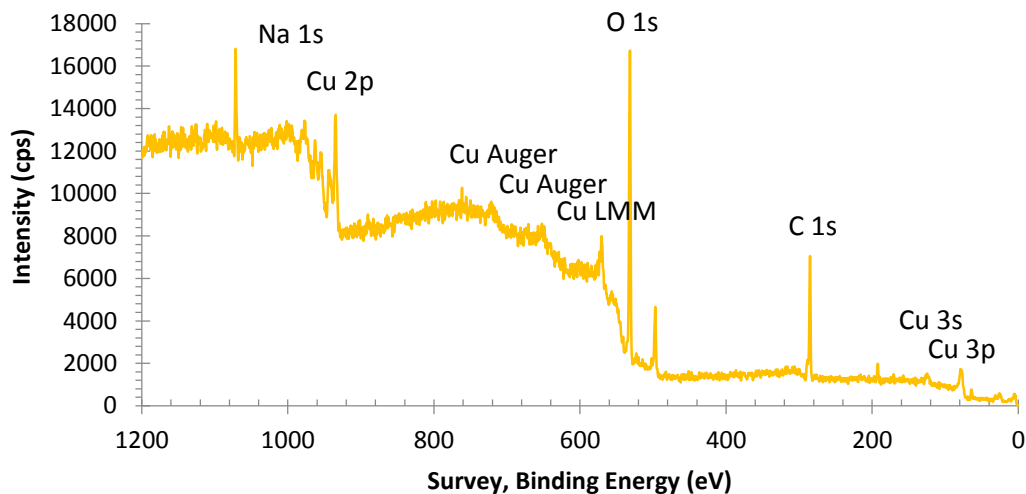
Figure 5.33. XPS survey of Cu/$_{TH}$CuO/$_{ECD}$Cu$_2$O electrode before CO$_2$ reduction.

The XPS profile after CO$_2$ reduction is given in Figure 5.34. The Na 1s peak has disappeared which indicate that these species where only physically lodged at the surface. The O 1s and C 1s peaks diminished while the Cu 2p peak intensified.
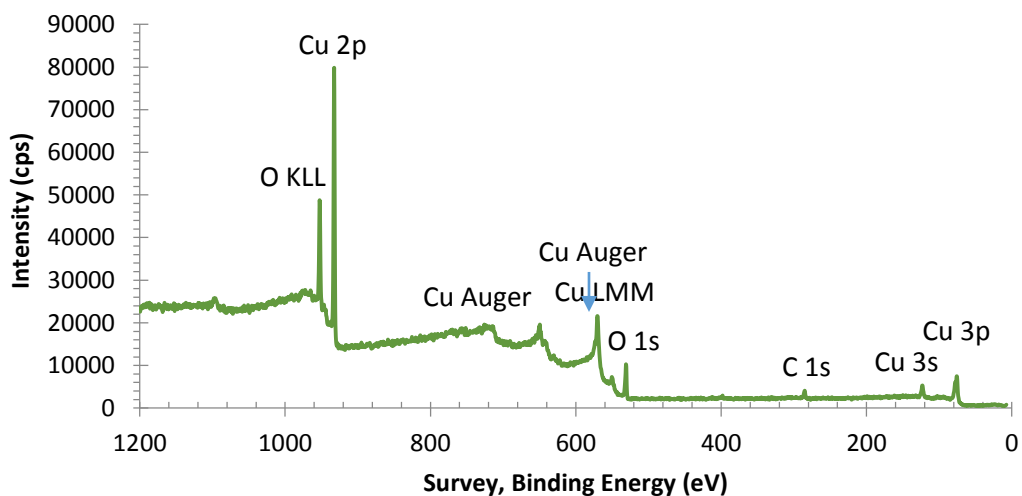
Figure 5.34. XPS survey of Cu/$_{TH}$CuO/$_{ECD}$Cu$_2$O electrode after CO$_2$ reduction.

We then determined the composition of the electrode using peak areas obtained from the XPS plot and it is listed in Table 5.4. The atomic Cu/O ratio before CO$_2$ reduction

was 0.2 which increased to 2.4 after CO_2 reduction. The increase in Cu/O ratio was a result of the reduction of CuO and Cu_2O to Cu. We also observed an initially high carbon content which decreased significantly after CO_2 reduction. While carbon contamination is common with XPS instrumentation, the reason for the decrease in the carbon content is not clear. Cu electrodes has been observed to lose activity due to the formation of carbonaceous compounds during electrolysis with bicarbonate solution. However, in this particular experiment, the XPS is suggesting that the initial carbon impurities were stripped off during electrolysis.

Table 5.4. Surface composition of Cu/$_{TH}$CuO/$_{ECD}$Cu$_2$O electrode.

Element	Before CO_2 ECR		After CO_2 ECR	
	[Atomic] %	[Mass] %	[Atomic] %	[Mass] %
Cu, 2p	10.4	34.3	57.4	85.7
O, 1s	47.8	39.8	23.7	8.9
C, 1s	41.5	26.0	18.9	5.3

5.3.4.2. Current Profile

The current profile is given in Figure 5.35. The plot shows a gradual increase in current between 0 and 65 minutes. The rise in current could have resulted from the increase in conductivity of the surface as Cu_2O crystals became Cu crystals.
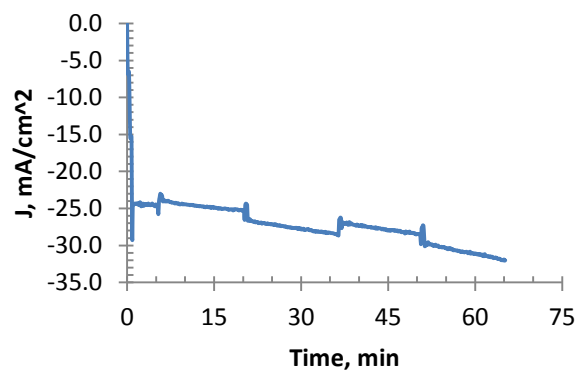
Figure 5.35. Current density versus time profile of Cu/$_{TH}$CuO/$_{ECD}$Cu$_2$O electrode during CO_2 reduction at -1.5V$_{NHE}$.

5.3.4.3. GC Product Analysis

Product Formation Rates. Finally, we used GC to identify and quantify the different products of CO_2 reduction. The formation rates are given in Figure 5.36. CO had the highest average formation rate of 16 μmol/cm^2*hr, followed by ethylene at 9.1 μmol/cm^2*hr. We observed very low rates of methane formation, at 0.04 μmol/cm^2*hr. With this electrode, we observed a relatively stable production rates for CO and C_2H_4. The kinetic pattern of H_2, CO, C_2H_4 and CH_4 formation were alike.

We also observed ethanol and n-propanol products at 3.7 μmol/cm^2*hr and 1.8 μmol/cm^2*hr respectively. The ethanol and n-propanol rates were dynamic with relatively high initial rates that slowed towards the end of the process.
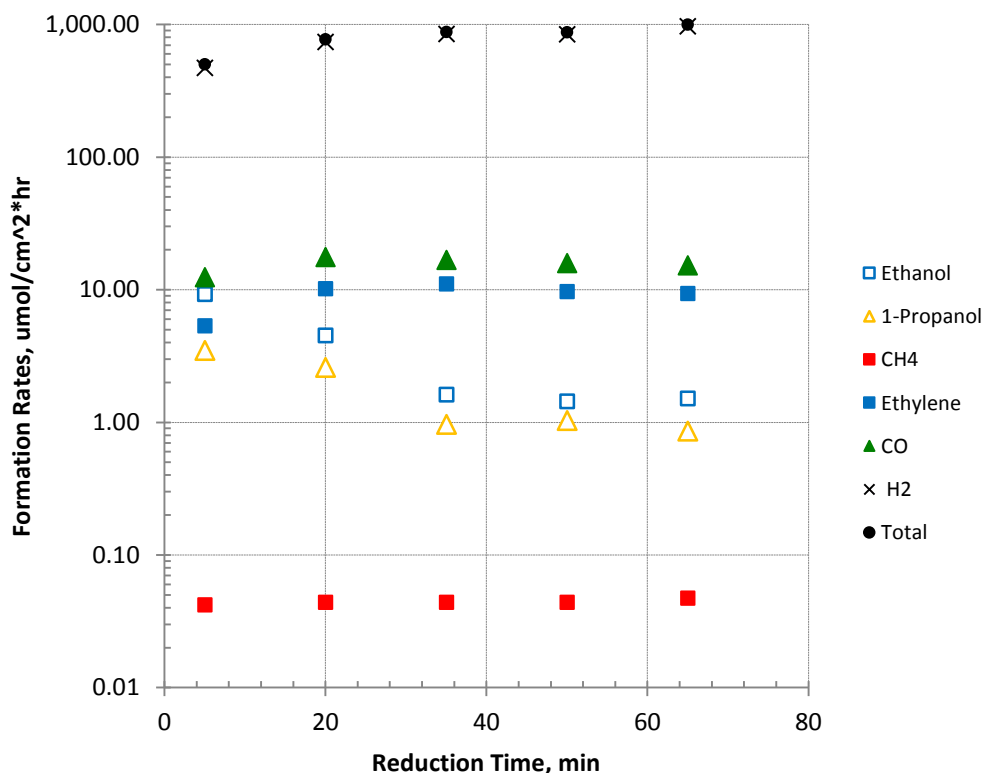
Figure 5.36. Formation rate of products on Cu/$_{TH}$CuO/$_{ECD}$Cu$_2$O electrode during CO_2 reduction at -1.5V$_{NHE}$.

Product Faradaic Efficiencies. The faradaic efficiency of ethanol, n-propanol, methane, ethylene, CO and H_2 are given in Figure 5.37. The electrocatalyst had an initially high selectivity for alcohol compared to the $Cu/_{ECD}Cu_2O$ catalyst with 13.2% ethanol and 7.5% n-propanol respectively versus 2% ethanol and 0.7% n-propanol in the latter. We observed formation of these alcohols instead of methanol. The $Cu/_{TH}CuO/_{ECD}Cu_2O$ electrode also showed higher mean selectivity for alcohol compared to the $Cu/_{ECD}Cu_2O$ electrode with 5.0% ethanol and 3.6% n-propanol versus 1.1% ethanol and 0.6% n-propanol in the latter.
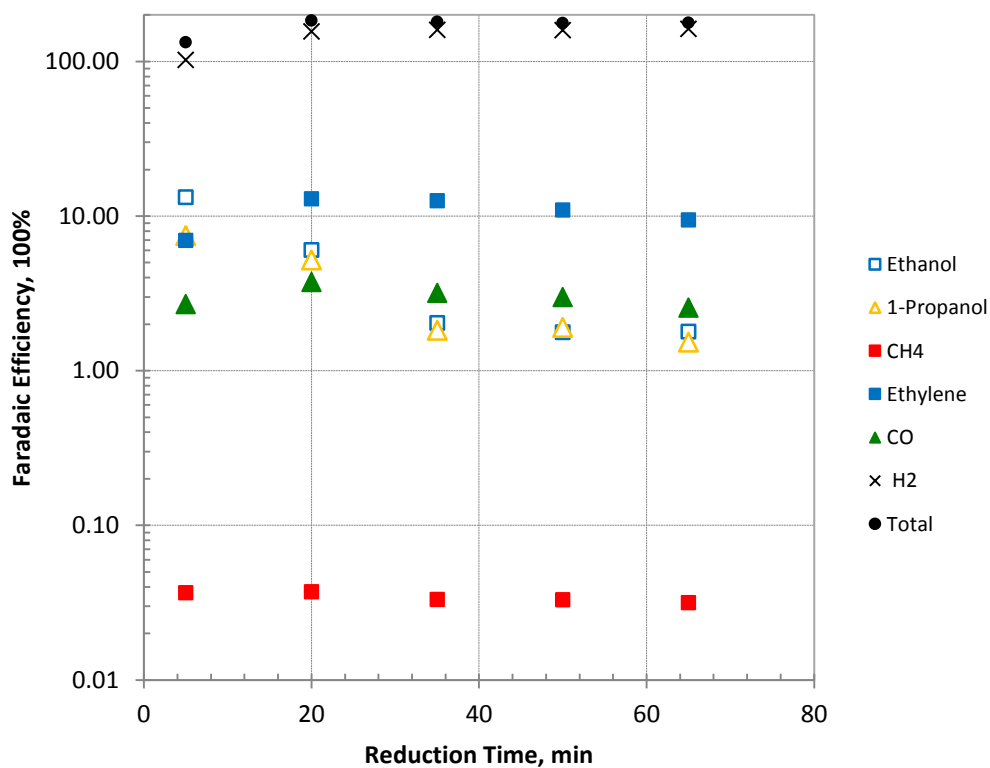
Figure 5.37. Faradaic efficiency of products on $Cu/_{TH}CuO/_{ECD}Cu_2O$ electrode during CO_2 reduction at $-1.5V_{NHE}$.

We also observed better selectivity for ethylene and CO in the $Cu/_{TH}CuO/_{ECD}Cu_2O$ electrode with 11% ethylene and 3.0% CO efficiency versus 5.2% ethylene and 1.5% CO efficiency in $Cu/_{ECD}Cu_2O$.

The presence of CuO as nucleation and growth precursor to electrodeposited Cu_2O may have promoted the formation of more low-coordinated sites during subsequent reduction of Cu_2O to Cu which enhanced selectivity of hydrocarbons and oxygenates. The XRD result also indicated that the CuO layer was stable although phase transformation occurred. The XRD of $Cu-Cu_2O$ after CO_2 reduction consisted of $Cu(200) > Cu(220) > Cu_2O(202) > Cu(111)$. The XRD of $Cu/_{TH}CuO/_{ECD}Cu_2O$ electrode after CO_2 reduction consisted of $Cu(200) > CuO(202) > Cu_2O(200)$.

With Ghadimkhani's electrode, the Cu_2O catalyst was photoelectrochemically stable. The formation of methanol may be associated with presence of a stable Cu_2O catalyst while the formation of ethanol and n-propanol may be associated with reduced Cu_2O particles.

5.4. Summary and Conclusion

In this Chapter, we studied the electrocatalytic activity of Cu_2O film electrochemically deposited on Cu foil and Toray carbon fiber paper. The Cu_2O film had a cubic architecture. Cu_2O film electrodeposited on Cu were mostly oriented in the (111) direction while those electrodeposited on Toray were mostly oriented in the (110) direction.

In the first section, we have determined that thicker oxide improves CO formation while suppressing H_2 formation.

In the second part, we looked at the kinetics of CO_2 reduction on $Cu/_{ECD}Cu_2O$. We observed more products with this electrode than in polycrystalline Cu of Chapter 4 with

the detection of ethanol and n-propanol. The order of preference also changed, particularly at $-1.5V_{NHE}$. In Cu, selectivity was in the order of $CH_4 > CO > C_2H_4$. In $Cu/_{ECD}Cu_2O$, selectivity was in the order of $C_2H_4 > CO > CH_4$. After CO_2 reduction, majority of Cu_2O crystal planes disappeared.

These results indicate that Cu derived from Cu_2O film is different from polycrystalline Cu. With Cu, CO_{ads} were more reducible to CH_4 than C_2H_4. With $Cu/_{ECD}Cu_2O$, CO_{ads} were more reducible to C_2H_4 than CH_4 despite having more $Cu(200)$ particles present after the reduction of Cu_2O.

In the third section, we observed that Nafion stabilized the selectivity of C_2H_4 and CO and also inhibited the formation of CH_4.

Finally in the last section, we observed additional Cu_2O crystal planes as a result of using CuO as growth template. The use of a CuO layer as growth substrate for electrodeposited Cu_2O particles appeared to improve the selectivity of Cu_2O to hydrocarbons, especially ethylene, ethanol and n-propanol.

CHAPTER 6
CO$_2$ ELECTROCHEMICAL REDUCTION
ON SUPPORTED Cu$_2$O PARTICLES

6.1. Introduction

In this Chapter, we studied the electrocatalytic activity of colloidal Cu$_2$O particles supported on three different substrates; namely, (1) Toray, (2) glassy carbon and (3) copper. In Section 6.3.2, we examined the kinetics of CO$_2$ reduction on Toray supported Cu$_2$O particles. First, we looked at the reproducibility of product distribution on Cu$_2$O particles by applying two sets of CO$_2$ reduction on the same electrode 12 days apart. Then we studied the effect of different catalyst preparation conditions; namely (1) effect of aging time during Cu$_2$O synthesis, (2) effect of Nafion, (3) effect of reagent composition during Cu$_2$O synthesis, particularly on the amount of NaOH and (4) effect of Cu$_2$O polarization. Finally, we examined the product distribution at different potentials. We compared two sets of Cu$_2$O particles, the larger Cu$_2$O MP and the smaller Cu$_2$O particles. We also compared these results to polycrystalline Cu.

We then studied the effect of using two other support substrates. In Section 6.3.3, we deposited Cu$_2$O particles on glassy carbon and studied both the kinetics and the potential dependence of CO$_2$ reduction on this electrode. In Section 6.3.4, we deposited Cu$_2$O particles on Cu and studied the kinetics at -1.5V$_{NHE}$.

6.2. Materials and Methods

6.2.1. Preparation of Toray, Glassy Carbon and Copper Support Substrates

Several pieces of 1 cm x 2 cm x 0.019 cm Toray carbon fiber paper (Toray, TGP-H-060, Fuel Cell Store), 1 cm x 2 cm x 0.0254 cm Cu sheet (ESPI Metals) and 1 cm x 2 cm x 0.1 cm Glassy Carbon plate (Alfa Aesar) were cut from source materials.

Cu sheets and GL plates were first cleaned in 1.0M HCl (35.5-38% reagent bottle, Aristar) for 10 minutes, then sonicated in 2-propanol (99.5%, Mallinckrodt), acetone (99.5%, Mallinckrodt) and deionized H_2O, sequentially for 10 minutes. Toray was used without any additional pre-treatments.

6.2.2. Synthesis of Colloidal Cu_2O Particles

Cu_2O particles were synthesized by two different but similar procedures, the first followed the steps described by Chang et al. in 2009 while the second followed the steps described by Li et al. in 2013. The details are given in Section 3.1.2. After collecting dried powders of Cu_2O particles, they were deposited to three different support substrates.

6.2.3. Application to Support Substrate

With Toray, the substrate was immersed in a 10 mL ethanol solution consisting of defined amount of Cu_2O particles, Nafion (perfluorinated ion-exchange resin, 5 wt% solution in lower aliphatic alcohols/H_2O mix, Sigma-Aldrich) and ethanol (CH_3CH_2OH, Sigma-Aldrich, ≥99.5%). The solvent was allowed to evaporate in open container which allowed Cu_2O particles to settle on the surface.

With GL, a Cu_2O-nafion ink was prepared instead of Cu_2O-nafion mixture. In this case, 1 mL of ethanol was used as solvent to Cu_2O and Nafion blend. The ink was composed of 17 wt% Cu_2O and 83 wt% Nafion. The ink was brush-coated on the front and back side of GL and allowed to dry in open air. The Cu_2O and Nafion loading was 0.83 mg/cm^2 and 3.99 mg/cm^2 respectively.

With Cu, a hole was drilled on the sleeve part of the Cu sheet for attachment to the 4N Cu wire. The Cu_2O-nafion ink was brush-coated to the Cu surface. The ink mixture

contained 17 wt% Cu_2O and 83 wt% Nafion. The Cu_2O and Nafion loading were 0.9 mg/cm^2 and 4.3 mg/cm^2 respectively.

6.2.4. CO$_2$ Reduction on Control Electrodes (Support Substrates)

CO_2 electrochemical reduction was applied on (1) Toray without Nafion pre-treatment, (2) Toray with Nafion pre-treatment and (3) Glassy carbon plate (GL) at -1.5V$_{NHE}$ for 110 minutes.

6.2.5. CO$_2$ Reduction on Toray Supported Cu$_2$O Particles

6.2.5.1. Effect of Electrode Preparation Condition

We made several modifications to the standard procedure on Cu_2O electrocatalysts preparation and investigated their effects on the electrocatalytic activity of Cu_2O. We considered three factors; namely, (1) composition of reagent ingredients during the synthesis of Cu_2O particles (2) aging time during post Cu_2O synthesis and (3) Nafion/Cu_2O ratio. CO_2 reduction was performed on these electrodes at -1.5V$_{NHE}$ for 110 minutes.

The standard chemical reduction synthesis of Cu_2O involved mixing 4 different reagents with the following composition, (1) 0.005M $CuCl_2$, (2) 0.002M PEG, (3) 0.2M NaOH, (4) 0.05M LAAS. For the effect of reagent concentration, we examined +/- concentrations of PEG, NaOH, and LAAS from standard values; (1) 0.03M and 0.07M L-AAS, (2) 0.1M and 0.3M NaOH and (3) 0.001M and 0.003M PEG.

To study the effect of aging time, we aged the Cu_2O particles for 0, 30 min and 360 minutes. To examine the effect of Nafion, we considered Nafion/Cu_2O mass ratio of 0, 1.2 and 2.4.

6.2.5.2. Effect of Cyclic Voltammetry

In this section, we subjected two Cu_2O electrodes to four cycles of voltammetry before CO_2 reduction, the first one was without Nafion and the second one was with Nafion. The cyclic voltammetry was conducted between $-1.2V_{Ag/AgCl}$ and $+0.6V_{Ag/AgCl}$ at a sweep rate of 50 mV/s under CO_2 electrolysis condition.

6.2.5.3. Effect of Particle Size on Product Distribution

In this section, we compared two sets of Cu_2O electrocatalysts with distinct particle size; namely, (1) Cu_2O MP and (2) Cu_2O NP. Cu_2O MP and Cu_2O NP were synthesized by wet chemical reduction method as described by Chang et al. (2009) and Li et al. (2013) respectively. We examined the product distribution of these particles at different potentials by performing CO_2 reduction between $-1.0V_{NHE}$ and $-1.7V_{NHE}$, with 30 minute electrolysis at each potential.

6.2.6. CO₂ Reduction on Glassy Carbon Supported Cu₂O Particles

In this section, we performed two batches of CO_2 reduction on a single GL/Cu_2O electrode. The first batch was conducted at $-1.5V_{NHE}$ for 110 minutes. The second batch was conducted at a series of potential step from $-1.1V_{NHE}$ to $-1.7V_{NHE}$ for 60 minutes on each potential.

6.2.7. CO₂ Reduction on Copper Supported Cu₂O Particles

In this section, we performed CO_2 reduction at $-1.5V_{NHE}$ for 110 minutes.

6.3. Results and Discussion

6.3.1. CO₂ Reduction on Control Electrodes (Support Substrates)

Before we examined the electrocatalytic activity of Cu_2O particles, we first determined the electrocatalytic activity of the support substrates. Both carbon fiber paper

(Bidault et al. 2009, Huanga and Wang 2014, Sharma and Pollet, 2012, de Jongh 2012) and glassy carbon (Van Der Linden and Dieker 1980) are materials commonly used as electrodes or support substrates in fuel cells and other electrochemical applications due to their excellent mechanical and thermal properties. They do not decompose under high potential electrolysis, although they catalyze the reduction of H_2O molecules. Additionally, Toray offers high surface area and accessibility to gaseous species while GL has the rigidity that makes it flexible to a wide variety of reactor configuration.

6.3.1.1. Toray and Toray/Nafion

Current Profile. Figure 6.1 shows the current profile generated by Toray and Toray/Nafion electrodes. With Toray, electrolysis started with a low current of 1 mA but gradually increased to 28 mA towards the end of the reduction period. The Toray sample obtained from Fuel Cell Store was pre-coated with Teflon in order to suppress liquid wetting and promote gas phase reactions on the surface and is likely the reason for the initially low current.
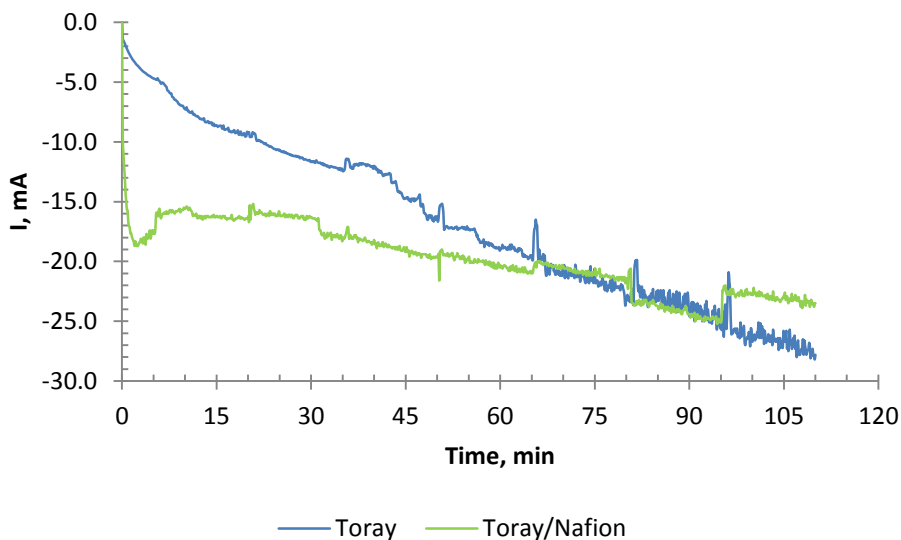
Figure 6.1. Current profile of Toray and Toray/Nafion electrodes at -1.5V$_{NHE}$ CO$_2$ reduction.

With Toray/Nafion electrode, CO_2 reduction immediately produced high current near its high of 24 mA. The presence of Nafion allowed for the immediate onset of electrochemical reactions which where otherwise restrained on the purely Toray electrode. Near the end of the process, the two electrodes exhibited fairly identical current flow.

Product Distribution on Toray. The graphs in Figure 6.2 and 6.3 show the formation rates and faradaic efficiencies of H_2, CO and CH_4 on Toray electrode respectively.
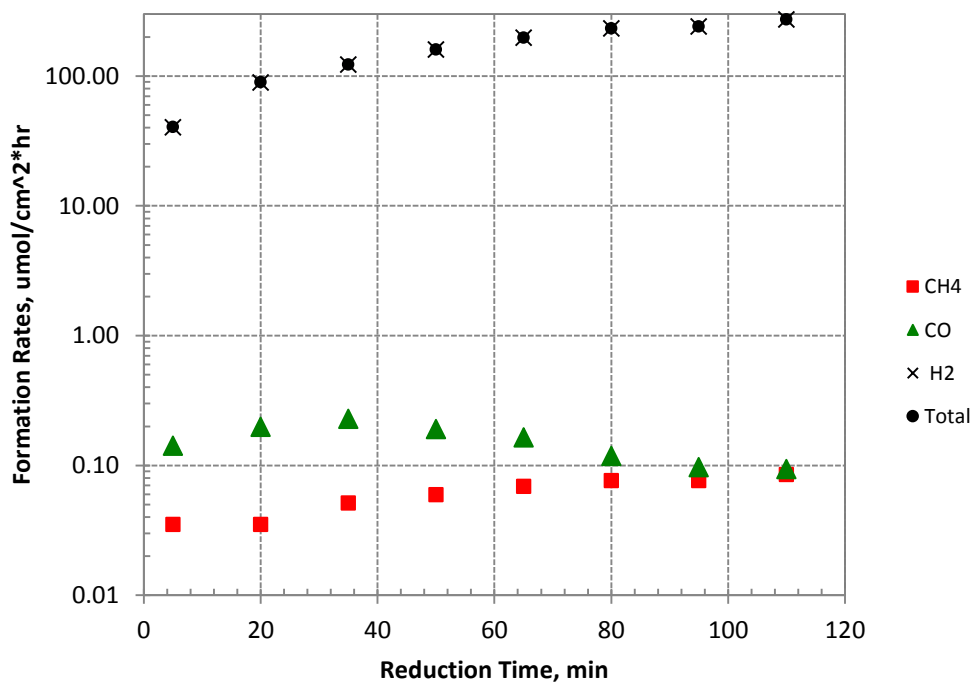
Figure 6.2. Product formation rates during CO_2 reduction on Toray at $-1.5V_{NHE}$.

Toray mainly produced H_2 with an initial, final and average production rates of 40, 273 and 170 $\mu mol/cm^2*hr$. Toray also produced trace amounts of CO and CH_4 products at less than 0.3 $\mu mol/cm^2*hr$.

Faradaic efficiency plot in Figure 6.3 expectedly showed high H_2 faradaic efficiency that was close to or slightly exceeding 100%. We also observed CO and CH_4

but at faradaic efficiencies of less than 0.5%. Majority of measured current was therefore used to reduce H_2O to H_2.
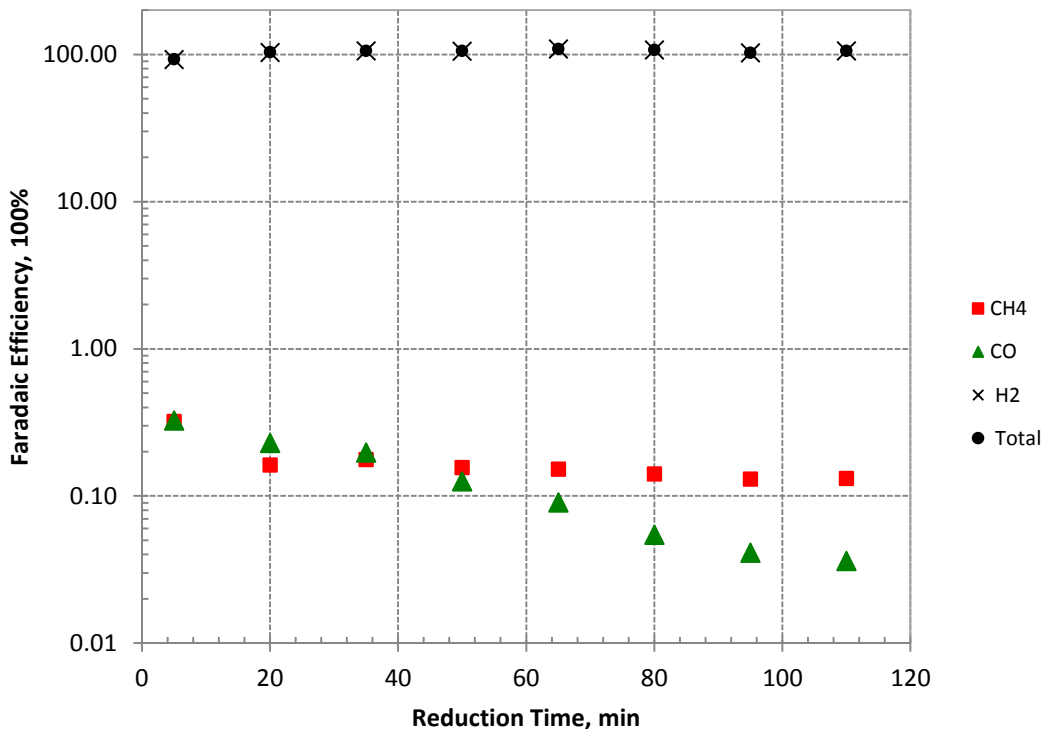
Figure 6.3. Faradaic efficiency of products during CO_2 reduction on Toray at -1.5V_{NHE}.

Product Distribution on Toray/Nafion. Meanwhile, the graph in Figure 6.4 shows the formation rates and faradaic efficiencies of H_2, CO and CH_4 on Toray/Nafion electrode. Again, the electrode mainly produced H_2 with an initial, final and average production rates of 163, 236 and 198 $\mu mol/cm^2*hr$. The measured initial H_2 rate was higher in Toray/Nafion than in Toray which was expected from the current profile in Figure 6.1, while the average H_2 rate was close to that of Toray. The electrode also produced trace amounts of CO and CH_4 products at less than 0.1 $\mu mol/cm^2*hr$.
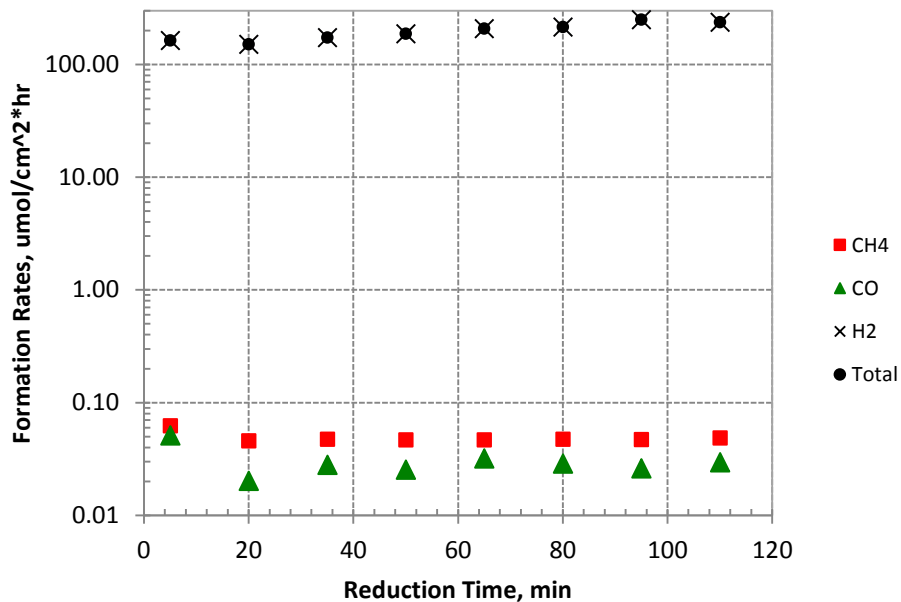
Figure 6.4. Product formation rates during CO_2 reduction on Toray/Nafion at $-1.5V_{NHE}$.

Faradaic efficiency plot in Figure 6.5 also showed high H_2 faradaic efficiency that was close to or slightly exceeding 100%.
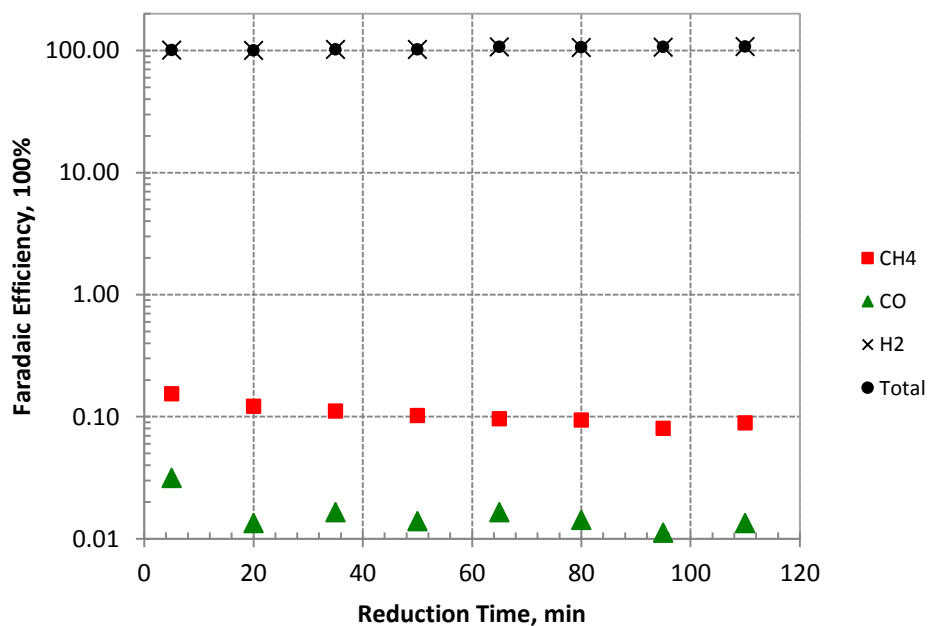
Figure 6.5. Faradaic efficiency of products during CO_2 reduction on Toray/Nafion at $-1.5V_{NHE}$.

We also observed CO and CH$_4$ but at faradaic efficiencies of less than 0.2%. Majority of measured current was therefore used to reduce H$_2$O to H$_2$.

6.3.1.2. Glassy Carbon

Current Profile. CO$_2$ reduction on GL generated a mean current of 7.6 mA (electrode area of 1.9 cm^2) as shown in Figure 6.6 which was lower than in Toray. This is because GL has lower surface area per square length than Toray. The current profile was similar to that of Toray electrode.
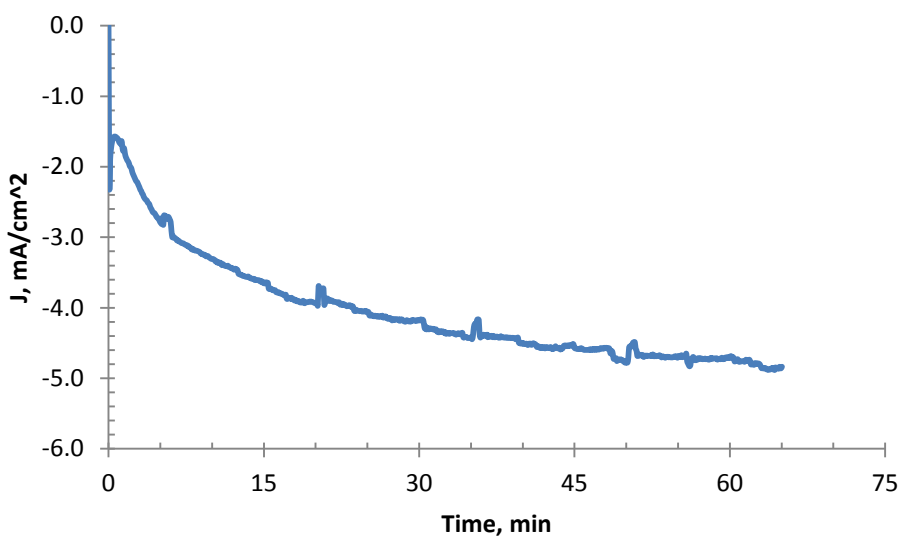
Figure 6.6. Current profile of glassy carbon at -1.5V$_{NHE}$ CO$_2$ reduction.

Product Distribution. The graphs in Figure 6.7 and 6.8 show the formation rates and faradaic efficiencies of H$_2$, CO and CH$_4$ on glassy carbon electrode. The electrode mainly produced H$_2$ with an initial, final and average production rates of 32, 96 and 73 μmol/cm^2*hr. These values were less than what were generated on Toray electrodes. GL also produced trace amounts of CO and CH$_4$ products at less than 0.6 μmol/cm^2*hr.
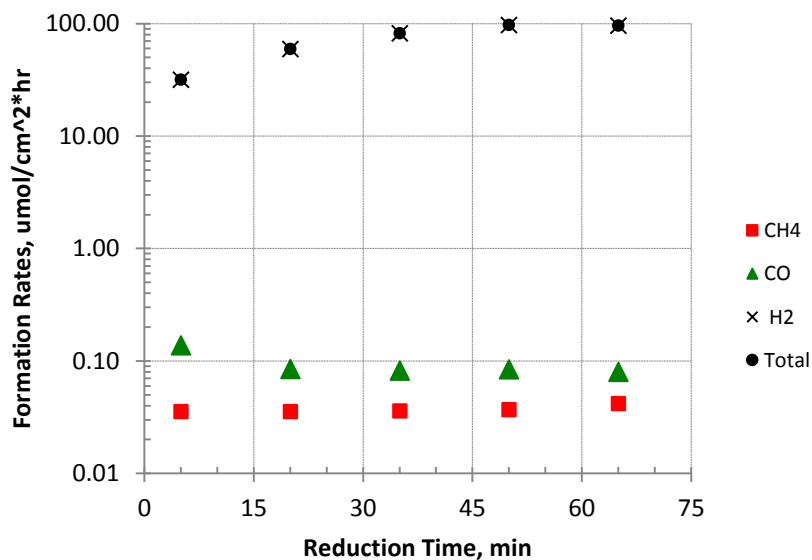
Figure 6.7. Product formation rates during CO_2 reduction on glassy carbon electrode at -1.5V_{NHE}.

Like Toray, GL showed very high selectivity towards H_2 and the product was responsible for most of the current activity. CO and CH_4 current efficiencies were limited to less than 0.7%.
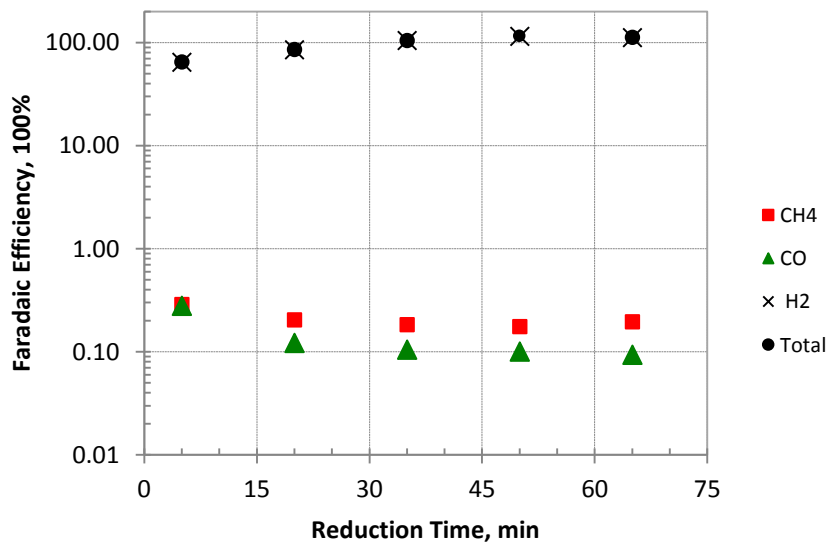
Figure 6.8. Faradaic efficiency of products during CO_2 reduction on glassy carbon electrode at -1.5V_{NHE}.

These results suggest that any hydrocarbon formation from CO_2 will only occur on Cu_2O particles. Nevertheless, H_2 formation would also be expected to occur and compete with CO_2 on these Cu_2O surfaces.

6.3.2. CO_2 Reduction on Toray Supported Cu_2O Particles[2]

We now examine the electrocatalytic CO_2 activity on Toray supported Cu_2O particles. In this section, we looked at the effect of different synthesis conditions and reaction conditions on the formation rate and selectivity of Cu_2O particles towards ethanol, n-propanol, methane, ethylene and CO. We have also considered H_2 formation, although they are not derived from CO_2 reduction. While H_2O is reduced to H_2, some H atoms from H_2O species are also utilized in the hydrogenation of CO intermediates.

6.3.2.1. Reproducibility Test[3]

We started this section by examining the reproducibility of product distribution on Toray/Nafion/Cu_2O electrode which represents our baseline sample. The electrode consisted of 26.5 mg Cu_2O and 21.1 mg Nafion. We conducted two separate batches of CO_2 reduction with a time difference of 12 days.

SEM Analysis. Figure 6.9 shows an SEM image of colloidal Cu_2O particles with Nafion binder before and after the first CO_2 reduction. The Cu_2O particles were cubic with a set of 80 nm particles and 400 nm particles. Thermodynamically and kinetically, Cu_2O particles are expected to get reduced to Cu particles at the applied potential of $-1.5V_{NHE}$. However, in this particular image scan area, the SEM image does not show physical evidence of a change in the cubic structure or decoration of particles. Nafion, which can be seen here like a transparent paste may have prevented the reduction of Cu_2O that it is in

contact with. The smaller Cu_2O particles also appeared to agglomerate into larger Cu_2O particles.
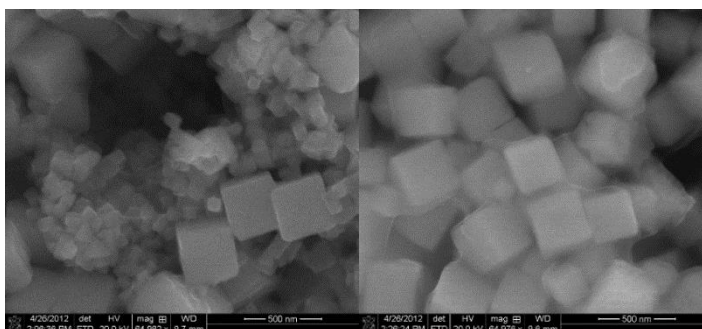
Figure 6.9. SEM of fresh Cu_2O (left) and Cu_2O after CO_2 reduction at -1.5V_{NHE} (right).

Current Profile. Figure 6.10 shows current profile on the two batches of CO_2 reduction applied on the electrode. The first run had an average current of 24 mA while the second run had an average current of 18 mA. The second process therefore showed about 25% less current than the first process which would indicate a lower total formation rate. The brief spikes in the plot at regular interval was caused by liquid sampling taken every 15 minutes. In both runs, the total current steadily decreased with time.
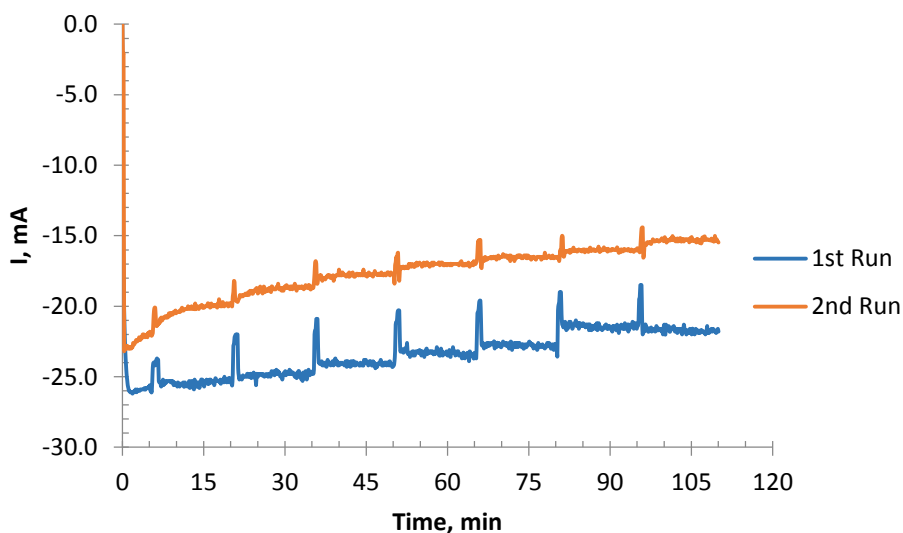
Figure 6.10. Current profile of the first and second CO_2 reduction on the baseline Toray/Nafion/Cu_2O electrode at -1.5V_{NHE}.

[3]This section previously appeared in reference: 3.Bugayong, J. and G.L. Griffin. 2013. "Electrochemical Reduction of CO2 using Supported Cu2O Catalysts." MRS Proceedings 1542. [Reproduced with permission from the Cambridge University Press.]

Product Formation Rates. Figure 6.11 shows the formation rates of ethanol, methane, ethylene, CO and H_2 during the first CO_2 reduction. CO showed the highest formation rates, with a mean production rate of 41 $\mu mol/cm^2*hr$. This was followed by ethylene with 13 $\mu mol/cm^2*hr$. On the other hand, we observed a low methane production rate of only 0.3 $\mu mol/cm^2*hr$. We also observed ethanol with a stable formation rate of 2.3 $\mu mol/cm^2*hr$. The kinetics of CO, CH_4 and C_2H_4 formation agrees with the branch point identified by Hori's reaction pathway, desorption of CO_{ads} intermediate versus hydrogenation of CO_{ads} intermediate to hydrocarbon. Additionally, CO formation appeared to be more favorable during the early stage of the process whereas hydrocarbon formation are more favorable during the later part of the reduction process.
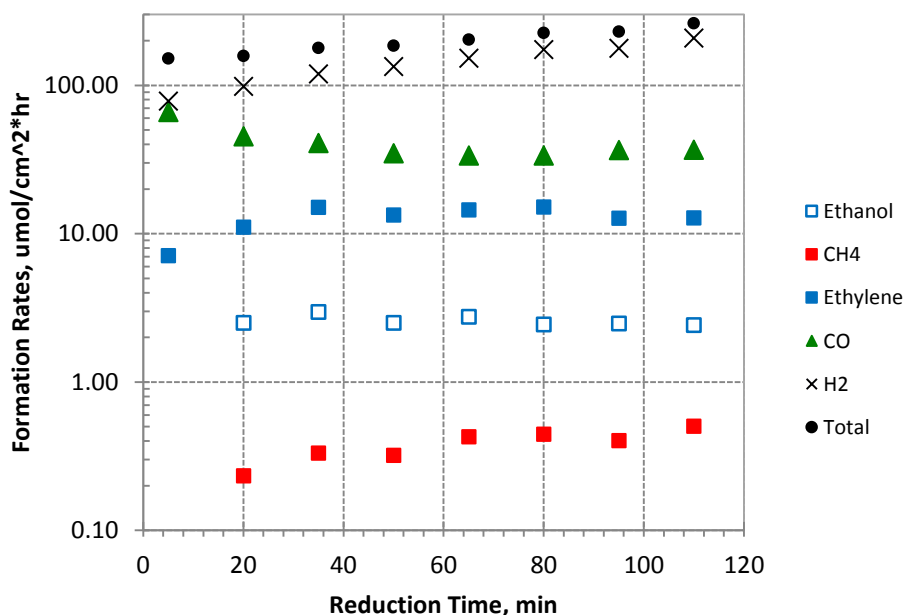
Figure 6.11. Formation rate of products during the first CO_2 reduction on the baseline Toray/Nafion/Cu_2O electrode at -1.5V_{NHE}.

The total formation rate increased despite a decrease in the total current. This may suggest slow process of Cu_2O reduction that occur throughout the process.

Meanwhile, Figure 6.12 shows the formation rates of ethanol, methane, ethylene, CO and H_2 during the second CO_2 reduction. The kinetics of CO, CH_4 and C_2H_4 formations are identical to that of the first CO_2 reduction. Again, CO registered the highest formation rate, at 45 $\mu mol/cm^2$*hr. This was followed by ethylene and ethanol, at 9.5 and 1.2 $\mu mol/cm^2$*hr respectively. Methane formation was again low, at only 0.6 $\mu mol/cm^2$*hr. The total formation rate decreased in the first half then increased in the second half of the process.
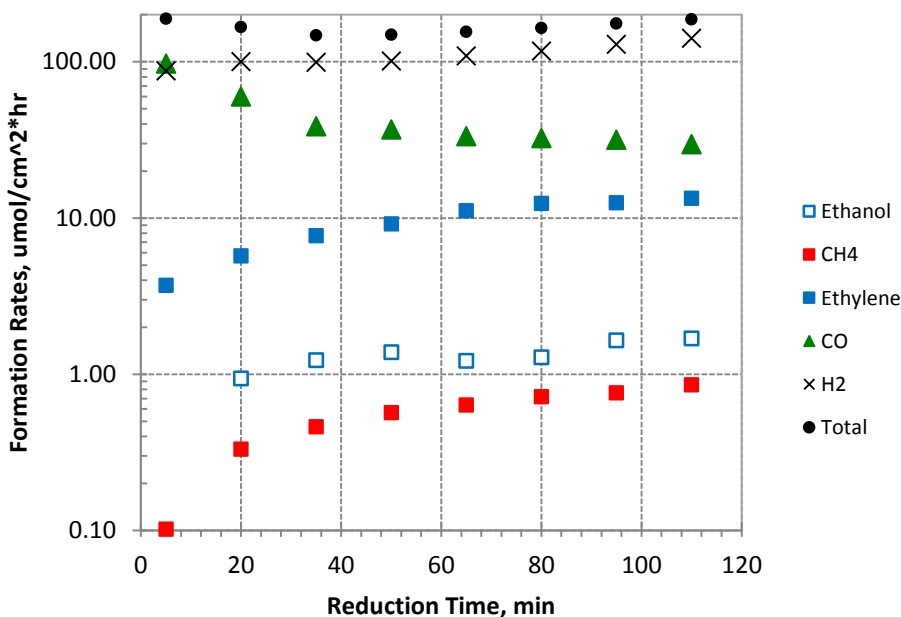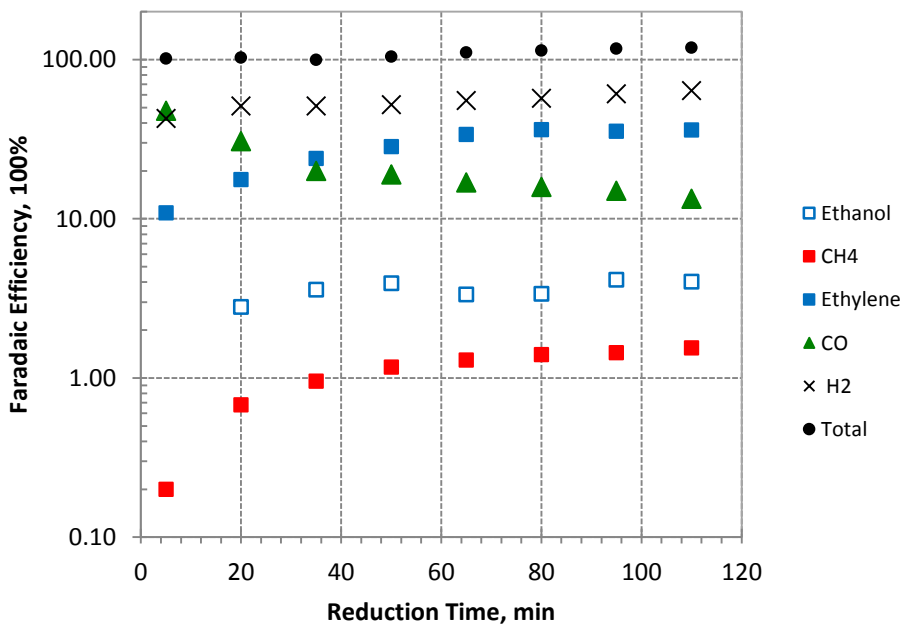

Figure 6.12. Formation rate of products during the second CO_2 reduction on the baseline Toray/Nafion/Cu_2O electrode at -1.5V_{NHE}.

Product Faradaic Efficiencies. Figure 6.13 shows the product distribution of ethanol, methane, ethylene, CO and H_2 during the first CO_2 reduction. The catalyst had an average 49% selectivity towards hydrocarbon formation. CO and C_2H_4 were the major hydrocarbon products with 16% and 28% faradaic efficiencies respectively. Intermediate amount of ethanol was produced at 4.8% faradaic efficiency with minor levels of CH_4 at

0.5% faradaic efficiency. The faradaic efficiency of C_2H_4 and CH_4 increased while the CO faradaic efficiency decreased.

The average C_2H_4/CH_4 selectivity ratio from this sample was 58.7 compared to a ratio of 0.2 from our Cu electrode and to a ratio of 14 on single crystal Cu(711) obtained by Hori's group. Additionally, the average (C_2H_4 + CH_4)/CO selectivity ratio was 1.85 which is only slightly higher than 1.3 with our Cu electrode. This suggests that Cu_2O catalysts exhibit a different mechanism of CO_2 conversion compared to Cu.
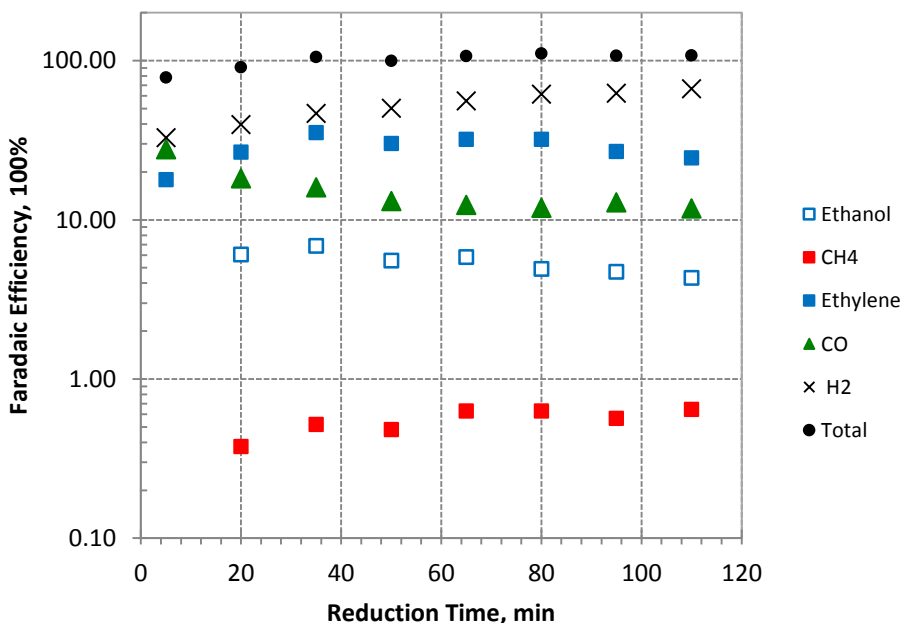
Figure 6.13. Faradaic efficiency of products during the first CO_2 reduction on the baseline Toray/Nafion/Cu_2O electrode at -1.5V_{NHE}.

At this point in our results, we don't have SEM images to show that Cu_2O particles were reduced to Cu although related studies on Cu_2O have shown that these particles will be reduced under these potential condition (Le et al. 2011, Li and Kanan 2012). With our other experiments on Cu_2O, which will be presented in the succeeding sections, we have simultaneously observed considerable morphological change in the Cu_2O particles and formation of Cu XRD peaks. As such, in the event of Cu_2O particle reduction, there would

107

be formation of dispersed Cu clusters. These surfaces have higher number of low coordinated sites were C_{2+} hydrocarbons are formed. Li (2012) suggested that the reduction of thick thermal copper oxide produced denser Cu grain boundaries that are abundant in sites that enhance CO selectivity and lower its kinetic potential requirement.

The selectivity of ethanol changed proportionately with ethylene which suggests these two products may proceed through a parallel reaction pathway. It is not clear which intermediates participate in the coupling reaction. Likely candidates include CO_{ads}, CH_{2ads}, COH_{ads} and CHO_{ads} intermediates. Kuhl suggested that glyoxal (HO-CH=C-(OH)$_2$) and/or acetaldehyde (H$_3$C-CH=O) maybe a common intermediate and branch point towards ethanol and ethylene.

During the second CO_2 reduction, the catalyst had a slightly better over-all hydrocarbon selectivity at 54% (see Figure 6.14).

Figure 6.14. Faradaic efficiency of products during the second CO_2 reduction on the baseline Toray/Nafion/Cu$_2$O electrode at -1.5V$_{NHE}$.

The kinetic variation in selectivity is similar to the first run, except that the CO selectivity was higher while ethanol selectivity was slightly lower. The average faradaic efficiencies were 28% ethylene, 22% CO, 3.2% ethanol and 0.5% methane. These results show that CO_2 reduction on colloidal Cu_2O electrocatalyst is reproducible.

6.3.2.2. Effect of NaOH Concentration During Cu_2O Synthesis

SEM Analysis. We have examined the electrocatalytic activity of colloidal Cu_2O particles that were prepared by wet chemical reduction using 0.2M NaOH added to 0.005M Cu^{2+} ions. Stoichiometrically, the amount of NaOH added to the mixture is sufficient to precipitate all available Cu^{2+} ions to $Cu(OH)_2$ while leaving excess NaOH in the mixture (0.19M). However, we observed that by further increasing the amount of NaOH, it started to cause formation of other morphologies (see Figure 6.15). The reduction of Cu_2O particles during CO_2 reduction also resulted in the evolution of more highly differentiated architecture of particles.
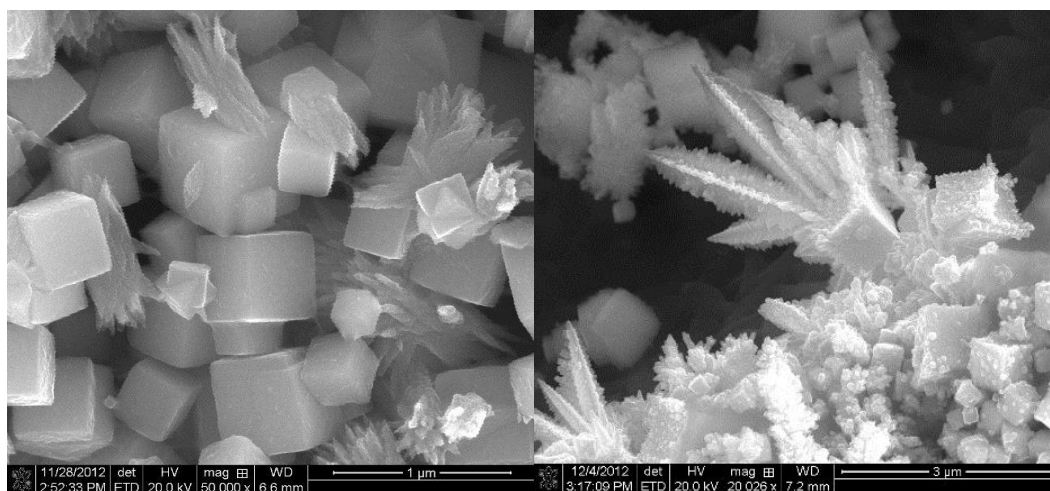
Figure 6.15. SEM of Cu_2O particles prepared using 0.3M NaOH (left) before CO_2 reduction and (right) after CO_2 reduction at $-1.5V_{NHE}$ for 110 minutes.

<u>Current Profile</u>. The current profile at $-1.5V_{NHE}$ CO_2 reduction was compared with that obtained from the baseline Cu_2O electrode (refer to Figure 6.16). Higher total current was observed, with an average of 37 mA, compared to 24 mA from the baseline Cu_2O electrode.
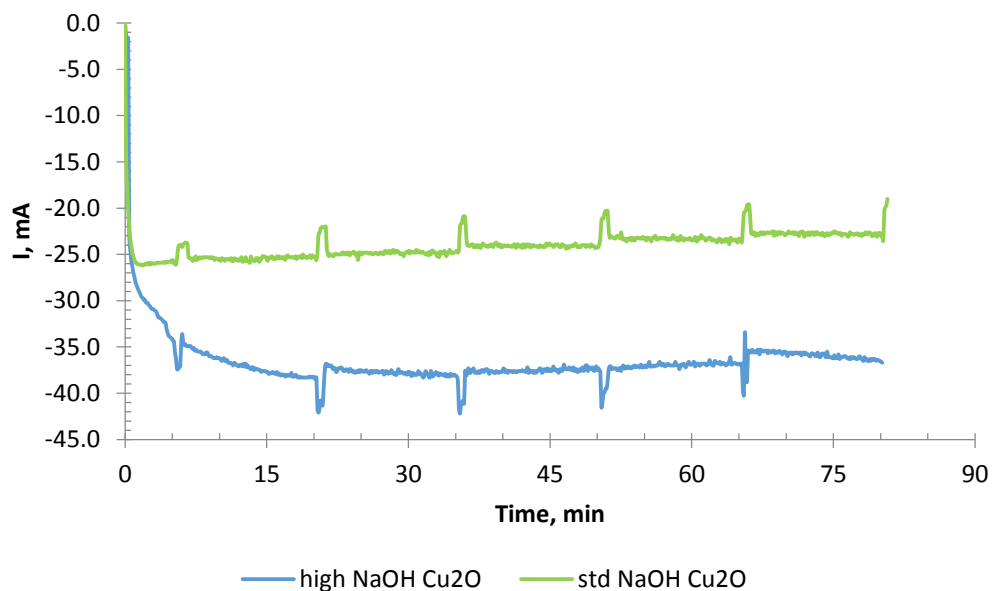
Figure 6.16. Current profile of the high NaOH Cu_2O and baseline Cu_2O electrodes.

<u>Product Distribution</u>. We then examined the product distribution on this catalyst by comparing the formation rate and faradaic efficiencies of ethanol, CH_4, ethylene, CO and H_2 with that of the baseline Toray/Nafion/Cu_2O sample (Cu_2O-360B). We observed the same sequence with formation rates (see Figure 6.17). The electrode showed highest activity towards CO formation, at 37 $\mu mol/cm^2*hr$ which is comparable to the baseline Cu_2O electrode. This was followed by ethylene at 9.6 $\mu mol/cm^2*hr$ and ethanol at 1.1 $\mu mol/cm^2*hr$. Methane was only produced at trace level of 0.2 $\mu mol/cm^2*hr$.
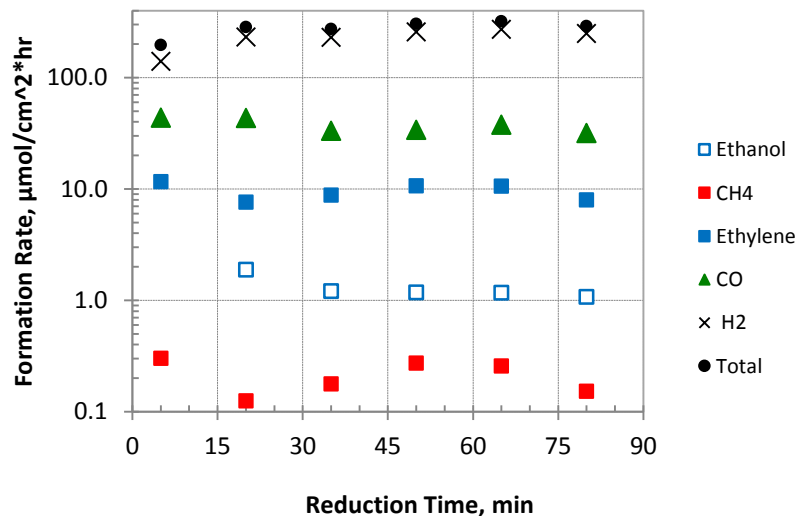
Figure 6.17. Formation rate of products during CO_2 reduction on Cu_2O prepared with high NaOH concentration at $-1.5V_{NHE}$.

In terms of selectivity, we saw a 36% decrease in ethylene faradaic efficiency, 33% decrease in CO faradaic efficiency and 42% increase in H_2 faradaic efficiency (see Figure 6.18). There was also a decrease in ethanol and methane products. These results suggest that the more homogeneous Cu_2O particles exhibited better selectivity towards ethylene, CO and ethanol than Cu_2O particles with mixed structures.
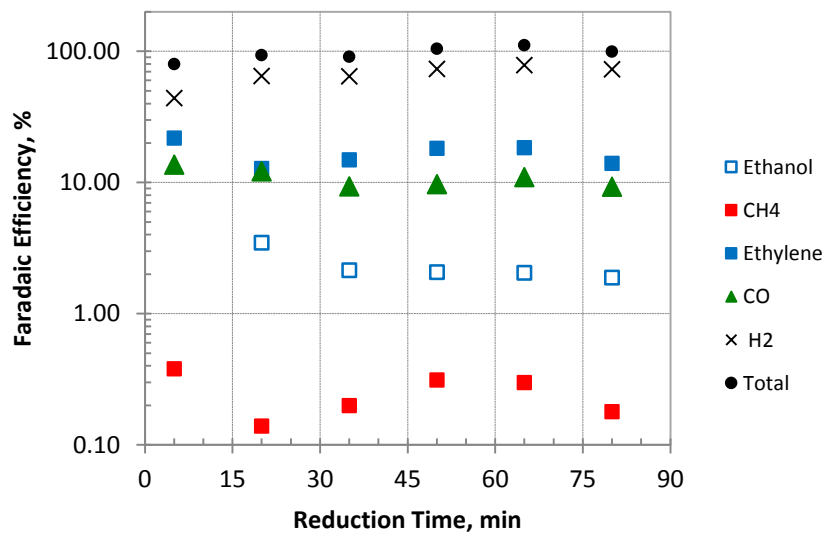
Figure 6.18. Faradaic efficiency of products during CO_2 reduction on Cu_2O prepared with high NaOH concentration at $-1.5V_{NHE}$.

111

6.3.2.3. Effect of Cu_2O Synthesis Aging Time

Next, we studied the effect of aging time during nucleation step of Cu_2O synthesis on the initial particle size and on the product distribution. We confirmed any variation in the size of the particle using SEM. In the electrocatalyst that we studied in the previous section, the particles were aged for 6 hours. In here, we attempted to vary the particle size by lowering the aging times to 0 and 30 minutes.

We considered comparing 4 different electrodes; (1) zero minute Cu_2O (Cu_2O-0), (2) 30 minute Cu_2O (Cu_2O-30), (3) 360 minute Cu_2O (Cu_2O-360A, with comparable Cu_2O loading as the first two samples and pre-characterized by cyclic voltammetry) and (4) Cu_2O electrode from the previous section (Cu_2O-360B, aged for 360 minutes and had a high Cu_2O loading). The data in Table 6.1 shows the Cu_2O loading of the different electrodes but with the same Nafion/Cu_2O mass ratio.

Table 6.1. Composition of Cu_2O electrode with different aging time and loading.

Electrode	Cu_2O Loading, mg	Nafion/Cu_2O Mass Ratio
Cu_2O-0	0.9	0.8
Cu_2O-30	1.9	0.8
Cu_2O-360A	1.1	0.8
Cu_2O-360B	26.5	0.8

SEM Analysis. The SEM image of the Cu_2O-0 electrode before and after CO_2 reduction is given in Figure 6.19. The approximate size of the Cu_2O-0 particles were 200 nm with variations in the range of 100 – 300 nm. After CO_2 reduction, we observed nanoparticle decorations on the surface of the cubes.
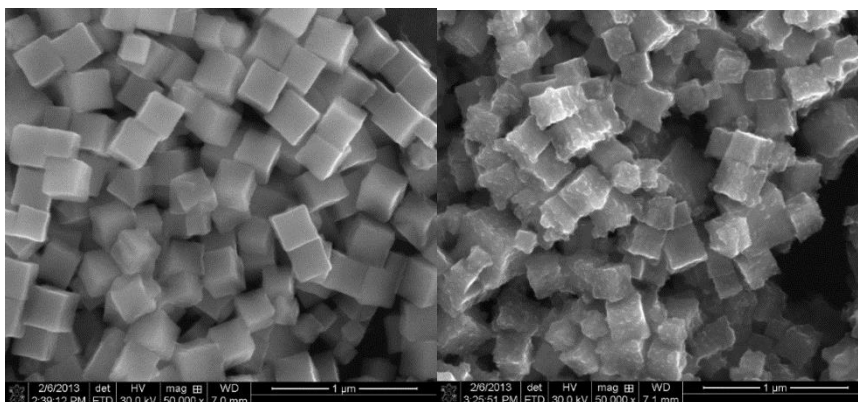
Figure 6.19. SEM of Cu_2O-0 sample (left) before CO_2 reduction and (right) after 110 minute CO_2 reduction at $-1.5V_{NHE}$.

Meanwhile, the SEM image of the Cu_2O-30 electrode before and after CO_2 reduction is given in Figure 6.20. The approximate size of the Cu_2O-30 particles were slightly larger, at 250 nm with variations in the range of $150 - 350$ nm. After CO_2 reduction, we also observed nanoparticle decorations on the surface of the cubes.
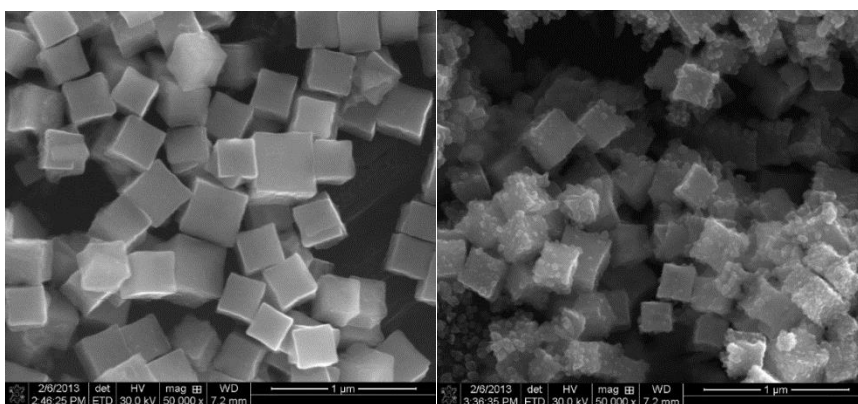
Figure 6.20. SEM of Cu_2O-30 sample (left) before CO_2 reduction and (right) after 110 minute CO_2 reduction at $-1.5V_{NHE}$.

Lastly, the SEM image of the Cu_2O-360B electrode is given in Figure 6.21. The electrode generated a mixture of distinct 400 nm and 80 nm sized particles. After CO_2

reduction, we did not observe formation of nanoparticle decorations on the surface of the cubes. A thin layer of Nafion could also be seen coated on these particles.
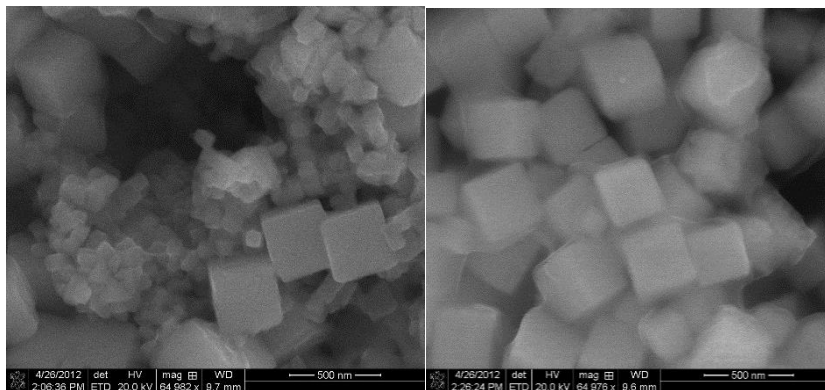
Figure 6.21. SEM of baseline Cu_2O-360B sample (left) before CO_2 reduction and (right) after 110 minute CO_2 reduction at $-1.5V_{NHE}$.

Controlling the particle size by changing the aging time during Cu_2O nucleation stage appeared to be not sufficient. The bulk of particle growth may have taken place immediately after the reducing agent (ascorbate) was added.

Additionally, these images suggest that Nafion was stabilizing the surface morphology of the Cu_2O particles. Although Nafion was present in all these electrodes by the same Nafion/Cu_2O ratio, the Nafion and Cu_2O mixture did not achieve even distribution during the evaporation of the Nafion solvent. In the regions of the electrode where Nafion were not effectively coating the Cu_2O particles, these particles were reduced to Cu.

Current Profile. We also compared the current flow in these electrodes and have included the result from the control electrodes, Toray (T) and Toray/Nafion (T/N) (see Figure 6.22). The graph from the Cu_2O-0 sample showed a current flow (I_{ave} = -30 mA) that increased with electrolysis time, exhibiting high noise level that was more pronounce than the one in the Toray sample. The graph of the Cu_2O-30 sample showed a stable current

114

flow that gradually increased with electrolysis time. The graph of the Cu_2O-360A sample showed a stable and steady-state current flow. This sample underwent four cycles of voltammetry prior to electrolysis which may have helped equilibrate the surface of the electrode. The graph of the Cu_2O-360B minute growth sample showed a stable current flow that gradually decreased with electrolysis time.
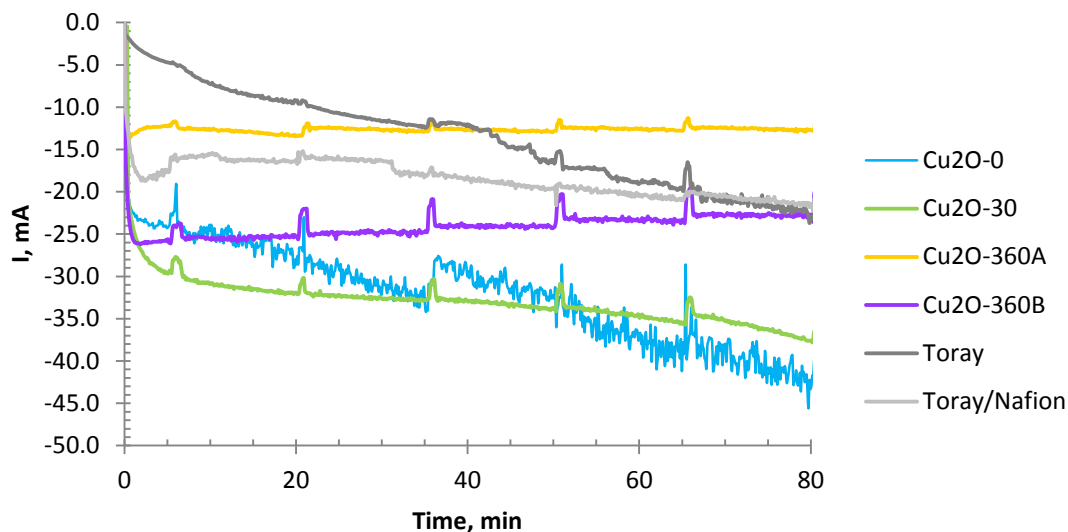
Figure 6.22. Current profile of Cu_2O particles with different synthesis aging time generated during CO_2 reduction at -1.5V_{NHE}.

Comparison of Product Distribution. Finally, we compared the product distribution of these electrodes. Different from the previous sections and Chapters, we present our comparison here by grouping the data based on the individual products of CO_2 (and H_2O) reduction rather than by electrode. The electrodes were compared in this manner because of the number of products and electrodes being compared.

H₂ Formation. First, we compared the electrodes based on H_2 formation, which is formed solely from H_2O reduction on exposed Toray surfaces. Foremost, the H_2 formation rate increased with time for all the electrodes as seen in Figure 6.23. The Cu_2O-0 electrode showed the highest average H_2 formation rate and fastest increase in product generation

115

from 118 to 402 μmol/cm^2*hr. Meanwhile, the Cu$_2$O-360A electrode showed the lowest average H$_2$ formation rate and slowest increase in product generation from 31 to 130 μmol/cm^2*hr.
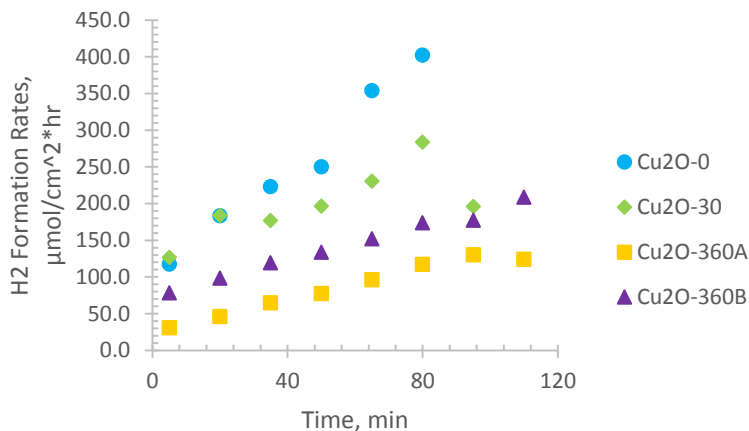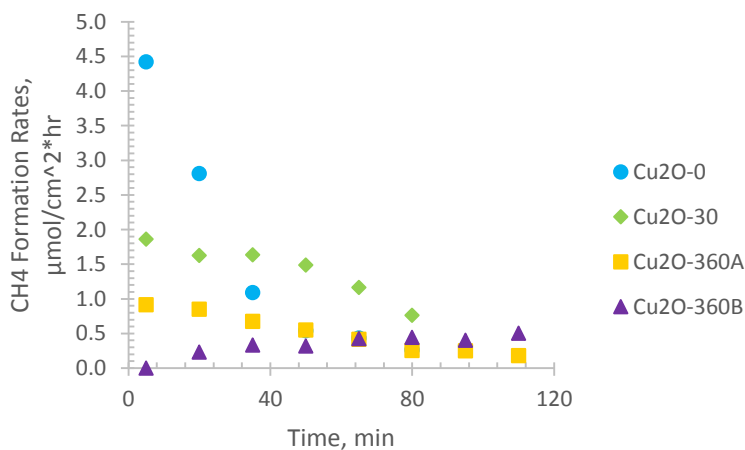

Figure 6.23. Formation rate of H$_2$ on Cu$_2$O particles with different synthesis aging time during CO$_2$ reduction at -1.5V$_{NHE}$.

In terms of faradaic efficiency shown in Figure 6.24, the Cu$_2$O-0 electrode still showed the highest faradaic efficiency although the rate of increase in value is now more identical to that of the other electrodes. Meanwhile, the two Cu$_2$O-360 electrodes showed identical faradaic efficiencies especially in the first half of the process.
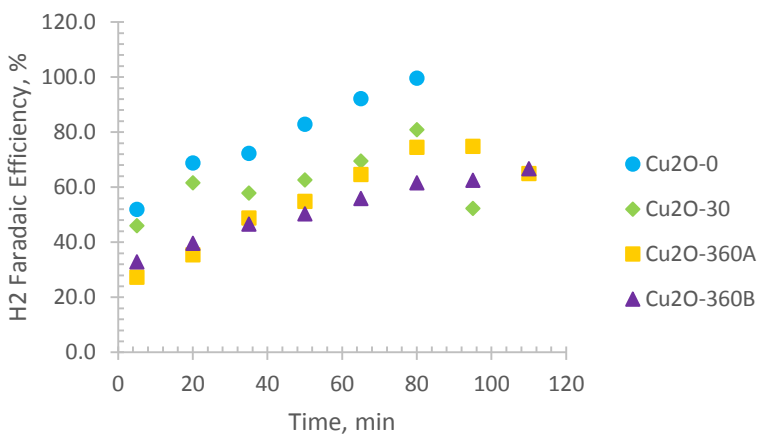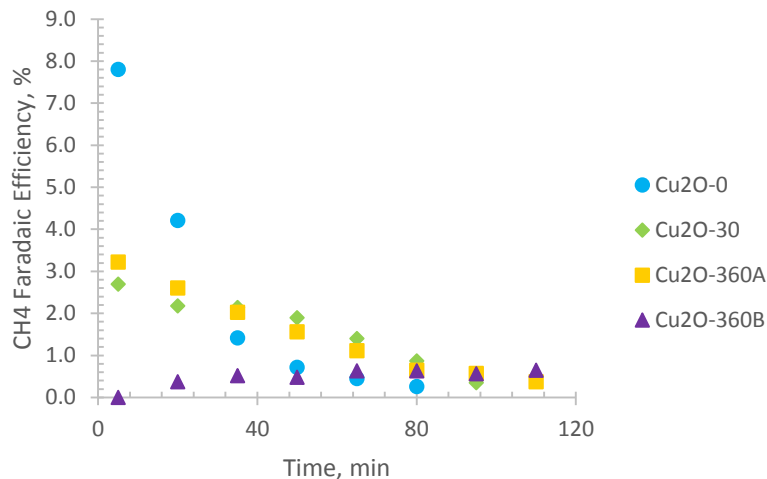

Figure 6.24. Faradaic efficiency of H$_2$ on Cu$_2$O particles with different synthesis aging time during CO$_2$ reduction at -1.5V$_{NHE}$.

CO Formation. Next, we compared the electrodes based on their selectivity to CO which is the second reduced form of CO_2 after $HCOO^-$ (see Figure 6.25).
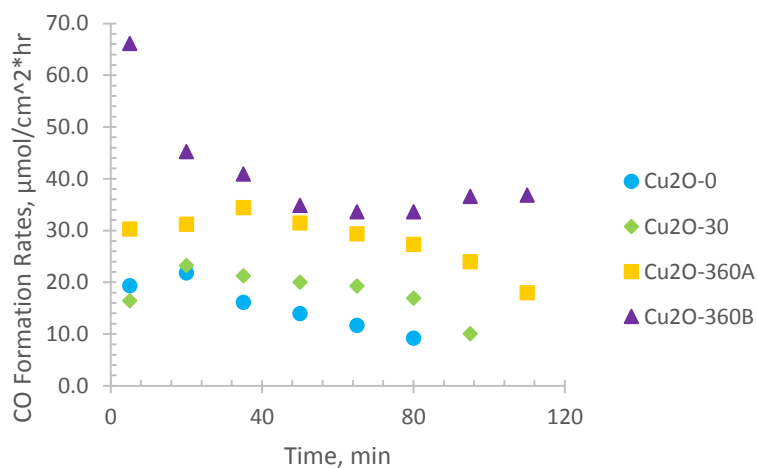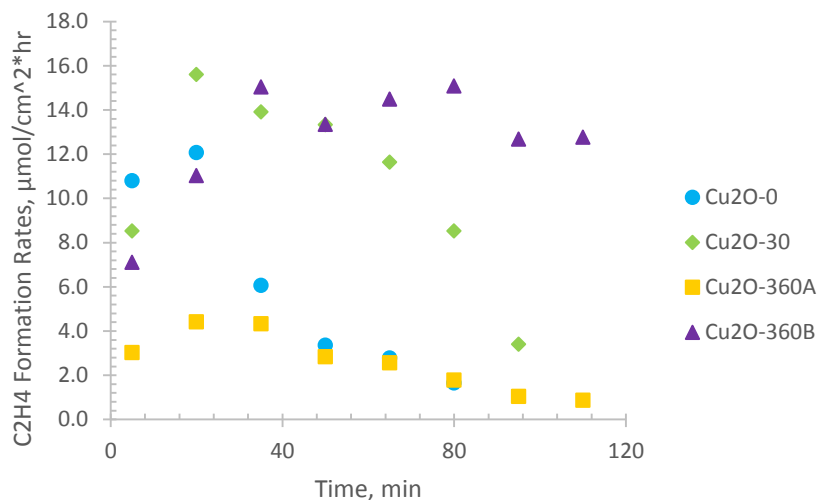

Figure 6.25. Formation rate of CO on Cu_2O particles with different synthesis aging time during CO_2 reduction at $-1.5V_{NHE}$.

The Cu_2O-360B electrode showed the highest initial CO formation rate of 66 $\mu mol/cm^2$*hr measured at the 5 minute sampling time and the highest over-all average rate of 41 $\mu mol/cm^2$*hr. This was followed by the Cu_2O-360A electrode at an average rate of 28 $\mu mol/cm^2$*hr. Meanwhile, the Cu_2O-0 electrode showed the lowest average CO formation rate of 15 $\mu mol/cm^2$*hr.

In terms of faradaic efficiency, the graph in Figure 6.26 shows that the CO faradaic efficiency decreased with time for all the electrodes. Despite producing CO at a lower rate, the Cu_2O-360A electrode showed better over-all CO faradaic efficiency of 20% compared to the Cu_2O-360B electrode which had 16% faradaic efficiency. The Cu_2O-0 electrode still registered the lowest average faradaic efficiency of 5.3%.
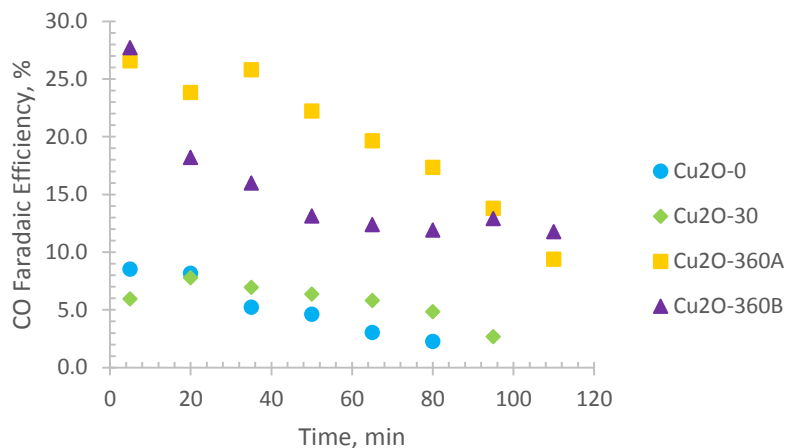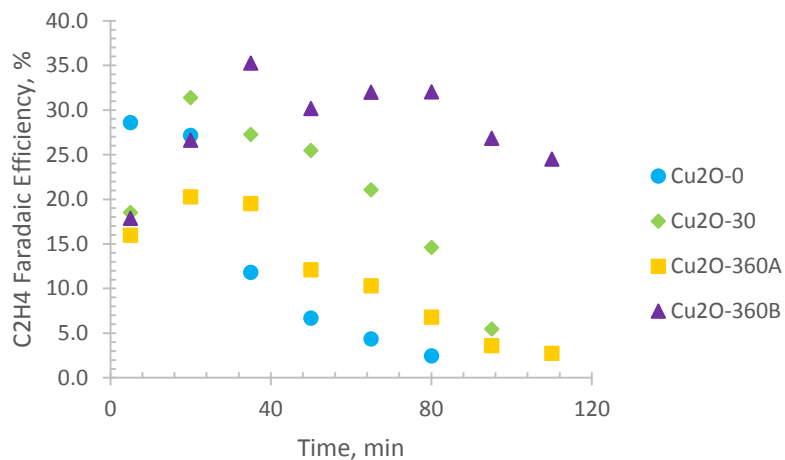
Figure 6.26. Faradaic efficiency of CO on Cu_2O particles with different synthesis aging time during CO_2 reduction at $-1.5V_{NHE}$.

Methane Formation. Next, we compared the electrodes based on their productivity and selectivity to methane. The methane formation rates decreased with time for all samples except in the Cu_2O-360B electrode where the rates were already the lowest but slightly increased with time (see Figure 6.27). The Cu_2O-0 electrode exhibited an initially high methane formation rate of 4.4 $\mu mol/cm^2*hr$ but the rate also dropped steeply for an average of 1.6 $\mu mol/cm^2*hr$. This was followed closely by the Cu_2O-30 electrode with an average CH_4 formation rate of 1.3 $\mu mol/cm^2*hr$.
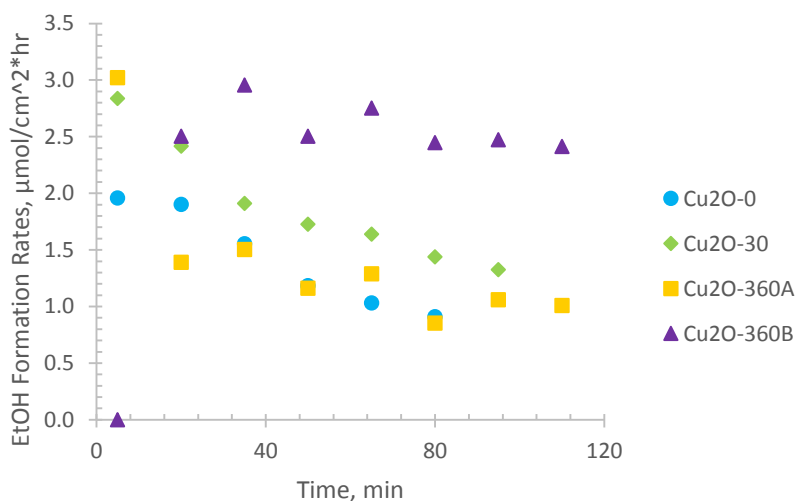

Figure 6.27. Formation rate of methane on Cu_2O particles with different synthesis aging time during CO_2 reduction at $-1.5V_{NHE}$.

The graph in Figure 6.28 still showed that the CH_4 faradaic efficiency decreased with time for all the electrodes. Again, the Cu_2O-0 electrode exhibited an initially high methane faradaic efficiency of 8% relative to the other samples. This level represents the second highest methane faradaic efficiency achieved among the Cu_2O particles studied and was about the same with our Cu electrode. The Cu_2O-30 and Cu_2O-360A electrodes this time had about the same faradaic efficiencies even though their formation rates were different. The CH_4 faradaic efficiencies of the four electrodes approached to an identical value of about 0.6% at the end of the process.
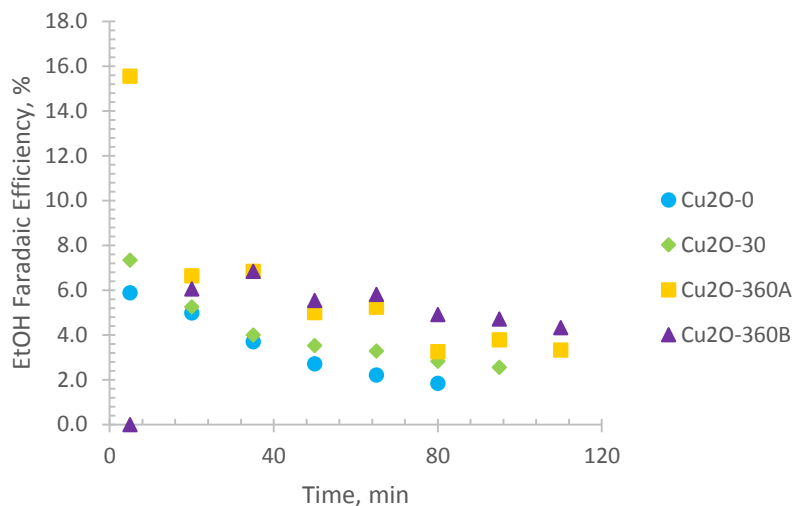

Figure 6.28. Faradaic efficiency of methane on Cu_2O particles with different synthesis aging time during CO_2 reduction at -1.5V_{NHE}.

Ethylene Formation. Next, we compared the electrodes based on their electrocatalytic activity towards ethylene formation. The graph in Figure 6.29 shows the catalysts were more dynamic with their activity towards ethylene compared to their activity towards CO and CH_4. Over-all, the Cu_2O-360B electrode showed the highest average C_2H_4 formation rate of 13 $\mu mol/cm^2$*hr. Meanwhile, the other Cu_2O-360A electrode showed the lowest C_2H_4 formation rate of 2.6 $\mu mol/cm^2$*hr. At 20 minutes, the Cu_2O-30 electrode produced

the highest ethylene formation rate at 16 µmol/cm²*hr. However, the production rate decreased rapidly after that.

Figure 6.29. Formation rate of ethylene on Cu_2O particles with different synthesis aging time during CO_2 reduction at $-1.5V_{NHE}$.

In terms of faradaic efficiency (refer to Figure 6.30), the Cu_2O-360B electrode still showed the highest C_2H_4 faradaic efficiency, followed by the Cu_2O-30, Cu_2O-360A and Cu_2O-0 electrode.

Figure 6.30. Faradaic efficiency of ethylene on Cu_2O particles with different synthesis aging time during CO_2 reduction at $-1.5V_{NHE}$.

Ethanol Formation. Finally, we compared the activity of these electrodes toward ethanol formation (see Figure 6.31). The ethanol formation rates decreased with time in all samples except for the Cu_2O-360B electrode where the rates were relatively more flat than the rest and also showed the highest average ethanol formation rate of 2.3 $\mu mol/cm^2*hr$. This was followed by the Cu_2O-30 electrode with ethanol formation rate of 1.9 $\mu mol/cm^2*hr$.

Figure 6.31. Formation rate of ethanol on Cu_2O particles with different synthesis aging time during CO_2 reduction at $-1.5V_{NHE}$.

In terms of faradaic efficiency, the Cu_2O-360A electrode showed an initially high selectivity towards ethanol at about 16% (see Figure 6.32). The selectivity of these electrodes toward ethanol did not differ by more than an order of magnitude and ranged between 2-8 %.

Figure 6.32. Faradaic efficiency of ethanol on Cu_2O particles with different synthesis aging time during CO_2 reduction at $-1.5V_{NHE}$.

To summarize, the main result was the high CO and ethylene selectivity on the Cu_2O-360B electrode and the high CO selectivity on the Cu_2O-360A electrode compared to the other two electrodes. The reduction of larger Cu_2O particles may result in more kinks, steps and defects than the smaller Cu_2O particles. We also observed a copper-like behavior on the Cu_2O-0 electrode which showed a relatively high initial methane faradaic efficiency.

The reduction of larger Cu_2O particles may have produced more dispersed Cu clusters that stabilize the high rate of ethylene formation and its selectivity. Li et al. (2012) observed that thicker Cu_2O films grown by thermal oxidation exhibited higher CO faradaic efficiency because the resulting Cu have higher concentration of unstable grain boundaries than polycrystalline Cu. They also suggested that grain boundary is a key design feature to improving selectivity towards C_{2+} hydrocarbons (Li et al. 2014).

The amount of Cu_2O particles present on the surface of Toray also affected the product formation rates, particularly CO, ethylene and ethanol. The Cu_2O-360B electrode

which had a Cu_2O loading of 26.5 mg showed higher CO, ethylene and ethanol formation rates than the Cu_2O-360A electrode which had a Cu_2O loading of only 1.1 mg. However, whereas the Cu_2O loading increased by a factor of 24, the CO, ethylene and ethanol formation rates only increased by a factor of 1.5, 5 and 1.6. This suggest that only the particles in the outermost layer were the most active in the electrochemical reduction of CO_2. Those particles located in the inner region of the electrode did not encounter as many CO_2 molecules as those on the surface due to mass transfer limitation.

6.3.2.4. Effect of Nafion

After studying the effect of NaOH composition and particle aging time during nucleation stage of the Cu_2O synthesis, we then looked at the effect Nafion on the electrocatalytic activity of colloidal Cu_2O particles. Nafion was added during the electrode assembly primarily to provide a binding support to foreign Cu_2O particles on Toray.

In Section 6.3.2.3, we observed that Cu_2O particles encapsulated with Nafion did not undergo a change in structure, whereas those Cu_2O particles without Nafion covering had decorations on the surface of the cubes. In Chapter 5, we also observed that Nafion helped stabilize the formation of CO and C_2H_4. In this section we examined the effect of Nafion on colloidal Cu_2O particles by considering three different Nafion/Cu_2O ratios; namely, 0.0, 1.2 and 2.4.

$\underline{Cu_2O\ Loading}$. The three electrodes compared were labelled as follows: (1) TC − Toray + Cu_2O, (2) TLC − Toray + Low Nafion + Cu_2O (TLC) and (3) Toray + High Nafion + Cu_2O (THC). Table 6.2 shows the amount of Cu_2O on Toray as well as the mass ratio of Nafion to Cu_2O for each sample. The TLC and THN samples prepared have high Cu_2O loading compared to the TC sample. The low loading in the TC sample relative

to the TLC and THN samples is due to difference in preparation condition, particularly on the amount of reagents used during Cu_2O synthesis.

Table 6.2. Composition of Cu_2O Electrodes with Different Amounts of Nafion.

Electrode	Cu_2O Loading, mg	Nafion/Cu_2O Mass Ratio
Toray + Cu_2O (TC)	3.0	0.0
Toray + Low Nafion + Cu_2O (TLC)	38.0	1.2
Toray + High Nafion + Cu_2O (THC)	30.6	2.4

Current Profile. We monitored the current profile generated by these electrodes during CO_2 reduction at $-1.5V_{NHE}$ (refer to Figure 6.33). The TC samples showed a stable and steady state current flow of about 20 mA. The TLC sample registered the highest amount of current among the three samples, with a mean value of 40 mA which was twice that of TC. Meanwhile the THC sample had a mean current of 24 mA. We observed transient current in all three samples which indicate reduction of Cu_2O particles.
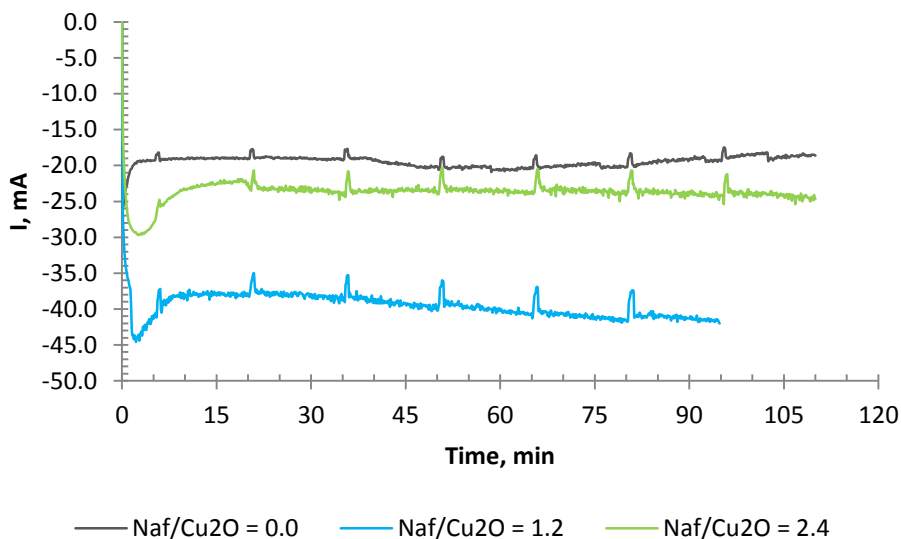
Figure 6.33. Current profile generated by CO_2 reduction on Cu_2O particles with different amounts of Nafion at $-1.5V_{NHE}$.

H$_2$ Formation. First, we compared H$_2$ formation of these electrocatalysts. Figure 6.34 shows the H$_2$ formation rates where the TLC electrode showed highest H$_2$ activity which increased with time from an initial rate of 143 µmol/cm^2*hr to the final rate of 325 µmol/cm^2*hr for an average of 270 µmol/cm^2*hr. This was followed by the THC electrode with initial, final and average rates of 120, 187 and 162 µmol/cm^2*hr. The TLC electrode showed the least H$_2$ rates at initial, final and average rates of 97, 103 and 116 µmol/cm^2*hr. H$_2$ formation rate generally increased with time similar to what we have observed on Toray. However, the TC electrode showed a peak in H$_2$ rates halfway through the process.
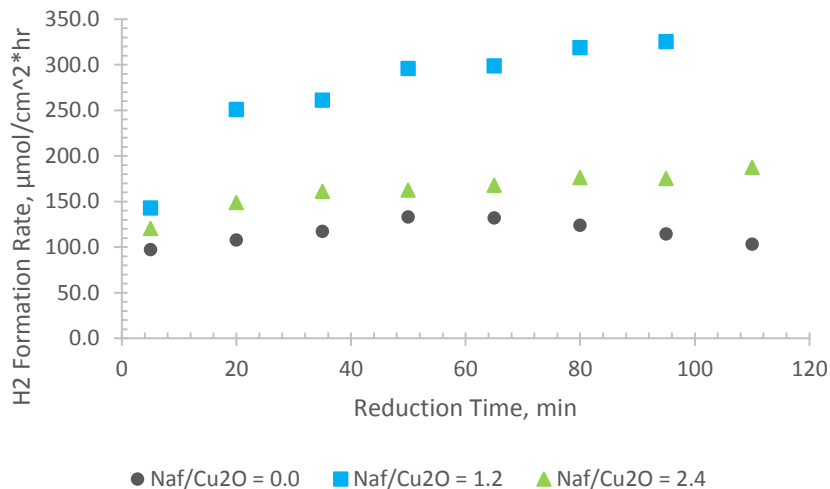
Figure 6.34. H$_2$ formation rates on Cu$_2$O particles with different amounts of Nafion during CO$_2$ reduction at -1.5V$_{NHE}$.

The three electrodes showed closer faradaic efficiency values as seen in Figure 6.35. The H$_2$ selectivity for all three samples increased with time at a decreasing rate. Additionally, the TC electrode showed a maximum H$_2$ faradaic efficiency around 50 minutes.
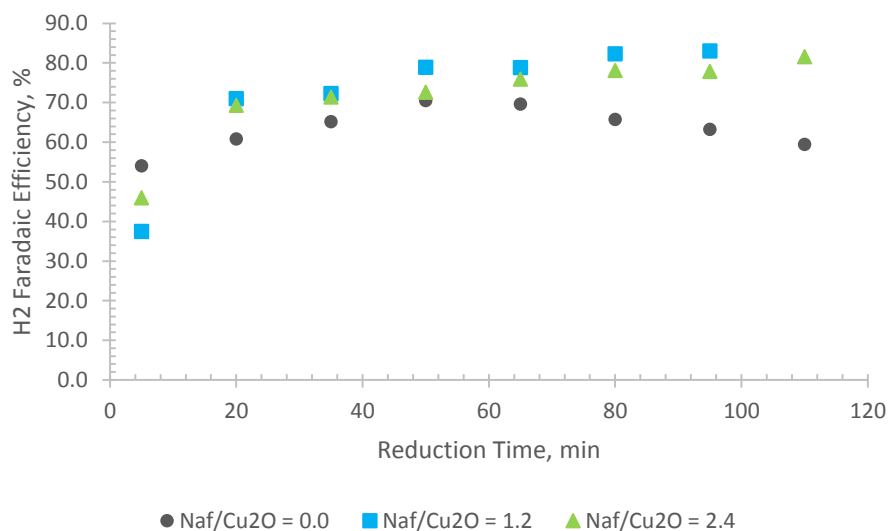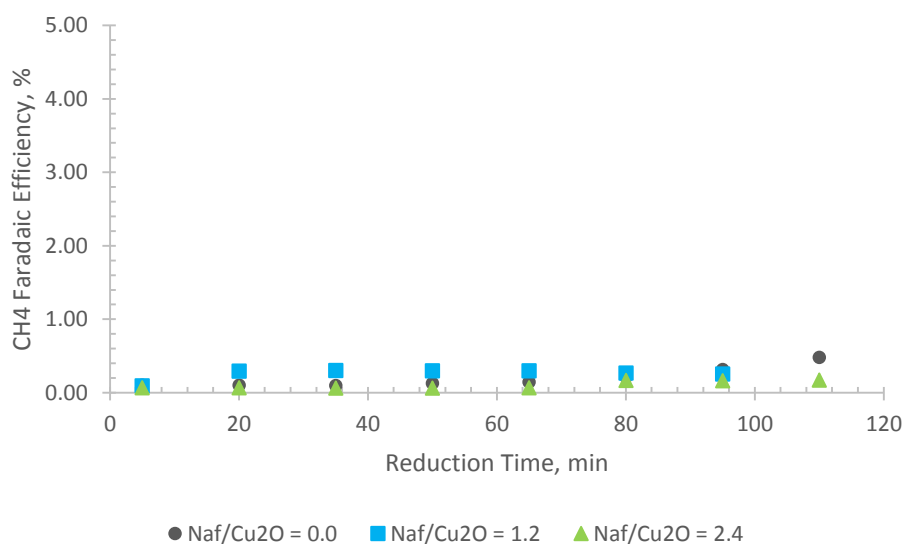
Figure 6.35. Faradaic efficiency of H_2 formation on Cu_2O particles with different amounts of Nafion during CO_2 reduction at $-1.5V_{NHE}$.

CO Formation. Next, we look at CO formation in Figure 6.36. The TC electrode showed highest CO activity but decreased with time from an initial rate of 21 μmol/cm^2*hr to the final rate of 14 μmol/cm^2*hr for an average of 16 μmol/cm^2*hr. This was followed closely by the TLC electrode which showed a steadier CO formation rate.
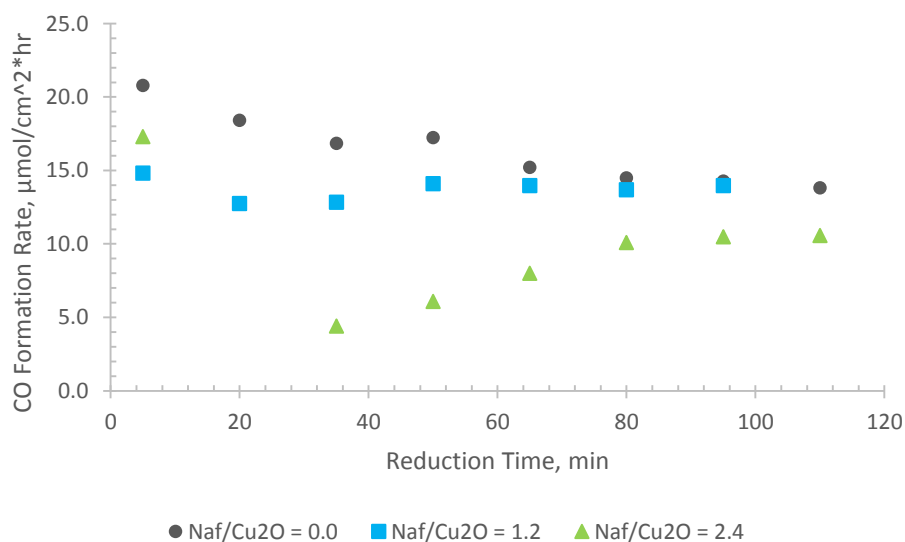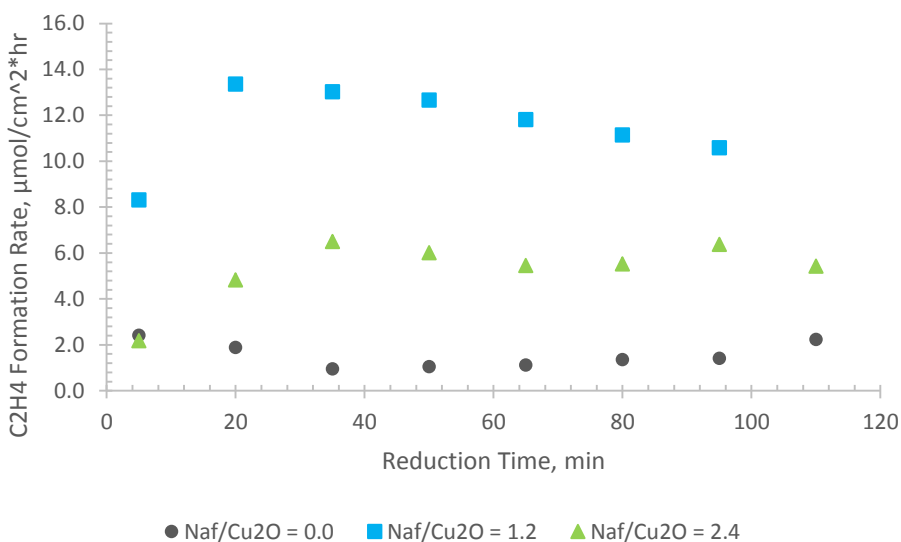

Figure 6.36. CO formation rates on Cu_2O particles with different amounts of Nafion during CO_2 reduction at $-1.5V_{NHE}$.

126

The initial, final and average rates were 15, 14 and 14 μmol/cm^2*hr. The THC electrode showed the least CO rates at initial, final and average rates of 17, 11 and 8 μmol/cm^2*hr and the kinetics was also very dynamic.

In terms of faradaic efficiency, The TC electrode showed the highest average CO selectivity of 9% faradaic efficiency with a high of 12% near the start of reduction and gradually decreased to 8% by the end of the process. The TLC and THC electrodes had about the same average faradaic efficiency of 4%. The CO selectivity on the TLC electrode was kinetically stable (refer to Figure 6.37).
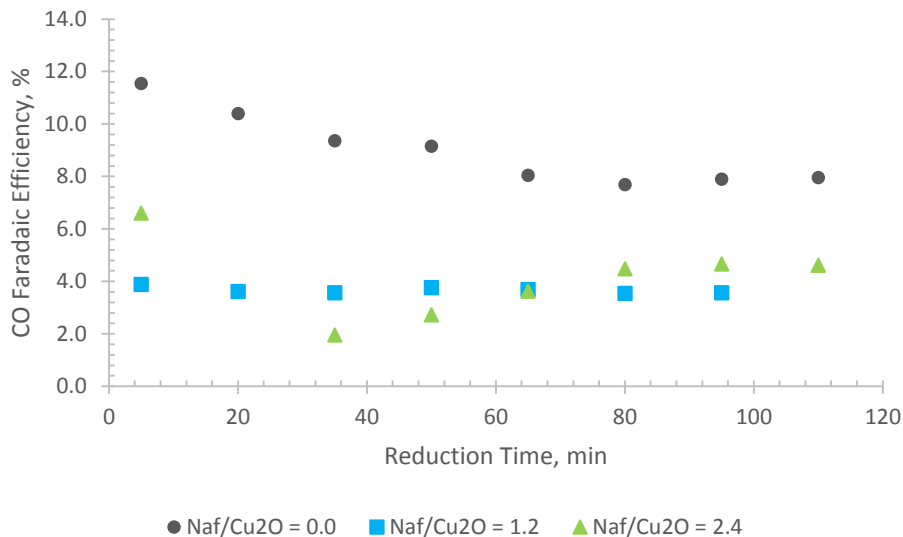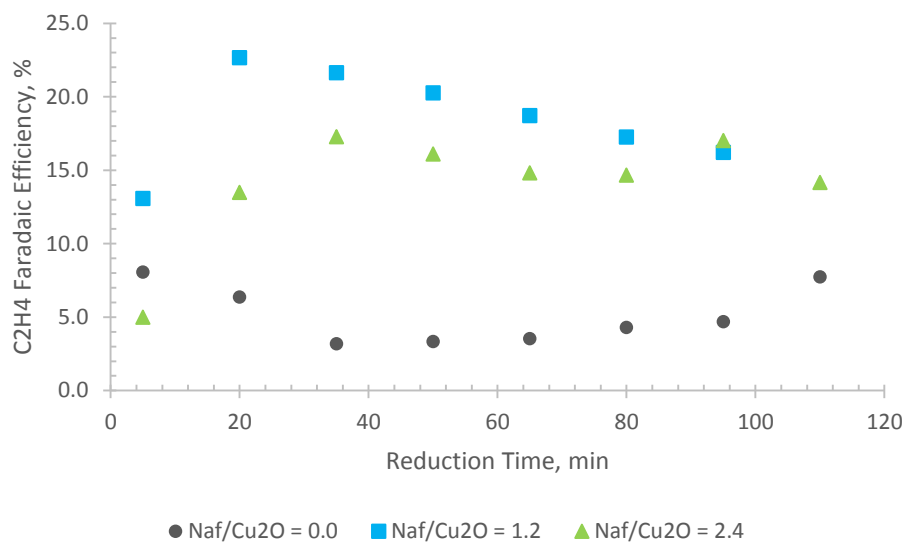

Figure 6.37. Faradaic efficiency of CO formation on Cu$_2$O particles with different amounts of Nafion during CO$_2$ reduction at -1.5V$_{NHE}$.

Methane Formation. Next, we look at methane where all the samples exhibited less than 0.3 μmol/cm^2*hr formation rate (see Figure 6.38) and one order of magnitude lower than CO. The TLC electrode showed the highest average methane formation rate of 0.2 μmol/cm^2*hr.
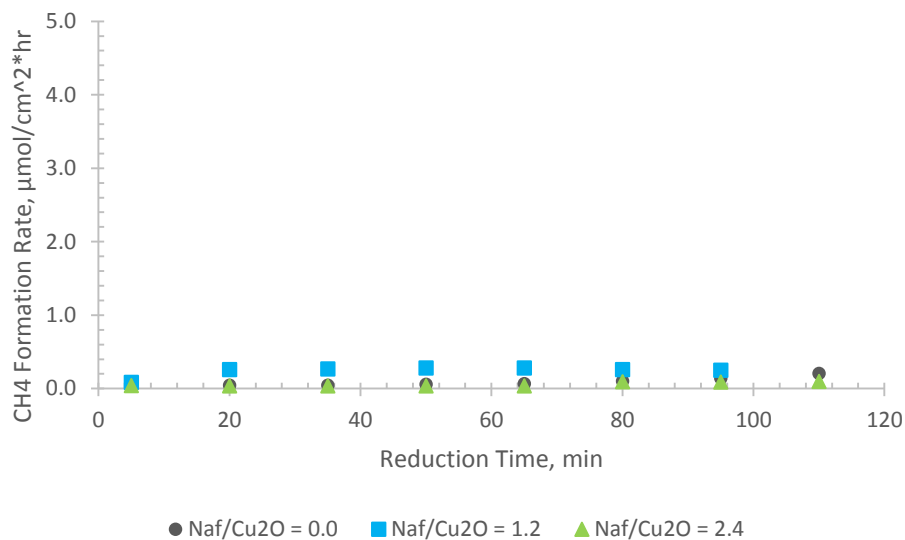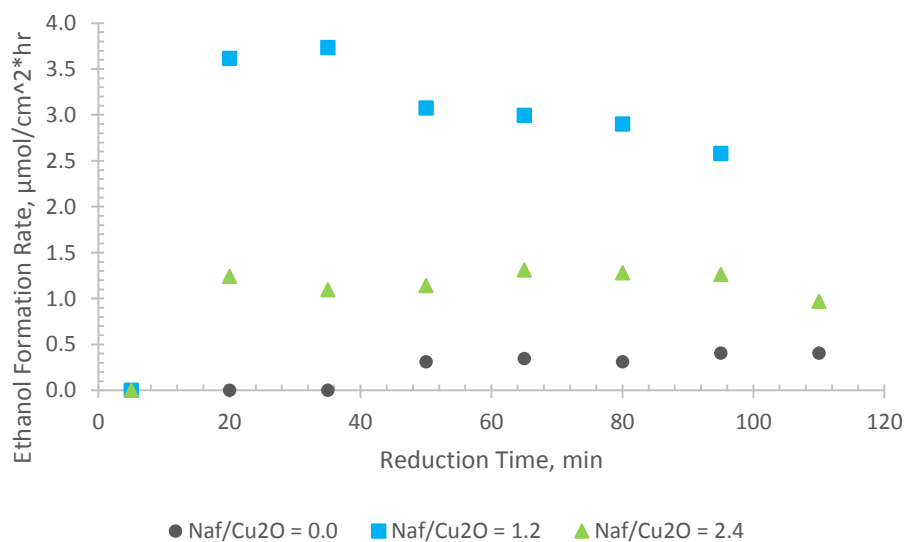
Figure 6.38. Methane formation rates on Cu_2O particles with different amounts of Nafion during CO_2 reduction at $-1.5V_{NHE}$.

Meanwhile, the faradaic efficiency of the three electrodes were less than 0.5% (see Figure 6.39). In Section 6.3.2.3, we observed CH_4 efficiencies between 0.5-3.0% on Cu_2O particles with different aging times. In those samples, the Nafion/Cu_2O ratio was 0.8. CH_4 selectivity may be constrained with increased Nafion content.
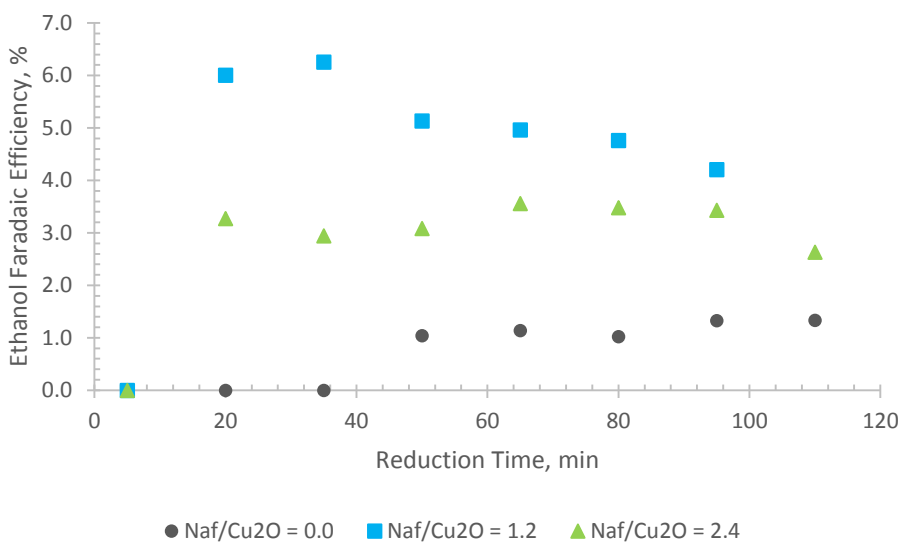

Figure 6.39. Faradaic efficiency of methane formation on Cu_2O particles with different amounts of Nafion during CO_2 reduction at $-1.5V_{NHE}$.

Ethylene Formation. Next, we look at ethylene formation in Figure 6.40. The TC electrode showed the lowest ethylene rates at initial, final and average rates of 2.4, 2.2 and 1.2 μmol/cm^2*hr. On the other hand, the TLC electrode showed the highest ethylene activity with an initial, final and average rates of 8, 11 and 12 μmol/cm^2*hr. This was followed by the THC electrode with an initial, final and average rates of 2.2, 5.4 and 5.3 μmol/cm^2*hr.

Figure 6.40. Ethylene formation rates on Cu$_2$O particles with different amounts of Nafion during CO$_2$ reduction at -1.5V$_{NHE}$.

In terms of faradaic efficiency shown in Figure 6.41, the TLC electrode again showed the highest ethylene selectivity with an initial, final and average percentage of 13%, 16% and 19%. This was followed by the THC electrode with an initial, final and average percentages of 5%, 14% and 14%. The TC electrode showed the lowest ethylene selectivity at initial, final and average percentages of 2.4%, 2.2% and 1.2%.

Figure 6.41. Faradaic efficiency of ethylene formation on Cu_2O particles with different amounts of Nafion during CO_2 reduction at $-1.5V_{NHE}$.

Ethanol Formation. Finally, we look at the ethanol product distribution of the three electrodes. As seen in Figure 6.42, the TC electrode showed the lowest average ethanol rate of 0.2 $\mu mol/cm^2*hr$. Meanwhile, the TLC electrode showed the highest ethanol activity with a 20 minute, final and average rates of 3.6, 2.6 and 2.7 $\mu mol/cm^2*hr$.

Figure 6.42. Ethanol formation rates on Cu_2O particles with different amounts of Nafion during CO_2 reduction at $-1.5V_{NHE}$.

130

This was followed by the THC electrode with a 20 minute, final and average rates of 1.2, 1.0 and 1.0 μmol/cm^2*hr. We noticed that there were no measurable ethanol products early in the reduction process. This suggest that ethanol is kinetically slower to develop compared to ethylene.

In terms of faradaic efficiency shown in Figure 6.43, the TLC electrode again showed the highest ethanol selectivity with a 20 minute, final and average percentage of 6.0%, 4.2% and 4.5%. This was followed by the THC electrode with a 20 minute, final and average percentages of 3.3%, 2.6% and 2.8%. The TC electrode showed the lowest average ethanol faradaic efficiency of 0.7%.

Figure 6.43. Faradaic efficiency of ethanol formation on Cu$_2$O particles with different amounts of Nafion during CO$_2$ reduction at -1.5V$_{NHE}$.

Over-all, the results suggest that moderate amounts of Nafion help improve the selectivity of Cu$_2$O particles to ethylene and ethanol. However, excessive amounts of Nafion also lowers their selectivity to these products.

6.3.2.5. Effect of Cyclic Voltammetry

In the previous sections, we studied the effect of different electrode preparation conditions on the electrocatalytic activity of Cu_2O particles towards CO_2 reduction. In this section, we examined the product distribution on Cu_2O particles after they were characterized by cyclic voltammetry. Cyclic voltammetry was conducted on two different electrodes, (1) Toray/Cu_2O (CV) and (2) Toray/Nafion/Cu_2O (CV).

Toray/Cu_2O (CV) Electrode

Cyclic Voltammetry. As shown in Figure 6.44, there was no visible peak associated with the reduction of Cu_2O to Cu in the first cathodic sweep, although we observed a minor shoulder in the blue line between -0.35V and -0.6V.
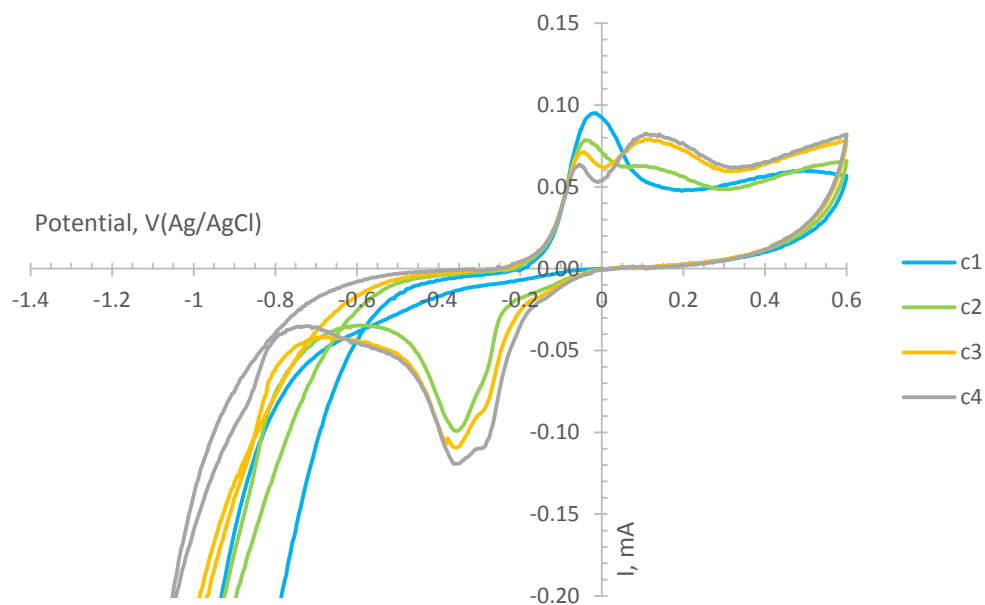
Figure 6.44. Four cycle voltammetry of Toray/Cu_2O (CV) electrode (50 mV/s).

Cu_2O may not have become readily reduced during the first cathodization at the expected potential and may have occurred at more negative potential. In the first anodic sweep, peak due to Cu oxidation appeared. The anodized Cu was reduced more easily compared to the colloidal Cu_2O as seen by the appearance of cathodic peaks.

Current Profile of the First Reduction. We then performed CO_2 reduction after cyclic voltammetry. The current versus time profile is shown in Figure 6.45. The mean total current was 12.5 mA. We note that the reduction between 20 and 35 minutes occurred without a CO_2 carrier bubbling. As such, the current became flat during this period.
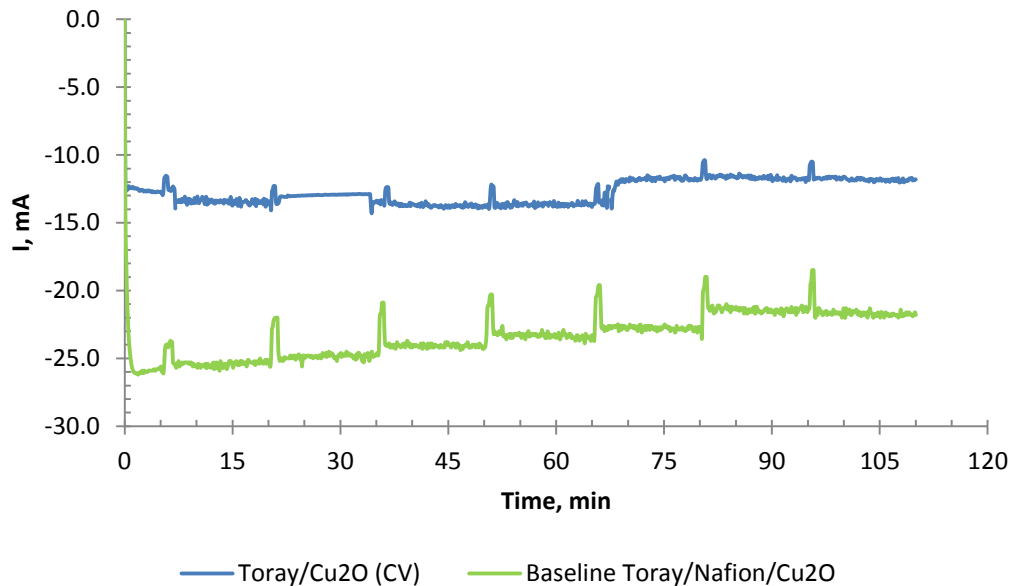
Figure 6.45. Current profile of Toray/Cu_2O (CV) and baseline Toray/Nafion/Cu_2O electrodes.

Product Distribution During the First Reduction. The graph in Figure 6.46 shows the formation rate of different CO_2 products. The production rates at 35 minute sampling were not included because their values were unusually high as a result of interrupted CO_2 bubbling. Over-all, we observed a decrease in the formation rates of CO_2 products with

concurrent increase in H_2 production. CO formation had the highest productivity averaging 6.8 µmol/cm^{2*}hr (ranging between 3.6 – 10.2 µmol/cm^{2*}hr). This was followed by ethylene at 2.5 µmol/cm^{2*}hr (ranging between 0.1 – 7.0 µmol/cm^{2*}hr), methane at 1.0 µmol/cm^{2*}hr (ranging between 0.2 – 2.3 µmol/cm^{2*}hr) and ethanol at 0.5 µmol/cm^{2*}hr (ranging between 0.3 – 0.8 µmol/cm^{2*}hr).
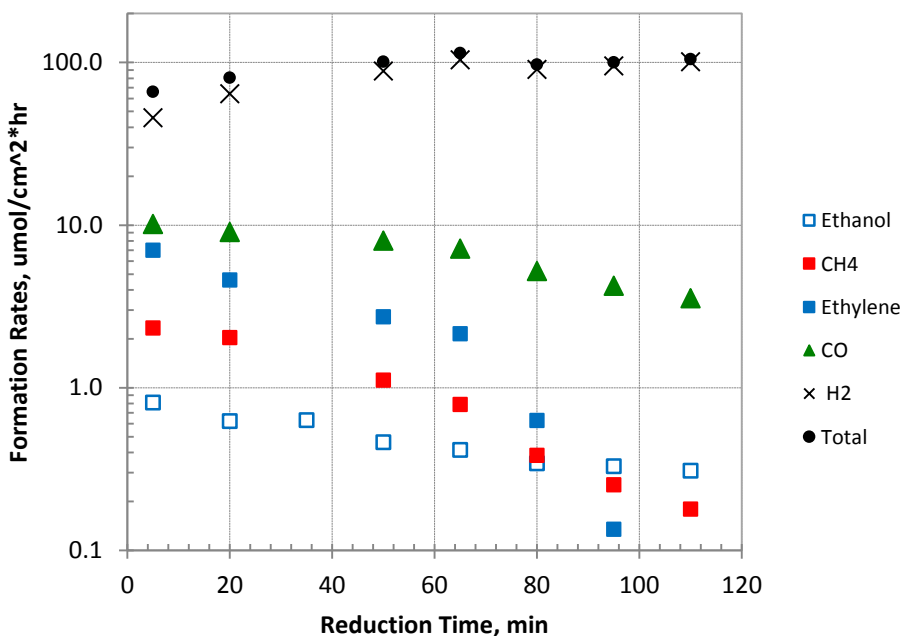
Figure 6.46. Product formation rates during CO_2 reduction on Toray/Cu_2O (CV) at -1.5V$_{NHE}$.

In terms of faradaic efficiency (refer to Figure 6.47), the electrode showed higher selectivity towards ethylene versus CO due to difference in electron requirements between the two products. Ethylene was a major product only during the first half of the process. Ethylene showed an initial faradaic efficiency of 39% which decreased by 3 orders of magnitude to 0.7% for an average of 12%. CO was produce at intermediate faradaic efficiency with an initial and final selectivity of 8.6% and 3.2% respectively for an average of 5.6%.

The other CO_2 products were produced at intermediate efficiencies. Methane had an initial faradaic efficiency of 7.9% which decreased by two orders of magnitude to 0.7% for an average of 3.3%. Finally, ethanol had an initial faradaic efficiency of 4.2% which decreased to 1.6% for an average of 2.4%.

The decrease in CO_2 product efficiency occurred despite a relatively steady state current. The decline was offsetted by rising H_2 production. The decrease in ethylene faradaic efficiency was the most severe, followed by methane then ethanol. These results indicate that the cathodized Cu_2O particles without a Nafion binder experienced surface deactivation likely from formation of carbon deposits which lowered the number of active sites that generate hydrocarbons. H_2 productivity increased from 46 to 101 $\mu mol/cm^2*hr$ while it selectivity increased from 39% to 92%.
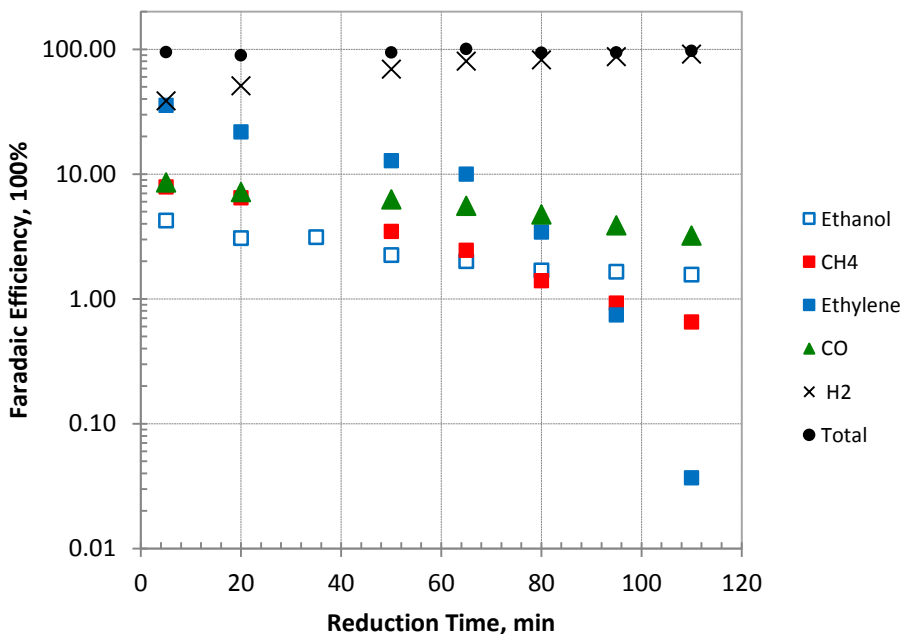
Figure 6.47. Faradaic efficiency of products during CO_2 reduction on Toray/Cu_2O (CV) at -1.5V_{NHE}.

Current Profile of the Second Reduction. We also performed a second electrolysis on the characterized Cu_2O sample and unintentionally generated a pulsating current flow (see Figure 6.48). The current which averaged at 26 mA fluctuated by approximately 17 mA. This was likely a result of a mechanically unstable connection on the electrode which subjected the particles to a very dynamic current at the interface to maintain a fix applied potential.
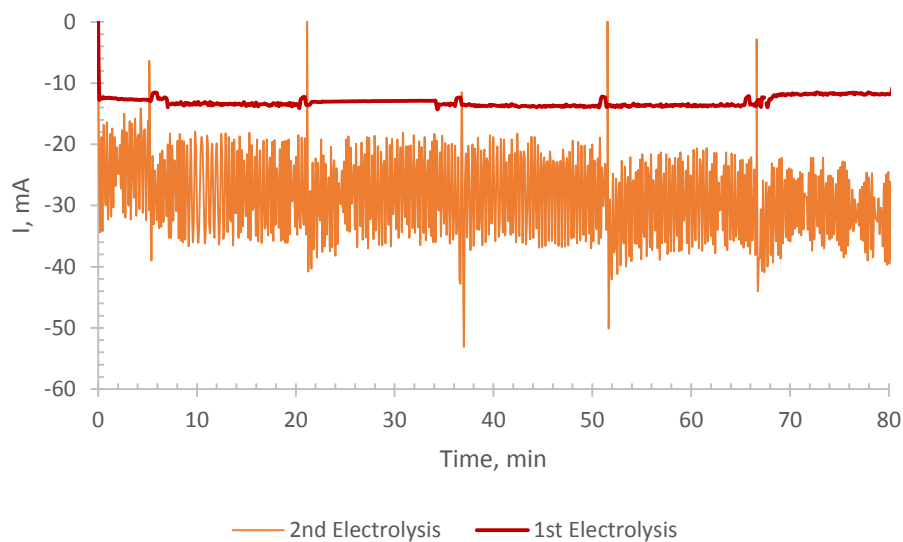
Figure 6.48. Current profile of the Toray/Cu_2O (CV) electrode during the two CO_2 reductions at -1.5V$_{NHE}$.

Product Distribution During the Second Reduction. We then examined the CO_2 product distribution on the electrode after generating this type of behavior. The catalyst showed an over-all improvement in the product formation rates that were also kinetically more stable compared to the first CO_2 reduction (see Figure 6.49). For example, the average ethylene formation rate was 16 $\mu mol/cm^2*hr$, which was up from 2.5 $\mu mol/cm^2*hr$. The average CO formation rate was 13 $\mu mol/cm^2*hr$ which was higher than 6.8 $\mu mol/cm^2*hr$. The average methane formation rate was 5.4 $\mu mol/cm^2*hr$ which was better than 1.0

136

μmol/cm^2*hr. Finally, the average ethanol formation rate was 0.6 μmol/cm^2*hr but was only slightly higher than 0.5 μmol/cm^2*hr.
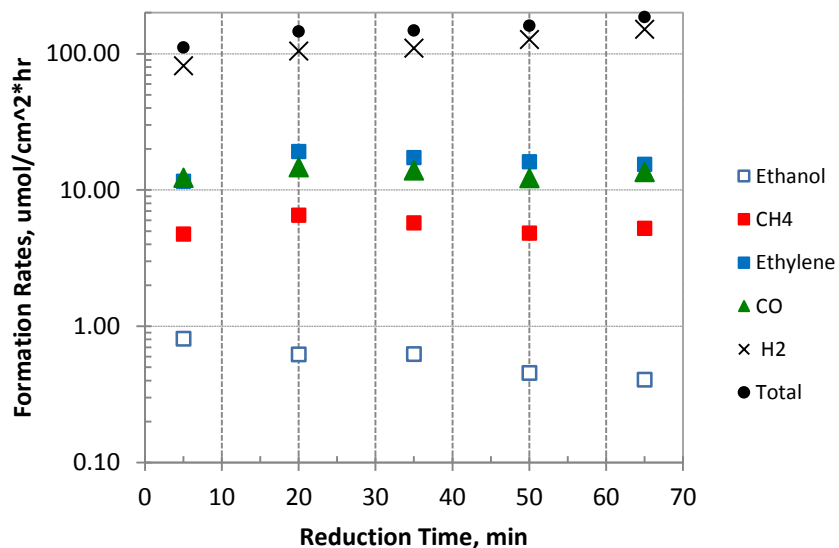
Figure 6.49. Product formation rates during the second CO_2 reduction on Toray/Cu_2O (CV) electrode at -1.5V$_{NHE}$.

In terms of faradaic efficiency, the catalyst again showed an over-all improvement in the hydrocarbon faradaic efficiency and stability (see Figure 6.50).
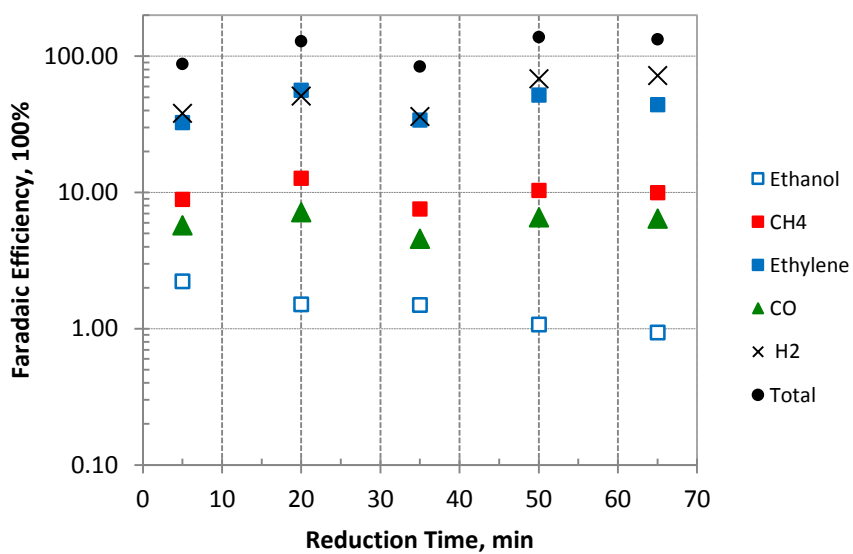
Figure 6.50. Faradaic efficiency of products during the second CO_2 reduction on Toray/Cu_2O (CV) electrode at -1.5V$_{NHE}$.

The over-all CO_2 product faradaic efficiency increased from 23% to 61%. Individually, the average ethylene faradaic efficiency went up from 12% to 44%. The average CO faradaic efficiency was 6.1%, almost unchanged from 5.6%. The average methane faradaic efficiency was 9.9% versus 3.3%. This value represents the highest CH_4 efficiency obtained from our Cu_2O samples. On the other hand, the average ethanol faradaic efficiency slightly decreased from 2.4% to 1.4%.

The constantly shifting current experienced by the catalyst enhanced and stabilized hydrocarbon selectivity and particularly promoted CH_4 formation. Modulated/pulsed potential experiment during CO_2 reduction was shown to improve the performance of Cu_2O (Shiratsuchi et al. 1993, Nogami et al. 1994).

Toray/Nafion/Cu_2O Electrode

Cyclic Voltammogram. The plot in Figure 6.51 showed that during the first
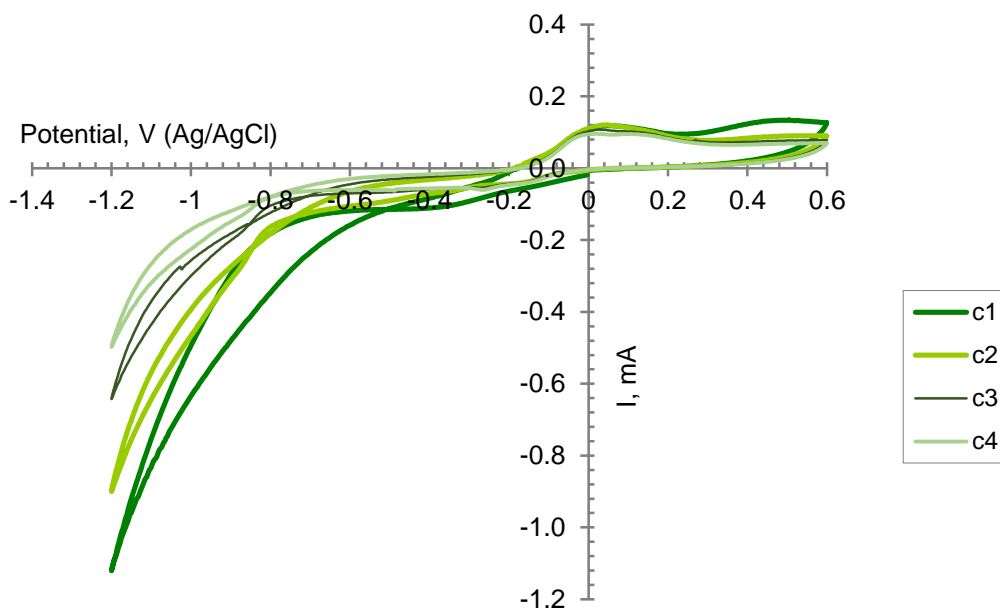
Figure 6.51. Cyclic voltammetry of Toray/Nafion/Cu_2O (CV) electrode on CO_2 saturated 0.5M $KHCO_3$ solution at 50 mV/s.

cathodic sweep, a reduction peak was already observed which indicate a small number Cu_2O particles were converted to Cu. During the first anodic sweep, higher current flowed than during the first cathodic sweep and produced an oxidation peak attributed to conversion of Cu to Cu_2O and CuO. The succeeding sweeps continued to show peaks attributed to Cu redox reactions.

Current Profile. After conducting cyclic voltammetry, CO_2 electrochemical reduction was performed which generated current profile that is shown in Figure 6.52. The graph also includes data from the baseline Toray/Nafion/Cu_2O electrode. We observed a more flat current at around 13 mA, which represent 45% less current than in the baseline Toray/Nafion/Cu_2O sample.
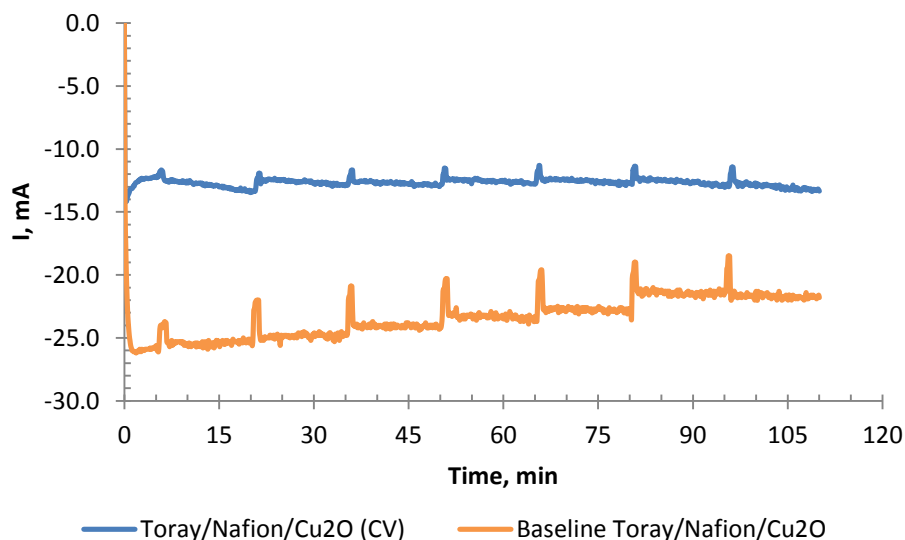
Figure 6.52. Current profile on Toray/Nafion/Cu_2O (CV) generated during CO_2 reduction at $-1.5V_{NHE}$.

Product Distribution. We then obtained the product distribution of ethanol, methane, ethylene, CO and H_2. Figure 6.53 shows the product formation rates. The

electrode had the highest productivity towards CO, at an average of 28 µmol/cm^2*hr. This was followed by ethylene and ethanol at 2.6 and 1.4 µmol/cm^2*hr respectively. Methane was again the least produced product of Cu_2O at 0.5 µmol/cm^2*hr. Meanwhile, the average H_2 formation rate was 86 µmol/cm^2*hr.
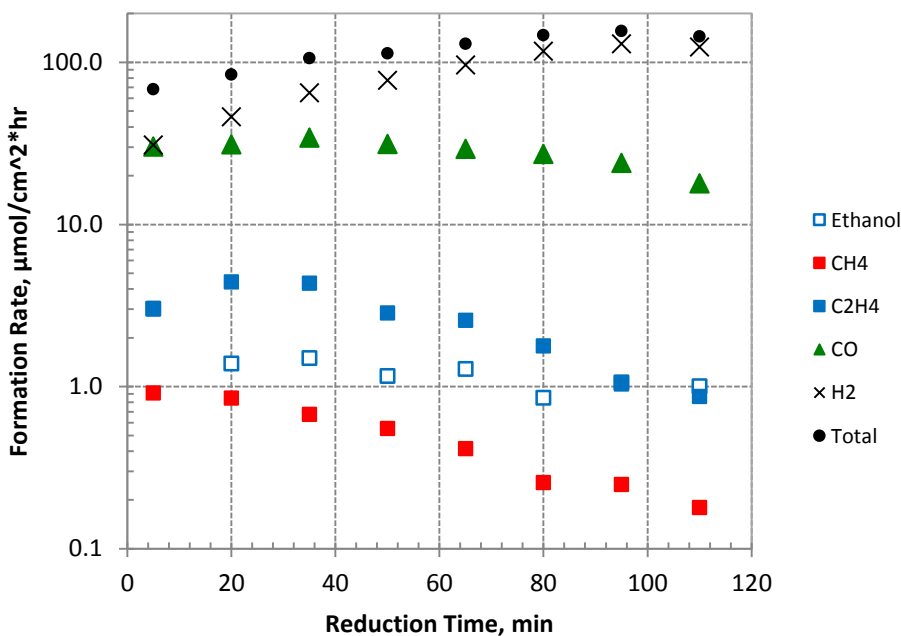
Figure 6.53. Product formation rates during CO_2 reduction on Toray/Nafion/Cu_2O (CV) electrode at -1.5V$_{NHE}$.

Compared to our baseline Toray/Nafion/Cu_2O electrode, the pre-anodized Toray/Nafion/Cu_2O (CV) electrode showed lower H_2, CO and hydrocarbon formation. The order of productivity was CO > ethylene > ethanol > methane which was the same with the baseline electrode. The over-all lower formation rates were likely due to lower Cu_2O loading of 1.1 mg compared to 26.5 mg.

Meanwhile, Figure 6.54 shows the product distribution in terms of faradaic efficiency. We observed an over-all decrease in the faradaic efficiency of CO_2 products

similar to the pre-anodized Toray/Cu_2O (CV) electrode. CO was a major product at 20% average faradaic efficiency. This was followed by ethylene and ethanol at 11% and 6.2% average faradaic efficiencies, respectively. This electrode showed the highest initial ethanol faradaic efficiency of 16%. CH_4 was an intermediate product at 1.5% average faradaic efficiency. Meanwhile, the average H_2 faradaic efficiency was 56%.
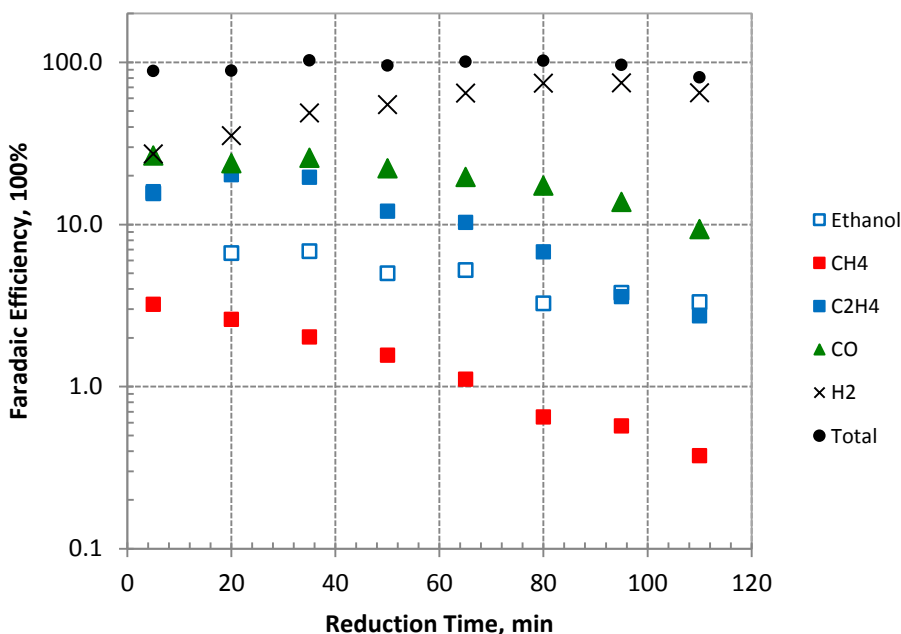
Figure 6.54. Faradaic efficiency of products during the CO_2 reduction on Toray/Nafion/Cu_2O (CV) at -1.5V_{NHE}.

Compared to our baseline Toray/Nafion/Cu_2O electrode, the pre-anodized Toray/Nafion/Cu_2O (CV) electrode showed higher H_2, CO, methane and ethanol selectivity but lower ethylene selectivity. As such, there was a minor change in the order of selectivity, particularly on CO and ethylene, as follows, CO > ethylene > ethanol > methane. The pre-anodization step did not significantly alter the productivity and selectivity of the electrode.

141

For this electrode, the Nafion/Cu$_2$O ratio was 0.8. With our study on the effect of Nafion, we have shown that the electrode with the Nafion/Cu$_2$O ratio of 1.2 showed the best productivity and selectivity to ethylene. Meanwhile, the electrode with the Nafion/Cu$_2$O ratio of 0.0 showed the best productivity and selectivity to CO.

6.3.2.6. Effect of Particle Size on Product Distribution

In this section, we compared the electrocatalytic activity of two sets of Cu$_2$O catalyst having distinct particle size. The first one was synthesized based on a wet chemical reduction method described by Chang et al. (2009). These Cu$_2$O particles (Cu$_2$O MP) typically have an average size of 200-400 nm. The second one was synthesized based on the wet chemical reduction method described by Li et al. (2013). These Cu$_2$O particles (Cu$_2$O NP) typically have an average size of 40-50 nm. The difference in particle size was derived from the difference in the relative concentration of reagents added to make these particles. Table 6.3 summarizes their compositions.

Table 6.3. Composition of reagents used for the two Cu$_2$O synthesis methods.

Reagent, in M	Chang et al. (2009)	Li et al. (2013)
Cu^{2+}	0.005 *(in acetate)*	0.001 *(in chloride)*
PEG	0.002 *(in PEG 200)*	0.05 *(in PEG 10,000)*
NaOH	0.2	0.3
Ascorbate	0.05	0.2

The first reason for the difference in particle size was the use of different amount of Cu^{2+} in the starting mixture. The Li method used 5x less amount of Cu^{2+} than the Chang method. The second reason was the difference in the amount of capping agent added to the mixture. With Chang's method, we used 1.3 g PEG / g Cu^{2+}, whereas with the Li method, we used 606.8 g PEG / g Cu^{2+}. The combination of lower amount of Cu^{2+} and higher amount of ion dispersing agent (PEG) led to an over-all decrease in the Cu$_2$O particle size.

The Cu$_2$O loading on both samples were 1.2 mg. Nafion was added to both set of Cu$_2$O particles at the same proportion of 1.1 mg Nafion / mg Cu$_2$O before they were brush-coated to the support electrode assembly.

These two Cu$_2$O particles were then compared by examining their morphologies and their electrocatalytic activity towards conversion of CO$_2$ to hydrocarbons and oxygenates at different potentials between -1.0V$_{NHE}$ and -1.7V$_{NHE}$. Selectivity was compared among these electrodes and against polycrystalline Cu.

SEM Analysis. First we checked on the structure of both sets of Cu$_2$O particles on the SEM before and after CO$_2$ reduction (refer to Figures 6.55 and 6.56). The Cu$_2$O MP catalyst was made up mainly of cubes with a small number of dual cubes and other irregularly-shaped structures. The average particle size of these Cu$_2$O MP particles was 200 nm. On the other hand, the Cu$_2$O NP particles were also cubes but the average particle size was 50 nm. The Cu$_2$O NP particles were only 4x smaller than the Cu$_2$O MP particles despite using 50x more capping agent per Cu^{2+} ion with the Li method.
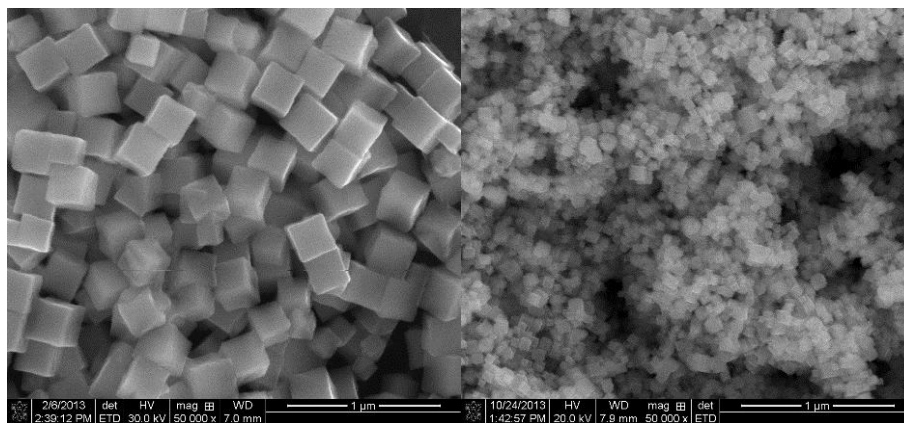
Figure 6.55. SEM of Cu$_2$O MP (left) Cu$_2$O NP (right) before CO$_2$ reduction.

After nearly 4 hours of CO_2 electrolysis, the SEM indicated that both set of particles evolved to about the same size and feature. The Cu_2O MP disintegrated into smaller multi-faceted nanoparticles while the Cu_2O NP particles agglomerated into multi-faceted nanoparticles. This results suggest that with sufficient electrolytic time, particles having initially different particle size will evolve into identical structure and size. Both set of Cu_2O particles lost their original cubic architecture.
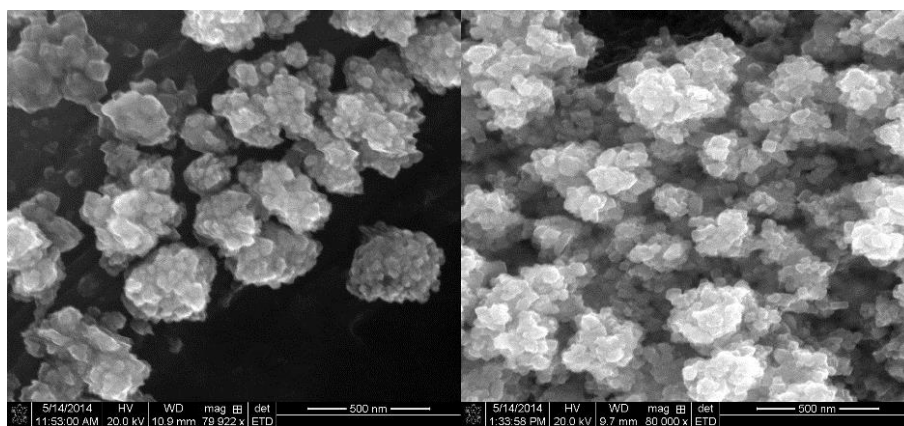
Figure 6.56. SEM of Cu_2O MP (left) and Cu_2O NP (right) after 4 hours of potential step CO_2 reduction.

Current Profile. We monitored the current flow on both samples during the 4 hour electrolysis. As seen in the Figure 6.57, both electrodes showed comparable amount of current between $-1.0V_{NHE}$ and $-1.5V_{NHE}$. We would expect to obtain similar total formation rates from the two sample at this range. Meanwhile at $-1.6V_{NHE}$ onwards, the current flow on the Cu_2O MP increased with potential more strongly than on the Cu_2O NP and also increased with time. This unsteady rise in current was likely due to expanding H_2 evolution on the electrode surface which we have also observed previously with fixed potential experiment.
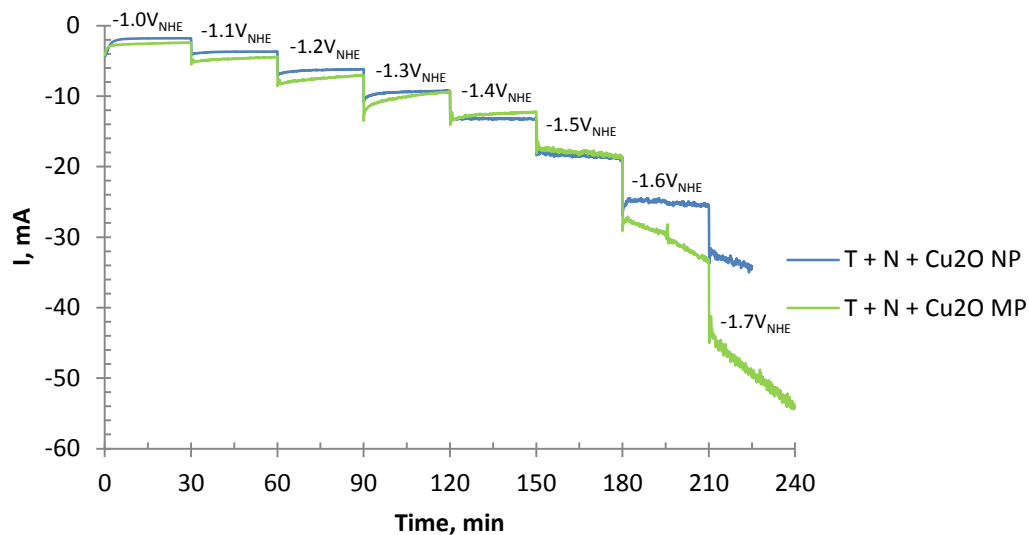
Figure 6.57. Current profile of Cu_2O MP and Cu_2O NP during 4 hours of potential step CO_2 electrolysis.

We also plotted the IR-corrected potential versus average current on both samples in Figure 6.58 and showed that the electrolysis was operating in a kinetically limited potential region characterized by high H_2 activity.
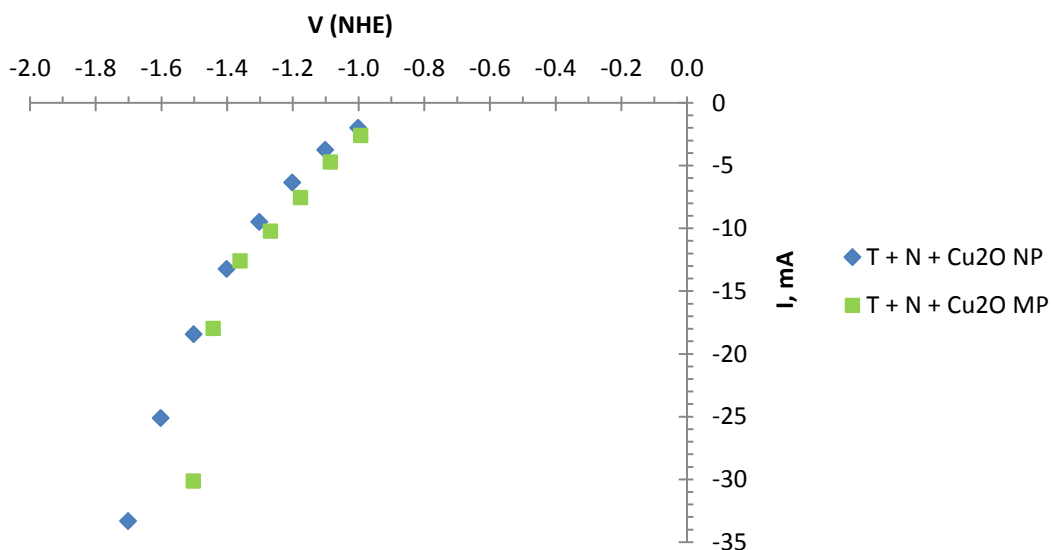
Figure 6.58. Equivalent voltammogram of the potential step electrolysis of CO_2 on Cu_2O MP and Cu_2O NP electrodes.

Product Distribution on Cu_2O MP Electrode. We then analyzed the CO_2 product distribution on Cu_2O MP and Cu_2O NP particles. First we looked at composite formation rate on the Cu_2O MP electrode (refer to Figure 6.59). We observed an increase in H_2 formation rate from 55 μmol/cm²*hr at $-0.99V_{NHE}$ to 1,066 μmol/cm²*hr at $-1.54V_{NHE}$. Meanwhile, the total CO + hydrocarbon formation rate increased from 1.6 μmol/cm²*hr at $-1.09V_{NHE}$ to 25 μmol/cm²*hr at $-1.44V_{NHE}$ then decreased to 21 μmol/cm²*hr at $-1.54V_{NHE}$. CO and ethylene productivity peaked at $-1.44V_{NHE}$ to 8.2 and 13 μmol/cm²*hr respectively. Methane productivity peaked at $-1.50V_{NHE}$ to 1.7 μmol/cm²*hr.
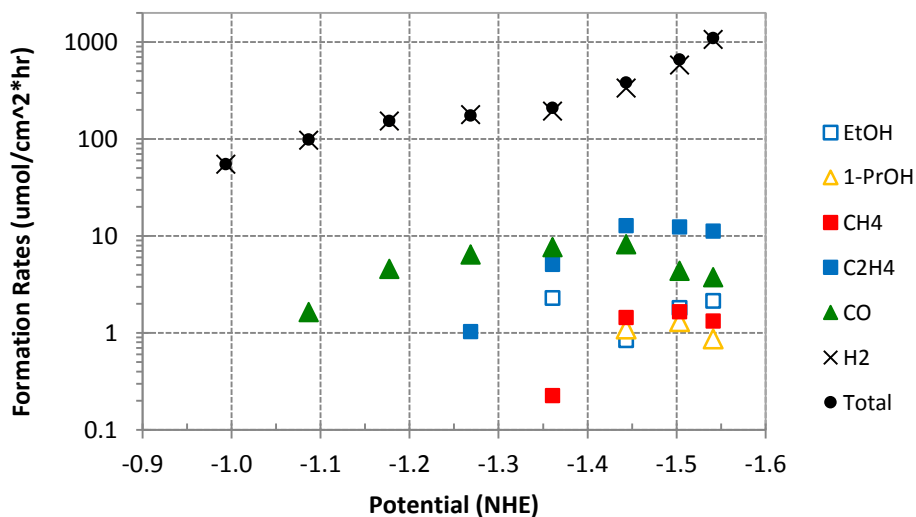
Figure 6.59. Product formation rates during CO_2 reduction on Cu_2O MP electrode at different potentials.

Now we looked at faradaic efficiency data in Figure 6.60. At potentials less negative than $-1.27V_{NHE}$, we only detected CO and H_2. The CO selectivity increased incrementally before reaching a maximum of 3.6% at $-1.27V_{NHE}$. From its peaks value, the selectivity declined to a low of 0.4% at $-1.54V_{NHE}$. H_2 selectivity decreased between

-0.99V$_{NHE}$ and -1.36V$_{NHE}$, which coincided with an increase in CO selectivity. H$_2$ selectivity then increased from -1.36V$_{NHE}$ to -1.54V$_{NHE}$.

At -1.27V$_{NHE}$, we started to detect hydrocarbons and oxygenates with ethylene as the first product observed with a selectivity of 3.4%. Its selectivity peaked to 22% at -1.44V$_{NHE}$ then decreased to 6.9% at -1.54V$_{NHE}$. Ethanol was first observed at more negative potential of -1.36V$_{NHE}$ where it achieved its highest peak of 5.9% efficiency before decreasing to 0.9% at -1.54V$_{NHE}$. Methane first formed at the same potential as ethanol with a selectivity of 0.4%. Its selectivity climbed slightly to 1.7% at -1.44V$_{NHE}$ before decreasing to 0.6% at -1.54V$_{NHE}$.
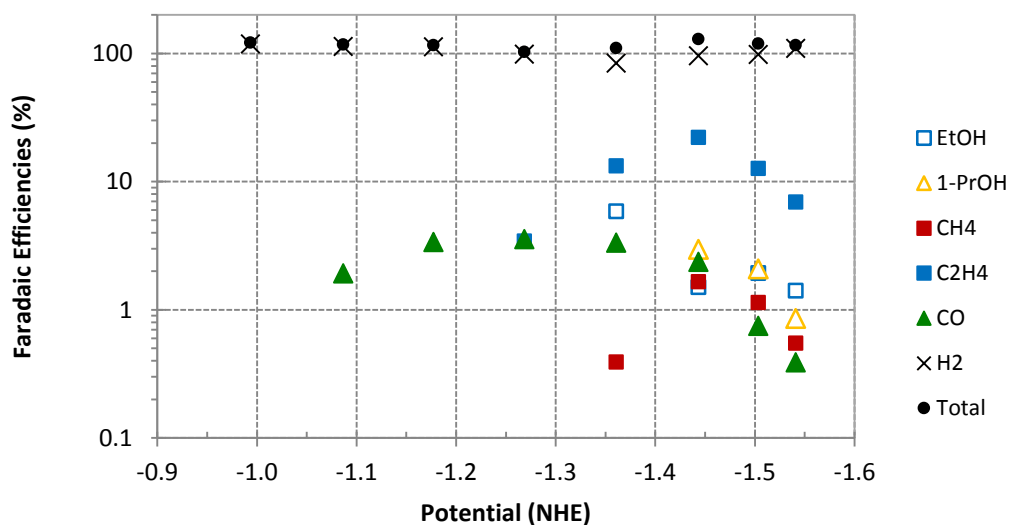
Figure 6.60. Faradaic efficiency of products during CO$_2$ reduction on Cu$_2$O MP electrode at different potentials.

At the potential window where CO selectivity decreased (between -1.27V$_{NHE}$ and -1.54V$_{NHE}$), hydrocarbon products were formed and their selectivities peaked at -1.44V$_{NHE}$. Between -1.44V$_{NHE}$ and -1.54V$_{NHE}$, the selectivity of CO and hydrocarbons decreased while that of H$_2$ increased. These shifts in product selectivity of the Cu$_2$O MP electrode demonstrate the different reaction intermediates that prevail during the potential steps. At

low negative potential, only H_{ads} were reduced to H_2. At more negative potential, CO_{ads} were also formed then desorbed to CO. Then at sufficiently more negative potential, some of the CO_{ads} intermediates were also reduced further into CHO_{ads} and COH_{ads} intermediates either as monomer or dimer.

We also looked at comparing the selectivity ratio C_2H_4/CH_4 and $(C_2H_4 + CH_4)/CO$ with our reduced Cu_2O electrode and those from Hori's results. The C_2H_4/CH_4 selectivity ratio of this oxide derived Cu at $-1.5V_{NHE}$ was 11.1 which is significantly higher than 0.9 on Hori's polycrystalline Cu at the same applied potential but lower than 14 on Hori's single crystal high index Cu (711) electrode. Meanwhile, the average $(C_2H_4 + CH_4)/CO$ selectivity ratio was 18.4 compared to 32 (upper limit range of 9-32) on Hori's polycrystalline Cu sample at the same applied potential.

<u>Product Distribution on Cu_2O NP Electrode</u>. Next we looked at the potential dependent product distribution on Cu_2O NP electrode. First we examined the formation rates shown in Figure 6.61.
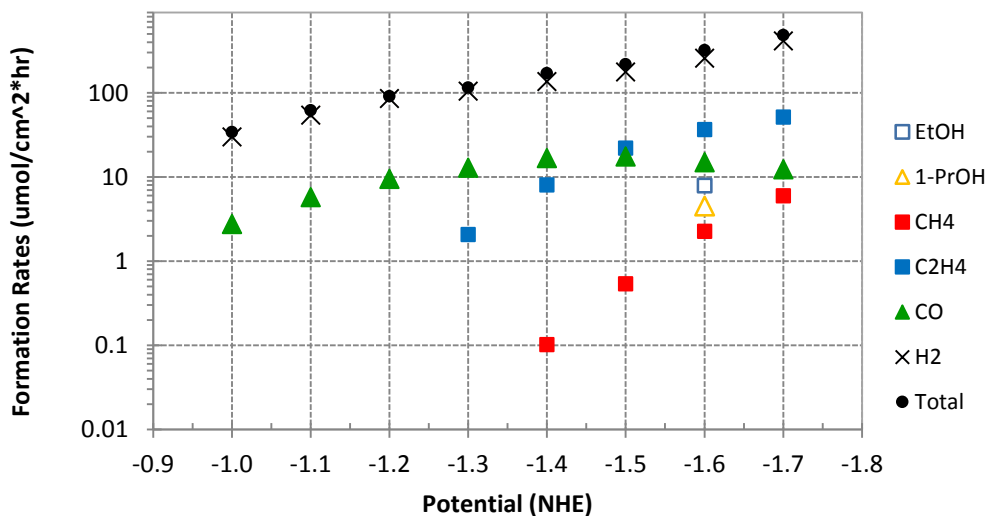
Figure 6.61. Product formation rates during CO_2 reduction on Cu_2O NP electrode at different potentials.

We again observed an increase in H_2 formation rate from 30 $\mu mol/cm^2*hr$ at $-1.0V_{NHE}$ to 413 $\mu mol/cm^2*hr$ at $-1.7V_{NHE}$. Meanwhile, the total CO + hydrocarbon formation rate increased from 2.8 $\mu mol/cm^2*hr$ at $-1.0V_{NHE}$ to 71 $\mu mol/cm^2*hr$ at $-1.6V_{NHE}$.

CO productivity peaked at $-1.5V_{NHE}$ to 18 $\mu mol/cm^2*hr$. Ethylene productivity increased from 2.1 $\mu mol/cm^2*hr$ at $-1.3V_{NHE}$ to 51 $\mu mol/cm^2*hr$ at $-1.7V_{NHE}$. Methane productivity increased from 2.1 $\mu mol/cm^2*hr$ at $-1.4V_{NHE}$ to 6.0 $\mu mol/cm^2*hr$ at $-1.7V_{NHE}$.

Then we looked at the faradaic efficiency data in Figure 6.62. At potentials less negative than $-1.3V_{NHE}$, we only detected CO and H_2. H_2 selectivity decreased between $-1.0V_{NHE}$ and $-1.5V_{NHE}$ and then increased from $-1.5V_{NHE}$ and $-1.7V_{NHE}$. The CO selectivity was steady at 8% between $-1.0V_{NHE}$ and $-1.2V_{NHE}$ before it started to decrease at $-1.3V_{NHE}$ falling to 1.9% at $-1.7V_{NHE}$. At that point ($-1.3V_{NHE}$), hydrocarbons were observed.
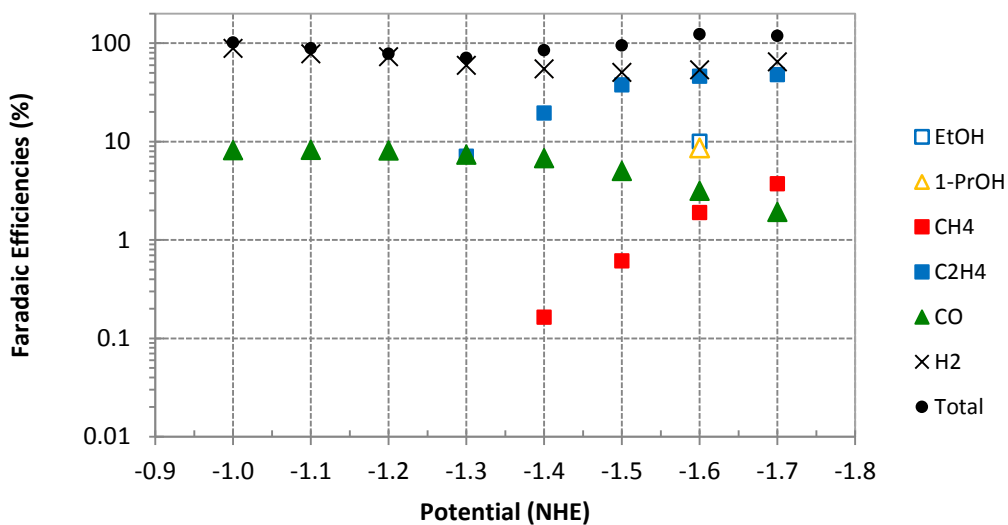
Figure 6.62. Faradaic efficiency of products during CO_2 reduction on Cu_2O NP electrode at different potentials.

The first hydrocarbon detected was ethylene at $-1.3V_{NHE}$ with a 7.1% faradaic efficiency. Its selectivity increased to 48% at $-1.7V_{NHE}$ without a maxima. The second hydrocarbon detected was methane at $-1.4V_{NHE}$ with a 0.2% faradaic efficiency. Its selectivity increased to 3.8% faradaic efficiency and also without a maxima. Ethanol and n-propanol products were only observed at $-1.6V_{NHE}$ with faradaic efficiencies of 10.1% and 8.7% respectively.

We also looked at comparing the selectivity ratio C_2H_4/CH_4 and $(C_2H_4 + CH_4)/CO$ with our reduced Cu_2O electrode and those from Hori's results. The C_2H_4/CH_4 selectivity ratio of this oxide derived Cu at $-1.5V_{NHE}$ was 61.3 which is significantly higher than 0.9 on Hori's polycrystalline Cu sample at the same applied potential and higher than 14 on Hori's single crystal high index Cu (711) electrode. Meanwhile, the average $(C_2H_4 + CH_4)/CO$ selectivity ratio was 7.7 compared to 32 (upper limit range of 9-32) on Hori's polycrystalline Cu sample at the same applied potential.

At the potential range where H_2 selectivity decreased (between $-1.0V_{NHE}$ and $-1.2V_{NHE}$), the CO selectivity was constant. This suggests an increasing CO_{ads} coverage on the surface of the electrode. At the potential window where CO selectivity decreased (between $-1.2V_{NHE}$ and $-1.7V_{NHE}$), hydrocarbon products were formed and their total faradaic efficiencies increased to their peak values at $-1.6V_{NHE}$. As explained earlier, these changes in product selectivity on the Cu_2O NP electrode again demonstrate the different reaction intermediates that prevail at different potentials.

Our CO_2 product distribution at different potentials supports the mechanisms that have been established on the reaction pathways of CO_2 on copper. For example, our results support Hori's theory that H_{ads} and CO_{ads} compete for coverage on the active sites on Cu.

At low and high potentials, H_2O molecules are more favorably adsorbed. At intermediate potentials, CO_2 molecules also become favorably adsorbed. Depending on the relative barrier between the kinetics of CO desorption and CO hydrogenation, either CO or hydrocarbons will be produced. We have shown that CO are kinetically favored at low to intermediate potential while hydrocarbons are kinetically favored at higher potential.

Comparison of Individual Products on Cu_2O MP, Cu_2O NP and Cu Electrodes

H_2 Formation. We then compared the Cu_2O MP, Cu_2O NP and Cu electrodes by the individual CO_2 (and H_2O) products. First, we looked at data on H_2 formation shown in Figure 6.63. We observed an increase in H_2 formation rates on all three electrodes. The Cu_2O MP electrode showed higher H_2 rates than Cu_2O NP and Cu electrodes. The Cu_2O NP electrode showed lower H_2 rates than Cu between $-1.5V_{NHE}$ and $-1.7V_{NHE}$.
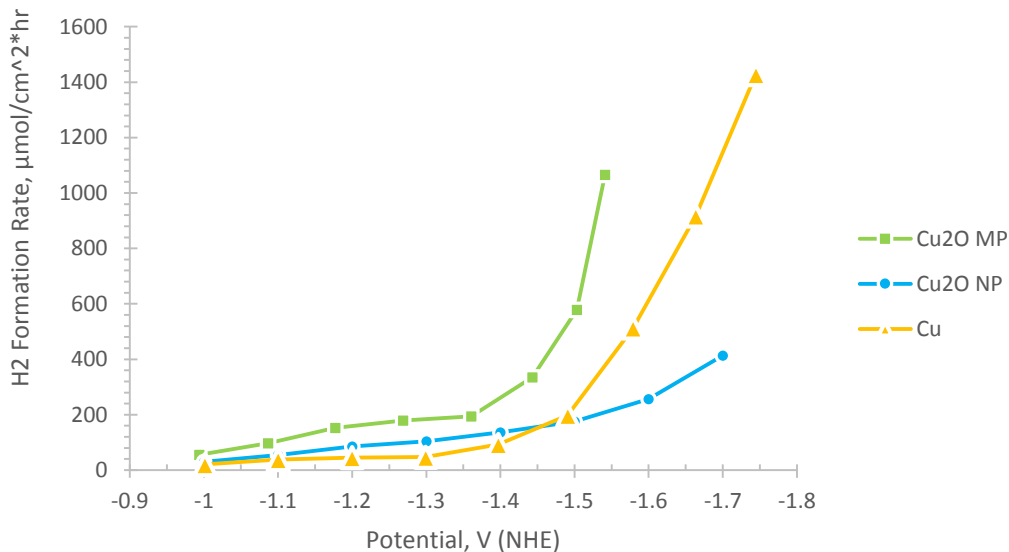
Figure 6.63. Formation rate of H_2 on Cu_2O MP, Cu_2O NP and Cu at different potentials.

Next we looked at H_2 faradaic efficiency of the three electrodes (see Figure 6.64). The Cu_2O NP electrode showed over-all lowest H_2 selectivity in which its faradaic efficiency decreased to 51% at $-1.5V_{NHE}$ from its initial faradaic efficiency of 89% at $-1.0v_{NHE}$. This was followed by Cu electrode whose H_2 faradaic efficiency showed two minima, the first one was at $-1.3V_{NHE}$ with 83% faradaic efficiency and the second one was at $-1.5V_{NHE}$ with 82% faradaic efficiency. The Cu_2O MP electrode showed over-all highest H_2 selectivity in which its faradaic efficiency reached its lowest value of 84% at $-1.36V_{NHE}$.
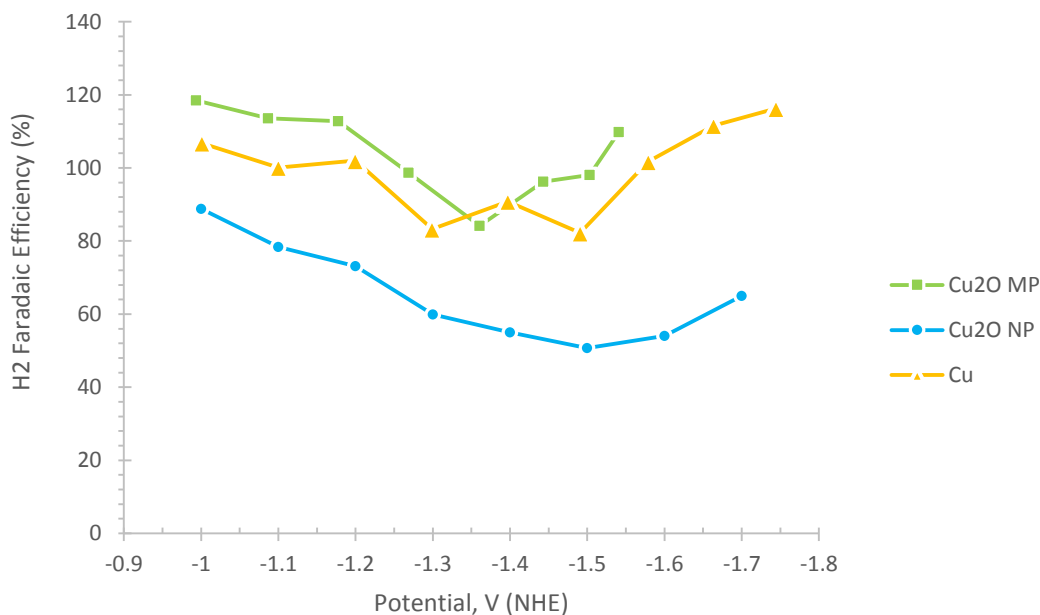
Figure 6.64. Faradaic efficiency of H_2 on Cu_2O MP, Cu_2O NP and Cu at different potentials.

CO Formation. We then compared CO formation on these electrocatalysts. First, we looked at formation rates shown in Figure 6.65. The Cu_2O NP electrode showed the highest over-all CO formation rate, followed by the Cu_2O MP electrode and the Cu electrode.

152
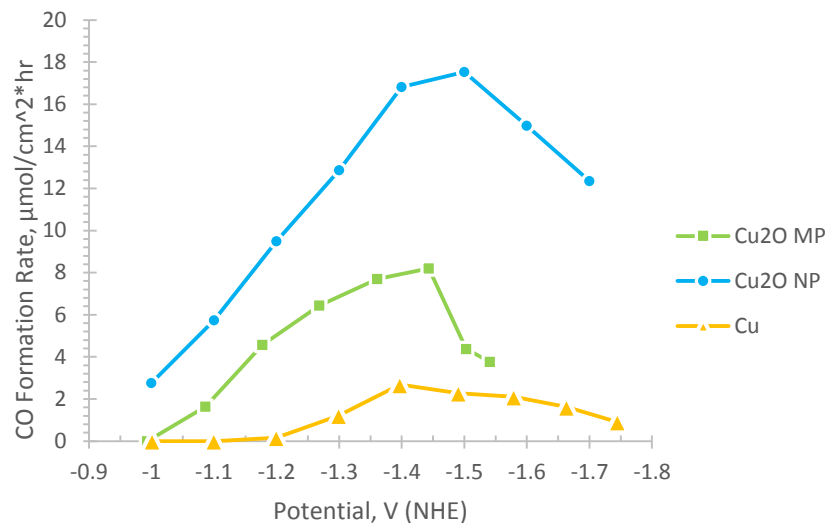
Figure 6.65. Formation rate of CO on Cu_2O MP, Cu_2O NP and Cu at different potentials.

In terms of faradaic efficiencies (see Figure 6.66), the Cu_2O NP electrode again showed the highest over-all CO faradaic efficiency and at lower potential. Meanwhile, the Cu electrode showed the lowest over-all CO faradaic efficiency although it showed identical CO selectivity between $-1.40V_{NHE}$ and $-1.54V_{NHE}$ with that of the Cu_2O MP electrode.
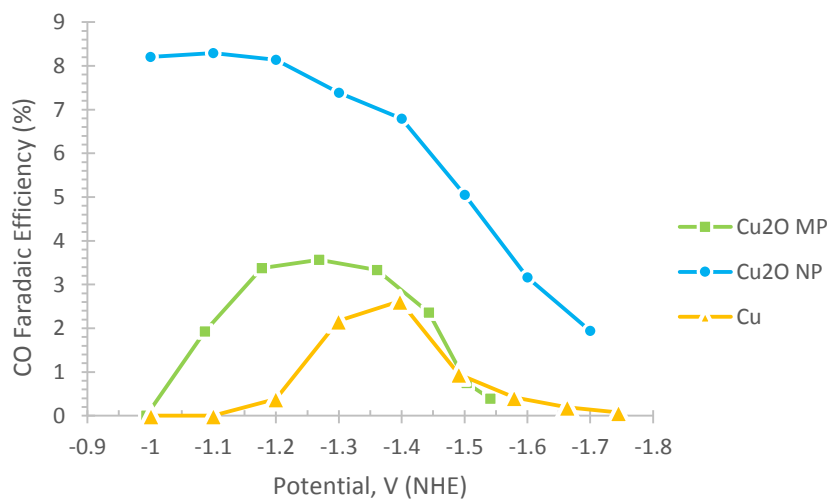
Figure 6.66. Faradaic efficiency of CO on Cu_2O MP, Cu_2O NP and Cu at different potentials.

153

The CO selectivity on both the Cu and Cu_2O MP electrodes was essentially zero at $-1.0V_{NHE}$ while the Cu_2O NP electrode still showed 8.2% faradaic efficiency. In comparison, Li's thermally oxidized Cu_2O achieved 30% faradaic efficiency at $-1.0V_{NHE}$. These results suggest that Cu clusters derived from wet reduction and thermal oxidation are still different from each other.

Methane Formation. Next, we looked at methane formation. First, we compared their formation rates which are shown in Figure 6.67. The Cu electrode showed over-all highest methane productivity than the Cu_2O MP and NP electrodes. However, at more negative potentials ($> 1.7V_{NHE}$), we observed that the methane production began to exceed that of the Cu electrode.
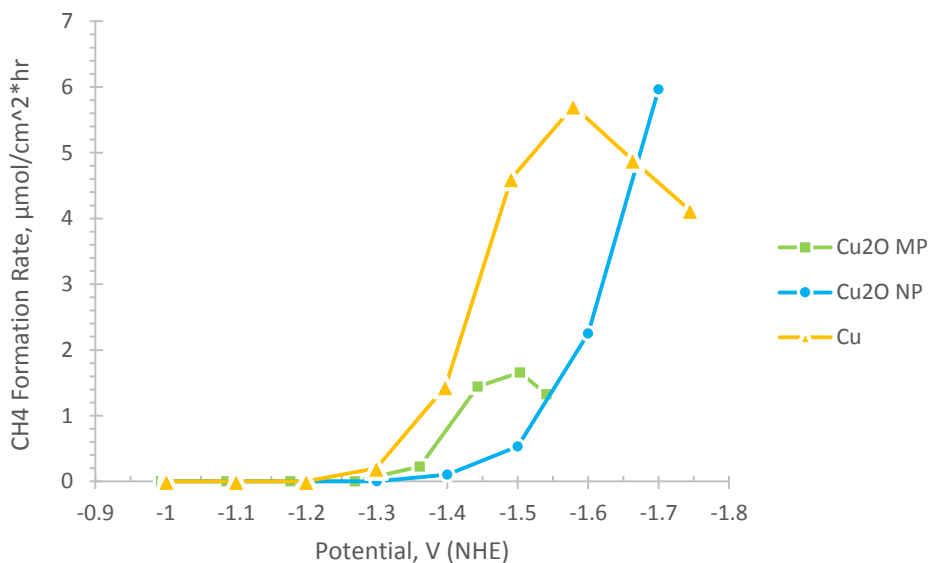
Figure 6.67. Formation rate of methane on Cu_2O MP, Cu_2O NP and Cu at different potentials.

We then compared their selectivity to methane (see Figure 6.68). Again, the Cu electrode showed the highest over-all methane faradaic efficiency at lower potential

relative to the other two electrodes. However at around -1.65V_{NHE}, we again observed that the methane selectivity of the Cu$_2$O NP electrode began to exceed that of the Cu electrode.
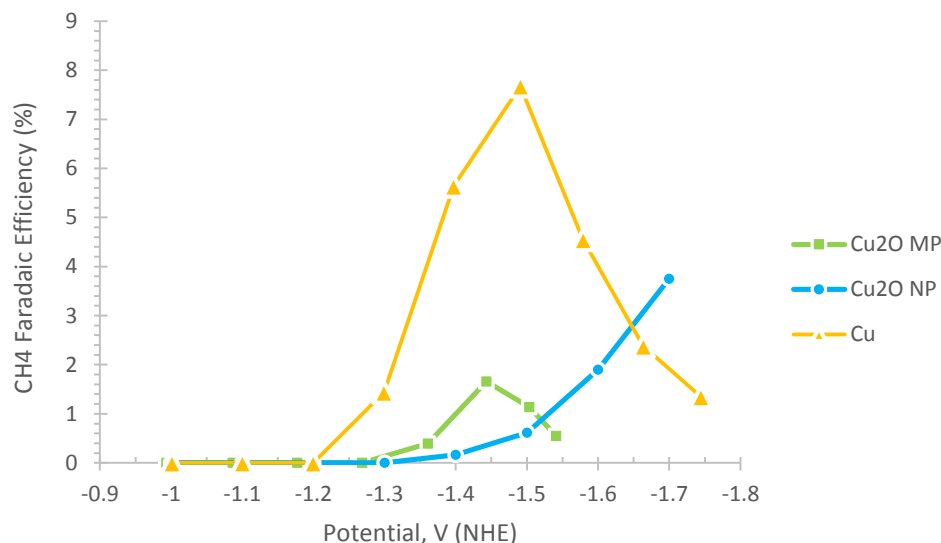
Figure 6.68. Faradaic efficiency of methane on Cu$_2$O MP, Cu$_2$O NP and Cu at different potentials.

We note that Li's group did not detect any methane with their oxide derived Cu particles. Instead they observed ethane (C$_2$H$_6$). This indicate that our oxide derived Cu particles still have Cu-like features that were completely absent from thermally oxidized Cu particles.

Both Hori and Schouten have suggested that methane forms on Cu(111) surfaces. However, we did not detect comparable amounts of CH$_4$ in our sample. Likely these Cu(111) oriented particles were in close proximity to Cu(200) oriented particles.

Ethylene Formation. Finally, we compared the three electrodes based on ethylene formation. Again, we looked at their formation rates (refer to Figure 6.69). Both the Cu$_2$O NP and Cu$_2$O MP electrodes showed identical ethylene formation rates up to -1.5V_{NHE}.
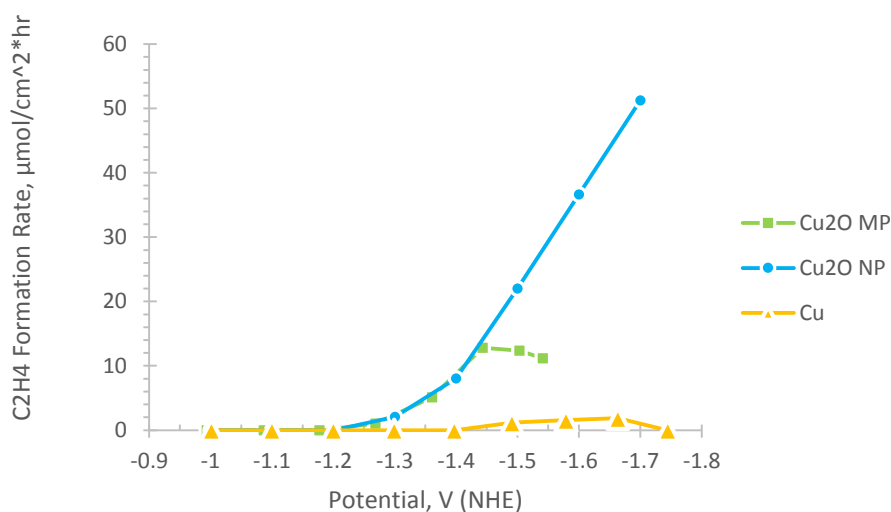
Figure 6.69. Formation rate of ethylene on Cu_2O MP, Cu_2O NP and Cu at different potentials.

Then the ethylene productivity continued to increase on the Cu_2O NP electrode beyond $-1.5V_{NHE}$ while that of the Cu_2O MP electrode declined. Meanwhile, the Cu electrode showed little ethylene productivity.

We then compared their faradaic efficiencies (see Figure 6.70). Both the Cu_2O NP and Cu_2O MP electrodes again showed identical ethylene selectivity up to $-1.5V_{NHE}$. Then the ethylene productivity continued to improve on the Cu_2O NP electrode beyond $-1.5V_{NHE}$ while that of the Cu_2O MP electrode declined. Meanwhile, the Cu electrode showed little ethylene selectivity.

In the previous sections, we have consistently observed higher ethylene and higher ethylene to methane ratio from Cu_2O particles at $-1.5V_{NHE}$. We extended our study to examine ethylene selectivity at other potentials. Our results showed that ethylene selectivity differ between Cu_2O MP and Cu_2O NP at potentials more negative than

156

-1.45V_{NHE}. While the ethylene selectivity on Cu_2O MP fell after -1.45V_{NHE}, that of Cu_2O NP continued to increase reaching 48% faradaic efficiency at -1.7V_{NHE}, which is the highest ethylene selectivity measured on Cu_2O particles under stable current electrolysis.
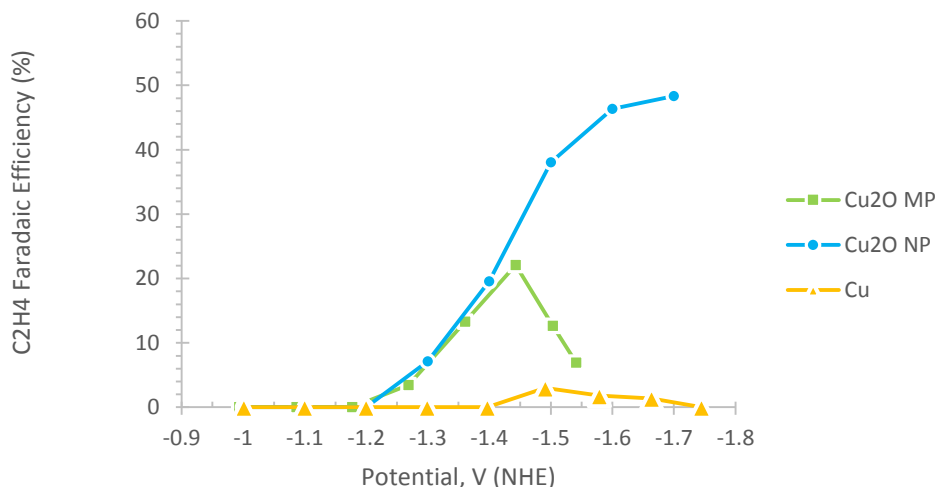
Figure 6.70. Faradaic efficiency of ethylene on Cu_2O MP, Cu_2O NP and Cu at different potentials.

Hori and Schouten have suggested that ethylene preferably forms on Cu(100) and on steps in Cu(111). The XRD scan of our Cu_2O particles showed that the orientation of oxide derived Cu particles were mainly Cu(111), followed by Cu(200) then Cu(222). Although there were no Cu(100) surfaces in our sample, Cu(200) is the same as Cu(100). The reduced Cu_2O particles likely generated a lot of Cu(200) steps on Cu(111) and Cu(222) planes at the surface.

Metallic Cu surfaces generated ethylene efficiency of 22% at -1.3V_{NHE} (Hori et al. 1989). Though Cu_2O surfaces showed very high ethylene selectivity (>22%), they were obtained at more negative potential (greater than -1.4V_{NHE}) compared to Cu. However, we

obtained higher ethylene efficiency of 16% at -1.4V_{NHE} compared to just 4% from thermally oxidized Cu sample. This indicate that the resulting surface of our oxide-derived Cu particles have more preference to ethylene than CO.

6.3.3. CO$_2$ Reduction on Glassy Carbon Supported Cu$_2$O Particles[4]

In this section, we used GL as support substrate to the Cu$_2$O particles in order to minimize mass transfer effects associated with using porous materials. Glassy carbon is a suitable support material because it is rigid and has low electrical resistance (van der Linden and Dieker 1980). It is also stable under high potential electrolysis. Nevertheless, it is an electrochemically active surface towards H$_2$O reduction.

Cu$_2$O samples were prepared by colloidal synthesis, mixed with Nafion, then brush coated to the glassy carbon plate. Due to the mirror like surface of GL, we increased the Nafion to Cu$_2$O mass ratio to 4.8 to improve the adhesion of the Cu$_2$O particles. For this particular electrocatalyst, the initial Cu$_2$O Loading was 5.8 mg while the Nafion loading was 27.6 mg.

Two sets of CO$_2$ electrochemical reduction were performed. The first one involved electrolysis at a constant potential of -1.5V_{NHE} for 125 minutes. The second electrolysis consisted of a sequence of potentials starting from -1.1V_{NHE} to -1.7V_{NHE}, with 60 minute electrolysis at each potential, with the exception of -1.3V_{NHE} which ran for 120 minutes.

6.3.3.1. SEM Analysis

The SEM image of Cu$_2$O particles before the first electrolysis is shown in Figure 6.71. The particles ranged in size from 700 – 900 nm. Majority of the particles were cubes while a few have dual cubic structures. Some particles were fully covered with Nafion while others were only partially covered. Some areas of the glassy carbon plate were not

[4]This section previously appeared in reference: Griffin, G.L. and J. Bugayong. 2014. "Electrochemical Reduction of CO2 Using Copper Oxide Nanoparticles Supported on Glassy Carbon Electrodes." MRS Proceedings 1677. [Reproduced with permission from the Cambridge University Press.]

covered by Cu_2O particles and were therefore exposed to the electrolyte during electrolysis. Nevertheless, the Cu_2O particles were mechanically stable.
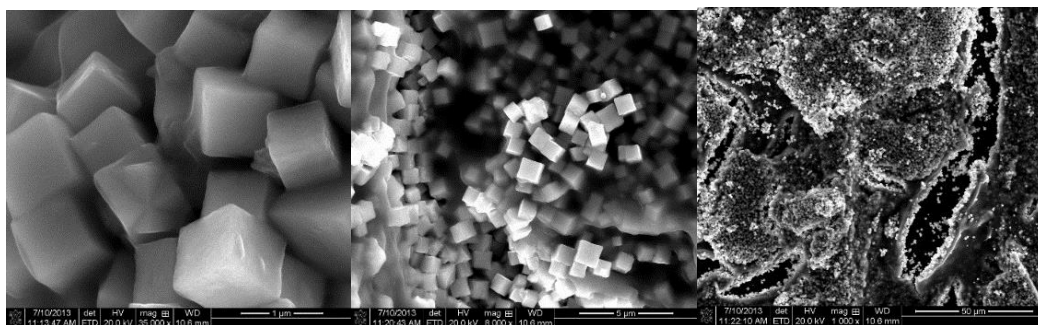
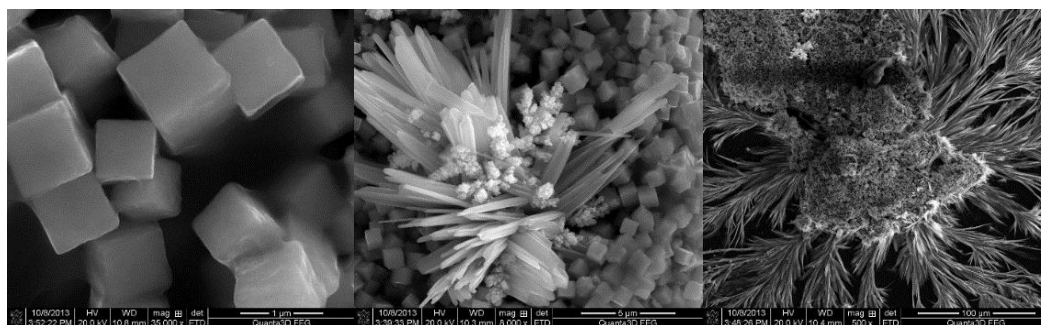Figure 6.71. SEM images of GL/Nafion/Cu_2O electrode before CO_2 reduction at (left) 35,000x (center) 8,000x and (right) 1,000x magnification.

After 7 hours of CO_2 electrochemical reduction, the architecture of particles became more diverse as shown in Figure 6.72. A percentage of Cu_2O cubes evolved into particles with multiple structures such as nanoparticles, pyramidal rods and branching fibers. However, some of the cubes remained intact.

Figure 6.72. SEM images of GL/Nafion/Cu_2O electrode after two batches of CO_2 reduction at (left) 35,000x (center) 8,000x and (right) 500x magnification.

6.3.3.2. XRD Analysis

The XRD scan was performed before the first CO_2 reduction (ECR) and after the second CO_2 reduction. The XRD scans shown in Figure 6.73 revealed different Cu_2O

159

crystal peaks on Cu_2O before CO_2 reduction. Based on peak intensity, the electrode consisted of (200) > (111) > (220) > (311) oriented particles. After two batches of CO_2 reduction which covered a total time of 7 hours, we observed new peaks that were characteristic of Cu crystals. However, we still observed significant signals from the listed Cu_2O crystal planes. The XRD profile shifted by approximately 0.5°.

This result suggests that the bulk of Cu_2O particle were not reduced to Cu particles. The SEM also showed presence of cubes after CO_2 reduction which is indicative of Cu_2O particles. The Nafion that was in contact with the Cu_2O particles may have prevented the particles from reducing to Cu possibly by providing a barrier for electron transfer. It is also possible that these particles experienced significantly lower localized potential gradient.
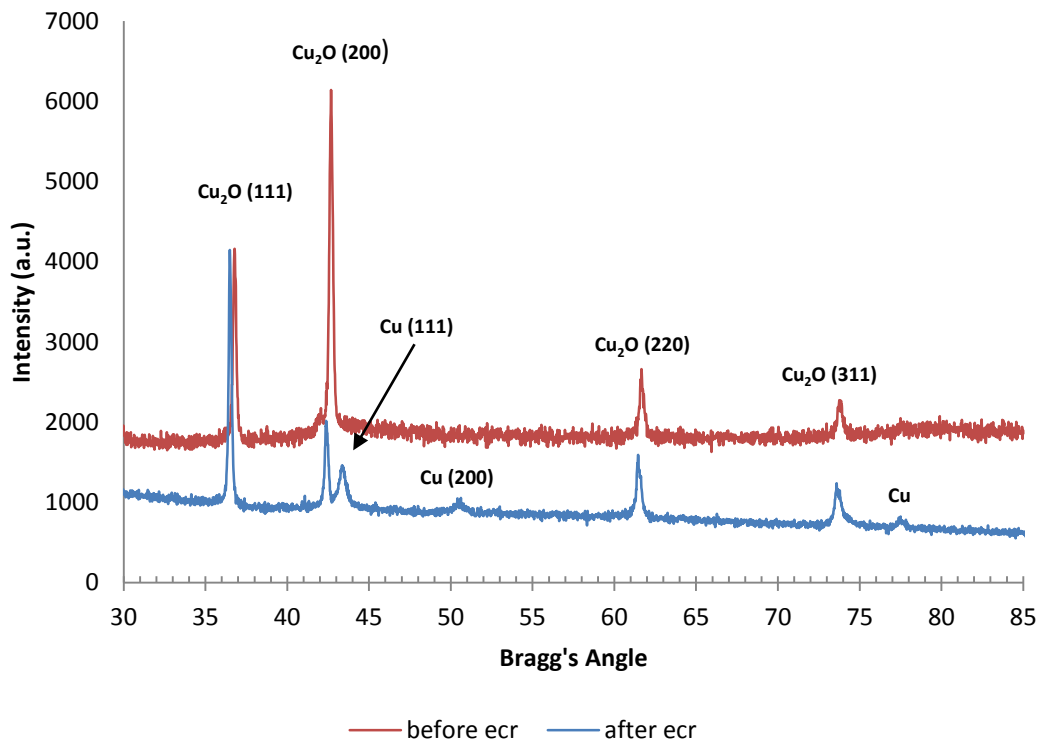
Figure 6.73. XRD profile of GL/Nafion/Cu_2O electrode before and after CO_2 reduction.

6.3.3.3. Current Profile of the Fixed Potential Reduction

Figure 6.74 shows the current profile generated by the first CO_2 reduction which included the data from the baseline Toray/Nafion/Cu_2O sample. The current slowly increased with time but a plateau was observed between 65 and 80 minutes. During this short period, there was no CO_2 fed into the solution. The absence of convection caused by purging of the CO_2 carrier gas temporarily lowered the current flow by 2-5 mA. The over-all total current were higher than the one generated by the baseline Toray/Nafion/Cu_2O electrode.
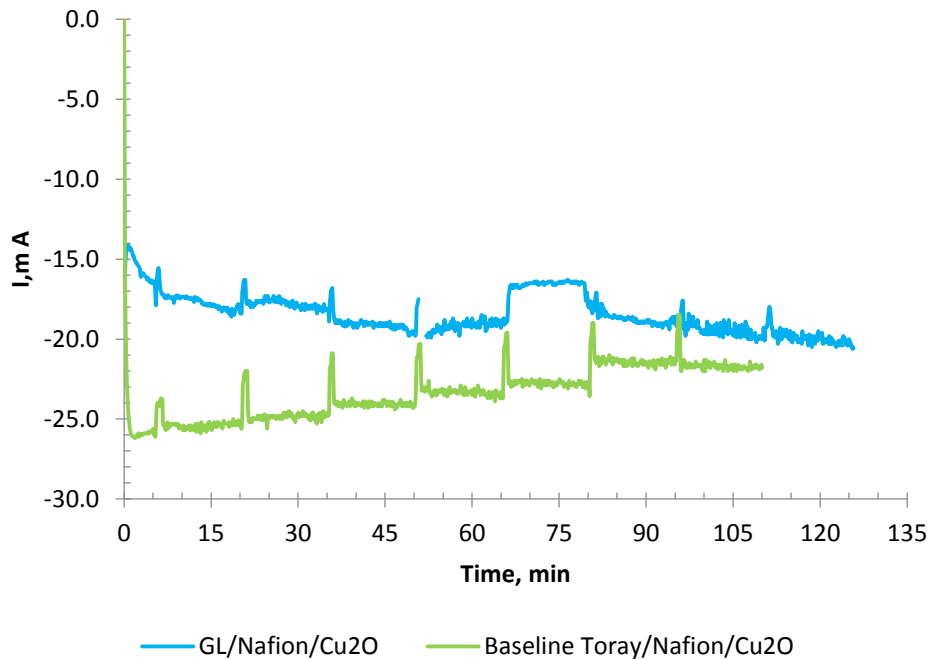
Figure 6.74. Current profile of GL/Nafion/Cu_2O and baseline Toray/Nafion/Cu_2O electrodes during CO_2 reduction at -1.5V_{NHE} for 110 minutes.

6.3.3.4. Current Profile of the Potential Step Reduction

Figure 6.75 shows the current profile of the potential step reduction from -1.1V_{NHE} to -1.7V_{NHE}. The current was steady at -1.1V_{NHE} and -1.3V_{NHE}. At -1.5V_{NHE}, we observed

a slow increase in current flow. Finally at -1.7V_{NHE}, there was fluctuation of current revolving around -39 mA. The noise was driven by formation of large H_2 bubbles.
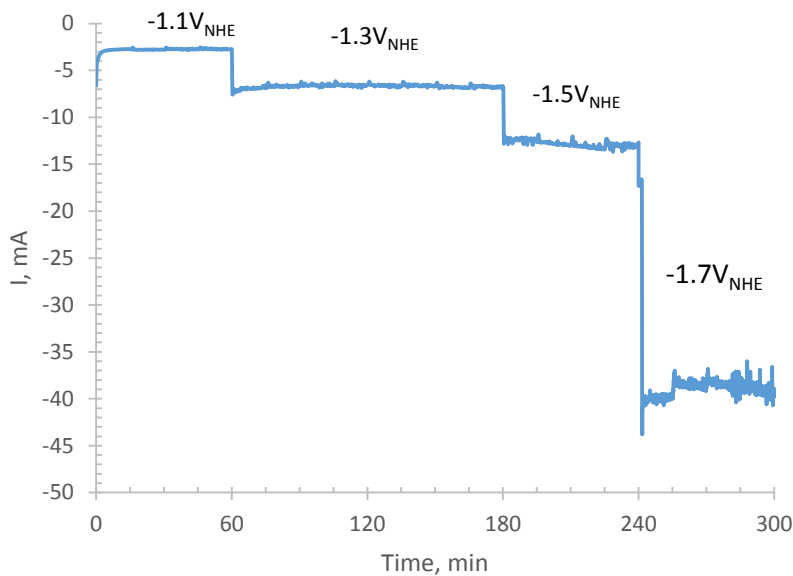
Figure 6.75. Current profile of the GL/Nafion/Cu_2O electrode during potential step electrolysis of CO_2.

6.3.3.5. Kinetic Study

We then analyzed the kinetics of first CO_2 reduction and the product formation rates are given in Figure 6.76. We observed high H_2 formation rates which increased from 99 µmol/cm^2*hr to 192 µmol/cm^2*hr at 65 minutes into the process and then levelled off around that rate. The CO formation rate meanwhile increased in the first 65 minutes from 5.8 µmol/cm^2*hr to 17 µmol/cm^2*hr before the process was interrupted by a cut off in CO_2 supply. Upon resumption, the CO productivity fell to 9.6 µmol/cm^2*hr but increased again to 14 µmol/cm^2*hr by the end of the electrolysis.

Meanwhile, the kinetics of ethylene formation followed the same pattern seen in the CO curve. The ethylene formation rate increased in the first 65 minutes from 3.2 µmol/cm^2*hr to 10 µmol/cm^2*hr before the process was interrupted. Upon resumption, the ethylene productivity fell to 8.2 µmol/cm^2*hr before increasing again with time to 10

162

μmol/cm^2*hr by the end of the process. The ethylene productivity from this electrode was slightly on par with the baseline Toray/Nafion/Cu$_2$O electrode.

Meanwhile, the methane product had an average formation rate at 2.0 μmol/cm^2*hr which is higher than in the baseline Toray/Nafion/Cu$_2$O electrode. The GC also observed ethanol and n-propanol at lower average rates of 0.6 and 0.2 μmol/cm^2*hr respectively but were lower than in the baseline Toray/Nafion/Cu$_2$O electrode.
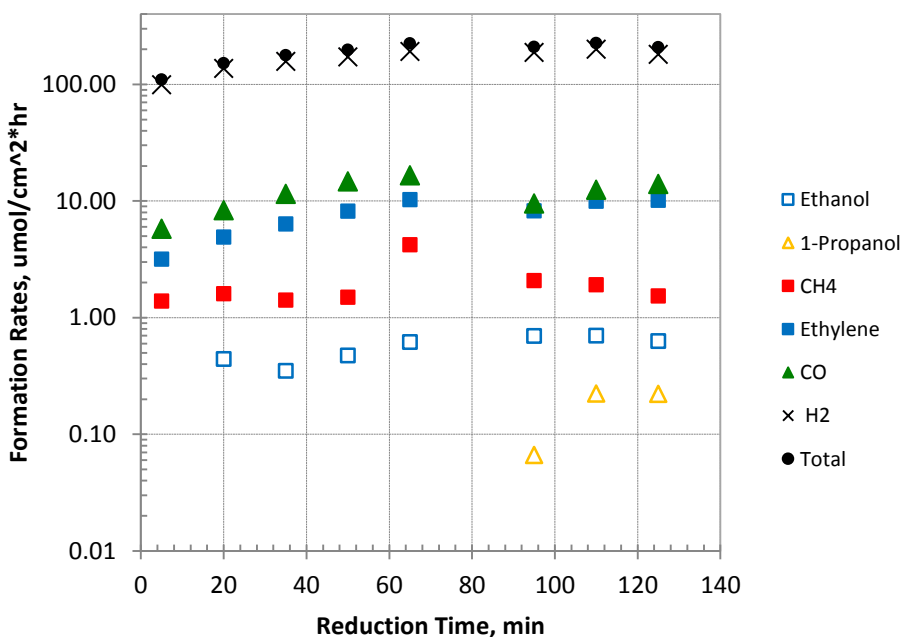
Figure 6.76. Formation rate of products during CO$_2$ reduction on GL/Nafion/Cu$_2$O electrode at -1.5V$_{NHE}$.

Unique with this sample was that the selectivity of H$_2$, C$_2$H$_4$ and CO increased with time between 0 and 65 minutes. We did not observe a switch in selectivity between H$_2$ and CO$_2$ products, as well as between CO and the hydrocarbons. This would suggest that either the number of active sites in the electrocatalyst or the turnover frequency increased during this period.

We then looked at the faradaic efficiencies of these products (see Figure 6.77). We observed ethylene as the only major CO_2 product with peak faradaic efficiency of 41% and a mean of 31%. This Cu_2O electrocatalyst produced one of the highest ethylene selectivity at $-1.5V_{NHE}$ and is also slightly better than the baseline Toray/Nafion/Cu_2O electrode.

The methane selectivity was also above 1% faradaic efficiency with an average of 5.3% which is also one of the highest we have achieved with our Cu_2O electrode and an order of magnitude better than with our baseline Toray/Nafion/Cu_2O electrode. The rest of the CO_2 products were also produced at intermediate selectivity. The electrode showed an average CO, n-propanol and ethanol faradaic efficiency of 7.9%, 2.4% and 1.1% respectively. The enhancement of ethylene and methane formation may be due to lower mass transfer limiting effect.
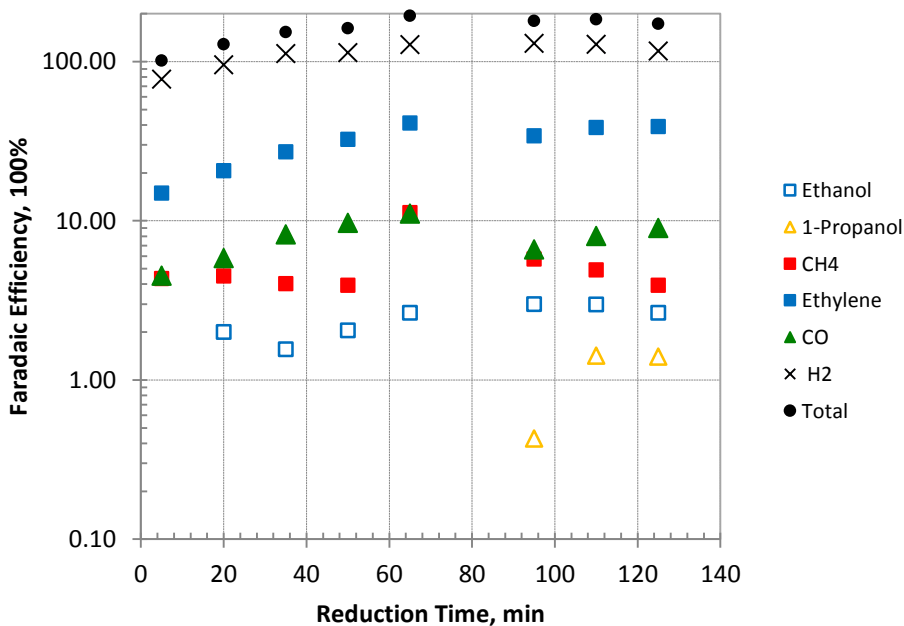
Figure 6.77. Faradaic efficiency of products during CO_2 reduction on GL/Nafion/Cu_2O electrode at $-1.5V_{NHE}$.

We then compared the selectivity ratio C_2H_4/CH_4 and $(C_2H_4 + CH_4)/CO$ of our Cu$_2$O electrode with Hori's results. The C_2H_4/CH_4 selectivity ratio was 5.8 which was significantly higher than 0.9 on Hori's polycrystalline Cu sample at the same applied potential but lower than 14 on Hori's single crystal high index Cu (711) electrode. Meanwhile, the average $(C_2H_4 + CH_4)/CO$ selectivity ratio was 4.6 compared to 32 (upper limit range of 9-32) on Hori's polycrystalline Cu sample at the same applied potential. This is because the gap in faradaic efficiency between hydrocarbons and CO in the Cu$_2$O electrode was not as wide as in their Cu electrode.

6.3.3.6. Effect of Potential

We then look at the effect of potential on the formation rates of ethanol, n-propanol, methane, ethylene, CO and H_2 shown in Figure 6.78. We observed that the formation rate of these products increased with potential. At -1.1V$_{NHE}$, the GC only detected CO and H_2 at average rates of 3.4 and 55 µmol/cm^2*hr. At -1.3V$_{NHE}$, ethylene was produced with an initial rate of 0.5 µmol/cm^2*hr that increased to 40 µmol/cm^2*hr at -1.7V$_{NHE}$.
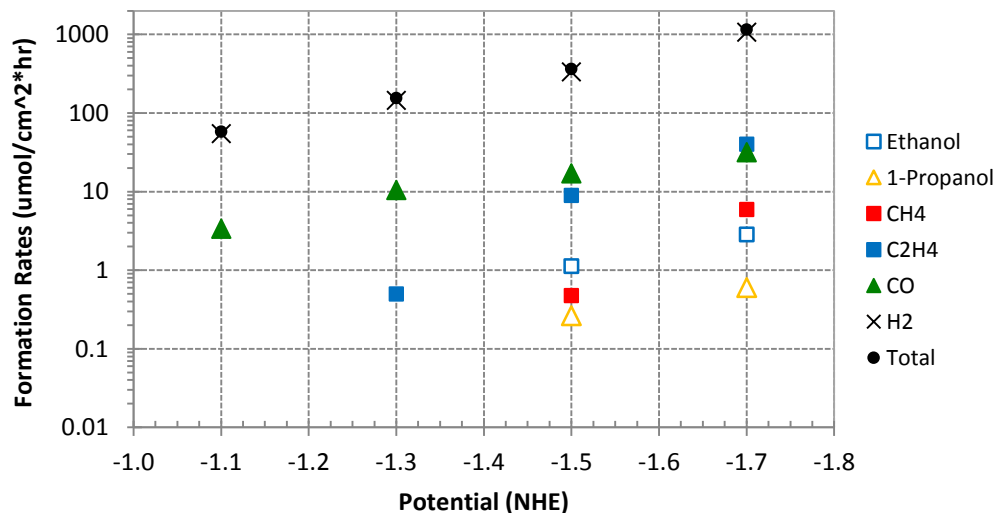
Figure 6.78. Formation rate of products during CO_2 reduction on GL/Nafion/Cu$_2$O electrode at different potentials.

165

Between -1.3V$_{NHE}$ and -1.5V$_{NHE}$, CO had higher measured formation rate than ethylene but was slightly exceeded by the latter at -1.7V$_{NHE}$. CO formation rate was 32 µmol/cm^2*hr at -1.7V$_{NHE}$. The products methane, ethanol and n-propanol were first measured at -1.5V$_{NHE}$ at rates of 0.5, 1.1 and 0.3 µmol/cm^2*hr respectively. Their productivity increased to 6.0, 2.9 and 0.6 µmol/cm^2*hr respectively at -1.7V$_{NHE}$.

We now looked at the faradaic efficiency of these products at different potential. From Figure 6.79, we observed a peak in CO selectivity of 9.5% at -1.3V$_{NHE}$. At this potential, ethylene had a lower selectivity of 2.7%. At -1.5V$_{NHE}$, ethylene became a major product and showed the highest current efficiency among the CO$_2$ products at 25%. This was followed by CO at 7.8%, ethanol at 3.2%, n-propanol at 1.1% and CH$_4$ at 0.9%. Meanwhile, at the more negative potential of -1.7V$_{NHE}$, the ethylene selectivity continued to improve, increasing to 37%. The methane selectivity also improved to 3.6%. At this potential, the CO efficiency further decreased to 4.9%.
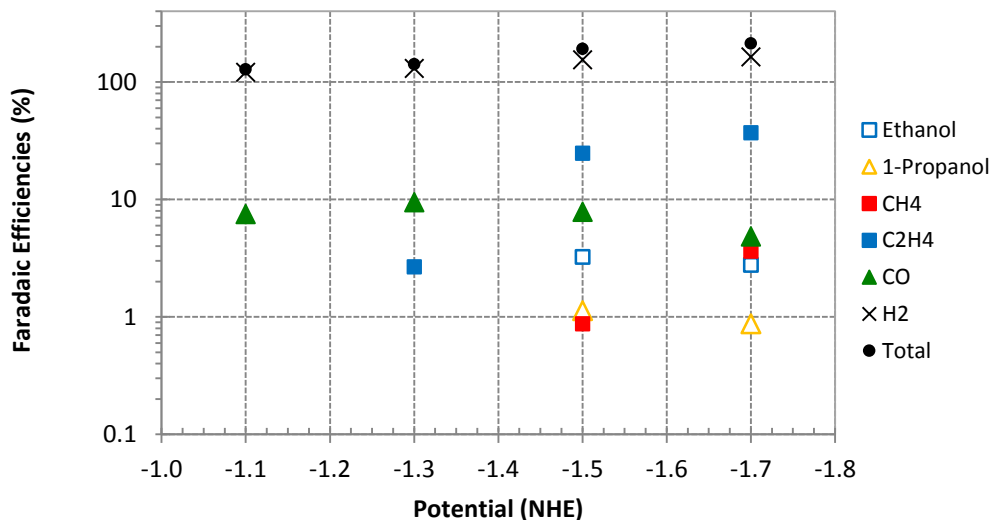
Figure 6.79. Faradaic efficiency of products during CO$_2$ reduction on GL/Nafion/Cu$_2$O electrode at different potentials.

The shift in selectivity from CO to C_2H_4 and CH_4 at more negative potentials is consistent with the results observed by Hori's group and also supports a key step in the CO_2 reaction pathway proposed by Hori, Kuhl, Schouten and Nie. In particular, the branch point between the formation of CO versus the reduction of CO_{ads} to hydrocarbons.

6.3.4. CO₂ Reduction on Copper Supported Cu₂O Particles

Finally, we examined the electrocatalytic activity of Cu_2O supported on polycrystalline Cu substrate. With the previous Cu_2O electrode, we observed that the oxide derived Cu showed different selectivity towards C_2H_4 and CH_4 compared to polycrystalline Cu. These electrodes consisted of Cu-carbon, Cu-Nafion and Cu-carbon-Nafion interfaces. At this point, it is not clear if the Cu-carbon interface also contributed to enhanced ethylene selectivity. With this Cu_2O electrode, we replaced the carbon support substrate with a copper support substrate and examined any changes on the product distribution.

The Cu_2O particles were synthesized according to the method described by Chang et al. (2009). They were then physically deposited to Cu using a Nafion binder. The Cu substrate had a Cu_2O loading of 1.8 mg and a Nafion/Cu_2O ratio of 4.8.

6.3.4.1. SEM Analysis

The SEM of fresh Cu/Nafion/Cu_2O electrode is shown in Figure 6.80. The left image has a 50,000x magnification while the right image has a 10,000x magnification. The particles were made up mostly of cubes with a few dual cube structures. The average particle size was approximately 600 nm. Some of the particles were fully covered by Nafion while those at the surface were partially covered by Nafion.
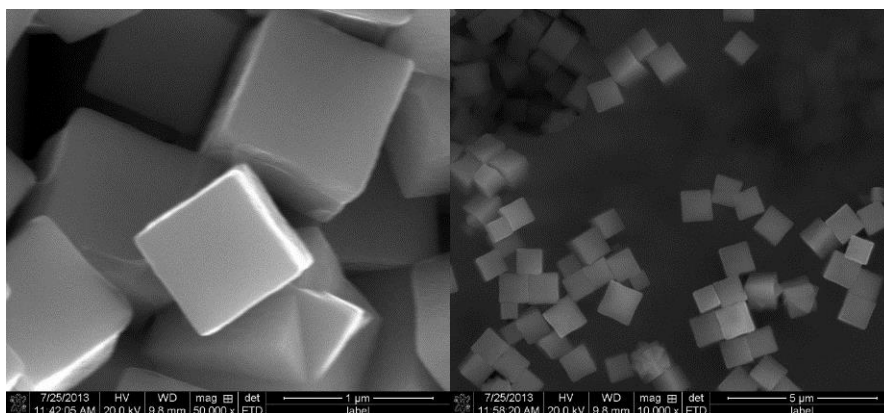
Figure 6.80. SEM of Cu/Nafion/Cu_2O electrode before CO_2 reduction at -1.5V_{NHE}, (left) at 50,000x magnification and (right) at 10,000x magnification.

Figure 6.81 shows the morphology of Cu_2O particles after CO_2 reduction. We observed decorations at the surface of the cube. Some cubes were partially deformed with decorations more confined at the side that was in contact with the electrolyte. The other cubes exhibited less distortion in their structure. About 35% of the Cu_2O particles were lost during electrolysis due to aggressive H_2 evolution. Similar to our GL-supported Cu_2O, the Cu substrate was not fully covered.
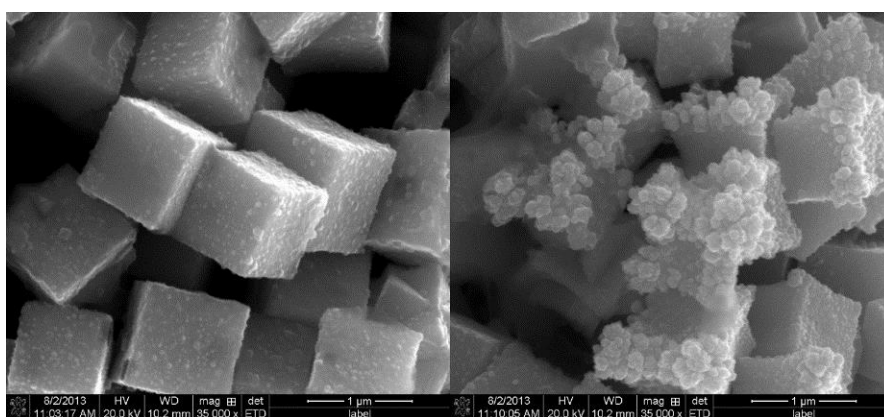
Figure 6.81. SEM of Cu/Nafion/Cu_2O electrode after CO_2 reduction at -1.5V_{NHE}, (left) at area 1, 35,000x magnification and (right) at area 2, 35,000x magnification.

6.3.4.2. XRD Analysis

The XRD scan before and after CO_2 reduction generated peaks for a variety of Cu and Cu_2O crystal planes (refer to Figure 6.82). Before CO_2 reduction, the $Cu_2O(200)$ particles showed the highest intensity, followed by $Cu_2O(111)$ and $Cu_2O(220)$ particles. After CO_2 reduction, the XRD scan indicated that Cu_2O particles were present since most of the original Cu_2O peaks were still detected except $Cu_2O(110)$.
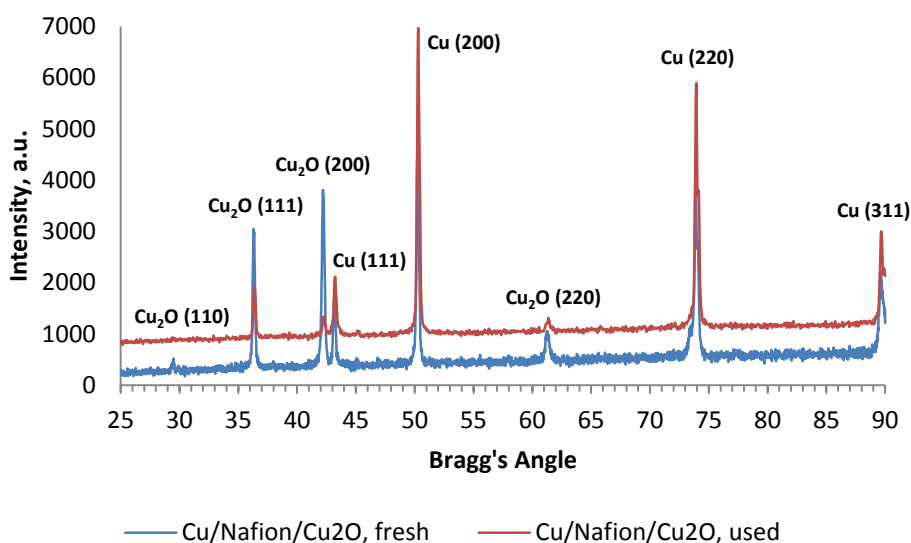
Figure 6.82. XRD profile of $Cu/Nafion/Cu_2O$ electrode before and after CO_2 reduction.

6.3.4.3. Current Profile

The CO_2 reduction on $Cu/Nafion/Cu_2O$ electrode generated a current profile shown in Figure 6.83. The data on Cu studied in Chapter 4 was also included for reference point. While the charge transfer on the Cu electrode decreased with time, the charge transfer on the $Cu/Nafion/Cu_2O$ electrode was relatively constant around 13 mA/cm^2. However, we observed a noise in the current between 0 and 65 minutes which disappeared from 65 to 110 minutes.

The presence of instability in the current during the first part of the process can be attributed to physical movements at the surface as a result of the electrode losing Cu_2O particles. When the electrode surface reached a mechanically stable condition, bubbles became smaller in size. Transient current related to Cu_2O reduction to Cu was not observed from the graph although SEM and XRD showed evidence of partial Cu_2O reduction to Cu.
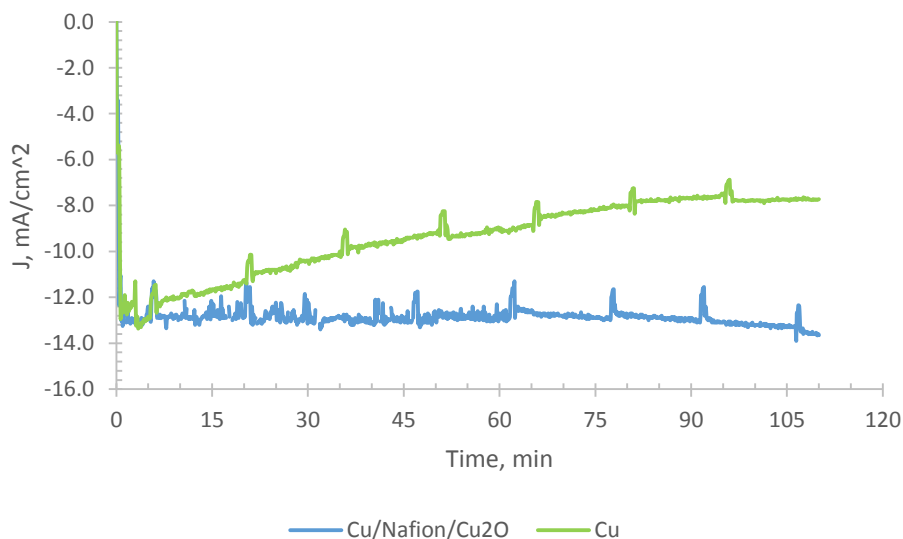
Figure 6.83. Current density profile of Cu/Nafion/Cu_2O and Cu electrodes during CO_2 reduction at -1.5V$_{NHE}$.

6.3.4.4. Comparison of Product Formation Rates with Cu

We then compared the formation rates of products between Cu/Nafion/Cu_2O electrode shown in Figure 6.84 and Cu electrode shown in Figure 6.85 (also given in Figure 4.5). The sampling points before 65 minutes were omitted because the high noise in current on the Cu/Nafion/Cu_2O electrode caused uncharacteristic pattern on its product distribution.

170
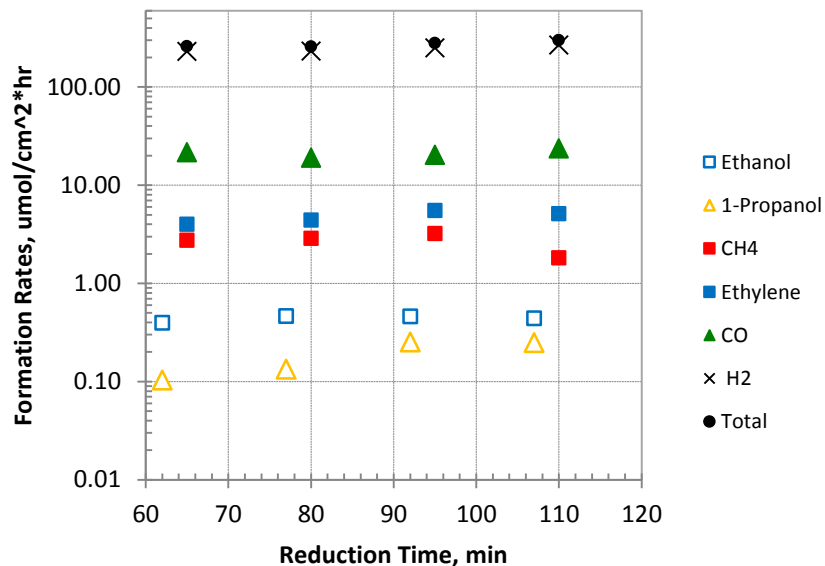
Figure 6.84. Formation rate of products during CO_2 reduction on $Cu/Nafion/Cu_2O$ electrode at $-1.5V_{NHE}$.

With our Cu electrode in Chapter 4, we observed methane, ethylene and CO products but did not detect any alcohol products. With our $Cu/Nafion/Cu_2O$ electrode, we observed ethanol and n-propanol, in addition to methane, ethylene and CO.
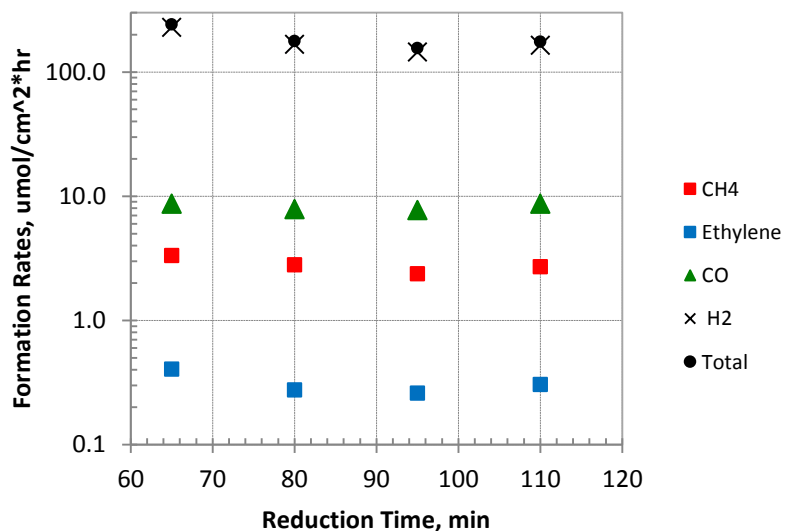
Figure 6.85. Formation rate of products during CO_2 reduction on Cu electrode at $-1.5V_{NHE}$.

171

We obtained higher CO formation rate of 21 µmol/cm^2*hr versus 8.3 µmol/cm^2*hr on Cu. We also achieved higher ethylene formation rate of 4.8 µmol/cm^2*hr versus 0.3 µmol/cm^2*hr on Cu. However this rate was not as high as those we have obtained on Toray supported and glassy carbon supported Cu_2O particles. Meanwhile, the methane rates were about the same at 2.7 µmol/cm^2*hr versus 2.8 µmol/cm^2*hr.

6.3.4.5. Comparison of Product Faradaic Efficiencies with Cu

We then compared the faradaic efficiencies of CO_2 products on Cu/Nafion/Cu_2O electrode shown in Figure 6.86 and on Cu electrode shown in Figure 6.87 (also given in Figure 4.6).
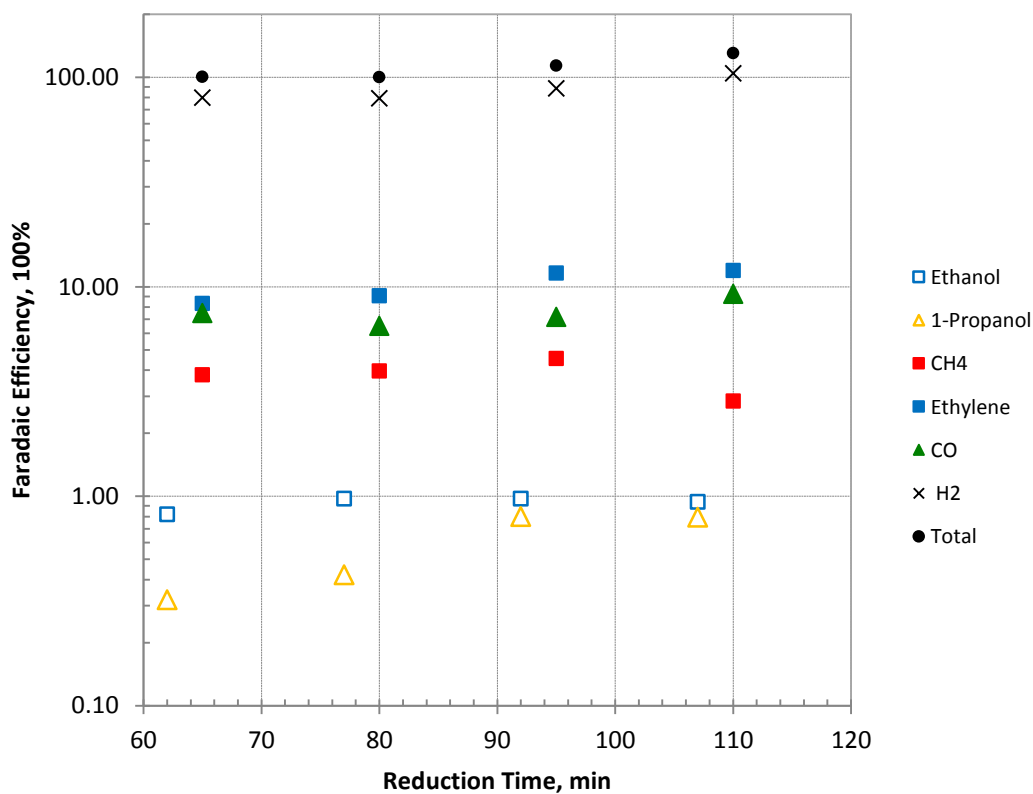
Figure 6.86. Faradaic efficiency of products during CO_2 reduction on Cu/Nafion/Cu_2O electrode at -1.5V$_{NHE}$.

The Cu/Nafion/Cu$_2$O and Cu electrodes showed completely different product distribution. With Cu, all products were at intermediate level, with selectivity in the order of 7.5% methane > 5.5% CO > 1.2% ethylene. With Cu/Nafion/Cu$_2$O electrode, the selectivity was in the order of 10% ethylene > 7.6% CO > 3.8% methane.

With these data, we computed the selectivity ratio C$_2$H$_4$/CH$_4$ and (C$_2$H$_4$ + CH$_4$)/CO. The C$_2$H$_4$/CH$_4$ selectivity ratio at -1.5V$_{NHE}$ was 2.6 which is higher than 0.9 on Hori's polycrystalline Cu sample at the same applied potential but lower than 14 on Hori's single crystal high index Cu(711) electrode.
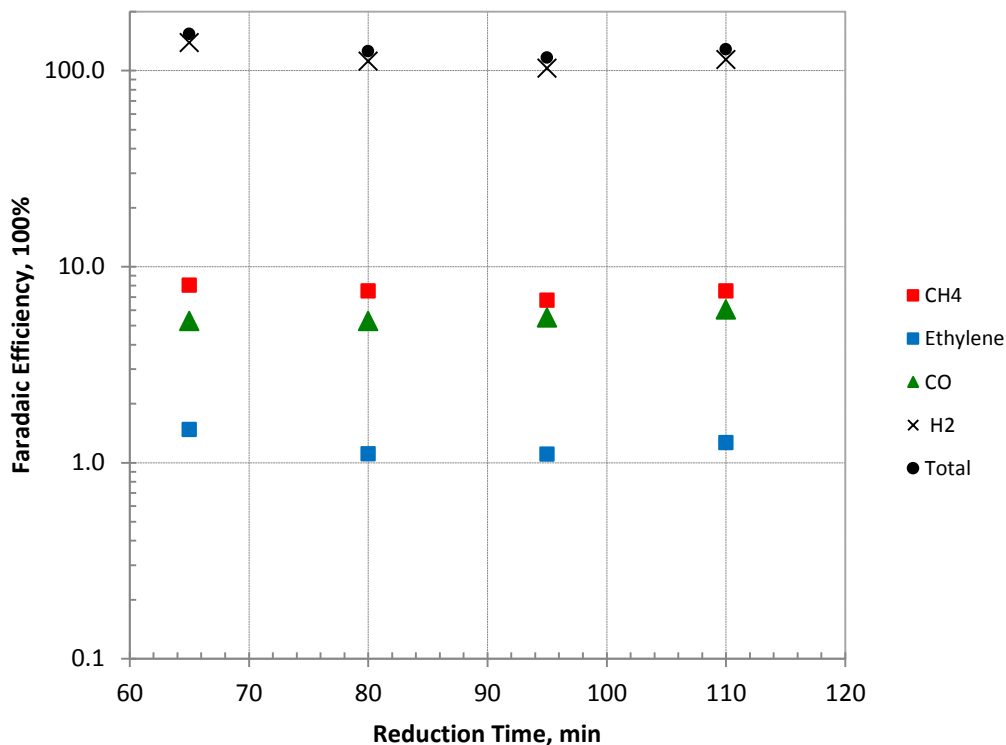
Figure 6.87. Faradaic efficiency of products during CO$_2$ reduction on Cu electrode at -1.5V$_{NHE}$.

The C$_2$H$_4$/CH$_4$ ratio was also lower compared to our Toray and glassy carbon supported Cu$_2$O catalysts. Meanwhile, the average (C$_2$H$_4$ + CH$_4$)/CO selectivity ratio was 1.8

compared to 32 (upper limit range of 9-32) on Hori's polycrystalline Cu sample at the same applied potential.

The lower C_2H_4/CH_4 ratio compared to our Toray and glassy carbon supported Cu_2O catalysts was expected because of the additional methane products generated by the Cu support substrate. Since we observed higher ethylene formation rates and better ethylene faradaic efficiencies with our Toray and glassy carbon supported Cu_2O particles, these results suggest that ethylene formation may also be promoted at the Cu-carbon interfaces.

6.4. Summary and Conclusion

To summarized, we examined the electrocatalytic activity of colloidal Cu_2O particles deposited on Toray, GL, and Cu support substrate. We looked at the products of CO_2 reduction on the Toray and GL support substrate and found that they only made trace amounts of CH_4 and CO.

With our baseline Toray/Nafion/Cu_2O electrode, we reproducibly achieved CO and hydrocarbon selectivity up to 50%, led by ethylene and CO. We obtained a C_2H_4/CH_4 selectivity ratio of 58.7 which was significantly higher than in Hori's polycrystalline Cu and Cu(711).

We observed better CO and ethylene selectivity with our baseline Toray/Nafion/Cu_2O sample (Cu_2O-360B) compared to the Cu_2O-0 and Cu_2O-30 electrodes. The reduction of larger Cu_2O particles may have resulted in the formation of denser grain boundaries which enhanced CO formation and selectivity to ethylene.

We have evidences which suggest that Nafion may be stabilizing the formation of ethylene by minimizing the degradation of Cu_2O sites that promote the latter. In the absence

of Nafion, hydrocarbon formation may be stabilized alternatively by applying an oscillating current flow. We have shown that the precipitating agent NaOH influenced the morphological uniformity of Cu_2O at higher concentration and consequently lowered the selectivity of Cu_2O to CO and hydrocarbon. As such, cubic Cu_2O particles perform better if they are not mixed with degenerate particles.

Finally, we obtained the CO_2 product distribution from two distinct Cu_2O particles at different potentials. We achieved 48% ethylene faradaic efficiency on reduced Cu_2O NP at $-1.7V_{NHE}$. These reduced Cu_2O particles consisted of Cu(111) surfaces which are known to preferably make methane, but may immediately be adjacent to Cu(100) surfaces. We also observed that in Cu_2O NP particles, high C_2H_4 selectivity was maintained even at more negative potential but not in the Cu_2O MP particles. Other effects may be influencing this difference and we have not monitored them at this point.

With our GL/Nafion/Cu_2O sample, we also observed similar CO_2 product distribution in that the ethylene to methane selectivity ratio was higher compared to that of polycrystalline Cu. We obtained higher ethylene and methane selectivity versus our Toray supported Cu_2O particles. Meanwhile our results on Cu/Nafion/Cu_2O suggest that ethylene formation may be promoted both at the oxide derived Cu surfaces and Cu-carbon boundaries.

CHAPTER 7
SUMMARY, CONCLUSIONS AND RECOMMENDATIONS

7.1. Summary and Conclusions

We have compared the electrocatalytic activity of polycrystalline Cu, electrochemically deposited Cu_2O and colloidal Cu_2O particles using kinetics and potential dependence experiments in order to determine the role of oxide during the electrochemical reduction of CO_2. The Cu_2O particles were made up of low index cubes with size ranging from 40 nm to 900 nm, depending on the catalyst preparation condition. The Cu_2O electrodes were deposited to Toray carbon fiber, glassy carbon and polycrystalline copper support substrates using different Nafion/Cu_2O mass ratios.

With polycrystalline Cu, we achieved 7.5% methane faradaic efficiency with formation rate of 2.8 $\mu mol/cm^2*hr$, 5.5% CO faradaic efficiency with formation rate of 8.3 $\mu mol/cm^2*hr$ and 1.2% ethylene faradaic efficiency with formation rate of 0.3 $\mu mol/cm^2*hr$ during CO_2 reduction at $-1.5V_{NHE}$. Our potential dependence results showed methane formation started at $-1.3V_{NHE}$ while ethylene formation started at $-1.5V_{NHE}$. The methane faradaic efficiency was higher than ethylene faradaic efficiency at the potential range considered ($-1.30V_{NHE}$ to $-1.75V_{NHE}$). We did not detect ethanol and n-propanol.

With electrodeposited Cu_2O film supported on Cu ($Cu/_{ECD}Cu_2O$), we achieved 0.09% methane faradaic efficiency with formation rate of 0.06 $\mu mol/cm^2*hr$, 1.5% CO faradaic efficiency with formation rate of 4.3 $\mu mol/cm^2*hr$, 5.2% ethylene faradaic efficiency with formation rate of 2.5 $\mu mol/cm^2*hr$, 1.1% ethanol faradaic efficiency with formation rate of 0.5 $\mu mol/cm^2*hr$ and 0.6% n-propanol faradaic efficiency with formation rate of 0.2 $\mu mol/cm^2*hr$ during CO_2 reduction at $-1.5V_{NHE}$.

We obtained better ethylene formation with Cu_2O film electrodeposited on CuO sublayer ($Cu/_{TH}CuO/_{ECD}Cu_2O$ electrode). The product distribution was 9.5% ethylene faradaic efficiency with formation rate of 9.0 $\mu mol/cm^2*hr$, 3.7% ethanol faradaic efficiency with formation rate of 3.0 $\mu mol/cm^2*hr$, 3.0% CO faradaic efficiency with formation rate of 17 $\mu mol/cm^2*hr$, 2.8% n-propanol faradaic efficiency with formation rate of 1.5 $\mu mol/cm^2*hr$ and 0.05% methane faradaic efficiency with formation rate of 0.05 $\mu mol/cm^2*hr$.

With colloidal Cu_2O particles supported on Cu, we achieved 3.8% methane faradaic efficiency with formation rate of 2.7 $\mu mol/cm^2*hr$, 7.6% CO faradaic efficiency with formation rate of 21 $\mu mol/cm^2*hr$, 10% ethylene faradaic efficiency with formation rate of 4.8 $\mu mol/cm^2*hr$, 1.0% ethanol faradaic efficiency with formation rate of 0.5 $\mu mol/cm^2*hr$ and 0.5% n-propanol faradaic efficiency with formation rate of 0.2 $\mu mol/cm^2*hr$ during CO_2 reduction at -1.5V_{NHE}.

We achieved better ethylene formation with Cu_2O NP particles supported on Toray. The product distribution was 38% ethylene faradaic efficiency with formation rate of 18 $\mu mol/cm^2*hr$, 5.1% CO faradaic efficiency with formation rate of 18 $\mu mol/cm^2*hr$ and 0.6% methane faradaic efficiency with formation rate of 0.5 $\mu mol/cm^2*hr$.

The baseline $Toray/Nafion/Cu_2O$ electrode showed the best over-all hydrocarbon formation. The product distribution was 28% ethylene faradaic efficiency with formation rate of 13 $\mu mol/cm^2*hr$, 4.8% ethanol faradaic efficiency with 2.3 $\mu mol/cm^2*hr$, 16.0% CO faradaic efficiency with formation rate of 41 $\mu mol/cm^2*hr$ and 0.5% methane faradaic efficiency with formation rate of 0.4 $\mu mol/cm^2*hr$.

These results show that Cu_2O catalysts are different from Cu catalysts. Particularly, Cu catalysts have better methane selectivity while Cu_2O catalysts have better ethylene selectivity. Quantitatively, the C_2H_4/CH_4 ratio on Cu was 0.2 while the ratio on both electrodeposited Cu_2O film and colloidal Cu_2O particles was near 60. The Cu_2O particles were reducible and the derived particles consisted of higher number of low-coordinated active sites than Cu which we propose were responsible for the increased ethylene selectivity. The colloidal Cu_2O particles also showed better hydrocarbon formation than electrodeposited Cu_2O film and better CO selectivity than Cu. Meanwhile, a number of SEM images indicated that Nafion preserved some of the Cu_2O particles and helped improve and stabilize hydrocarbon formation, particularly ethylene.

Our different kinetics and potential dependence studies have shown that Cu_2O particles reduce CO_2 differently than Cu particles. The results were consistent with the most agreed aspects of the CO_2 reduction pathways. The first one is the branch point between desorption of CO_{ads} intermediate and further reduction of CO_{ads} intermediate to hydrocarbons/alcohols. The second one is the C-C coupling step. The reduced Cu_2O particles produced catalytic sites that better promote the coupling of C_{ads} intermediate to form C_{2+} products such as ethylene, ethanol and n-propanol. At this point, it is not clear which C_{ads} intermediates participate in the coupling step and could possibly be via the dimerization of CO_{ads} as suggested by Schouten's group or coupling of CH_{2ads} as suggested by Nie's group. In addition to coupling step, the additional steps to ethanol and n-propanol also remain unclear. Our results showed that ethanol and n-propanol were kinetically more difficult routes than ethylene.

Besides the type of catalyst used, the product distribution was kinetically dynamic and primarily influenced by potential. At low cathodic potential (less than -1.25V_{NHE}), we only observed H_2 and CO. H_2 is produced from reduction of H_2O while CO is the first step of CO_2 activation. At high cathodic potential (greater than -1.25V_{NHE}), ethylene, methane, ethanol and n-propanol were also produced. At these potentials, CO_{ads} intermediates acquired sufficient potential energy to undergo several hydrogenation steps.

7.2. Recommendations

We have provided multiple quantitative results that showed Cu_2O catalysts have significantly higher C_2H_4/CH_4 selectivity ratio than polycrystalline Cu. Colloidal Cu_2O particles would be the preferred catalyst to improve production of the industrially important product ethylene.

For future work, we suggest two ways of stabilizing the active sites. The first one involves controlling the size of the oxide-derived Cu particles. Since dispersed Cu particles are more active towards ethylene formation due to the presence of greater fraction of low coordinated Cu atoms, the surface area of these nanoparticles must be maintained. We suggest introducing carbon black during the wet reduction synthesis of Cu_2O.

The second one involves stabilizing the Cu(I) active site by adding an ALD layer of TiO_2. We have observed unreduced Cu_2O particles that have been subjected to high potential electrolysis. Meanwhile, Li and Kanan (2012) never ruled out the possibility of residual oxide. If the oxidized state of Cu can be maintained, the role of oxide on the electrocatalytic activity of Cu can be better understood. Cu supported on TiO_2 was observed to lower the activation energy towards CO_2 formation in Water Gas Shift Reaction (WGS). In particular, the metal-oxide interface improved the dissociation of H_2O

to OCOH intermediate (Rodriguez et al. 2009). We suggest dipping a thermally oxidized Cu electrode in 1% titanium isopropoxide, $Ti[OCH(CH_3)_2]_4$ solution followed by a second thermal oxidation.

We also suggest further examining the role of Nafion on the enhancement and stabilization of ethylene (and ethanol) formation observed in Chapter 5 Section 5.3.3 and Chapter 6 Section 6.3.2.4 by performing CO_2 reduction on Nafion-coated colloidal Cu_2O electrode and Cu foil.

Finally, we suggest applying electrochemical preparation techniques to synthesize ZnO/Cu_2O catalyst used in other energy applications e.g. water gas shift reactions and methanol synthesis. Reports have suggested that ZnO stabilizes oxidized Cu in hydrogenation reactions (Le et al. 2011). Introduction of Zn helped disperse Cu atoms and enhanced binding of intermediates in methanol synthesis (Behrens et al. 2012). Suggested technique is to electrodeposit a thin layer of ZnO to electrodeposited Cu_2O film from a plating bath consisting of 0.01M $Zn(NO_3)_2.6H_2O$. We had performed preliminary studies on ZnO electrochemical deposition.

BIBLIOGRAPHY

Aurian-Blajeni, B., M.H. Habib, I. Taniguchi and J.O'M. Bockris. 1983. "The Study of Adsorbed Species During the Photoassisted Reduction of Carbon Dioxide at a p-Cadmium Telluride Electrode." *Journal of Electroanalytical Chemistry and Interfacial Electrochemistry* 157(2): 399-404.

Aylmer-Kelly, A.W.B., A. Bewick, P.R. Cantrill and A.M. Tuxford. 1973. "Studies of Electrochemically Generated Reaction Intermediates Using Modulated Specular Reflectance Spectroscopy." *Faraday Discussions of the Chemical Society* 56: 96-107.

Bard, A. J. and L. R. Faulkner. 2001. "Electrochemical Methods: Fundamentals and Applications." *John Wiley and Sons, Inc*.

Bard, A. J., R. Parsons and J. Jordan. 1985. "Standard Potentials in Aqueous Solutions." *CRC Press*.

Beden, B., A. Bewick, M. Razaq and J. Weber. 1982. "On the Nature of Reduced Carbon Dioxide: An IR Spectroscopic Investigation." *Journal of Electroanalytical Chemistry and Interfacial Electrochemistry* 139(1): 203-206.

Behrens, M., F. Studt, I. Kasatkin, S. Kühl, M. Hävecker, F. Abild-Pedersen, S. Zander, F. Girgsdies, P. Kurr, B-L Kniep, M. Tovar, R.W. Fischer, J.K. Nørskov and R. Schlögl. 2012. "The Active Site of Methanol Synthesis over $Cu/ZnO/Al_2O_3$ Industrial Catalysts." *Science* 336: 893-897.

Bidault, F., D.J.L. Brett, P.H. Middleton and N.P. Brandon. 2009. "Review of Gas Diffusion Cathodes for Alkaline Fuel Cells." *Journal of Power Sources* 187: 39–48.

Bowker, M., R.A. Hadden, H. Houghton, J.N.K. Hyland, K.C. Waugh. 1988. "The Mechanism of Methanol Synthesis on Copper/Zinc Oxide/Alumina Catalysts." *Journal of Catalysis* 109 (2): 263–273.

Bugayong, J. and G.L. Griffin. 2013. "Electrochemical Reduction of CO_2 using Supported Cu_2O Nanoparticles." Electrochemical Synthesis of Fuels 2, *Electrochemical Society Transactions* 58 (2): 81-89.

Bugayong, J. and G.L. Griffin. 2013. "Electrochemical Reduction of CO_2 using Supported Cu_2O Catalysts." Electrochemical Interfaces for Energy Storage and Conversion - Fundamental Insights from Experiments to Computations, *Materials Research Society Proceedings* 1542.

Chandrasekaran, K. and J.O'M. Bockris. 1987. "In-situ Spectroscopic Investigation of Adsorbed Intermediate Radicals in Electrochemical Reactions: Carbon Dioxide(1-) (CO2-) on Platinum." *Surface Science* 185(3): 495-514.

Chang, T. Y., R. M. Liang, P. W. Wu, J. Y. Chen and Y. C. Hsieh. 2009. "Electrochemical Reduction of CO_2 by Cu_2O-Catalyzed Carbon Clothes." *Materials Letters* 63: 1001-1003.

Chen, K. and D. Xue. 2013. "Crystallisation of Cuprous Oxide." *International Journal of Nanotechnology* 10 (1/2): 4-12.

Ciobica, I.M. and R. A. van Santen. 2003. "Carbon Monoxide Dissociation on Planar and Stepped Ru(0001) Surfaces." *Journal of Physical Chemistry B* 107 (16): 3808–3812.

Cook, R. L., R. C. MacDuff and A. F. Sammells. 1988. "On the Electrochemical Reduction at Carbon Dioxide at In Situ Electrodeposited Copper." *Journal of the Electrochemical Society* 135(6): 1320-1326.

De Jongh, P. 2012. "Porous Materials as Catalysts and Catalyst Supports." *Catalysis*: 431-444.

Desimoni, E. and B. Brunetti. 1980. "Glassy Carbon as Electrode Material in Electroanalytical Chemistry." *Analytica Chimica Acta* 119: l-24.

Det Norske Veritas. 2011. "Carbon Dioxide Utilization: Electrochemical Conversion of CO_2 – Opportunities and Challenges." *Research and Innovation*, Position Paper 07-2011: 1-20.

DeWulf, D.W. and A.J. Bard. 1988. "The Electrochemical Reduction of CO_2 to CH_4 and C_2H_4 at Cu/Nafion Electrodes (Solid Polymer Electrolyte Structures)." *Catalysis Letters* 1: 73-80.

DeWulf, D. W., T. Jin and A. J. Bard. 1989. "Electrochemical and Surface Studies of Carbon Dioxide Reduction to Methane and Ethylene at Copper Electrodes in Aqueous Solutions." *Journal of the Electrochemical Society* 136(6): 1686-1691.

Durand, W. J., A. A. Peterson, F. Studt, F. Abild-Pederson and J. K. Norskov. 2011. "Structure Effects on the Energetics of the Electrochemical Reduction of CO_2 by Copper Surfaces." *Surface Science* 605: 1354-1359.

Filipic, G. and U. Cvelbar. 2012. "Copper Oxide Nanowires: A Review of Growth." *Nanotechnology* 23: 1-16.

Frese, K. W. 1991. "Electrochemical Reduction of CO_2 at Intentionally Oxidized Copper Electrodes." *Journal of Electrochemical Society* 138 (11): 3338 – 3344.

Frese Jr, K.W. in: B.P. Sullivan, K. Krist, H.E. Guard (Eds.). 1993. "Electrochemical and Electrocatalytic Reactions of Carbon Dioxide." <u>Electrochemical Reduction of CO_2 at Solid Electrodes</u> (Chapter 6): Elsevier, Amsterdam, 145.

Friebe, P., P. Bogdanoff, N. Alonso-Vante and H. Tributsch. 1997. "A Real-Time Mass Spectroscopy Study of the (Electro)chemical Factors Affecting CO_2 Reduction at Copper." *Journal of Catalysis* 168: 374-385.

Gabriele, C., E.A. Quadrelli and S. Perathoner. 2013. "Catalysis for CO_2 Conversion: A Key Technology for Rapid Introduction of Renewable Energy in the Value Chain of Chemical Industries." *Energy and Environmental Science* 6: 1711-1731.

Gattrell, M., N. Gupta and A. Co. 2006. "A Review of the Aqueous Electrochemical Reduction of CO_2 to Hydrocarbons at Copper." *Journal of Electroanalytical Chemistry* 594: 1-19.

Ghadimkhani, G., N. R. de Tacconi, W. Chanmanee, C. Janaky and K. Rajeshwar. 2013. "Efficient Solar Photoelectrosynthesis of Methanol from Carbon Dioxide Using Hybrid $CuO-Cu_2O$ Semiconductor Nanorod Arrays." *Chemical Communications* 49: 1297-1299.

Golden, T.D., M.G. Shumsky, Y. Zhou, R.A. VanderWerf, R.A. Van Leeuwen and J.A. Switzer. 1996. "Electrochemical Deposition of Copper (I) Oxide Films." *Chemistry of Materials* 8: 2499.

Griffin, G.L. and J. Bugayong. 2014. "Electrochemical Reduction of CO_2 Using Copper Oxide Nanoparticles Supported on Glassy Carbon Electrodes." Electrochemical Interfaces for Energy Storage and Conversion - Fundamental Insights from Experiments to Computations, *Materials Research Society Proceedings* 1677.

Henrie, J., S. Kellis, S.M. Schultz and A. Hawkins. 2004. "Electronic Color Charts for Dielectric Films on Silicon." *Optics Express* 12 (7): 1464-1469.

Hori Y., K. Kikuchi, A. Murata and S. Suzuki. 1986. "Production of Methane and Ethylene in Electrochemical Reduction of Carbon Dioxide at Copper Electrode in Aqueous Hydrogencarbonate Solution." *Chemistry Letters* 897-898.

Hori, Y., A. Murata, R. Takahashi and S. Suzuki. 1988. "Enhanced Formation of Ethylene and Alcohols at Ambient Temperature and Pressure in Electrochemical Reduction of Carbon Dioxide at a Copper Electrode." *Journal of the Chemical Society, Chemical Communications*: 17-19.

Hori, Y., A. Murata and R. Takahashi. 1989. "Formation of Hydrocarbons in the Electrochemical Reduction of Carbon Dioxide at a Copper Electrode in Aqueous Solution." *Journal of the Chemical Society, Faraday Transactions* 85(8): 2309-2326.

Hori, Y., R. Takahashi, Y. Yoshinami and A. Murata. 1997. "Electrochemical Reduction of CO at a Copper Electrode." *The Journal of Physical Chemistry B* 101 (36): 7075–7081.

Hori Y., O. Koga, Y. Watanabe and T. Matsuo. 1998. "FTIR Measurements of Charge Displacement Adsorption of CO on Poly- and Single Crystal (100) of Cu Electrodes." *Electrochimica Acta* 44 (8–9): 1389–1395.

Hori, Y. 2008. "Electrochemical CO_2 Reduction on Metal Electrodes." Edited by C. Vayenas et al.. *Modern Aspects of Electrochemistry* 42: 89 – 189.

Hori, Y., I. Takahashi, O. Koga and N. Hoshi. 2002. "Selective Formation of C_2 Compounds from Electrochemical Reduction of CO_2 at a Series of Copper Single Crystal Electrodes." *Journal of Physical Chemistry* 106: 15-17.

Hori, Y., I. Takahashi, O. Koga and N. Hoshi. 2003. "Electrochemical Reduction of Carbon Dioxide at Various Series of Copper Single Crystal Electrodes." *Journal of Molecular Catalysis A:* Chemical 199 (1-2): 39-47.

Hori, Y. in: W. Vielstich, H.A. Gasteiger, A. Lamm (Eds.). 2003. <u>Handbook of Fuel Cells</u> (Chapter 48), Vol. 2, Wiley, West Sussex, England, 720–733.

Huanga, H. and X. Wang. 2014. "Recent progress on carbon-based support materials for electrocatalysts of direct methanol fuel cells." *Journal of Materials Chemistry A* 2 (18): 6266-6291.

Inderwildi, O.R.; S.J. Jenkins and D.A. King. 2008. "Fischer−Tropsch Mechanism Revisited: Alternative Pathways for the Production of Higher Hydrocarbons from Synthesis Gas." *Journal of Physical Chemistry C* 112 (5): 1305–1307.

Intergovernmental Panel on Climate Change. 2007. "Climate Change 2007: Synthesis Report." *An assessment of the Intergovernmental Panel on Climate Change* 1-73.

Ito, H., T. Maeda, A. Nakano and H. Takenaka. 2011. "Properties of Nafion Membrane Under PEM Water Electrolysis Conditions." *International Journal of Hydrogen Energy* 36: 10527-10540.

Jermann, B. and J. Augustynski. 1994. "Long-term Activation of the Copper Cathode in the Course of CO_2 Reduction." *Electrochimica Acta* 39 (11-12): 1891-1896.

Kostecki, R. and J. Augustynski. 1994. "Electrochemical Reduction of CO_2 at an Activated Silver Electrode." *Berichte der Bunsen-Gesellschaft* 98(12): 1510-15.

Kuhl, K. P., E. R. Cave, D. N. Abram and T. F. Jaramillo. 2012. "New Insights into the Electrochemical Reduction of Carbon Dioxide on Metallic Copper Surfaces." *Energy and Environmental Science* 10: 1039 – 1048.

Kuo, C. H. and M. H. Huang. 2010. "Morphologically Controlled Synthesis of Cu_2O Nanocrystals and their Properties." *Nano Today* 5: 106-116.

Kyriacou, G. and A. Anagnostopoulos. 1992. "Electroreduction of CO_2 on Differently Prepared Copper Electrodes. The Influence of Electrode Treatment on the Current Efficiencies." *Journal of Electroanalytical Chemistry* 322: 233-246.

Le, M., M. Ren, Z. Zhang, P. T. Sprunger, R. L. Kurtz and J. C. Flake. 2011. " Electrochemical Reduction of CO_2 to CH_3OH at Copper Oxide Surfaces." *Journal of the Electrochemical Society* 158(5): E45-E49.

Lewis, N. S. 2007. "Powering the Planet." *Engineering and Science* 2: 12-23.

Lewis, N. S. and D. G. Nocera. 2006. "Powering the Planet: Chemical Challenges in Solar Energy Utilization." *Proceedings of the National Academy of Sciences* 103(43): 15729-15735.

Li, C. W. and M. W. Kanan. 2012. "CO_2 Reduction at Low Overpotential on Cu Electrodes Resulting from the Reduction of Thick Cu_2O Films." *Journal of the American Chemical Society* 134: 7231-7234.

Li, C.W., J. Ciston and M.W. Kanan. 2014. "Electroreduction of Carbon Monoxide to Liquid Fuel on Oxide-Derived Nanocrystalline Copper." *Nature*: 1-5.

Li, Q., P. Xu, B. Zhang, H. Tsai, S. Zheng, G. Wu and H.L. Wang. 2013. "Structure-Dependent Electrocatalytic Properties of Cu_2O Nanocrystals for Oxygen Reduction Reaction." *The Journal of Physical Chemistry C* 117: 13872−13878.

McQuillan, A.J., P.J. Hendra and M. Fleischmann. 1975. "Raman Spectroscopic Investigation of Silver Electrodes." *Journal of Electroanalytical Chemistry and Interfacial Electrochemistry* 65(2): 933-44.

Meyer, B.K., A. Polity, D. Reppin, M. Becker, P. Hering, B. Kramm, P.J. Klar, T. Sander, C. Reindl, C. Heiliger, M. Heinemann, C. Muller and C. Ronning. 2013. "The Physics of Copper Oxide (Cu_2O)." *Semiconductors and Semimetals* 88 (Oxide Semiconductors): 201-226.

Nakatsuji, H. and Z-M Hu. 2000. "Mechanism of Methanol Synthesis on Cu(100) and Zn/Cu(100) Surfaces: Comparative Dipped Adcluster Model Study." *International Journal of Quantum Chemistry* 77 (1): 341–349.

Nie, X., M. R. Esopi, M. J. Janik and A. Ashtagiri. 2013. "Selectivity of CO_2 Reduction on Copper Electrodes: The Role of the Kinetics of Elementary Steps." *Angewandte Chemie International Edition* 52: 2459-2462.

Noda, H., S.Ikeda, Y. Oda and K. Ito. 1989. "Potential Dependencies of the Products on Electrochemical Reduction of Carbon Dioxide at a Copper Electrode." *Chemistry Letters*: 289-292.

Nogami, G., H. ltagaki and R. Shiratsuch. 1994. "Pulsed Electroreduction of on Copper Electrodes-II." *Journal of the Electrochemical Society* 141 (5): 1138-1142.

Oda, I., H. Ogasawara and M. Ito. 1996. "Carbon Monoxide Adsorption on Copper and Silver Electrodes during Carbon Dioxide Electroreduction Studied by Infrared Reflection Absorption Spectroscopy and Surface-Enhanced Raman Spectroscopy." *Langmuir* 12 (4): 1094–1097.

Peighambardoust, S.J., S. Rowshanzamir and M. Amjadi. 2010. "Review of the Proton Exchange Membranes for Fuel Cell Applications." *International Journal of Hydrogen Energy* 35: 9349-9384.

Peterson, A. A., F. Abild-Pederson, F. Studt, J. Rossmeisl and J. K. Norskov. 2010. "How Copper Catalyzes the Electroreduction of Carbon Dioxide Into Hydrocarbon Fuels." *Energy and Environmental Science* 3: 1311-1315.

Rapier, R. and M. Thurber. 2013. "The Experts: What's the Best Way Forward on Nuclear Power?" *Journal Reports: Energy of The Wall Street Journal*. http://online.wsj.com/article/SB100014241278873238093045784285701530329336.html.

Rodrıguez, J.A., J. Evans, J. Graciani, J-B Park, P. Liu, J. Hrbek and J.F. Sanz. 2009. "High Water-Gas Shift Activity in $TiO_2(110)$ Supported Cu and Au Nanoparticles: Role of the Oxide and Metal Particle Size." *Journal of Physical Chemistry C* 113: 7364–7370.

Roy, Somnath C., Oomman K. Varghese, Maggie Paulose and Craig A. Grimes. 2010. "Toward Solar Fuels: Photocatalytic Conversion of Carbon Dioxide to Hydrocarbons." *ACSNano* 4 (3): 1259-1278.

Schouten, K. J. P., Y. Kwon, C. J. M. Van der Ham, Z. Qin and M. T. M. Koper. 2011. "A New Mechanism for the Selectivity to C_1 and C_2 Species in the Electrochemical Reduction of Carbon Dioxide on Copper Electrodes." *Chemical Science* 2: 1902-1909.

Sharma, S. and B.G. Pollet. 2012. "Support Materials for PEMFC and DMFC Electrocatalysts—A Review." *Journal of Power Sources* 208: 96–119.

Shetty, S.G., A.P.J. Jansen and R.A. van Santen. 2009. "Direct Versus Hydrogen-assisted CO Dissociation." *Journal of the American Chemical Society* 131(36): 12874-12875.

Shetty, S.G. and R.A. van Santen. 2010. "Hydrogen Induced CO Activation on Open Ru and Co Surfaces." *Physical Chemistry Chemical Physics* 12(24): 6330-6332.

Shiratsuchi, R., Y. Aikoh and G. Nogami. 1993. "Pulsed Electroreduction of C02 on Copper Electrodes." *Journal of the Electrochemical Society* 140 (12): 3479-3482.

Smith, B.D., D. E. Irish, P. Kedzierzawski and J. Augustynski. 1997. "A Surface Enhanced Roman Scattering Study of the Intermediate and Poisoning Species Formed during the Electrochemical Reduction of CO_2 on Copper." *Journal of the Electrochemical Society* 144 (12): 4288-4296.

Tang, W., A. A. Peterson, A. S. Varela, Z. P. Jovanov, L. Bech, W. J. Durand, S. Dahl, J. K. Norskov and I. Chorkendorff. 2012. "The Importance of Surface Morphology in Controlling the Selectivity of Polycrystalline Copper for CO_2 Electroreduction." *Physical Chemistry Chemical Physics* 14: 76-81.

Taniguchi, I. in: J.O'M. Bockris, R.E. White, B.E. Conway (Eds.). 1989. "Electrochemical and Photoelectrochemical Reduction of Carbon Dioxide." <u>Modern Aspects of Electrochemistry</u>: 20, 327-400.

Tsai, C-C., J. Bugayong, G.L. Griffin. 2012. "Role of Surface Oxide Layer during CO_2 Reduction at Copper Electrodes." Materials for Catalysis in Energy: Jiang, D., H.K. Kung, R. Jin, R.M. Rioux. *Materials Research Society Proceedings* 1446:59-64.

US Energy Information Administration. 2009. "Emissions of Greenhouse Gases in the United States 2009." *Independent Statistics and Analysis* March 2011: 1-78.

US Energy Information Administration. 2013. "February 2013 Monthly Energy Review." *Independent Statistics and Analysis* February 2013: 1-201.

Van der Linden, W.E. and J.W. Dieker. 1980. "Glassy Carbon as Electrode Material in Electroanalytical Chemistry." *Analytica Chimica Acta* 119: l-24.

Varcoe, J. R. and R. C. T. Slade. 2004. "Prospects for Alkaline Anion-Exchange Membranes in Low Temperature Fuel Cells." *Fuel Cells* 5: 187–200.

Wang, J., M. Musameh and Y. Lin. 2003. "Solubilization of Carbon Nanotubes by Nafion Towards the Preparation of Amperometric Biosensors." *Journal of the American Chemical Society* 25 (9): 2408-2409.

Wasmus, S., E. Cattaneo and W. Vielstich. 1990. "Reduction of Carbon Dioxide to Methane and Ethene - An On-line MS Study with Rotating Electrodes." *Electrochimica Acta* 35 (4): 771-775.

Whipple, D. T. and P. J. A. Kenis. 2010. "Prospects of CO_2 Utilization via Direct Heterogeneous Electrochemical Reduction." *The Journal of Physical Chemistry Letters* 1: 3451 – 3458.

Working Group III of the Intergovernmental Panel on Climate Change [Metz, B., O. Davidson, H.C. de Coninck, M. Loos, and L.A. Meyer (Eds.)]. 2005. "IPCC Special Report on Carbon Dioxide Capture and Storage." *Cambridge University Press*, Cambridge, United Kingdom and New York, NY, USA, 1-442.

Yaroslavtsev, A.B. 2013. "Perfluorinated Ion-Exchange Membranes." *Polymer Science, Ser. A* 55 (11): 674–698.

Zhao, Y.F., Y. Yang, C. Mims, C.H.F. Peden, J. Li and D. Mei. 2011. "Insight into Methanol Synthesis from CO_2 Hydrogenation on Cu(111): Complex Reaction Network and the Effects of H_2O." *Journal of Catalysis* 281(2): 199-211.

Zoolfakar, A.S., R.A. Rani, A.J. Morfa, A.P. O'Mullane and K. Kalantar-zadeh. 2014. "Nanostructured Copper Oxide Semiconductors: A Perspective on Materials, Synthesis Methods and Applications." *Journal of Materials Chemistry C* 2: 5247–5270.

APPENDIX I

PERMISSION TO REPRODUCE

ROYAL SOCIETY OF CHEMISTRY LICENSE
TERMS AND CONDITIONS

Sep 24, 2014

This is a License Agreement between Joel Bugayong ("You") and Royal Society of Chemistry ("Royal Society of Chemistry") provided by Copyright Clearance Center ("CCC"). The license consists of your order details, the terms and conditions provided by Royal Society of Chemistry, and the payment terms and conditions.

All payments must be made in full to CCC. For payment instructions, please see information listed at the bottom of this form.

License Number	3456290752570
License date	Aug 26, 2014
Licensed content publisher	Royal Society of Chemistry
Licensed content publication	Chemical Science
Licensed content title	A new mechanism for the selectivity to C1 and C2 species in the electrochemical reduction of carbon dioxide on copper electrodes
Licensed content author	K. J. P. Schouten,Y. Kwon,C. J. M. van der Ham,Z. Qin,M. T. M. Koper
Licensed content date	Jul 21, 2011
Volume number	2
Issue number	10
Type of Use	Thesis/Dissertation
Requestor type	academic/educational
Portion	figures/tables/images
Number of figures/tables /images	1
Format	print and electronic
Distribution quantity	7
Will you be translating?	no
Order reference number	None
Title of the thesis/dissertation	Electrochemical Reduction of CO2 on Supported Cu2O Catalysts
Expected completion date	Nov 2014
Estimated size	140
Total	0.00 USD
Terms and Conditions	

COPYRIGHT PERMISSION REQUEST FORM

Date: August 25 2014

To: The Chemical Society of Japan
5,Kanda-Surugadai,Chiyoda-ku,
Tokyo 101-8307, Japan

From: Joel Nino G. Bugayong
W339 Chemical Engineering Bldg.
Louisiana State University
South Stadium Drive,
Baton Rouge, LA, USA, 70803

Fax: +81-3-3292-6318
E-mail: info@chemistry.or.jp

Phone: 765-714-7882
Fax: 225-578-1476
E-mail: jbugay1@lsu.edu

I am preparing a paper entitled:

Electrochemical Reduction of CO$_2$ on Supported Cu$_2$O Catalysts

to appear in

Ph.D. Dissertation

which is published by

Louisiana State University Graduate School

Expected publication date: November 2014

I request your permission to include the following material in this and in all subsequent editions of this work to be published by Joel Nino G Bugayong or its licensees for distribution throughout the world, in all media including electronic/online and microfilm.

Title of Publication: Potential Dependencies of the Products on Electrochemical Reduction of Carbon Dioxide at a Copper Electrode

Author(s)/Editor(s): Hidetomo NODA, Shoichiro IKEDA, Yoshiyuki ODA and Kaname ITO

Title of Selection: Chemistry Letters

Year: 1989 Vol.: 18 No.: 2

Figure(s)/Table(s): 1, 2 and 3   Page(s): 291-292

We hereby grant permission for the use of the material requested above.

Nobuyuki Kawashima
Executive Director
The Chemical Society of Japan

Date: August. 26. 2014

Our Ref. No. CY-RT 14-224

194

CAMBRIDGE UNIVERSITY PRESS LICENSE
TERMS AND CONDITIONS

Oct 27, 2014

This is a License Agreement between Joel Bugayong ("You") and Cambridge University Press ("Cambridge University Press") provided by Copyright Clearance Center ("CCC"). The license consists of your order details, the terms and conditions provided by Cambridge University Press, and the payment terms and conditions.

All payments must be made in full to CCC. For payment instructions, please see information listed at the bottom of this form.

License Number	3497390558356
License date	Oct 27, 2014
Order Content Publisher	Cambridge University Press
Order Content Publication	MRS Online Proceedings Library
Order Content Title	Electrochemical Reduction of CO_2 using Copper Oxide Nanoparticles supported on Glassy Carbon Electrodes
Order Content Author	Gregory L. Griffin and Joel Bugayong
Order Content Date	Jun 9, 2014
Volume number	1677
Issue number	-1
Start page	0
End page	0
Type of Use	Dissertation/Thesis
Requestor type	Author
Portion	Full article
Author of this Cambridge University Press article	Yes
Author / editor of the new work	Yes
Order reference number	None
Territory for reuse	World
Title of your thesis / dissertation	Electrochemical Reduction of CO2 on Supported Cu2O Catalysts
Expected completion date	Nov 2014
Estimated size(pages)	140
Billing Type	Invoice
Billing address	W209 Chem Engg Bldg S Stadium Dr
	Baton Rouge, LA 70803
	United States
TAX (0.00%)	0.00 USD
Total	**0.00 USD**

Request for Permission to Reproduce or Re-Publish ECS Material

Please fax this form to: The Electrochemical Society (ECS), Attn: Permissions Requests, 1.609.730.0629. You may also e-mail your request to: copyright@electrochem.org. Include all the information as required on this form. Please allow 3-7 days for your request to be processed.

I am preparing a (choose one): ☐ paper ☐ chapter ☐ book ☒ thesis

entitled: _ELECTROCHEMICAL REDUCTION OF CO2 ON SUPPORTED Cu2O CATALYSTS_

to be published by: _Joel Nino G Bugayong_

in an upcoming publication entitled: _LSU Electronic Thesis and Dissertation_

I request permission to use the following material in the publication noted above, and request nonexclusive rights for all subsequent editions and in all foreign language translations for distribution throughout the world.

Description of material to be used—Indicate what material you wish to use (figures, tables, text, etc.) and give the full bibliographic reference for the source publication. You may attach a separate list, organized by ECS title.

Full Article of Bugayong, J. and G.L. Griffin. 2013. "Electrochemical Reduction of CO2 using Supported Cu2O Nanoparticles," Electrochemical Synthesis of Fuels 2, Electrochemical Society Transactions 58 (2): 81-89.

Signature: **Joel Nino Bugayong** Digitally signed by Joel Nino Bugayong DN: cn=Joel Nino Bugayong, o, ou, email=jbugay5@lsu.edu, c=US Date: 2014.10.27 22:00:32 -05'00'   Date: October 27, 2014

Name: Joel Nino Bugayong

Address: W339 Chemical Engineering Bldg South Stadium Drive Baton Rouge LA 70803

Telephone: 7657147882   Fax: _____

E-mail: jbugay1@lsu.edu

Permission is granted to reproduce the above-referenced material. Please acknowledge the author(s) and publication data of the original material, and include the words: "Reproduced by permission of The Electrochemical Society."

10/30/14
Date

John Lewis, Associate Director of Publications

198

LSU

permission to reproduce content
3 messages

Joel Bugayong <jbugay1@tigers.lsu.edu>   Thu, Oct 30, 2014 at 11:01 AM
To: Narasi.Sridhar@dnv.com, Davion.M.Hill@dnv.com

Dear Sridhar and Hill,

Greetings from Louisiana.

I would like to obtain your permission to reproduce Figure 2 from your paper in 2011 on:

"Carbon Dioxide Utilization Electrochemical Conversion of CO2 – Opportunities and Challenges."

I will be using this figure for my Ph.D dissertation.

Thank you for your attention. I look forward to hearing from you.

Sincerely yours,

Joel

Sridhar, Narasi <Narasi.Sridhar@dnvgl.com>   Thu, Oct 30, 2014 at 12:26 PM
To: Joel Bugayong <jbugay1@tigers.lsu.edu>, "Hill, Davion M." <Davion.M.Hill@dnvgl.com>

Yes, you may do so with proper attribution. Thank you.

Best regards

Sridhar

Dr. Narasi Sridhar, FNACE

Director, Materials and Sensors Program
DNV GL - Strategic Research & Innovation

E-mail narasi.sridhar@dnvgl.com
Mobile +1 614 787 8249 | Direct +1 614 761 6920| Fax +1 614 761 1633

From: Joel Bugayong [mailto:jbugay1@tigers.lsu.edu]
Sent: Thursday, October 30, 2014 12:01 PM
To: Sridhar, Narasi; Hill, Davion M.
Subject: permission to reproduce content

[Quoted text hidden]

Joel Bugayong <jbugay1@tigers.lsu.edu>   Thu, Oct 30, 2014 at 12:31 PM
To: "Sridhar, Narasi" <Narasi.Sridhar@dnvgl.com>

Thank you very much Dr. Sridhar!
[Quoted text hidden]

VITA

Joel, a graduate student from the Philippines, is in the process of completing his Ph.D. degree in Chemical Engineering at Louisiana State University (LSU). He is married to Dr. Patrisha. They are expecting a baby boy around December of 2014 and will be given the name Lorenzo Theodore.

Joel earned his Bachelor's degree in Chemical Engineering at the University of the Philippines Los Baños (UPLB) in 2004 with the distinction *magna cum laude* and *#1 ranking* from the engineering class of 175 students. While in college, he participated in a study abroad program at Michigan State University in spring of 2002 where he experienced his first ever snow. After college, he taught at the UPLB Institute of Chemistry as an Instructor for 2 ½ years. He then pursued further studies in the United States where he finished his Master's degree in Chemical Engineering at LSU in 2011.

Joel is a lifetime member of the Phi Kappa Phi Honor Society and received the Phi Kappa Phi Award of Excellence in 2007 and the Chevron Engineering Graduate Assistantship Supplement Award in 2014. His interests include catalysis, renewable energy, electrochemical processes, separation methods, interface phenomena, semiconductor device fabrication, analytical techniques and teaching.

During his free time, he was actively engaged in both on campus and off campus volunteer works. Among his most memorable participations were during the grass planting activities at the Barataria Waterway in Lafitte, Louisiana in August of 2010 and at the Bayou Sauvage National Wildlife Refuge in Lacombe, Louisiana in May of 2011. In those activities, he was half submerged in muddy swamp.